



UNIVERSIDADE FEDERAL DO CEARÁ
CENTRO DE TECNOLOGIA
DEPARTAMENTO DE ENGENHARIA METALÚRGICA E DE MATERIAIS
PROGRAMA DE PÓS-GRADUAÇÃO EM ENGENHARIA E CIÊNCIA DE
MATERIAIS

FRANCISCO ANDERSON DE SOUSA LIMA

APPLICATION OF TRANSITION-METAL-OXIDE-BASED
NANOSTRUCTURED THIN FILMS ON THIRD GENERATION
SOLAR CELLS

FORTALEZA - CE - BRASIL

2015

FRANCISCO ANDERSON DE SOUSA LIMA

APPLICATION OF TRANSITION-METAL-OXIDE-BASED
NANOSTRUCTURED THIN FILMS ON THIRD GENERATION
SOLAR CELLS

Thesis submitted to the Graduate Program in Materials Science and Engineering in partial fulfillment of the requirements for the degree of Doctor in Materials Science and Engineering. Concentration area: Physical and Mechanical Properties of Materials.

Advisors: Prof. Dr. Igor Frota de Vasconcelos

Prof. Dr. Mónica Lira-Cantú

FORTALEZA - CE - BRASIL

Dados Internacionais de Catalogação na Publicação
Universidade Federal do Ceará
Biblioteca de Pós-Graduação em Engenharia - BPGE

-
- L698a Lima, Francisco Anderson de Sousa.
Application of transition-metal-oxide-based nanostructured thin films on third generation solar cells / Francisco Anderson de Sousa Lima. – 2015.
247 f. : il. color. , enc. ; 30 cm.
- Tese (doutorado) - Universidade Federal do Ceará, Centro de Tecnologia, Departamento de Engenharia Metalúrgica e de Materiais, Programa de Pós-Graduação em Engenharia e Ciência de Materiais, Fortaleza, 2015.
Área de Concentração: Propriedades Físicas e Mecânicas dos Materiais
Orientação: Prof. Dr. Igor Frota de Vasconcelos
Coorientação: Prof. Dr. Mônica Lira-Cantú
1. Ciência dos materiais 2. Filmes finos. 3. Eletrodeposição. 4. Células solares. I. Título.

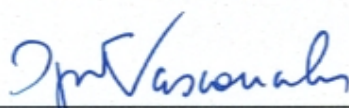
FRANCISCO ANDERSON DE SOUSA LIMA

APPLICATION OF TRANSITION-METAL-OXIDE-BASED
NANOSTRUCTURED THIN FILMS ON THIRD GENERATION
SOLAR CELLS

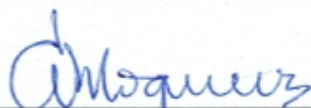
Doctorate Thesis submitted to the Graduate Program
in Materials Science and Engineering in partial ful-
fillment of the requirements for the degree of Doc-
tor in Materials Science and Engineering. Concen-
tration area: Physical and Mechanical Properties of
Materials.

Approval date: 30/October/2015

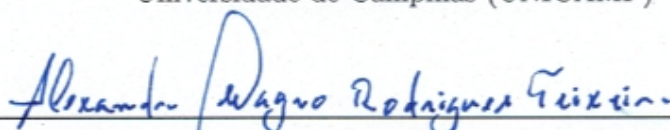
THESIS COMMITTEE



Prof. Dr. Igor Frota de Vasconcelos (Advisor)
Universidade Federal do Ceará (UFC)



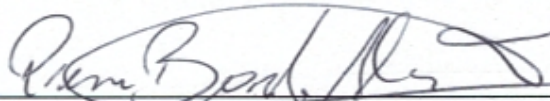
Prof. Dr. Ana Flávia Nogueira
Universidade de Campinas (UNICAMP)



Prof. Dr. Alexandre Magno Rodrigues Teixeira
Universidade Regional do Cariri (URCA)



Prof. Dr. Pedro de Lima Neto
Universidade Federal do Ceará (UFC)



Prof. Dr. Pierre Basílio Almeida Fachine
Universidade Federal do Ceará (UFC)

To Andrea, Carolina, my parents and my brothers

ABSTRACT

One of the greatest challenges of our time is to devise means to provide energy in a sustainable way to attend an exponentially growing demand. The energy demand is expected to grow 56% by 2040. In this context, the use of clean and sustainable sources of energy is imperative. Among these sources, solar energy is the only one which can meet the total world energy requirement even considering such large growth in demand. The solar power incident on the Earth's surface every second is equivalent to 4 trillion 100-watt light bulbs. Photovoltaic solar cells are one of several ways to harness solar energy. These cells convert solar energy directly into electricity. Commercial photovoltaic devices are already a reality, but their share of the world energy matrix is still quite small, mainly due to the high costs. Next generation photovoltaics open a number of new possibilities for photovoltaic energy applications that can potentially decrease the overall cost of energy production. Transition metal semiconductor oxides are promising materials that can be produced by low cost methods and offer interesting new features. The use of these materials in next generation photovoltaics is therefore a very promising and interesting application. In this thesis work zinc, titanium and vanadium oxides were used in next generation solar cells. Thin films of zinc oxide were synthesized by the low cost and environmentally friendly techniques of electrodeposition and hydrothermal synthesis and applied as working electrodes in highly efficient dye sensitized solar cells (DSSCs). The films were characterized by structural and optical techniques while the cells were tested by current *vs.* voltage and quantum efficiency measurements. The efficiencies of these cells were as high as 2.27% using ZnO thin films without any post deposition treatment. Moreover, natural dyes extracted from plants of northeastern Brazil were applied as sensitizers in DSSCs assembled with commercial available TiO₂ as working electrode. The natural dyes were extracted employing very simple methods and were characterized by XPS and UPS techniques. Their band alignments were shown to be compatible with the TiO₂ as well as with the mediator electrolyte. The efficiency of DSSCs sensitized with natural dyes were as high as 1.33%. Finally, water based V₂O₅ was used as hole transport medium (HTM) in conventional organic solar cells (OSCs) and ITO-free, plastic OSCs. The results obtained with V₂O₅ were compared with the results obtained from cells assembled with PEDOT:PSS, which is the most used HTM. This comparison showed that the use of V₂O₅ as HTM can lead to more efficient OSCs. The stability of these devices were evaluated by tests applying the ISOS standards ISOS-D-1, ISOS-L-1 and ISOS-O-1. A UV-filter and a protective graphene oxide (GO) layer were employed seeking to improve the stability of OSCs. The combination of both UV-filter and GO protective layer was shown to be the most effective way to improve the stability of these devices.

Keywords: Thin films, Electrodeposition, Solar cells, Oxide semiconductors.

RESUMO

Um dos maiores desafios do nosso tempo é desenvolver formas para fornecer energia de forma sustentável para atender uma demanda que cresce exponencialmente e que deverá crescer 56% até 2040. Neste contexto, o uso de fontes limpas e sustentáveis de energia é um imperativo. Entre essas fontes, a energia solar é a única que pode satisfazer a necessidade total de energia do mundo, mesmo considerando o crescimento na demanda. A potência solar incidente na superfície da Terra a cada segundo é equivalente a 4 trilhões de lâmpadas de 100 watts. Células solares fotovoltaicas são uma das várias maneiras de aproveitar a energia solar, convertendo-a diretamente em eletricidade. Dispositivos comerciais fotovoltaicos já são uma realidade, mas a sua participação na matriz energética mundial ainda é muito pequena, principalmente devido aos seus custos elevados. Células fotovoltaicas de nova geração abrem uma série de novas possibilidades para aplicações de energia fotovoltaica que pode diminuir o custo total de produção de energia. Óxidos semicondutores de metais de transição são materiais promissores que podem ser produzidos através de métodos de baixo custo e que possuem características interessantes. Por conseguinte, o uso destes materiais em energia fotovoltaica de próxima geração se apresenta com uma aplicação promissora. Nesta tese de doutorado óxidos de zinco, titânio e vanádio foram utilizados em células solares de próxima geração. Filmes finos de óxido de zinco foram sintetizados por eletrodeposição e síntese hidrotérmica. Os filmes foram aplicados como eletrodos de trabalho em células solares sensibilizadas por corante (DSSCs) altamente eficientes. Os filmes foram caracterizados por técnicas estruturais e óticas enquanto que as células foram testadas por medidas de corrente *vs.* voltagem e de eficiência quântica. A eficiência dessas células atingiu 2,27% utilizando filmes finos de ZnO sem qualquer tratamento pós-deposição. Além disso, corantes naturais extraídos de plantas do nordeste do Brasil foram aplicados como sensibilizadores em DSSCs montadas com TiO₂ comercial utilizado como eletrodo de trabalho. Os corantes naturais foram extraídas empregando métodos simples e foram caracterizados por espectroscopia de fotoelétrons excitados por raios X e por radiação ultravioleta, XPS e UPS respectivamente. Seus alinhamentos de banda se mostraram compatíveis com o TiO₂ e com o eletrodo de regeneração. A eficiência das DSSCs sensibilizadas com corantes naturais chegou a 1,33%. Finalmente, V₂O₅ à base de água foi usado como material transportador de buracos (HTM) em células solares orgânicas (OSCs) convencionais e OSCs de plástico construídas sem ITO. Os resultados obtidos com V₂O₅ foram comparados com os resultados de células construídas com PEDOT:PSS, que é o HTM mais utilizado. Esta comparação revelou que o uso de V₂O₅ como HTM pode levar a OSCs mais eficientes. A estabilidade destes dispositivos foi avaliada por testes aplicando os padrões ISOS-D-1, ISOS-L-1 e ISOS-O-1. O uso de filtros ultravioleta e de uma camada protetora de óxido de grafeno reduzido foi testado com o intuito de melhorar a estabilidade desses dispositivos. O uso de uma combinação de ambos se mostrou a forma mais efetiva de melhorar a estabilidade das OSCs.

Palavras-chave: Filmes finos, Eletrodeposição, Células solares, Óxidos semicondutores.

LIST OF FIGURES

2.1	Total primary power density supply from sunlight.	7
2.2	World energy production by source in 2012.	8
2.3	Potential energy production per year of various types of renewable energy sources.	9
2.4	Global photovoltaic cumulative installed capacity share in 2012 (MW; %).	10
2.5	Total irradiance on the horizontal plane on Germany (left) and on Brazil (right).	11
2.6	Solar spectrum at the top of the atmosphere and sea level.	12
2.7	Solar spectrum at the top of the atmosphere and sea level.	13
2.8	Schematic representation of indirect and direct energy band gap transitions.	19
2.9	Schematic representation of a simple conventional solar cell.	21
2.10	Schematic representation circuit of a photovoltaic cell.	23
2.11	Example of a typical $J - V$ curve for a solar cell.	25
2.12	Effect of the modification of series resistance and shunt resistance in $J - V$ curves of a solar cell.	26
2.13	Schematic overview of the exciton formation by the absorption of the light.	31
2.14	Schematic overview of the exciton formation in a molecule.	32
2.15	Schematic overview of a dye-sensitized solar cell.	34
2.16	Basic electron transfer process occurring within a DSSC.	35
2.17	Schematic representation of single layer, bilayer and bulk heterojunction organic solar cells.	37
2.18	Schematic energy level diagram of a typical bilayer organic solar cell.	39
2.19	Normal and inverted architecture bulk heterojunction solar cells.	41
2.20	Absorption and thermalization losses in a organic solar cell.	41
2.21	Film absorption of two polymers with different band gaps in a blend with PCBM.	42
2.22	Tandem OSCs with normal and inverted architectures.	43
2.23	Band alignment for different TMOs with photovoltaic polymers and electron-accepting fullerene derivatives.	47
2.24	Comparison between the stability of organic solar cells.	47
2.25	Stick-and-ball representation of ZnO crystal structures.	50
2.26	Stick-and-ball representation of TiO ₂ crystal structures.	51
2.27	Crystallization of V ₂ O ₅ thin films.	53
3.1	The X-ray diffraction of crystallographic planes.	74
3.2	Pear-shaped volume probed by different microprobe signals.	78
3.3	XPS setup.	79
4.1	Experimental set up for the electrodeposition of ZnO thin films.	88
4.2	The XRD diffractograms for electrochemically deposited ZnO thin films.	92

4.3	Raman spectra for as-prepared electrodeposited ZnO thin films.	94
4.4	The SEM micrographs of electrochemically deposited ZnO electrodes. . . .	95
4.5	The SEM micrographs for ZnO electrodes electrochemically deposited at different electrolyte concentrations.	97
4.6	High-resolution SEM micrographs for electrodeposited ZnO thin films. . . .	98
4.7	The TEM micrograph for an electrochemically deposited ZnO electrode. . . .	99
4.8	An overview of the XPS results for electrodeposited ZnO thin films.	101
4.9	high-resolution XPS results for electrodeposited ZnO thin films.	102
4.10	Valence band UPS spectrum for an electrodeposited ZnO thin film.	103
4.11	Details of valence band edge and secondary electron cutoff obtained for an electrodeposited ZnO thin film	104
4.12	Tauc's plot: calculation of bandgap of electrodeposited ZnO thin film. . . .	105
4.13	Band diagram for an electrodeposited ZnO thin film.	106
4.14	Band alignment for a DSSC using electrochemically deposited ZnO as a working electrode.	107
4.15	$J - V$ curves and IPCE spectra for DSSCs assembled with five samples of electrodeposited ZnO thin films.	108
4.16	Dye desorption study for DSSCs assembled with electrochemically deposited ZnO.	110
4.17	$J - V$ curves and IPCE spectra for the cell that presents a significant improvement in performance after aging under ambient conditions.	111
4.18	Time evolution of the photovoltaic parameters under ambient conditions for a DSSC assembled with electrodeposited ZnO.	112
5.1	Schematic representation of the growth of ZnO nanorods on ITO substrates using hydrothermal synthesis from an initial layer of ZnO nanoparticles. . . .	123
5.2	Experimental set up for the growth of ZnO nanorod thin films.	125
5.3	XRD diffractograms for hydrothermally synthesized ZnO thin films.	128
5.4	Comparison of XRD results for hydrothermally synthesized and electro- chemically deposited ZnO thin films.	129
5.5	Raman spectrum for hydrothermally synthesized ZnO thin films.	130
5.6	Raman spectra comparisons for hydrothermally synthesized and electro- chemically deposited ZnO thin films.	130
5.7	SEM images for the hydrothermally synthesized and electrodeposited thin films.	131
5.8	TEM images for a hydrothermally synthesized ZnO NR.	132
5.9	An overview of the XPS results for hydrothermally synthesized ZnO thin films.	133
5.10	High-resolution XPS results for hydrothermally synthesized ZnO thin films. . . .	134
5.11	Comparison between the valence band UPS spectra for ZnO thin films deposited by hydrothermal synthesis and electrochemical deposition.	135
5.12	Details of the secondary electron cutoff and valence band edge obtained for hydrothermally synthesized ZnO thin films.	136
5.13	Comparison between the optical bandgaps for ZnO thin films deposited by hydrothermal synthesis and electrochemical deposition.	137
5.14	Band diagram for hydrothermally synthesized and electrodeposited ZnO thin films.	137

5.15	Band alignment for DSSCs using hydrothermally synthesized and electrochemically deposited ZnO as working electrodes.	138
5.16	$J - V$ curve and IPCE spectra for the best devices using ZnO synthesized by hydrothermal synthesis assembled with different FTO substrates.	139
5.17	$J - V$ curves and normalized PCE for the dye loading time study.	140
5.18	Comparison between $J - V$ curves for devices assembled with ZnO working electrodes prepared by hydrothermal synthesis and electrochemical deposition.	141
6.1	UV-Vis absorption spectra of the extracts from the three natural dyes used as sensitizers in DSSCs.	153
6.2	Tauc's plot for the natural dyes used as sensitizers in DSSCs.	154
6.3	Valence band UPS spectra for the natural dyes used as sensitizers in DSSCs.	155
6.4	Band alignment diagrams for the natural dyes used as sensitizers in DSSCs.	156
6.5	$J - V$ curves for the DSSCs sensitized with the three natural dyes.	158
6.6	IPCE spectra for the DSSCs sensitized with the three natural dyes.	159
7.1	Structure of the ITO-Free flexible OPV.	165
7.2	LBG polymer P10 was used as active material for the second active layer.	166
7.3	Mini-roll coater used to fabricate ITO-free, plastic OSCs.	167
7.4	Effect of the thickness variation of V_2O_5 on the PCE of organic solar cells.	170
7.5	Comparison between PEDOT:PSS and V_2O_5 as HTL in plastic organic solar cells.	172
7.6	Light-beam induced-current image for the best OSCs with V_2O_5 as the HTL.	172
7.7	$J - V$ curve and IPCE spectrum for the best OSC with V_2O_5 as the HTL.	173
7.8	Effect of the use of highly conductive PEDOT:PSS as part of the back electrode in plastic organic solar cells.	174
7.9	Comparison between water-based V_2O_5 and ViPr-based V_2O_5 as HTL in plastic solar cells.	175
7.10	XPS survey for two different V_2O_5 thin films.	176
7.11	High-resolution XPS spectra of the V $2p$ and O $1s$ core-levels for two different V_2O_5 thin films.	177
7.12	Valence band UPS spectra for two different V_2O_5 thin films.	179
7.13	Optical microscopy images for the V_2O_5 thin film in the normal OSC configuration.	180
7.14	Comparison between water-based V_2O_5 and PEDOT:PSS as HTL in normal configuration plastic solar cells.	181
7.15	Optical microscopy images for the V_2O_5 thin film for the normal OSC configuration on top of silver nanowires.	182
7.16	$J - V$ curve for normal configuration OSCs.	182
7.17	$J - V$ curve and IPCE spectrum for a TPSC using V_2O_5 as part of the recombination layer.	184
8.1	$J - V$ curves for OSCs before and after an aging time of 90 days inside a glove box.	194
8.2	$J - V$ curves, for best performing, OSCs aged in air for 60 days without and with encapsulation.	195

8.3	Time evolution of the photovoltaic parameters for two OSCs under accelerated degradation test (solar simulator conditions) for 72 h, according to the ISOS-L-1 standard.	197
8.4	$J - V$ curves for OSCs degradation tests under solar simulator conditions over 72 h, according to the ISOS-L-1 standard.	198
8.5	Time evolution of the photovoltaic parameters for two OSCs tested under real outdoor conditions over 1000 h, according to the ISOS-O-1 standard.	200
8.6	$J - V$ curves for OSCs degradation tests under real outdoor conditions, according to the ISOS-O-1 standard. Insets show IPCE spectra.	201
8.7	Time evolution of the photovoltaic parameters of plastic OSCs under real outdoor degradation tests using V_2O_5 or PEDOT:PSS as HTL, according to the ISOS-O-1 standard.	202
8.8	Comparison between the PCE evolution for plastic OSCs under real outdoor degradation tests using V_2O_5 or PEDOT:PSS as HTL, according to the ISOS-O-1 standard.	203
8.9	$J - V$ curves for plastic OSCs under real outdoor degradation tests using V_2O_5 or PEDOT:PSS as HTL, according to the ISOS-O-1 standard.	204
8.10	Time evolution of the photovoltaic parameters for OSCs without UV filter with UV filter during real outdoor degradation tests according to the ISOS-O-1 standard.	206
8.11	$J - V$ curves for OSCs degradation tests, without and with UV filter, under real outdoor conditions, according to the ISOS-O-1 standard.	207
8.12	$J - V$ curves and IPCE spectra for OSCs degradation test, without UV filter, obtained under solar simulator conditions before and after the ISOS-O-1 2500-h stability test. The inset shows normalized IPCE spectra.	208
8.13	$J - V$ curves and IPCE spectra for OSCs degradation tests, with UV filter, obtained under solar simulator conditions before and after the ISOS-O-1 2500-h stability test. The inset shows normalized IPCE spectra.	209
8.14	$J - V$ curves for OSCs degradation tests, without and with a GO protective layer, under real outdoor conditions, according to the ISOS-O-1 standard.	210
8.15	Time evolution of the photovoltaic parameters for OSCs degradation tests, without and with a GO protective layer, under real outdoor conditions, according to the ISOS-O-1 standard.	211
8.16	$J - V$ curves and IPCE spectra for OSCs degradation tests with a GO protective layer under solar simulator conditions, before and after the ISOS-O-1 2500-h stability test. The inset shows normalized IPCE spectra.	212
8.17	Comparison between the time evolution of PCE for OSC with and without a GO protective layer.	213
8.18	$J - V$ curves for OSCs degradation tests, without and with a combination of UV filter and GO protective layer, under real outdoor conditions, according to the ISOS-O-1 standard.	214
8.19	Time evolution of the photovoltaic parameters for OSCs degradation tests without and with a combination of UV filter and GO protective layer, under real outdoor conditions, according to the ISOS-O-1 standard.	215
8.20	$J - V$ curves and IPCE spectra for OSCs degradation tests with a combination of UV filter and GO protective layer, before and after the ISOS-O-1 2500-h stability test. The inset shows normalized IPCE spectra.	215

LIST OF TABLES

2.1	Samples and deposition conditions.	48
2.2	General physical properties of ZnO semiconductor material.	49
4.1	Samples and deposition conditions for the electrodeposited ZnO thin films.	91
4.2	EDX results for the composition of electrodeposited ZnO electrodes.	100
4.3	XPS results for the composition of electrodeposited ZnO electrodes.	102
4.4	Photovoltaic parameters for DSSCs assembled with electrochemically deposited ZnO.	109
5.1	XPS results for the composition of hydrothermally synthesized ZnO electrodes.	133
5.2	Photovoltaic parameters for DSSCs assembled with hydrothermally synthesized ZnO on different FTO substrates.	139
5.3	Photovoltaic parameters for DSSC assembled with electrochemically deposited and hydrothermally synthesized ZnO.	142
7.1	Photovoltaic parameters for ITO-free OSCs: PEDOT:PSS or V ₂ O ₅ as HTL.	170
7.2	Comparison of the photovoltaic parameters for OSCs with and without highly conductive PEDOT.	174
7.3	Binding energy values of the main peaks in the XPS spectra for the two different V ₂ O ₅ thin films.	178
7.4	Comparison of the photovoltaic parameters for OSCs in normal configuration with PEDOT:PSS or V ₂ O ₅ as HTL.	180
8.1	Average photovoltaic parameters of OSCs before and after an aging time of 90 days inside a glove box.	195
8.2	Average photovoltaic parameters of OSCs aged in air for 60 days without and with encapsulation, according to the ISOS-D-1 standard.	196
8.3	Photovoltaic parameters for OSCs degradation tests under solar simulator conditions over 72 h, according to the ISOS-L-1 standard.	199
8.4	Photovoltaic parameters for OSCs degradation tests under real outdoor conditions, according to the ISOS-O-1 standard.	201
8.5	Photovoltaic parameters for OSCs degradation tests, without and with UV filter, under real outdoor conditions, according to the ISOS-O-1 standard.	207
8.6	Photovoltaic parameters for OSCs degradation tests, without and with UV filter, obtained under solar simulator conditions, before and after the ISOS-O-1 2500-h stability test.	209
8.7	Photovoltaic parameters for OSCs degradation tests, without and with a GO protective layer, under real outdoor conditions, according to the ISOS-O-1 standard.	211

8.8	Photovoltaic parameters for OSCs degradation tests, without and with a combination of UV filter and GO protective layer, under real outdoor conditions, according to the ISOS-O-1 standard.	214
-----	---	-----

LIST OF SYMBOLS AND ABBREVIATIONS

TMO	Transition metal oxide
TFPV	Thin film photovoltaics
TFT	Thin film transistor
FET	Field effect transistor
LED	Ligth emitted diode
BIPV	Building integrated photovoltaics
ZnO	Zinc oxide
TiO ₂	Titanium dioxide
V ₂ O ₅	Vanadium pentoxide
DSSC	Dye sensitized solar cell
OSC	Organic solar cell
SEM	Scanning electron microscopy
TEM	Transmission electron microscopy
UV-Vis	Ultraviolet-visible spectroscopy
XRD	X-ray diffraction
EDX	Energy dispersive X-ray spectroscopy
XPS	X-ray photoelectron spectroscopy
UPS	Ultraviolet photoelectron spectroscopy
$J - V$	Current-voltage
IPCE	Incident photon to collected electron efficiency
ITO	Indium doped tin oxide
FTO	Fluorine doped tin oxide
IEA	International Energy Agency
EIA	U.S. Energy Information Administration

EPIA	European Photovoltaic Industry Association
IR	Infrared
AM	Air mass
e.m.f.	Electron motive force
E_C	Conduction band
E_V	Valence band
E_G	Forbidden energy band gap
E_F	Fermi level
T	Absolute temperature
K	Boltzmann constant
N_C	Density of states in the conduction band
N_V	Density of states in the valence band
n	Electron density
p	Hole density
N_D	Donor concentration
N_A	Acceptor concentration
n	Electron density
I_L	Light generated current
I_D	Voltage dependent current lost
$I_s h$	Current lost due to shunt resistance
I_0	Saturation current
R_s	Series resistance
A	Ideality factor
V_T	Thermal voltage
R_s	Series resistance
T_c	Cell's working temperature
R_s	Shunt resistance
V_{oc}	Open circuit voltage
J_{sc}	Short circuit current density

P	Power density
P_{max}	Maximum power density
V_{max}	Maximum open circuit voltage
J_{max}	Maximum short circuit current density
FF	Fill factor
η	Solar cell efficiency
EQE	External quantum efficiency
IPCE	Incident photon to collected electron efficiency
TCO	Transparent conductive oxide
N_c	Number of generated charges
N_f	Number of incident photons per unit time
I_λ	Intensity of the source
N_c	Number of generated charges
AM	Air mass
OPV	Organic photovoltaic
XSC	Excitonic solar cell
CdTe	Cadmium teluride
CIGS	Copper indium gallium selenide
CZTS	Copper zinc tin sulfide
CZTS	Copper zinc tin selenide
CIS	Copper indium selenide
EBE	Exiton binding energy
DA	Donor acceptor interface
CT	Charge transfer
HOMO	Highest occupied molecular orbital
LUMO	Lower unoccupied molecular orbital
BHJ	Bulk heterojunction
η_A	Quantum efficiency for exciton generation
L_D	Difusion lenght

η_{ED}	Quantum efficiency for exciton diffusion
η_{CT}	Quantum efficiency for exciton separation
μ	Mobility
η_{CC}	Quantum efficiency for charge collection
NP	Nanoparticle
P3HT	Poly(3-hexylthiophene-2,5-diyl)
PCBM	[6,6]-phenyl-C ₆₁ -butyric acid methyl ester
PEDOT:PSS	Poly(3,4-ethylenedioxythiophene) polystyrene sulfonate
MoO ₃	Molybdenum oxide
HTL	Hole transport layer
ETL	Electron transport layer
F	Faraday constant
R	Gas constant
p	Pressure
I_k	Bragg intensity
F_k	Structure factor
TEM	Transmission electron microscopy
h	Planck's constant
SEM	Scanning electron microscopy
SAED	Selected-area electron diffraction
BF	Bright field
DF	Dark field
HREM	High-resolution electron microscopy imaging
KE	Kinetic energy
BE	Biding energy
ϕ	Work function
Z	Atomic number
VBM	Valence band maximum
DOS	Density of states

E_{ion}	Ionization energy
α	Absorption coefficient
WE	Working electrode
CE	Counter electrode
RE	Reference electrode
EBPVD	Electron beam physical vapor deposition
LO	Longitudinal-optical
TO	Transversal-optical
NR	Nanorod
HMT	Hexamethylenetetramine
ED	Electrodeposited
HS	Hydrothermally synthesized
LP	Lower binding energy peak
MP	Medium binding energy peak
HP	High binding energy peak
LC FTO	Less conductive fluorine doped tin oxide
MC FTO	More conductive fluorine doped tin oxide
HC-P	Highly conductive PEDOT:PSS
LBG	Low band gap
LBIC	Light-beam Induced-current
ICN2	Institut Català de Nanociència i Nanotecnologia
DTU	Danmarks Tekniske Universitet
TPSC	Tandem polymer solar cell
R2R	Roll-to-roll
ISOS	International summit on OPV stability
GO	Graphene oxide

CONTENTS

PREFACE	1
1. INTRODUCTION AND OBJECTIVES	3
1.1 Objectives	4
1.2 Outline	5
2. SOLAR CELLS	7
2.1 Solar cells: general aspects	7
2.1.1 The importance of solar energy	7
2.1.2 Solar spectrum	11
2.1.3 A brief history of the photovoltaic technology	13
2.1.4 Physical principles	14
2.1.5 Semiconductors	15
2.1.5.1 Properties of semiconductors	16
2.1.5.2 $p - n$ junctions	20
2.1.5.3 Solar cells operation	21
2.1.6 Characterization techniques	22
2.1.6.1 Current density <i>vs.</i> voltage: $J - V$ curves	22
2.1.6.2 External quantum efficiency	26
2.1.7 Thin Film Photovoltaics	28
2.1.7.1 Excitons	30
2.1.7.2 Dye sensitized solar cells	32
2.1.7.3 Organic solar cells	36
2.2 Transition metal oxides for next generation solar cells	43
2.2.1 Why transition metal oxides for next generation solar cells?	44
2.2.2 Introduction to transition metal oxides	46
2.2.3 Zinc oxide (ZnO)	48
2.2.4 Titanium dioxide (TiO_2)	50
2.2.5 Vanadium oxide (V_2O_5)	51
2.2.6 Synthesis of oxide semiconductors	53
2.2.6.1 Electrodeposition	53
2.2.6.2 Hydrothermal synthesis	55
2.2.6.3 Sol-gel	56
2.3 References	57
3. CHARACTERIZATION TECHNIQUES	73
3.1 X-ray diffraction	73
3.2 Electron microscopy	74
3.3 Energy dispersive X-ray spectroscopy	76

3.4	Photoelectron spectroscopy	77
3.4.1	X-ray photoelectron spectroscopy	78
3.4.2	Ultraviolet photoelectron spectroscopy	80
3.5	Ultraviolet-visible absorption spectroscopy	81
3.6	Raman spectroscopy	82
3.7	References	83
4.	ELECTRODEPOSITED ZINC OXIDE THIN FILMS FOR DYE SENSITIZED SOLAR CELLS	84
4.1	Introduction	84
4.2	Water-based fabrication of ZnO	85
4.2.1	Electrodeposition of ZnO	86
4.2.2	Practical matters	87
4.3	Experimental procedure	87
4.3.1	Synthesis of nanostructured ZnO thin films	87
4.3.2	Structural, morphological and electrical characterization of the films	89
4.3.3	Solar cell fabrication and characterization	90
4.4	Structural, morphological, compositional, and electrical analysis	90
4.4.1	X-ray diffraction	91
4.4.2	Raman spectroscopy	92
4.4.3	Electron microscopy	94
4.4.4	Energy dispersive X-ray spectroscopy	99
4.4.5	X-ray photoelectron spectroscopy	100
4.4.6	Band diagram	103
4.5	Photovoltaic performance	107
4.6	Conclusions	113
4.7	References	113
5.	HYDROTHERMALLY SYNTHESIZED ZINC OXIDE THIN FILMS FOR DYE SENSITIZED SOLAR CELLS	121
5.1	Introduction	121
5.2	Hydrothermal synthesis of ZnO	122
5.3	Experimental procedure	124
5.3.1	Synthesis of ZnO nanorod thin films	124
5.3.2	Structural, morphological and electrical characterization of the films	125
5.3.3	Solar cell fabrication and characterization	126
5.4	Structural, morphological, compositional, and electrical analysis	127
5.4.1	X-ray diffraction	127
5.4.2	Raman spectroscopy	128
5.4.3	Electron microscopy	131
5.4.4	X-ray photoelectron spectroscopy	132
5.4.5	Band diagram	134
5.5	Photovoltaic performance	138
5.5.1	Comparison between hydrothermally synthesized and electrodeposited ZnO thin films as working electrodes in DSSCs	140
5.6	Conclusions	143
5.7	References	143

6.	NATURAL DYES FOR DYE SENSITIZED SOLAR CELLS	149
6.1	Introduction	149
6.2	Experimental procedure	151
6.2.1	Preparation of dye sensitizer solutions	151
6.2.2	Preparation of electrodes	151
6.2.3	DSSC assembly	152
6.2.4	Characterization	152
6.3	Results and discussion	153
6.3.1	Light absorption by natural dyes	153
6.3.2	Determination of the HOMO and LUMO levels of the natural dyes	154
6.3.3	Band diagram	156
6.3.4	Photovoltaic performance	157
6.4	Conclusions	158
6.5	References	159
7.	VANADIUM PENTOXIDES FOR ITO-FREE PLASTIC ORGANIC SOLAR CELLS	163
7.1	Introduction	163
7.2	Experimental	164
7.2.1	Materials	164
7.2.2	Coating procedure	167
7.3	Application of water-based V_2O_5 in flexible ITO-free OPVs	169
7.3.1	Comparison between V_2O_5 and PEDOT:PSS as HTL for ITO-free plastic OPVs	169
7.3.2	Comparison between water-based V_2O_5 and ViPr-based V_2O_5 as the HTL for ITO-free plastic OPVs	173
7.3.3	Application of V_2O_5 as HTL in normal configuration, ITO-free flexible OPVs	179
7.3.4	Application of V_2O_5 as part of the recombination layer in tandem OPVs	183
7.4	Conclusions	184
7.5	References	184
8.	STABILITY OF ORGANIC SOLAR CELLS	191
8.1	Introduction	191
8.2	Experimental	192
8.2.1	Sample preparation	192
8.2.2	Stability tests	193
8.3	Results and discussion	194
8.3.1	Degradation under inert atmosphere in dark	194
8.3.2	Degradation of OSCs according to the ISOS-D-1 standard	195
8.3.3	Degradation of OSCs according to the ISOS-L-1 standard	196
8.3.4	Degradation of OSCs according to the ISOS-O-1 standard	199
8.3.4.1	V_2O_5 vs. PEDOT:PSS	202
8.3.5	Strategies for improving the stability of OSCs	204
8.3.5.1	UV filter	205
8.3.5.2	Graphene oxide protective layer	209

8.3.5.3	UV filter and graphene oxide protective layer	213
8.4	Conclusion	216
8.5	References	216
9.	CONCLUSIONS AND FUTURE WORK	223
9.1	Conclusions	223
9.2	Future work	224

PREFACE

This doctoral thesis was developed in partnership between the Graduate Program in Materials Science and Engineering of Universidade Federal do Ceará (UFC) and the Catalan Institute of Nanoscience and Nanotechnology (ICN2) of the Universitat Autònoma de Barcelona (UAB). The thesis work was directed by Prof. Igor Frota de Vasconcelos of UFC and Prof. Mónica Lira-Cantú of ICN2-UAB.

My first year in the program was spent in UFC attending courses and developing the idea for the research project. Some preliminary research work was done during this first year. The next two years were spent in ICN2 doing the core of the research work. The first year in Barcelona was financed by the Brazilian Research Council (CNPq) through a fellowship within the Science Without Borders program while the second year was financed by ICN2. My last few months were spent in UFC where I devoted my time to finish writing this thesis. This work was also partially funded by the Research Support Foundation of the State of Ceará (FUNCAP) through FUNCAP's International Cooperation Program.

.....

I would like to thank CNPq, FUNCAP and ICN2 for the financial support mentioned above, without which I would not have been able to finish this work. I also would like to thank UFC and the Graduate Program in Materials Science and Engineering for the opportunity to pursue a doctorate degree.

I would like to express my very deep gratitude to ICN2 for allowing me to use its impressive infrastructure and for the logistical support offered in Barcelona, besides the aforementioned financial support.

I am also extremely grateful to Dr. Monica Lira-Cantu for her generosity in giving me so many opportunities to learn, apply new knowledge and to participate in many new projects. Also by always willing to discuss new ideas and results and for trusting me by giving me autonomy and responsibilities which helped me develop new skills that are being very useful in my career.

I have been very lucky for having two advisors. I have to say an enormous thank you to Prof. Igor Frota de Vasconcelos for his always valuable lessons and discussions, his commitment to my education, his great help in the preparation of documents written and for always being open to new ideas.

I would like to thank the members of the committee Prof. Ana Flávia Nogueira, Prof. Alexandre Magno Rodrigues Teixeira, Prof. Pedro de Lima Neto, and Prof. Pierre Basílio Almeida Fechine for their valuable time.

I also would like to thank to my friends who have helped me during this journey. Oliveira Junior, Mauricio, and Kleyton of UFC for the help with the heavy courses; Thiago, Iran, and Gislania of UFC for the very interesting discussions; Irene and Gerardo of ICN2 for the help on my first contact with the next generation solar cells; Raphael and Aurelie for the good reception and the help in using the new equipment; Fernando and Andressa for the fruitful talks; Amador for the big number of good suggestions; Guillaume for the patience and the help with XPS and UPS.

Last but not least, I can not forget to thank the Government of the State of Ceará for the four-year leave I was granted in order to work on my doctorate.

1. INTRODUCTION AND OBJECTIVES

Transition metal oxides (TMOs), from the simplest binary oxides to the more complex oxide compounds, are a class of materials with great variety of functional properties. These span from insulating, semiconducting or metallic behavior, to ferroelectricity, magnetism, magneto resistance or superconductivity, among many more. TMOs are now regularly applied in many printed electronic and optoelectronic devices such as thin film photovoltaics (TFPVs), thin film and field effect transistors (TFTs and FETs respectively), light emitting diodes (LEDs), etc. Common to most of these devices are their maturity with respect to novel materials and high performance. The attention is also directed to their manufacture, which include large-scale, large-volume, flexible and recyclable, disposable and/or reusable devices. Novel deposition techniques are used to obtain high structural quality, which is slowly reaching that observed for conventional deposition methods (vacuum-based or similar). This is especially true for TFPVs (organic solar cells, polymer/oxide solar cells, all-oxide solar cells, perovskite solar cells, mesoscopic dye solar cells, quantum-dot solar cells) where large-scale, large volume applications allow low cost fabrication and the possibility to be competitive at the commercial level. In addition, oxide semiconductors can also confer higher lifetime stability to TFPVs through interface engineering. Mobile power generation demands 5 to 10 years of stable operation, while building integrated and outdoor applications require stability of about 20 years. In a future foresight, solution processable oxide semiconductors could also benefit from their versatile printing manufacture for the most desired solar cell application: building integrated photovoltaics (BIPVs). Printing can be applied on flat surfaces like walls or windows as well as on almost any surface shape, also allowing for transparent or semi-transparent elements. Thus, an easy integration of intelligent, CO₂-free, green buildings with beautifully designed facades is envisaged.

1.1 Objectives

The general objective of this work is to synthesize, characterize, and apply different transition metal-oxide semiconductors, such as ZnO, TiO₂, and V₂O₅, in thin film solar cells, such as dye-sensitized solar cells (DSSCs) and organic solar cells (OSCs).

This objective can be split into the following specific objectives:

- Synthesis of TMOs

The first specific objective of this work was to synthesize thin films of TMOs by electrodeposition, hydrothermal synthesis, and sol-gel. These synthesis techniques were selected due to their low-cost with the possibility to be carried out at low temperature.

- Characterization of materials

The second specific objective of this work was to characterize the thin films using different characterization techniques, such as scanning electron microscopy (SEM), transmission electron microscopy (TEM), ultraviolet-visible (Uv-Vis) spectroscopy, X-ray diffraction (XRD), energy dispersive X-ray (EDX) spectroscopy, X-ray photoelectron spectroscopy (XPS), and ultraviolet photoelectron spectroscopy (UPS).

- Application of TMOs in solar cells

Another specific objective for this work was to apply the thin films as working electrodes in DSSCs or as the electron or hole transport layer in OSCs, as well as to characterize the cells in terms of their power conversion efficiency and stability. The efficiency was evaluated by electrical characterization methods such as current-voltage curves and external quantum efficiency measurements, and the stability by accelerated or real outdoor degradation tests.

- Fabrication of solar cells by printing methods

Another objective was to fabricate organic solar cells by printing methods. This specific method was selected among others due to its low-cost and scalability.

- Interfacial engineering

The last specific objective of this work was to improve the stability of organic solar cells by means of interfacial engineering.

1.2 Outline

This thesis work is organized in the following way:

Chapter 2 reviews the literature in the field of solar cells, with special attention to the next generation solar cells and to the application of transition metal oxides as building blocks of these devices. This chapter is written in a way to provide the reader with a basic knowledge of the subjects and help achieve a full understanding of the results presented in later chapters.

Chapter 3 presents the materials characterization techniques used in this work. These techniques were briefly presented to support the discussion of results. Additional information about experimental procedures and characterization itself, are presented on demand, together with results.

Chapters 4 and 5 present results and analysis on the application of nanostructured ZnO thin films as photoanodes in dye sensitized solar cells. The ZnO films were produced by electrodeposition (results shown in chapter 4) and hydrothermal synthesis (results shown in chapter 5). In both chapters the ZnO photoanodes were characterized using the techniques presented in chapter 3. Solar cells assembled with these ZnO electrodes were characterized by current–voltage and IPCE (incident photon to collected electron efficiency) measurements.

Chapter 6 shows the results on the application of three different natural dyes as sensitizers for dye sensitized solar cells. The solar cells used to provide the results for this chapter were assembled with TiO₂ as photoanode. The natural dyes have been characterized by means of UV-Vis spectroscopy and ultraviolet photoelectron spectroscopy. The obtained solar cells were also characterized by current–voltage and IPCE measurements.

Chapters 7 presents results on the application of V₂O₅ as hole transport layer in organic solar cells. In this project V₂O₅ was applied in plastic ITO-free organic solar cells

fabricated with the roll-to-roll technique.

Chapter 8 shows the evaluation of the stability of organic solar cells by means of accelerated and real outdoor degradation tests. Some strategies to improve the stability of organic solar cells are also presented.

Conclusions, as well as suggestions for future work, are summarized in chapter 9.

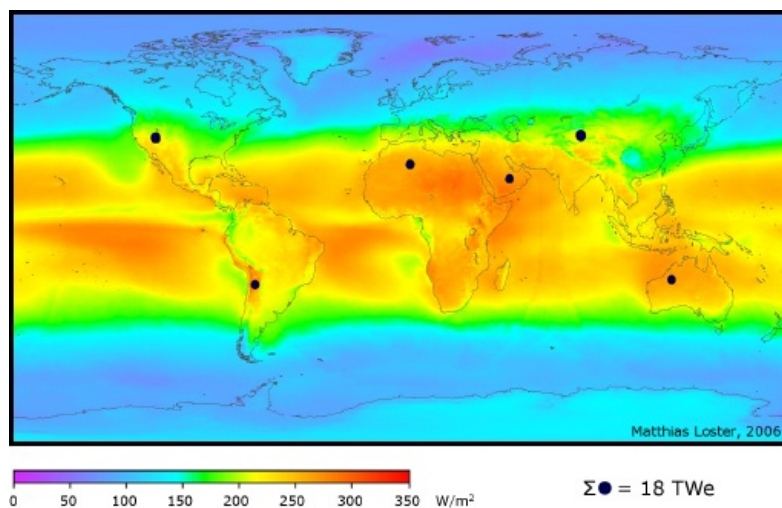
2. SOLAR CELLS

2.1 Solar cells: general aspects

2.1.1 *The importance of solar energy*

To date, more energy from sunlight strikes the Earth in one *hour* (4.3×10^{20} J) than all energy consumed on the planet in a *year* (4.1×10^{20} J). There is a huge gap between the present use of solar energy and its potential, which defines the grand challenge in energy research [1]. Sunlight does not strike the Earth's surface uniformly as is shown on Fig. 2.1 which depicts the world map of the irradiance, i.e., the power of electromagnetic radiation per unit area (radiative flux) incident on a surface.

Figure 2.1: Total primary power density supply from sunlight.

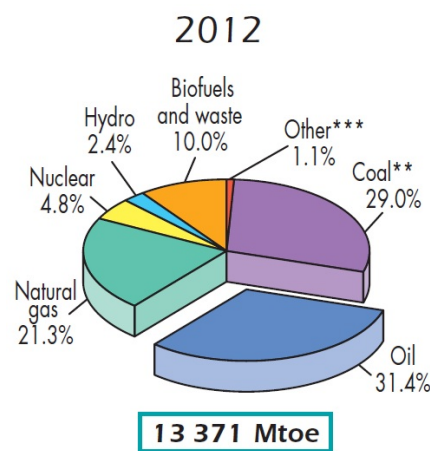


Source: http://www.ez2c.de/ml/solar_land_area/index.html

Despite the enormous potential for solar energy, our society still depends, to a great extent, on coal, oil and natural gas. These fossil fuels, however, will be depleted someday

in the future because they are limited. In fact, according to International Energy Agency (IEA) report [2] (see Fig. 2.2), 81% of the energy consumed in 2012 came from fossil fuels. In 2005, Würfel [3] pointed out that the reserves of fossil fuels, which have been accumulated over millions of years, will literally go up in smoke over a time of only about one hundred years.

Figure 2.2: World energy production by source in 2012.

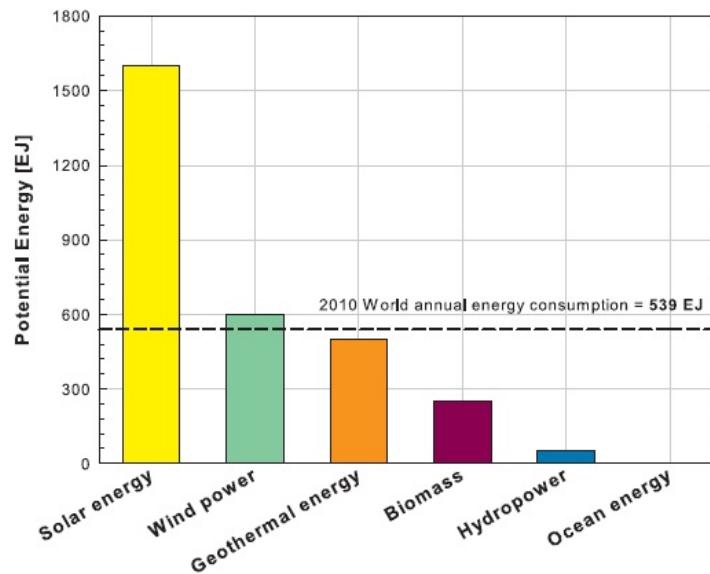


Source: International Energy Agency

Unfortunately the end of the reserves is not the biggest problem. The ever growing combustion of fossil fuels has provoked a rapid increase of carbon dioxide concentrations in the atmosphere resulting in the global warming effect [4] which has drastic consequences to the climate on the planet. Under these circumstances, the use of renewable and CO₂-free energy sources is imperative. Hence, the interest in clean energy sources is growing. Several renewable energy sources are being developed such as biomass, wind, hydroelectricity, geothermal and solar. Among them solar is an attractive source of energy since it is clean, easily accessible and abundant. Moreover, solar energy is the one alternative that possesses the higher potential of becoming the actual successor of fossil fuels. Figure 2.3 illustrates the world potential to different kind of renewable energy sources, which can replace fossil fuels as the main source of energy. According to this figure, wind energy or

solar energy, have the potential, alone, to meet the total global need for energy. It is also clear in this graph that the potential for the solar energy is, by far, the biggest one.

Figure 2.3: Potential energy production per year of various types of renewable energy sources.

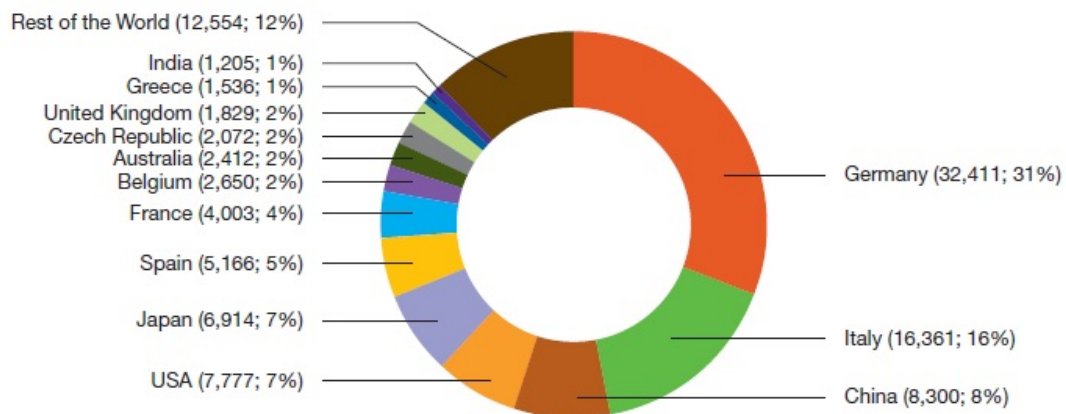


Source: Olindo [5]

The energy demand is perennially growing. One of the reasons for this growth is the increment in the world's population. By 2040, there will be nearly 9 billion people on the planet, up from about 7 billion today [6]. In other words, the population will grow by more than 30% over the next 30 years. This growth will not occur uniformly around the globe. Soubbotina [7] claims that most of this growth will take place in developing countries which have increased the consumption of energy in their path to development. As a consequence of this decentralized growth, the energy usage will increase with higher a rate than the rate of population growth. According to U.S. Energy Information Administration (EIA) [8] the energy consumption will increase by 56% by 2040 in reference to 2010. In this scenario, solar energy arises as the better choice to supply the large demand that is coming without increasing the concentration of CO₂ in the atmosphere. The overall participation of this technology in the generation of electricity is still quite small. However solar energy

presents the fastest growing rate among the sources of energy that are not dependent of fossil fuels [9]. Thus, if it keeps the trend of growth, in a few years solar energy will be the most important energy source not based on burning fossil fuels. According to European Photovoltaic Industry Association (EPIA) [9], in 2012 the global solar energy installed power reached the mark of 100 GW. As can be seen in Fig. 2.4, most of this installed power was found in Europe with Germany leading the World with about 31% of the total photovoltaic (PV) installed capacity. Germany, however, is far from presenting the best potential to generate electricity from sunlight.

Figure 2.4: Global photovoltaic cumulative installed capacity share in 2012 (MW; %).



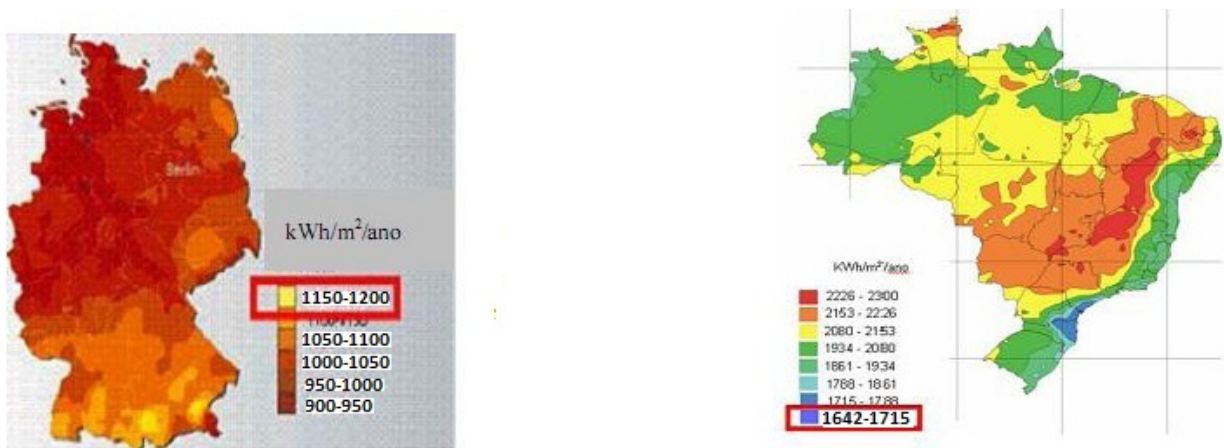
Source: European Photovoltaic Industry Association [9]

Figure 2.5 shows the total irradiance on the horizontal plane in Germany and Brazil. Comparing the irradiances on both countries it is possible to conclude that the worst scenario in Brazil is about 40% better than the best scenario in Germany. Therefore, there is a huge open market for PV in places like Brazil where the potential is enormous but the installed power is still very low.

Unfortunately, the cost of solar energy is still very high. According to The Economist magazine in an article published in 2012, photovoltaic cost have fallen from 76.67 US\$/Watt in 1977 to an estimated 0.74 US\$/Watt in 2013 for crystalline silicon solar cells. The cost of photovoltaic technology is about 165 US\$/MWh which is still high if compared with the

conventional energy sources from fossil fuels with an average cost of about 83 US\$/MWh. It should be mentioned here that current photovoltaic cost estimates are calculated on the price of Si-based solar cell technology which is the current technology on the marketplace. Thus, enormous research efforts are being directed towards the development of new types of solar cell devices characterized by low-cost, high efficiency and stable long lifetimes. The use of semiconductor oxides can be a strategy to reduce the price of photovoltaics.

Figure 2.5: Total irradiance on the horizontal plane on Germany (left) and on Brazil (right).



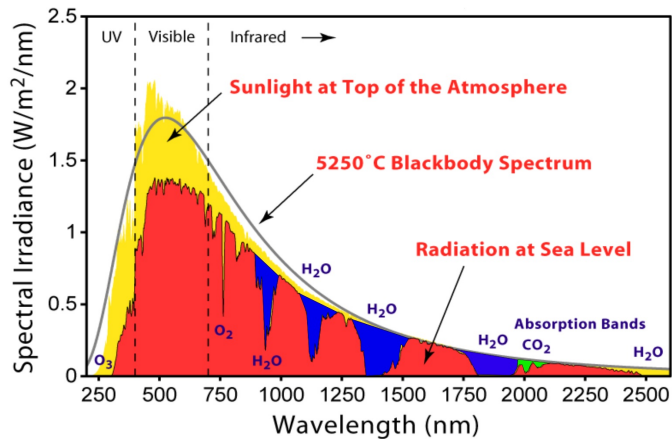
Source: Salamoni and R ther [10]

2.1.2 Solar spectrum

The Sun produces light with a distribution similar to what would be expected from a 5523 K (5250°C) black-body, which is approximately the Sun's surface temperature. The distribution of the emitted electromagnetic radiation by the Sun, as function of the incident wavelength, is called solar spectrum. Figure 2.6 shows the extraterrestrial solar spectrum (as measured on the top of the atmosphere) and the one at sea level. The figure also shows the black-body radiation spectrum at 5523 K, which is in good agreement with the extraterrestrial solar spectrum. The solar energy flux crossing a unit area normal to a solar ray at the mean path between the Sun and the Earth is referred to as the solar

constant. According to Kininguer [11], the value of the solar constant is 1367 W/m^2 . The solar spectrum covers energy values from ultraviolet (UV) to infrared (IR) where 45.7% is in the infrared region, 47.3% in the visible range, and 7.0% in the ultraviolet range [3]. Almost all absorbers used in solar cells have the ability to harvest light on the UV and visible ranges with IR photons simply lost. Nevertheless, a great deal of effort has been dedicated to the development of materials or structures that can harvest photons in the IR range [12–14].

Figure 2.6: Solar spectrum at the top of the atmosphere, at sea level, absorption bands and black-body radiation at 5523 K.



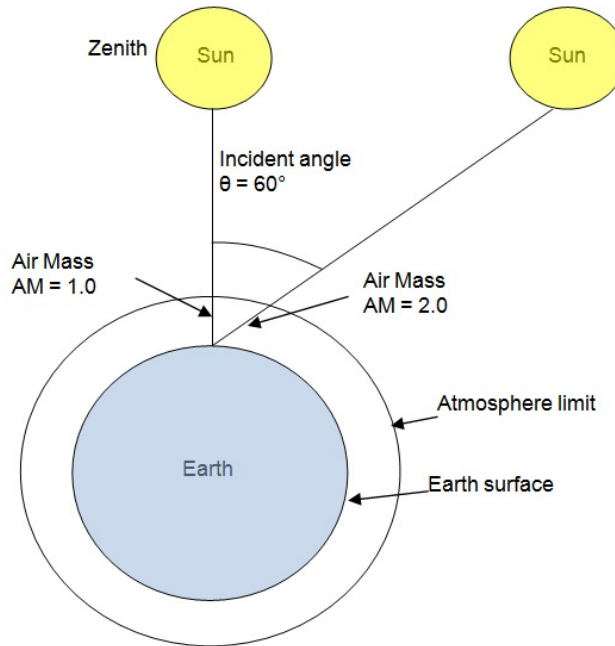
Source: Callister Jr and Rethwisch [15] *apud* Abreu [16]

As can be seen in Fig. 2.6, there are some absorption bands on the spectrum at sea level. The absorption on the spectrum depends on the air mass, AM, defined as:

$$AM = \frac{1}{\cos \theta} \quad (2.1)$$

where θ is the angle between the vertical line passing the observer and the line that connects the observer to the Sun as illustrated on Fig. 2.7. When the Sun is above the vertical axis this angle is called zenith angle. The absorption due to the bands in a solar spectrum increases when the AM increases. The standard AM for solar cells testing is $AM = 1.5$.

Figure 2.7: Solar spectrum at the top of the atmosphere, at sea level, absorption bands and black-body radiation for 5523 K.



Source: Own author

2.1.3 A brief history of the photovoltaic technology

Photo is the Greek word for light while *voltaic* is referred to electricity (from Alessandro Volta, Italian Physicist who invented the electric battery). Therefore, the term photovoltaics is commonly used as the process of transformation of light energy (or solar energy) into electric energy.

The basic science behind the photovoltaic effect was first observed in 1839 by the nineteen-year-old French physicist Alexandre Edmond Becquerel. Becquerel observed a physical phenomenon allowing light-electricity conversion while experimenting with metal electrodes and electrolytes. In 1883 Charles Fritts, an American inventor, described the first solar cells made from selenium wafers. In 1888 Edward Weston receives a first US patent for a "solar cell". Therefore, photovoltaics is an ancient technology more than 170 years old [17].

In 1901 Nikola Tesla receives a US patent for a "method of utilizing, and apparatus for the utilization of radiant energy" [17]. The pace of advancement really increased after the publication of the impressive Einstein's paper entitled *On a Heuristic Viewpoint Concerning the Production and Transformation of Light*. This paper, published in 1905,

proposed a theoretical explanation for the photoelectric effect [18]. Some years later, in 1916, Robert Millikan provided experimental proof of Einstein's theory of the photoelectric effect. Due to this success, Einstein received the 1922 Physics Nobel Prize for his work on the photoelectric effect. Approximately three decades later, a Bell laboratories team discovered that silicon had photoelectric properties and quickly developed Si solar cells achieving efficiency of 6%. Early satellites were the primary use for these first solar cells. The commercial solar age had then began. On the next years the advancements concentrated on spacial applications. By the occasion of the 1970's oil crisis, also referred as oil shock, when the price of the oil quadrupled in less than half a year [11], alternative sources of energy gained a big importance. Research drived PV costs down about 80%, allowing for applications such as offshore navigation warning lights and lighthouse horns, railroad crossings, and remote use where utility-grid connections are too costly.

More recently, global warming and climate change have become issues of evergrowing concern. The use of renewable sources of energy has become even more encouraged. In fact, the rising attention that global warming has increased, has forced the world leaders to embrace some goals in order to minimize this effect. The Kyoto Protocol is an example of how the leaders decided to face the problem. On the Kyoto Protocol the goal was the reduction, by 2012, of at least 5.2% on the emissions of greenhouse gases by developed countries regarding to levels recorded in 1990. Those conditions, together with considerable subsidy programs have provided the means for an extraordinary growth of the photovoltaic industry for a relatively long period of time. Nowadays the photovoltaic industry is one of the fastest growing industries in the world and exist largely without subsidies [11].

2.1.4 Physical principles

The PV effect may be described in simple terms as follows: light, which is pure energy, enters a PV cell in form of photons, and imparts enough energy to electrons (negatively charged atomic particles) in semiconducting materials to free them. A built-in-potential barrier in the cell acts on these electrons to produce a voltage (the so-called

photovoltage) [19]. Particularly, this occurs when the energy of the photons making up the light is larger than the forbidden band gap of the semiconductor. However, in normal conditions the excited electrons relax back quickly to their original or ground state. In a photovoltaic device, there is a built-in asymmetry which pulls the excited electrons away before they can relax, and feeds them to an external circuit. The extra energy of the excited electrons generates a potential difference or electron motive force (e.m.f.). This force drives the electrons through a load in the external circuit to do electrical work.

2.1.5 *Semiconductors*

According to quantum mechanics every atom presents a set of discrete electronic energy levels, which are separated by gaps on the energy scale. In a typical semiconductor's crystal structure, atoms are separated by few Å allowing interaction between these discrete energy levels spreading them into energy bands. The highest energy band containing electrons at 0 K is called the valence band, and the conduction band is defined as the energy band where electrons can conduct net current by moving through the unoccupied energy states.

The gap in energy between the top of the conduction band, E_C , and the bottom of the valence band, E_V , is the forbidden energy band gap $E_G = E_C - E_V$. On the ideal case no energy states are allowed inside the band gap. Photons with energy greater than or equal to E_G may be absorbed by electrons in the valence band, exciting them across the gap into the conduction band. In some cases, doping impurities and unintentional defects create energy levels in the forbidden band and are responsible for many semiconductor properties that lead to practical applications.

The Fermi level, E_F , is defined as the energy level above which there is no occupied states at temperature $T = 0$ K. Pauli exclusion principle states that each quantum state can only be occupied by one electron. Therefore, in the ground state, electrons start filling energy levels from the lowest energy up. At finite temperature, however, the system is no longer in the ground state, and electrons fill energy states above the Fermi level. The probability of occupation of an allowed energy state at a given energy E is given by the

Fermi-Dirac distribution function:

$$F(E) = \frac{1}{1 + \exp\left(\frac{E-E_F}{kT}\right)} \quad (2.2)$$

The band structure governs the electronic characteristics of solids. The solids can be classified in terms of its conducting properties as conductors, insulators and semiconductors. In a conductor, the conduction band is partially filled or there is an overlapping between the conduction and valence bands. This kind of material has a zero band gap. Electrons subject to a small applied field are free to move. On the other hand, the band gap in an insulator is so large that essentially no electrons can be excited to the conduction band to contribute to the current flow. Semiconductors present conducting properties in between those of conductors and insulators. A semiconductor possesses a relatively narrow band gap and, at low temperature, behaves like an insulator. At higher temperature, however, there is a reasonable probability of electron excitation from the valence band to the conduction band, so electrons can contribute to the current in the conduction band. The promotion of an electron to the conduction band leave a hole in the valence band, creating an electron-hole pair. Under the action of an external field the electrons and holes carry current in opposite directions. Hence, the sum of the motion of electrons in the conduction band and holes in the valence band contributes to the current flow in a semiconductor.

2.1.5.1 Properties of semiconductors

One of the most important properties of a semiconductor is that it can be doped with different types and concentrations of impurities to vary its resistivity. Also, when these impurities are ionized and the carriers are depleted, they leave behind a charge density that results in an electric field and sometimes a potential barrier inside the semiconductor. Such properties are absent in a metal or an insulator.

An intrinsic semiconductor, also called an undoped semiconductor or an *i*-type semiconductor, is a pure semiconductor without any significant dopant species present, or more precisely, contains a negligible amount of impurities comparing with the thermally

generated carriers. The conduction electron concentration, n , in intrinsic semiconductors in thermal equilibrium at a given temperature without any external excitations such as light or electric field is given by:

$$n = \int_{E_c}^{\infty} N(E)F(E)dE \quad (2.3)$$

where $N(E)$ is the number of states at the conduction band and $F(E)$ is the occupancy of its states [20]. By means of the Fermi-Dirac integral and Boltzman statistics, n can be written as:

$$n = N_C \exp\left(-\frac{E_C - E_F}{kT}\right) \quad (2.4)$$

where N_C is the effective density of states in the conduction band. Similarly, the hole density, p , in the valence band can be derived:

$$p = N_V \exp\left(-\frac{E_F - E_V}{kT}\right) \quad (2.5)$$

where N_V is the effective density of states in the valence band.

For intrinsic semiconductors, the electron density in the conduction band is equal to the hole density in the valence band:

$$n = p = n_i \quad (2.6)$$

where n_i is the intrinsic carrier density which may be obtained from eqs. 2.4 and 2.5 and written as:

$$n_i = (N_C N_V)^{1/2} \exp\left(-\frac{E_G}{2kT}\right) \quad (2.7)$$

where $E_G = E_C - E_V$ is the energy band gap.

Semiconductors doped with impurities are called extrinsic semiconductors. Dopants may introduce some energy levels that usually lie within the energy gap. Impurities that have the ability to create states with relatively small ionization energy regarding to the conduction band are known as donors. Electrons in the donor states may be ionized

to the conduction band at moderate temperatures. A semiconductor doped with donor impurities usually has additional negatively charged carriers and thus are called n -type semiconductors.

Similarly, impurities which create states with relatively small ionization energy regarding to the top of the valence band, are known as acceptors. Electrons can be excited from the valence band to the acceptor states at moderate temperatures leaving a hole in the valence band. Therefore, a semiconductor doped with acceptor impurities usually has additional positively charged carriers and are called p -type semiconductors.

Electrons are the majority carriers and holes are the minority carriers in n -type semiconductors while holes are the majority carriers and electrons are the minority carriers in p -type semiconductors. For extrinsic semiconductors, n is generally close to the donor concentration N_D in n -type semiconductors whereas p is close to the acceptor concentration N_A in p -type semiconductors [21]. Using eqs. 2.4 and 2.5, the Fermi energy of extrinsic semiconductors is given by:

$$E_F = E_C - kT \ln \left(\frac{N_C}{N_D} \right) \quad (2.8)$$

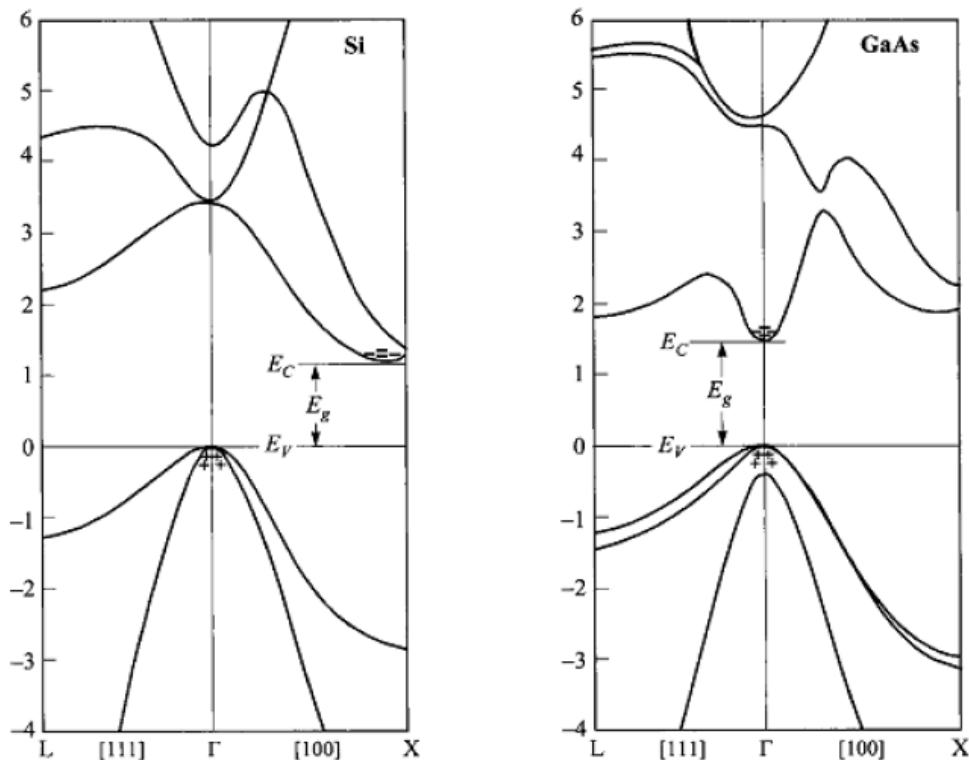
for n -type semiconductors, and

$$E_F = E_V + kT \ln \left(\frac{N_V}{N_A} \right) \quad (2.9)$$

for p -type semiconductors. With respect to intrinsic semiconductors, the Fermi energy level of a n -type semiconductor is closer to the conduction band while that of a p -type semiconductor is closer to the valence band.

As mentioned before, the band gap is the energy difference between the bottom of the conduction band and the top of the valence band. However, the bottom of the conduction band and the top of the valence band are not, in general, at the same point in reciprocal space. If E_V and E_C are aligned in reciprocal space the band gap is referred to as direct. When they are misaligned the band gap is said to be indirect. Figure 2.8 shows the band structures of the indirect and direct band gap semiconductors Si (left) and GaAs (right).

Figure 2.8: Energy band structure for Si on the left with indirect transition band gap and GaAs on the right with direct transition.



Source: Sze and Kwok [20]

This difference between direct and indirect band gaps is very important as a photon with energy of the order of a semiconductor band gap carries a very small momentum. In a direct gap semiconductor, a photon of energy E_G (or larger) can promote an electron from the valence to the conduction band (to produce an electron-hole pair) quite easily because the electron does not need to be given very much momentum.

However, to be promoted to the valence band of an indirect gap semiconductor, an electron must undergo a change in momentum that can not be provided by a photon. Therefore, an indirect transition is carried out by a simultaneous absorption, by the electron, of a photon and a phonon where the former provides the required energy and the latter the required momentum.

The process in which an electron undergoes a transition from the conduction band back to the valence band to annihilate an electron-hole pair is called recombination. The recombination process is much more efficient for a direct band gap semiconductor than for an indirect band gap semiconductor, where the process must be mediated by a phonon.

The carrier lifetime is defined as the average time it takes for carriers to recombine, and the carrier diffusion length is the average distance these carriers travel before they recombine.

There are three different recombination mechanisms: (a) Radiative recombination: It is a reverse process of the absorption. It occurs with emitted light and happens more rapidly in direct-band-gap semiconductors; (b) Auger recombination: In this recombination process, the released energy excites another electron to a higher energy level instead of emitting light. This excited electron then thermalizes back down to the conduction band edge. Auger recombination is especially probable in heavily doped material. (c) Recombination through traps: Impurities and defects can form energy levels in the forbidden band. Therefore, electrons can relax from the conduction band to these energy levels and then recombine with holes in the valence band. This process is particularly likely if the energy levels are near the middle of the band gap.

2.1.5.2 $p - n$ junctions

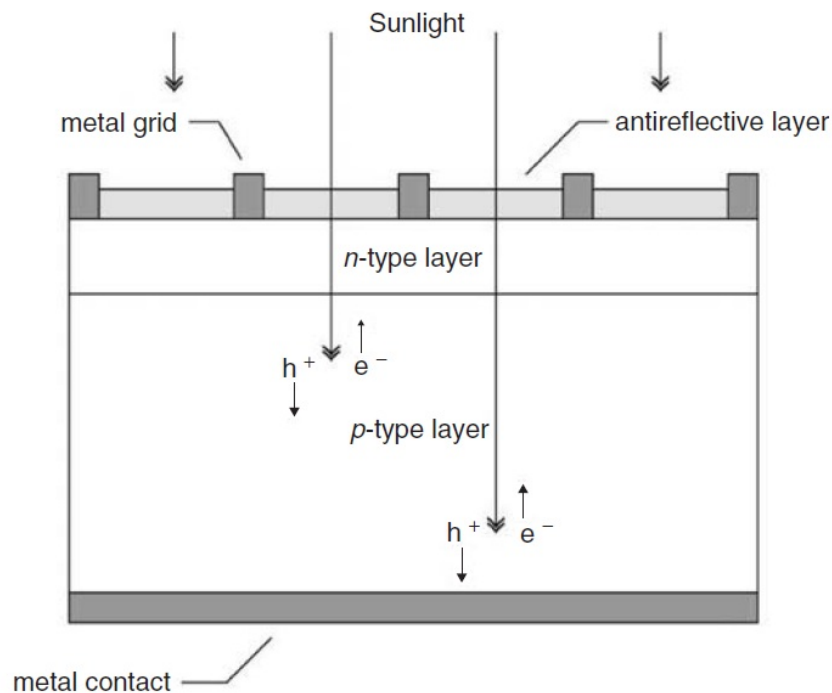
When a n -type semiconductor and a p -type semiconductor are put in contact, they form a $p - n$ junction. If the p -type and the n -type regions are composed by the same material, the junction is called homojunction, while when the materials are different, the junction is called heterojunction. As mentioned before, the Fermi energy of a n -type semiconductor is closer to the conduction band while it is closer to the valence band for a p -type semiconductor.

After the contact, due to a carrier density gradient, majority-carrier electrons diffuse from the n -type region to the p -type region, and majority-carrier holes diffuse from the p -type region to the n -type region. This carrier diffusion produces a diffusion current flow from the p -type region to the n -type region. The charged dopants will produce a built-in field in the opposite direction from the diffusion current followed by the creation of a drift current. This phenomenon gives rise to a region formed by the ionized impurities - donor impurities on the n side and acceptor impurities on the p side. This region is referred to as depletion region, or zone.

2.1.5.3 Solar cells operation

A solar cell can be considered as a two terminal device that functions like a diode in the dark and generates a photovoltage when illuminated. Under illumination a solar cell has the ability to convert light energy into electrical energy [21, 22]. The semiconductor diode is fashioned when an n -type and a p -type semiconductor are brought together to form a $p - n$ junction. This is typically achieved through diffusion or implantation of specific impurities (dopants) or via a deposition process. The diode's other electrical contact is formed by a metallic layer on the back of the solar cell [23]. A simple conventional solar cell structure is depicted in Fig. 2.9. As shown in the figure, the sunlight strikes the solar cell and it delivers electrical energy.

Figure 2.9: Schematic representation of a simple conventional solar cell.



Source: Gray [23]

It is possible to state that all photovoltaic devices present four important steps to convert sunlight into electrical energy [24]:

1. a light absorption process which causes a transition in a material (the absorber) from a ground state to an excited state,
2. the conversion of the excited state into (at least) a free negative and a free positive-charge carrier pair, and
3. a discriminating transport mechanism, which causes the resulting free negative-charge carriers to move in one direction (to a contact called the cathode) and the resulting free positive charge carriers to move in another direction (to a contact called the anode). The energetic, photogenerated negative-charge carriers arriving at the cathode result in electrons which travel through an external path (an electric circuit). While traveling this path, they lose their energy doing something useful at an electrical load and finally they return to the anode of the cell. At the anode, every one of the returning electrons completes the fourth step of photovoltaic energy conversion, which is closing the circle by
4. combining with an arriving positive-charge carrier, thereby returning the absorber to the ground state.

2.1.6 Characterization techniques

2.1.6.1 Current density *vs.* voltage: $J - V$ curves

A $J - V$ measurement under standard test conditions (AM 1.5 spectrum and 25°C) provides a fingerprint of a solar cell and it is the most common tool for solar cells characterization. The $J - V$ curve of an ideal solar cell follows the ideal diode equation:

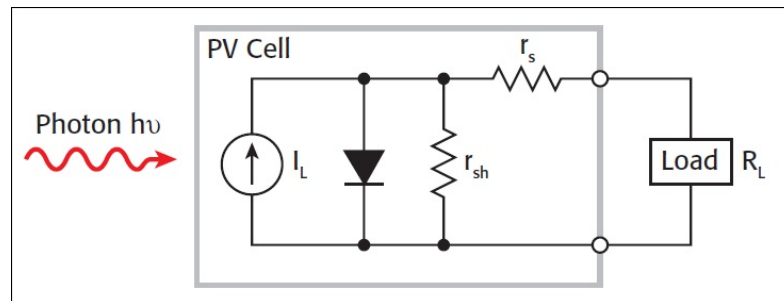
$$J = J_S \left(e^{\frac{qV}{kT}} - 1 \right) \quad (2.10)$$

where J_S is the saturation current density and V the applied voltage. When light is applied, the light-induced current flows from the p -type end to the n -type end through the outside circuit. This flow is opposite to the dark current, so the light $J - V$ curve will follow the ideal diode equation shifted by the amount of light-induced current density J_L :

$$J = J_S \left(e^{\frac{qV}{kT}} - 1 \right) - J_L \quad (2.11)$$

Under realistic conditions, additional parameters need to be considered. Equivalent circuit models define the entire $J - V$ curve of a cell, and it is a good tool to take into account these additional parameters. One basic equivalent circuit model in common use is the single diode model shown in Fig. 2.10.

Figure 2.10: Schematic representation circuit of a photovoltaic cell.



Source: Gray [23]

Using Kirchoff's current law the current I through the circuit shown in Fig. 2.10 can be written as:

$$I = I_L - I_D - I_{sh} \quad (2.12)$$

where I_L is the light-generated current in the cell, I_D is the voltage-dependent current lost to recombination, and I_{sh} is the current lost due to shunt resistances. In this single diode model I_D is modelled using the Shockley equation for an ideal diode:

$$I_D = I_0 \left[\exp \left(\frac{V + IR_s}{AV_T} \right) - 1 \right] \quad (2.13)$$

where I_0 is the saturation current, R_s is the series resistance, A is the dimensionless diode

ideality factor, and V_T is the thermal voltage given by:

$$V_T = \frac{kT_c}{q} \quad (2.14)$$

where k is Boltzmann's constant, T_c is the cell's working temperature and q is the elementary charge. Usually, $A = 1$ when ideal diffusion currents dominate, $A = 2$ when recombination currents dominate, and $1 \leq A \leq 2$ when both currents are comparable.

Writing the shunt current in terms of R_s and the shunt resistance R_{sh} as

$$I_{sh} = (V + IR_s) / R_{sh} \quad (2.15)$$

and substituting this expression together with eq. 2.13 in eq. 2.12 yields Kirchoff's current law for the current through the model circuit:

$$I = I_L - I_0 \left[\exp \left(\frac{V + IR_s}{AV_T} \right) - 1 \right] - \frac{V + IR_s}{R_{sh}} \quad (2.16)$$

As the current generated by a solar cell depends on its area, the current density J , defined as I/area , is more often used than the current itself.

A solar cell is characterized by a number of parameters. The open circuit voltage V_{oc} is the maximum value of the potential difference and is obtained when the terminals of the cell are isolated with infinite load resistance. The short circuit current density J_{sc} is the maximum current that a solar cell can produce and is measured when the terminals are connected to each other with zero load resistance. These parameters can be easily obtained by means of a $J - V$ curve like shown in Fig. 2.11.

The cell power density is given by $P = JV$. The maximum power density P_{max} determines the cell's efficiency. It occurs at a certain voltage V_{max} corresponding to a given current density J_{max} as shown in Fig. 2.11. The fill factor FF is defined as:

$$FF = \frac{V_{max} J_{max}}{V_{oc} J_{sc}} \quad (2.17)$$

and describes how "square" the $J - V$ curve is. The efficiency η is defined as the ratio of

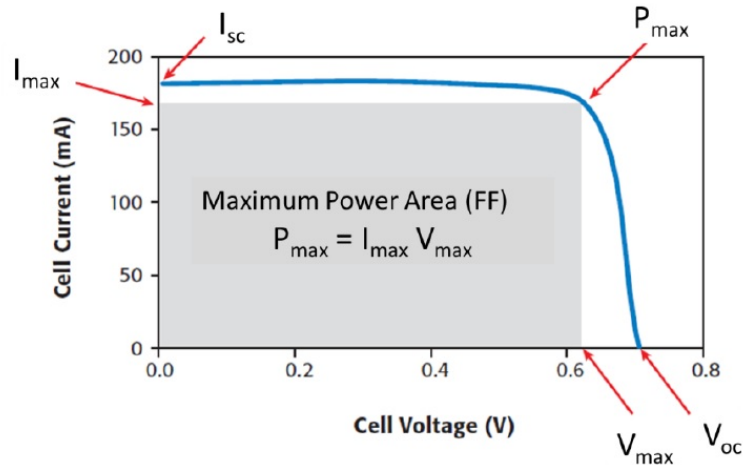
the maximum output power to the incident light power P_s as:

$$\eta = \frac{V_{max} J_{max}}{P_s} = \frac{V_{oc} J_{sc} FF}{P_s} \quad (2.18)$$

Typically, the power density of the AM 1.5 spectrum is used and thus:

$$\eta = \frac{V_{oc} J_{sc} FF}{100 \text{ mW/cm}^2} \quad (2.19)$$

Figure 2.11: Example of a typical $J - V$ curve for a solar cell.



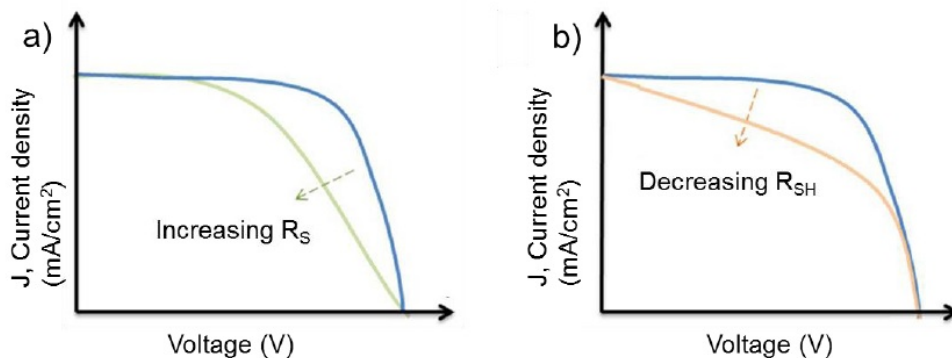
Source: Gonzalez-Valls [25]

The shape of the $J - V$ curve of a third generation solar cell is heavily affected by the presence of series and shunt resistances. Series resistance in a solar cell has three causes: firstly, the movement of current through the emitter and base of the solar cell; secondly, the contact resistance between the metal contact and the active solar cell; and finally the resistance of the top and rear metal contacts. The main impact of series resistance is to reduce the fill factor, although excessively high values may also reduce the short-circuit current. Series resistance does not affect the solar cell at open-circuit voltage since the overall current flow through the solar cell, and therefore through the series resistance, is

zero. A straightforward method of estimating the series resistance from a solar cell is to find the slope of the $J - V$ curve at the open-circuit voltage point.

Moreover, near the open-circuit voltage, the $J - V$ curve is strongly effected by the shunt resistance. Significant power losses caused by the presence of a shunt resistance are typically due to manufacturing defects, rather than poor solar cell design. Low shunt resistance causes power losses in solar cells by providing an alternative current path for the light-generated current. Such a diversion reduces the amount of current flowing through the solar cell junction and reduces the voltage from the solar cell. The effect of a shunt resistance is particularly severe at low light levels, since there will be less light-generated current. The loss of this current to the shunt therefore has a larger impact. In addition, at lower voltages where the effective resistance of the solar cell is high, the impact of a resistance in parallel is large. The effect of the series and shunt resistance in the $J - V$ curve is depicted on Fig. 2.12.

Figure 2.12: Effect of the modification of (a) series resistance and (b) shunt resistance in a solar cell $J - V$ curves.



Source: Gonzalez-Valls [25]

2.1.6.2 External quantum efficiency

External quantum efficiency (EQE), also referred to as incident photon to collected electron efficiency (IPCE), is defined as the ratio of electron-hole pairs collected to inci-

dent photons at a specified wavelength. IPCE is a product of light harvesting, injection and collection efficiencies. The spectral response is obtained through electrical measurements for a device under illumination in different wavelengths in open circuit condition. Under these circumstances the IPCE can be defined as the ratio between the photocurrent and the intensity of monochromatic incident light. Reflection and absorption on the superstrate, the TCO (transparent conductive oxide) layer, as well as the incomplete absorption of photons can contribute to the losses in external quantum efficiency.

The number of charges generated in the device per unit time and unit area is given by:

$$N_c = \frac{J_{sc}}{q} \quad (2.20)$$

and the number of incident photons per unit time and unit area is given by:

$$N_f = \frac{I_\lambda}{hc/\lambda} \quad (2.21)$$

where I_λ is the intensity of the source, h is the Planck constant, c the speed of light in vacuum and λ the wavelength of the incident radiation. The EQE can then be written as (plugging in the values of constants):

$$\text{EQE} = \frac{N_c}{N_f} = 1240 \times \frac{J_{sc}}{I_\lambda \lambda} \quad (2.22)$$

If the EQE is obtained under true J_{sc} conditions (AM1.5 illumination, $V = 0$), then it can be related to the photovoltaic parameter J_{sc}

$$J_{sc} = q \int \Phi_{AM1.5} \text{EQE}(\lambda) d\lambda \quad (2.23)$$

where $\Phi_{AM1.5}$ is the photon flux of AM1.5 illumination. It is usually impractical to perform EQE measurements under true J_{sc} conditions, and fortunately eq. 2.23 generally holds true for white-light illumination intensities of less than one sun.

2.1.7 Thin Film Photovoltaics

Thin film photovoltaics encompasses those called “excitonic solar cells” such as DSSCs (dye sensitized solar cells), OPVs (organic photovoltaics) ss-DSSCs (solid state dye sensitized solar cells). Excitonic solar cells (XSCs) consist of solar cells in which light absorption results on the production of a transiently localized excited state, called exciton, that cannot be thermally dissociated (binding energy $\gg kT$) in the chemical phase in which it was formed. Examples of XSC include molecular semiconductor solar cells, conducting polymer solar cells, dye-sensitized solar cells, quantum dot solar cells. These thin film photovoltaics (TFPV) devices also encompass a new type of solar cell called hybrid perovskite solar cell.

Currently, there are four generations of solar cells: silicon, inorganic, excitonic, and Perovskite solar cells [1, 25].

The first generation of solar cells refers to a single $p-n$ junction of crystalline Si (c-Si), exhibiting up to 25% conversion efficiency (laboratory scale). This efficiency approaches the theoretical energy conversion efficiency limit of 31%, which is known as the Shockley and Queisser (S-Q) limit. These silicon-based solar cells currently have the highest efficiency, which is being rapidly challenged by perovskite solar cells, but they are also the most expensive.

Second generation solar cells include inorganic thin films: amorphous silicon (a-Si), cadmium telluride (CdTe), or copper (gallium) indium selenide/sulphide. These solar cells are less expensive than conventional silicon solar cells, and they can be fabricated as flexible devices. Nevertheless, their lower efficiency compared to silicon solar cells and the use of toxic metals are important issues hindering commercialization.

Third generation photovoltaic technology utilizes organic semiconductors as part of the active layer of the device. These solar cells comprise organic solar cells (polymer solar cells, small-molecule organic solar cells), hybrid solar cells, and dye-sensitized solar cells, among others. Third generation solar cells are called excitonic solar cells because the charge generation mechanism is based on the formation of an exciton (a bound electron-hole pair). This charge generation could reach conversion efficiencies beyond the S-Q

limit. Because XSCs are less expensive than second generation solar cells, third generation solar cells are considered the most suitable solar cells for flexible and printable devices. However, their low efficiency and challenges with stability are significant issues preventing their entrance into the market.

Fourth generation solar cells are known as perovskite solar cells. Metal-organic perovskites could be the “missing link” between inorganic and organic semiconductors [26]. In only five years of development, hybrid perovskite solar cells have attained power conversion efficiencies that took decades to achieve with the top-performing conventional solar cell materials. Despite the incredible improvement in the photovoltaic performance of perovskite solar cells, critical questions must be answered such as: are the devices excitonic? If so, what is the exciton diffusion length? What are the carrier lifetime and recombination dynamics? Recently, Zhang et al. [27] have demonstrated that the spin configuration affects the rate at which electron-hole pairs split apart or recombine in perovskite solar cells, suggesting that these devices are not excitonic. Moreover, the generally low stability ascribed to perovskite solar cells is a significant obstacle for the commercial viability of metal-halide perovskite solar cells. However, a recent study has reported more than 2000 hours of stability for these devices [28].

In addition to the four well-known generations of solar cells, other types of solar cells exist that do not easily fit in any of these categories, such as kesterite solar cells and all-oxide solar cells. Kesterite solar cells are thin film solar cells, which differ from second generation solar cells because kesterite solar cells are only composed of abundant, non-toxic elements. In fact, the kesterite crystal structure represents a group of compound semiconductors such as $\text{Cu}_2\text{ZnSnS}_4$ (CZTS) and $\text{Cu}_2\text{ZnSnSe}_4$ (CZTSe). In fact, CZTS has been recently shown to be a promising alternative to copper indium gallium selenide (CIGS) or CdTe with 12.7% efficiency [29]. Lin et al. [30] have recently reported inkjet-printed kesterite solar cells with an efficiency of 6.4%. On the other hand, all-oxide solar cells are entirely composed of oxides, namely semiconductor oxides. All-oxide solar cells are also conceptually close to the second generation solar cells; however, in second generation solar cells, metal oxides (MOs) are mainly used as buffer layers and low bandgap

semiconductors, i.e., CdTe, copper indium selenide (CIS), or CIGS, are used as absorbing layers. In all-oxide solar cells, the metal oxides are also used as absorbing layers. This class of devices have recently attracted considerable attention due to their promising potential for reducing solar cell costs through inexpensive materials and production methods [31]. Heterojunction ZnO/Cu₂O cells are the most efficient system investigated so far, reaching efficiencies of almost 5% [32].

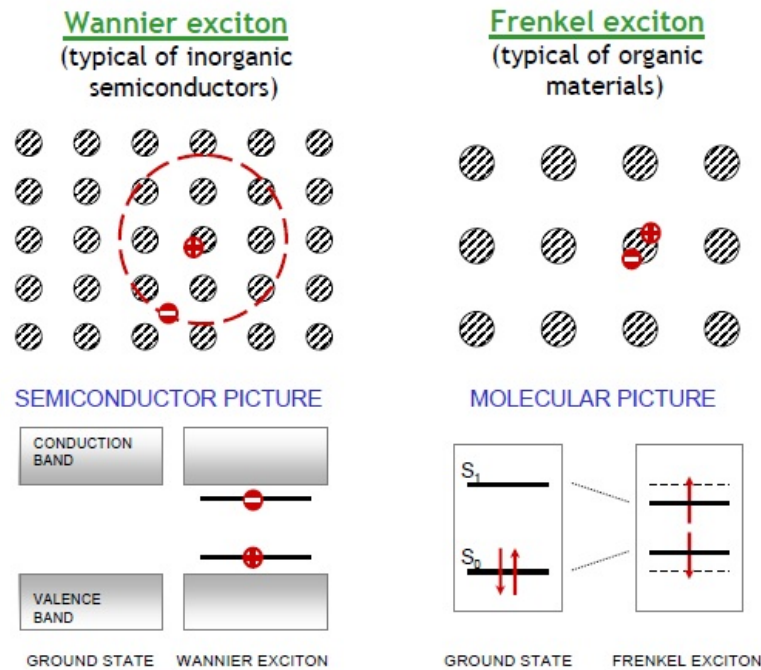
2.1.7.1 Excitons

An exciton is a quantum of electronic excitation energy travelling in the periodic structure of a crystal; it is electrically neutral and hence its movement through the crystal gives rise to the transportation of energy but not charge [33]. The neutrality of this quasiparticle comes from the fact that an exciton can also be described as a bound state of an electron and an electron hole. The electrical charge from the electron and electrical hole cancels each other. This electron-hole pair is kept bound due to Coulombic electrostatic attraction. The exciton can be treated as a particle, it moves, present spin and have a strong bind energy [34].

Excitons mediate the absorption and emission of light, particularly in disordered and low-dimensional materials. To understand the work principles of solar cells it is necessary the understanding of this excitation. Excitons behave slightly different in organic or inorganic semiconductors. In inorganic semiconductors they are easily separated into free electron-hole pairs, which does not happen in organic semiconductors. The reason for that is that the dielectric constant ϵ for inorganic semiconductors is relatively large compared to that of organic semiconductors. Figure 2.13 illustrates these two kinds of excitons on inorganic and organic semiconductors.

In inorganic semiconductors with generally large dielectric constant the electric field screening tends to reduce the Coulomb interaction between electrons and holes (binding energy around 10 meV), which results in an extended exciton with a radius larger than the lattice spacing (radius around 100 Å). This class of excitons is referred as Wannier-Mott excitons (see the left side of Fig. 2.13).

Figure 2.13: Schematic overview of the exciton formation by the absorption of the light.



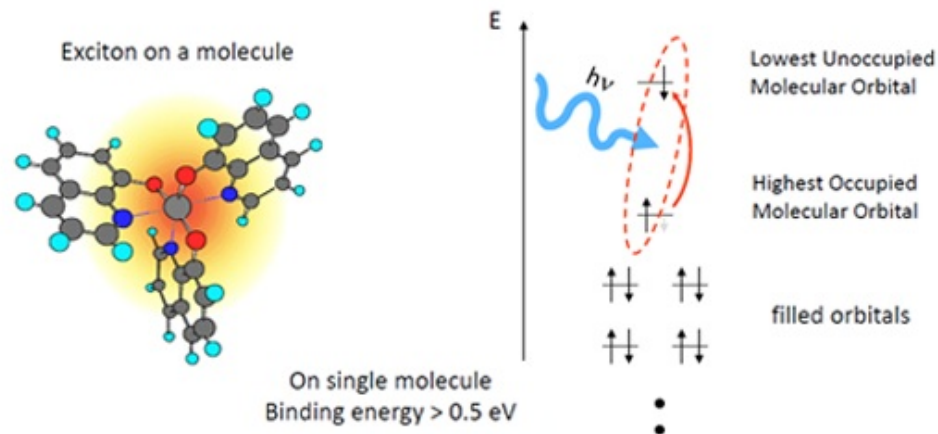
Source: Center for Excitonics / Massachusetts Institute of Technology [34]

The Coulomb interaction between an electron and a hole, in organic semiconductors (or molecular solids) with small dielectric constants, can be strong (binding energy around 1 eV); and the excitons thus tend to have radius of around 10 \AA . This is in the same order as the size of the unit cell (see the right side of Fig. 2.13) what makes them highly localized. These molecular excitons may even be entirely located on the same molecule. This class of excitons is referred to as Frenkel excitons. Figure 2.14 shows an schematic overview of the exciton formation in a molecule.

The excited state in excitonic solar cells is a highly localized and slightly bound Frenkel exciton. Their energetics and transport are central to solar energy processes. The separation of the exciton into a free electron and free hole is the source of usable electrical energy in third generation solar cells. The diffusion of excitons to an engineered interface that can subsequently split them into electrons and holes remains a central challenge in many photovoltaics applications.

The way which radiation is absorbed and carriers are separated are two of the main differences between XSCs; and a classical $p - n$ junction:

Figure 2.14: Schematic overview of the exciton formation in a molecule.



Source: Center for Excitonics / Massachusetts Institute of Technology [34]

- Conventional photovoltaics rely on differences in work functions between the electrodes of the cell in which photogenerated carriers could be separated. Therefore, an asymmetry through the cell is necessary to obtain electrical power. In classical $p-n$ junctions of solid state devices the separation of photogenerated carriers relies on separation through a depletion region built at the $p-n$ interface materials [35].
- The distinguishing characteristic of a XSC is that charge carriers are generated and simultaneously separated across a heterointerface. An absorbed photon produces an exciton which is a neutral excitation, not free carriers. Therefore, a dissociation interface is required. In contrast, photogeneration of free electron-hole pairs occurs throughout the bulk semiconductor in conventional cells, and carrier separation upon their arrival at the junction is a subsequent process. This apparently minor mechanistic distinction results in fundamental differences in photovoltaic behavior [36].

2.1.7.2 Dye sensitized solar cells

Dye sensitized solar cells have their origin in the discovery by Moser in 1887 that dye-sensitization of halogenated silver plates leads to an increased photocurrent. However, it was not until the 1970's that the underlying mechanism for current generation in these type of devices was established [37]. DSSCs attracted much attention since 1991, when

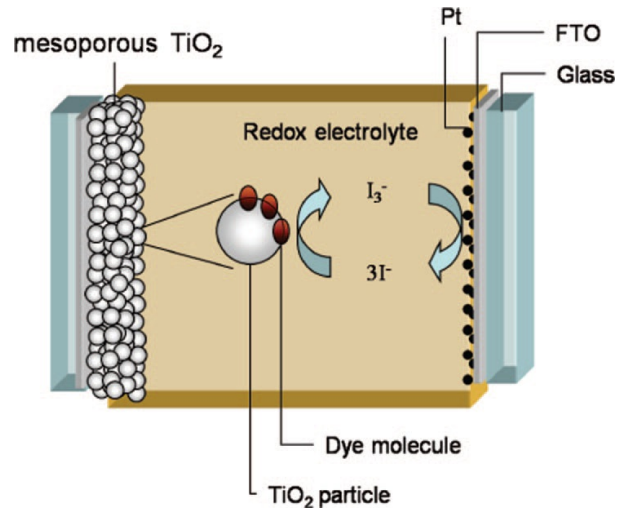
O'Regan and Grätzel published their seminal paper showing that is possible to fabricate highly efficient DSSCs [38]. Since then, this paper was cited more than 19,000 times, giving rise to a new research branch. In fact, one can say that this publication started the field of third generation solar cells.

The breakthrough of the O'Regan and Grätzel work O'Regan and Grätzel [38] came from the incorporation of mesoporous TiO_2 as electrode material which challenged the paradigm of that time that a high interfacial surface area needs to be avoided in solar cell devices. The device proposed by them was the first photovoltaic system that employs a 3-dimensional junction to convert sunlight into electricity.

A typical DSSCs comprises a working electrode which is conventionally constituted by a wide band gap semiconductor notably TiO_2 [39], ZnO [40, 41] and SnO_2 [42] covered with a dye monolayer, usually a ruthenium-based sensitizer such as N719, N3 and Black Dye [43–46]. A wide variety of organic dyes have also been reported in the literature, including porphyrin [47], phthalocyanine [48], coumarin [49], indoline [50], triarylene conjugated [51] and many other natural dyes [52, 53]. This working electrode is supported on conducting glass (transparent conducting oxide, TCO). Different materials as platinum, palladium and gold could be use as counter-electrode of the cell [54]. Finally, the gap between the electrodes is typically filled with a molten salt containing a redox couple (A/A^-) which plays a role similar to that of a hole conductor material, even though it is not a hole transporting material. Most DSSCs studied so far employ the redox couple iodide/tri-iodide I^-/I_3^- as electrolyte because of its good stability and reversibility [55]. However other hole conductors as solid [43] and ionic [47] electrolytes also can be used. A schematic of the interior of a DSSC showing the principle of how the device operates is shown in Fig. 2.15.

Since DSSCs are one of the excitonic solar cells, the generated photocurrent is inextricably related to the charge dissociation energy which is quantitatively proportional to the exciton binding energy (EBE) of the dye. Therefore the EBE is one of the most critical factors in improving the energy conversion efficiency. The EBE should be considered during the molecular design of an efficient photosensitizing dye [57]. The basic

Figure 2.15: Schematic overview of a dye-sensitized solar cell.

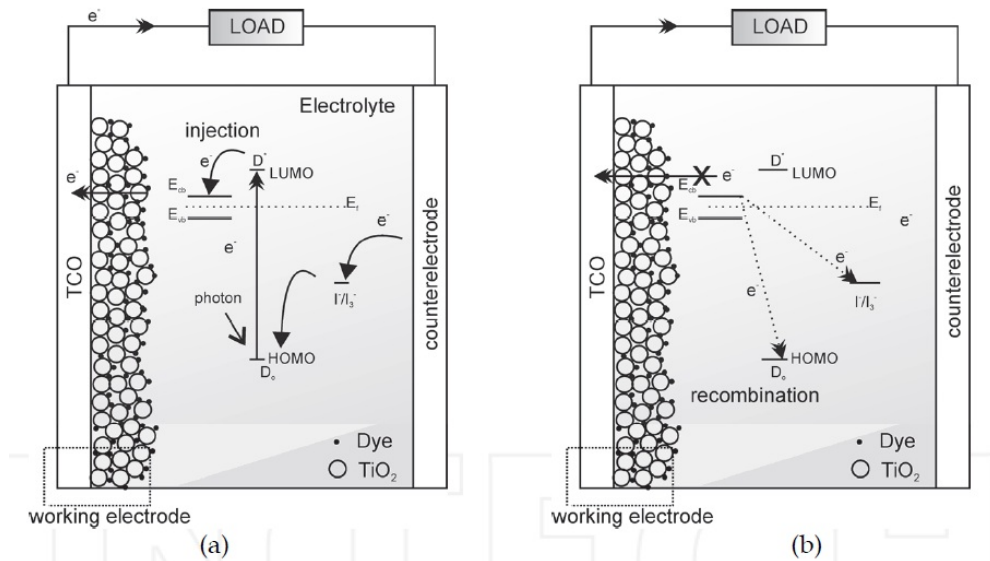


Source: Hagfeldt et al. [56]

photovoltaic principle relies on the visible photo-excitation of the dye molecule. The basic electron transfer process occurring within a DSSC is shown in Fig. 2.16 and described below:

- When light falls on the cells, the dye oxidizes and injects electrons into the conduction band of the semiconductor oxide. For Ru-complex dyes, electron injection from the excited dye into the conduction band of TiO_2 is believed to be ultrafast (10^{-10} – 10^{-15} s $^{-1}$) [56]. To be effective, the decay of the excited dye to its ground state must be slower than the injection time; decay time of 20–60 ns are typical for Ru-complex dyes.
- The photo-oxidized dye can be regenerated via reduction by the redox mediator (10^{-8} s $^{-1}$).
- The photo-oxidized dye captures an electron from iodide (I^-) from the electrolyte and I^- is oxidized to triiodide. Both process occur in the same time scale.
- Triiodide (I_3^-) regains its electron from the counter electrode when the cell is externally connected with the load.
- The charge transfer through the semiconductor oxide network occurs by a diffusion (or percolation) process (10^{-3} – 10^0 s $^{-1}$). The electron goes from one crystal to

Figure 2.16: Basic electron transfer process occurring within a DSSC: (a) electron migration from a dye molecule through the solar cell and (b) possible recombination process.



Source: Vallejo et al. [54]

another by a hopping mechanism.

- The recombination of photo-injected conduction band electrons with the oxidized form of the electrolyte redox couple (I_3^-/I^-) ions occurs in a different time scale (from microsecond to millisecond) depending upon the concentration of electrons in the semiconductor and the intensity of light.
- The low charge transfer resistance ($< 1 \Omega \text{ cm}^2$) of the counter electrode always favors better reduction of the electron acceptor (I_3^-) in the redox mediator, resulting in better long term stability and better performance of the DSSC [56].
- The voltage developed within the cell under illumination condition is due to the energy difference between the quasi-Fermi levels of the electron in the semiconductor oxide and the electrochemical potential (redox or Nernst) potential of the redox mediator.

Most of the improvement on DSSCs performance is due to a paradigm shift in the chemical components utilized within this photo-electrochemical device. A new generation of DSSCs is based on a combination of light-harvesting donor- π -acceptor (D- π -A) dyes in

conjunction with cobalt-based redox mediators. By replacing employed Ru(II)-based dyes and iodide-based electrolytes by porphyrin sensitizers and cobalt-based redox mediators, it is possible to achieve power conversion efficiencies as high as 13% [58].

2.1.7.3 Organic solar cells

The 2000 Chemistry Nobel Prize was shared by Alan J. Heeger, Alan G. MacDiarmid and Hideki Shirakawa for "for the discovery and development of conductive polymers". Their late 1970's seminal findings have been followed by the development of conductive polymers into a research field of great importance for chemists as well as physicists. Advances in the field of conductive polymers, have led to a number of applications. As their conductivity can be comparable to the one of semiconductors, the idea to apply them on solar cells arises naturally.

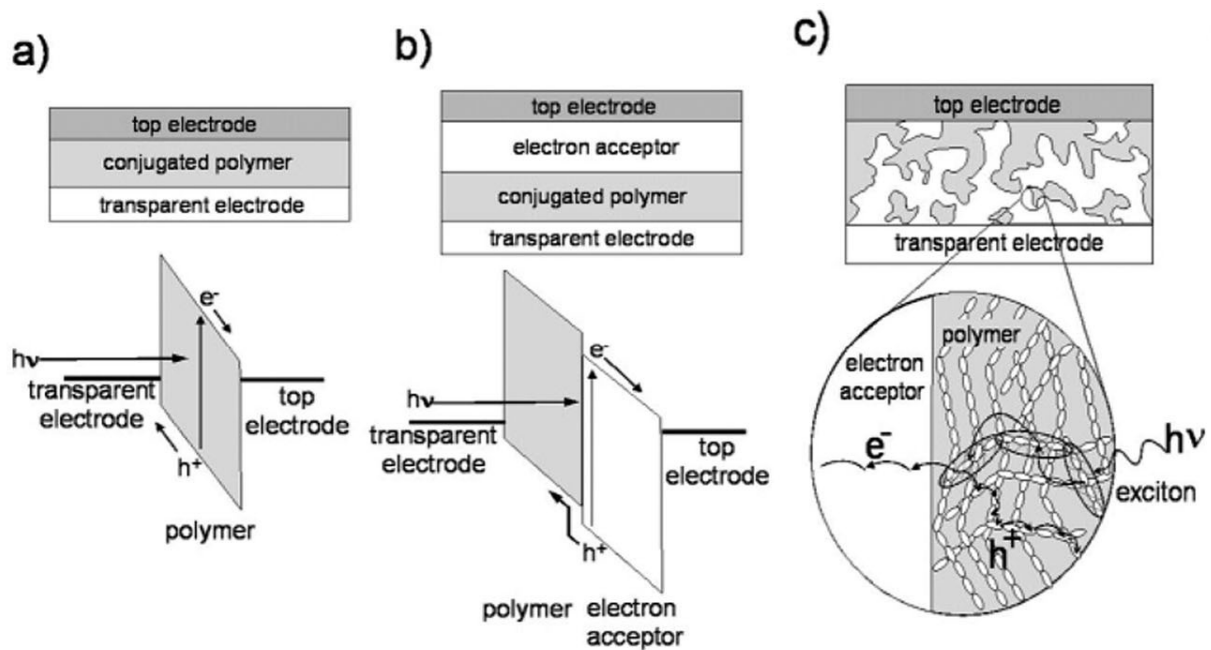
The first generation of organic solar cells (OSCs) was based on single organic layers sandwiched between two metal electrodes with different work functions [59]. This type of OSC is known as single layer solar cell. When an organic semiconductor is placed in between these two electrodes, their work functions will be equilibrated generating a built-in electric field which causes a band bending on the organic semiconductor.

Once the light is absorbed by this sandwiched organic semiconductor, an exciton is created within it. After its creation, the exciton cannot be easily dissociated. It must diffuse to the interface between the organic semiconductor and the cathode electrode in order to be separated. As the lifetime and mobility of excitons in organic semiconductors are very low, the organic layer cannot be ordinarily thick in order to absorb more light. In fact, the thickness of the layer is limited by the exciton diffusion length. The power conversion efficiency for these single layer devices is very low. A single junction organic solar cell is depicted in Fig. 2.17(a). The figure shows a polymer sandwiched between two electrodes with different work functions. This difference in the work functions induces a built-in electrical field on the polymer, which bends it. The figure also illustrates the absorption of one photon with energy $h\nu$, the generation and dissociation of one exciton as well as the charge carriers transport. At this geometry, the charge carriers must diffuse a

long way before it is collected by the electrodes. Therefore, a high degree of recombination is expected limiting the performance of the OSC.

One strategy applied to increase the performance of an organic photovoltaic solar cells was the development of the bilayer heterojunction structure. It has been recognized that the most efficient exciton dissociation mechanism in organic materials occurs at a donor-acceptor (DA) interface [60, 61]. At such an interface, the donor material with a low ionization potential forms a heterojunction with an acceptor material with a high electron affinity. Depending on the alignment of the energy levels of the donor and acceptor materials, the dissociation of the strongly bound excitons can become energetically favorable [62, 63], leading to the formation of a free electron polaron in the acceptor material and a free hole polaron in the donor material.

Figure 2.17: Device structures of OSCs: (a) single-layer cell; (b) bilayer cell; and (c) bulk heterojunction cell.



Source: Wang et al. [64]

The dissociation, or charge-transfer (CT) process, typically occurs over time scales τ_{CT} of a few hundred femto-seconds or less [65, 66]. Since τ_{CT} is much shorter than any

other competing process, the charge transfer efficiency approaches $\eta_{CT} = 100\%$ [67]. A schematic view of a bilayer solar cell is depicted in Fig. 2.17(b). The figure shows the DA interface and the discontinuity of the highest occupied molecular orbital (HOMO) to the lowest unoccupied molecular orbital (LUMO). The advantage of such a structure is that, under illumination, the exciton needs to diffuse only to the discontinuity of the HOMO-LUMO levels. For this reason, these organic semiconductors must be of different nature regarding the conductivity as one must transport electrons while the other must transport holes in order to allow charge flux to the electrodes. Excitons need to diffuse much less in these bilayer solar cells in comparison with the single layer structure which increases the probability of exciton dissociation leading to large charge carrier collection and higher power conversion efficiency. Tang [68] reported about 1% power conversion efficiency for two organic materials (a phthalocyanine derivative as *p*-type semiconductor and a perylene derivative as *n*-type semiconductor) sandwiched between a transparent conducting oxide and a semitransparent metal electrode.

The next breakthrough was achieved by introducing the bulk heterojunction (BHJ) structure [60, 69] in which the single active layer is composed by a mixture of two organic semiconductors to transport electrons and holes. A bulk heterojunction solar cell is depicted in Fig. 2.17(c). In BHJ solar cells, the exciton dissociation takes place much closer to the place where they are created since the interface is all around the active layer. The use of such structure increases even more the probability for this dissociation, and consequently the power conversion efficiency is higher. The power conversion efficiency for bulk heterojunction solar cells have increased very fast, reaching 2.5% in very few years [70], and now efficiencies above 10% have been demonstrated [71] for single junction solar cells. Tandem solar cells, in which two solar cells with different absorption characteristics are linked to use a wider range of the solar spectrum [72], have demonstrated efficiencies higher than 10-11% [73–76].

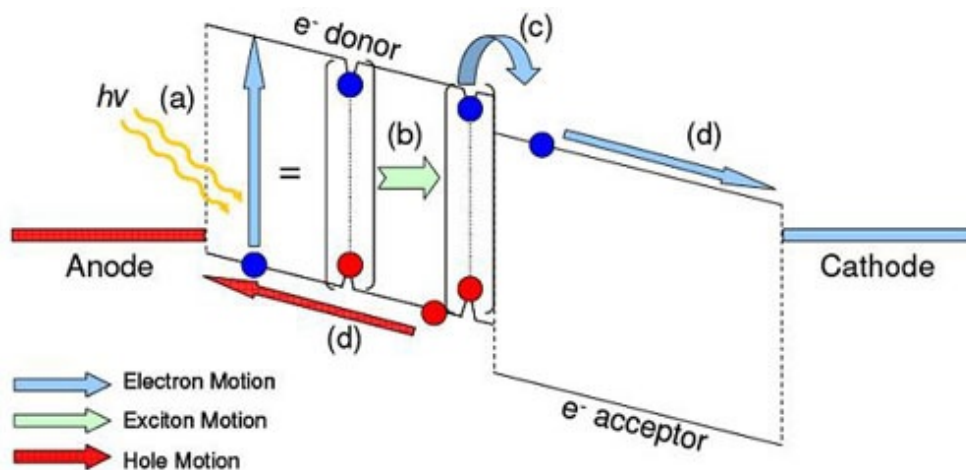
An additional advantage of bulk heterojunction solar cells is that it can be easily fabricated by solution process methods and on flexible substrates which makes them even more technologically interesting [77, 78]. Indeed, OSCs are particularly attractive because

of their ease of processing, mechanical flexibility and potential for low cost fabrication of large areas [79, 80]. Additionally, their material properties can be extensively tailored by modifying their chemical structure [81, 82].

Because OSCs are based on exciton dissociation by charge transfer at the DA interface, the conversion of photons to electrons flowing in an external circuit is a consequence of four steps, as illustrated in Fig. 2.18 [67]. The overall process can be detailed as follows:

1. The absorption of a photon with energy $h\nu$, in the active layer leads to the formation of an exciton, which has quantum efficiency η_A ;
2. The diffusion of the exciton to the interface is characterized by the diffusion length L_D , and the quantum efficiency for the exciton diffusion is η_{ED} ;
3. The exciton is likely separated at the interface between two materials with offset energy levels with a quantum efficiency of η_{CT} ;
4. Once separated, the charges must be collected at the respective electrodes after being transporting through organic layers with mobility μ , and the charge collection has a quantum efficiency η_{CC} .

Figure 2.18: Schematic energy level diagram of a typical bilayer device showing the operational mechanism in organic photovoltaic devices.



Source: Jones [83]

Thus, the overall external quantum efficiency, which is the number of charges collected per incident photon, is

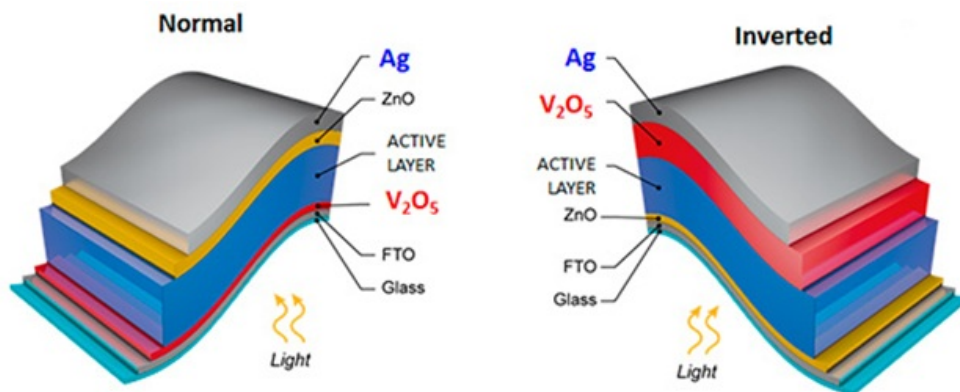
$$EQE = \eta_A \eta_{ED} \eta_{CT} \eta_{CC}. \quad (2.24)$$

Steps 1, 2, and 3 occur in the active layer of the OSC, which is the core of the device. However, there are additional layers which are vitally important to the functionality of such devices. For example, a standard bulk heterojunction solar cell is composed of five layers, as shown in Fig. 2.19. Moreover, the solar cell architecture can be designed in two different configurations: normal and inverted. The layer deposited on top of the front electrode transports the electrical carriers, which are generated in the active layer, to the transparent electrode. This layer can transport holes (normal architecture) or electrons (inverted architecture). The core of the solar cell is the active layer. In this layer, the light is absorbed, and excitons are generated, transported, and separated. A second transport layer is deposited on top of the active layer, which transports carriers that have the opposite signal as those transported by the first transportation layer. Finally, a metal (back) electrode with a low work function, such as aluminum or silver, is deposited to complete the solar cell. This metal electrode is used to extract carriers that have the opposite signal as those extracted by the front (transparent) electrode. In the normal architecture, the light enters the active area from the hole transport material layer. On the other hand, in the inverted architecture, the light enters the active area from the electron transport material layer.

Normally, the light enters the BHJ solar cells through the front (transparent) electrode, which must be as transparent as possible to allow the light to reach the photoactive materials and sufficiently conductive to extract the electrical carriers. Generally, a transparent conductive oxide (TCO) with high work function is used to extract the carriers. These carriers can be holes or electrons, depending if the solar cell has a normal or inverted architecture, respectively.

The active materials in OSCs can be used to harvest photons that have energy above the bandgap of the active material. Photons with energy below the bandgap are not useful for solar cells. Photons with an excess of energy will generate a hot charge carrier that

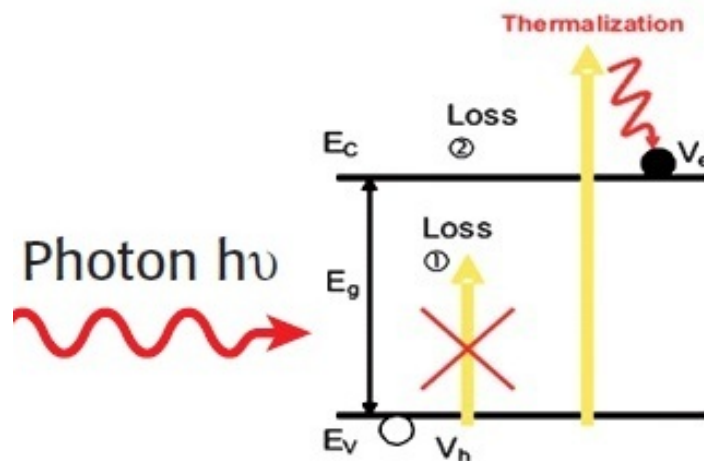
Figure 2.19: A five-layer bulk heterojunction solar cell with normal architecture (right) and inverted architecture (left).



Source: Own author

will quickly relax to the conduction band of the active material via the thermalization process. Figure 2.20 illustrates the loss mechanism when a photon cannot be absorbed due to insufficient energy and thermalization.

Figure 2.20: Absorption and thermalization losses occurring in a solar cell.

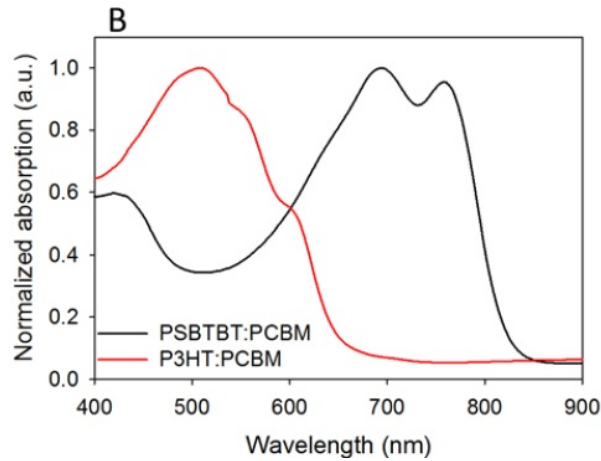


Source: Ameri et al. [84]

In molecular materials, such the donor materials in OSCs, the absorption spectrum differs from the continuous spectrum found in inorganic semiconductors. The absorption spectrum of molecular materials shows narrow and discrete peaks, as illustrated in

Fig. 2.21. Moreover, polymers with different bandgaps absorb light in different regions, which leads to better utilization of the solar irradiation spectrum. Thus, tandem OSCs have two major advantages in comparison to single junction OSCs [84–87]: reduced thermalization, and better utilization of the solar irradiation spectrum. Moreover, tandem OSCs can reach efficiencies above 10%.

Figure 2.21: Normalized film absorption of two polymers with different band gaps in a blend with [6,6]-phenyl-C₆₁-butyric acid methyl (PCBM) ester. Specifically, PCBM is a low bandgap polymer with a bandgap E_g of 1.4 eV, while poly(3-hexylthiophene-2,5-diyl) (P3HT) has E_g of about 1.9 eV.



Source: Andersen [88]

A schematic illustration of tandem OSCs is shown in Fig. 2.22 with two geometries, where the two sub-cells have complementary absorption spectra. In particular, the donor materials in the sub-cells consist of a high bandgap polymer and low bandgap polymer. The open circuit voltage V_{oc} of a tandem OSC, built up in series, will be the sum of V_{oc} for both sub-cells:

$$V_{oc,tandem} = V_{oc,bottom} + V_{oc,top}. \quad (2.25)$$

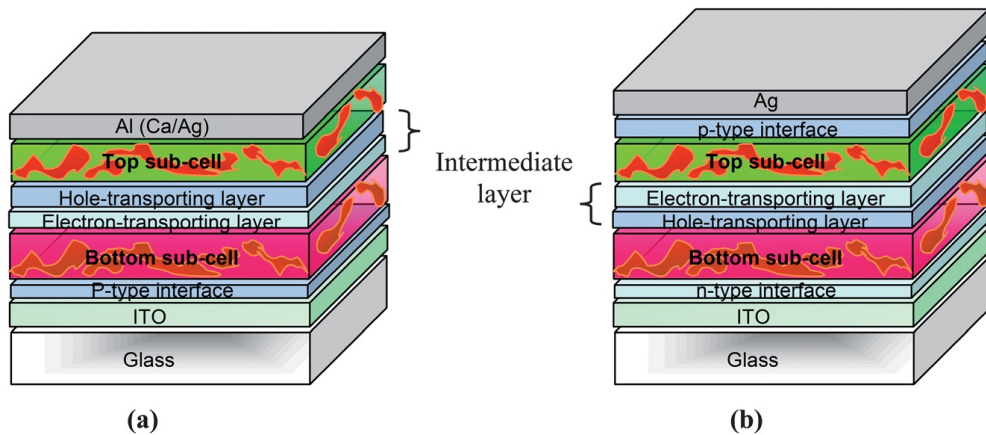
On the other hand, the short-circuit photocurrent density J_{sc} of the tandem OSC is

determined by the sub-cell with the lowest J_{sc} :

$$J_{sc,tandem} = \min[J_{sc,bottom}, J_{sc,top}]. \quad (2.26)$$

Based on this consideration, the maximum efficiency of a tandem OSC can be calculated as a function of the donor polymer bandgap for the two sub-cells. This calculation suggests that tandem cells have a 30% higher efficiency potential compared to single junction devices. Moreover, a maximum efficiency of up to 15% can be achieved by combining a bottom donor, which has a bandgap of 1.6 eV, with a top donor, which has a bandgap of 1.3 eV. Under these assumptions, the most efficient tandem cells require materials with a bandgap energy difference of only 0.3 eV [85].

Figure 2.22: Schematic representation of an organic tandem device comprised of two sub-cells with different, complementary absorption spectra in the (a) normal configuration and (b) inverted configuration.



Source: Ameri et al. [85]

2.2 Transition metal oxides for next generation solar cells

Transition metal oxides (TMOs) are suitable for use in third and fourth generation solar cells. In both cases, they can be used as hole or electron transport layers, but TMOs can also be used as part of the active layer in hybrid solar cells or all-oxide solar

cells. In general, TMOs are characterized by excellent semiconducting properties, good band alignment with the dyes or polymers commonly used in solar cells, and low-cost water-based solution-process synthesis methods.

2.2.1 Why transition metal oxides for next generation solar cells?

Metal oxides are, in general, chemically stable, mostly non-toxic, and abundant materials, often manufactured using inexpensive methods under ambient conditions. Consequently, MO-based devices are inexpensive, very stable, and environmentally safe. About 10 years ago, it was difficult to use these materials as semiconductors; nowadays, companies sell products based on these materials.

Third generation solar cells are an appealing technology because they can be fabricated with inexpensive materials and methods and they are environmentally friendly. Furthermore, the theoretical limit for the efficiency of these devices is beyond the the S-Q limit [89]. Organic solar cells are the most adaptable technology for printable applications, which are highly desired. Thus, TMO semiconductors are promising for third generation solar cells.

Titanium dioxide (TiO_2) is extensively used in DSSCs [90, 91], quantum dot solar cells [92, 93], organic solar cells [94, 95], and perovskite solar cells [89, 96]. The core of most efficient dye-sensitized solar cells and quantum dot solar cells is a mesoporous TiO_2 nanoparticle (NP) electrode, which not only provides a high surface area for accommodating the light-absorbing sensitizer but also serves as a stable conductor for photo-generated electrons.

In organic solar cells, the use of TiO_2 nanocrystals results in one of the highest reported efficiencies, 4.20%, for P3HT:PCBM inverted devices [94]. However, the electron states in TiO_2 must be filled by electrons from carrier excitation (bandgap of about 3.0–3.3 eV, [97] typically by ultraviolet (UV) irradiation) to provide favorable electron transport. Therefore, the devices usually require high-energy UV exposure before they are fully functional and efficient, which, in turn, may degrade the organic materials [98].

Recently, zinc oxide (ZnO) has emerged as promising candidate for XSC applications, especially because ZnO nanostructures can be obtained through simple, low-cost techniques such as hydrothermal and electrochemical synthesis. Despite the fact that TiO₂ is the most used semiconductor oxide in XSCs, ZnO has been intensively investigated and successfully applied in these types of cells [99–101].

Historically, ZnO was one of the first semiconductors used in dye-sensitized solar cells. The bandgap and conduction band edge of ZnO is similar to that of TiO₂ (anatase). Moreover, ZnO has a higher electron mobility than TiO₂, which should favor electron transport [56]. The longer electron lifetimes observed for ZnO mean lower charge recombination, which is beneficial for solar cell performance [99].

These emerging cost-effective photovoltaics can only be achieved through inexpensive, rapid production, low-temperature fabrication techniques. Among these process, electrodeposition is low-cost alternative that is well suited for producing high-quality ZnO thin films because it offers a high degree of control over the film characteristics through optimization of the deposition parameters [101]. The feasibility of electrodepositing ZnO suggests that the high-temperature processed TiO₂ compact layer could be eliminated [100], which is beneficial for decreasing the cost and increasing the applicability of such devices.

Vandium (V) oxide (V₂O₅) has been a promising candidate for a hole transport layer (HTL) in organic solar cells due to its favorable energy level alignment, low resistance, improved adhesion to the active layer, and higher stability in ambient atmosphere relative to poly(3,4-ethylenedioxythiophene) polystyrene sulfonate (PEDOT:PSS), which is the most common HTL material [102]. In recent years, V₂O₅ has been prepared using various synthetic methods [103, 104]. In particular, the sol-gel method has become the most common method, using vanadium(V) oxytriisopropoxide (VO(OiPr)₃) as precursor, which is a compound known for its high toxicity, reactivity, and high cost [105]. In a recent work, Teran-Escobar et al. [102] proposed V₂O₅ synthesis from a sodium metavanadate solution in water under ambient conditions, resulting in a thin film of V₂O₅·0.5H₂O.

2.2.2 Introduction to transition metal oxides

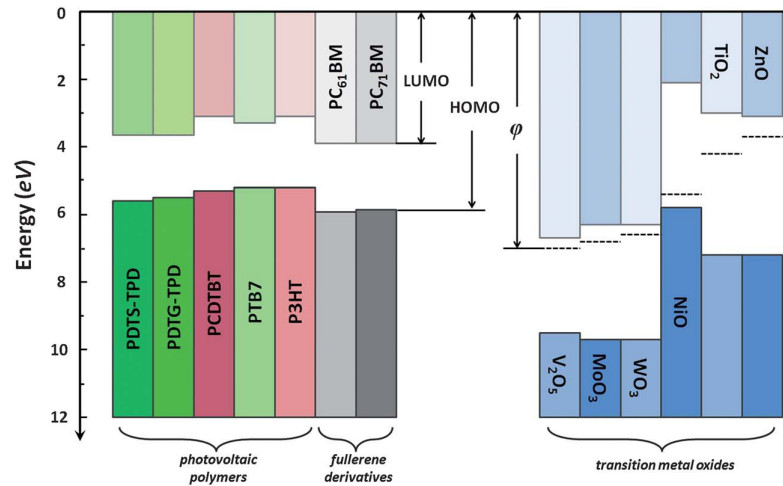
The favorable features of TMOs have led to the performance enhancement of solar cells and have been used for realizing efficient next-generation solar cells with long-term stability. They are widely used as the working electrode in DSSCs, as electron or hole transport layers in OSCs, or as active materials in hybrid and all-oxide solar cells. Metal oxides are useful for next-generation solar cells because their chemical and electrical properties can be tuned to enable charge exchange with a wide variety of organic molecules. Energetics play a key role in advancing device structure and performance, and the energy barrier at the interface critically depends on the work function of the electrodes. Thus, various types of thin-film metal oxides have been used as a buffer layer to modify the electrode work function. Indeed, TMOs are particularly attractive because they can present wide range of energy level alignment, have good transparency as thin films, are easy to manipulate, can provide low-resistance ohmic contacts, and can enhanced adhesion to the active layer [106, 107].

Moreover, TMOs can be very versatile as they can present work functions ranging from approximately 3.5 eV for defective ZrO_2 to approximately 7.0 eV for stoichiometric V_2O_5 [108]. Low work function TMOs such as ZnO and TiO_2 are used as electron injection buffer layers for cathodes [109–111]. On the other hand, high work function TMOs are often used as hole-injecting buffer layers for anodes [112–114]. The band alignment of different TMOs with photovoltaic polymers is depicted in Fig. 2.23. Furthermore, TMOs are very attractive environmentally.

Recently, the development of environmentally friendly solution-processable oxides, or “green inks,” have been applied in printable electronics. Table 2.1 summarizes recent initiatives on the development of green inks from TMOs. Their compatibility with low-cost, scalable process such as electrodeposition or roll-to-roll make these materials even more attractive. Compared with PEDOT:PSS, these inexpensive semiconductor oxides can be more stable [102]. In particular, Voroshazi et al. [115] have demonstrated that MoO_3 can be more stable than PEDOT:PSS. Figure 2.24 compares the stability of solar cells assembled with PEDOT:PSS and MoO_3 as the HTL, showing that devices containing

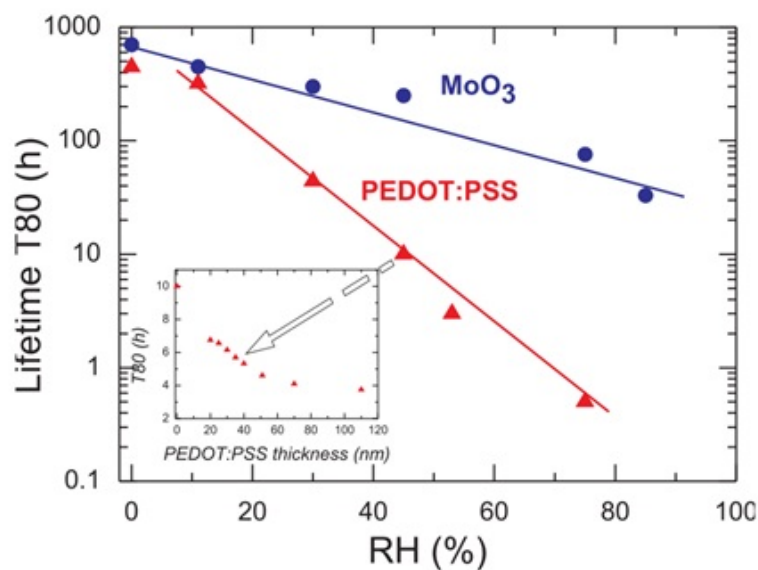
MoO₃ are more stable. A number of reviews on TMOs and their use in organic electronics are available [107, 108, 116, 117].

Figure 2.23: The energy level diagram of state-of-art photovoltaic polymers, electron-accepting fullerene derivatives, and transition metal oxides.



Source: Chen et al. [106]

Figure 2.24: Comparison between the stability of solar cells assembled with PEDOT:PSS and MoO₃ as hole transport layer.



Source: Voroshazi et al. [115]

Table 2.1: Samples and deposition conditions.

TMO	Synthesis method	Solvent	Temp. ° C	Ref.
WO ₃	Sol gel	Butanol	Room Temp	[118]
c-TiO ₂	CBD	H ₂ O	Room Temp	[119]
SnO ₂	CBD	H ₂ O	Room Temp	[120]
Cu ₂ O	CBD	H ₂ O	Room Temp	[121]
ZnO	Spray Pyrolysis	H ₂ O	Room Temp	No
InZnO	Spray Pyrolysis	H ₂ O	Room Temp	No
Cs ₂ CO ₃	Oxide suspension	Methanol	Room Temp	[122]
H ₃ PW ₁₂ O ₄₀	Solution	Methanol	Room Temp	[123]
ZnO	Spray Pyrolysis	H ₂ O	Room Temp	[124]
In _x Ga _y O ₂	Sol gel	2ME	75	[125]
In _x ZnO	Sol gel	2ME	75	[125]
In ₂ O ₃	Sol gel	2ME	75	[125]
MoO _x	Electroless-plating-like	H ₂ O	80	[126]
VO _x	Electroless-plating-like	H ₂ O	80	[126]
MoO ₃	Oxide suspension	H ₂ O	120	No
V ₂ O ₅	Sol gel	H ₂ O	130	[102]
Cs ₂ CO ₃	Oxide suspension	H ₂ O	150	[127]

2.2.3 Zinc oxide (ZnO)

Zinc oxide is a white powder that occurs naturally as the mineral zincite; however, most ZnO is produced synthetically. Numerous materials and products use ZnO as an additive, including rubbers, plastics, ceramics, glass, cement, lubricants, paints, ointments, adhesives, sealants, pigments, foods (source of Zn nutrient), batteries, ferrites, fire retardants, and first-aid tapes. Zinc oxide is a II-VI direct wide-gap semiconductor. In the presence of native defects such as oxygen vacancies or interstitial zinc atoms, ZnO has features of a n -type semiconductor [128]. Semiconducting ZnO has many applications such as sensors, photovoltaic cells, varistors, light-emitting diodes, nanogenerators, and piezoelectric transducers, among others [101, 129].

The interest in ZnO is fueled by its prospects in optoelectronics applications owing to its direct wide bandgap ($E_g \approx 3.3$ eV at 300 K). Some optoelectronics applications of

ZnO overlap with that of GaN, another wide-gap semiconductor ($E_g \approx 3.4$ eV at 300 K) which is widely used for the production of green, blue-ultraviolet, and white light-emitting devices. However, ZnO has some advantages over GaN, such as the wide availability of fairly high-quality ZnO bulk single crystals and a large exciton binding energy of 60 meV. Moreover, ZnO also has a much simpler crystal-growth technology, resulting in potentially lower costs for ZnO-based devices [128].

In XSCs, ZnO is being intensively investigated due to its similarities with TiO_2 , which is the most used oxide semiconductor in these cells. Moreover, ZnO presents some advantages over TiO_2 , such as higher electron mobility, which reduces charge recombination [130, 131]. Moreover ZnO is more suitable for deposition using simple and inexpensive techniques [100]. Table 2.2 shows a compilation of the basic physical parameters for ZnO.

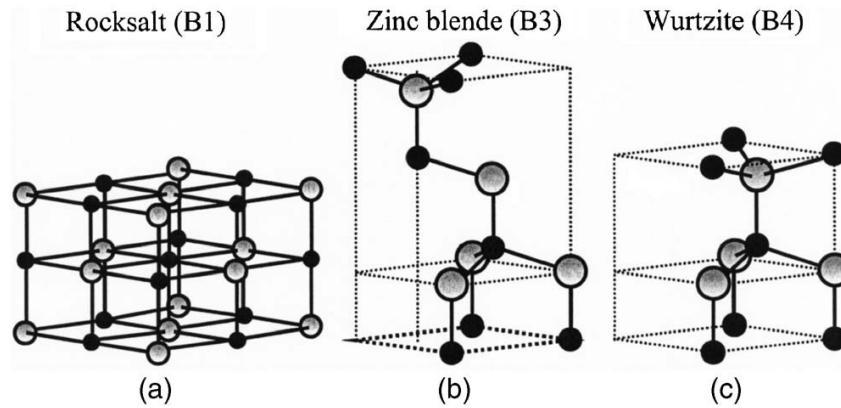
Table 2.2: General physical properties of ZnO semiconductor material.

Property	Symbol (units)	Value
Molecular weight	M_w (mol/g)	81.39
Density	ρ (g/cm ³)	5606
Melting point	mp (°C)	1975
Enthalpy of formation	ΔH_f (J/mol)	6.5×10^5
Entropy of formation	ΔHS (J/mol·K)	100
Heat capacity	C_p (J/mol·K)	41
Electron mobility	μ (cm ² /V·s)	200
Carrier concentration	n_i (cm ⁻³)	8×10^8
Refractive index	η_D (dimensionless)	2.008 - 2.029
Water solubility	K_{sp} (mg/L)	16 at 29°C

Source: Gonzalez-Valls [25]

As shown in Fig. 2.25, ZnO crystallizes in one of three structures: wurtzite (B4), zinc blende (B3), and rocksalt (B1). Under ambient conditions, the stable phase is wurtzite, which belongs to the spatial group $P6_3mc$ or C_{6v}^4 , with lattice parameters $a = 3.25$ Å and $c = 5.21$ Å with ratio of $c/a = \sqrt{8/3} = 1.633$. The other two ZnO crystalline structures, zinc blende and rocksalt, can only be obtained under special synthesis conditions.

Figure 2.25: Stick-and-ball representation of ZnO crystal structures: (a) cubic rocksalt (B1), (b) cubic zinc blende (B3), and (c) hexagonal wurtzite (B4). The shaded gray and black spheres denote Zn and O atoms, respectively.



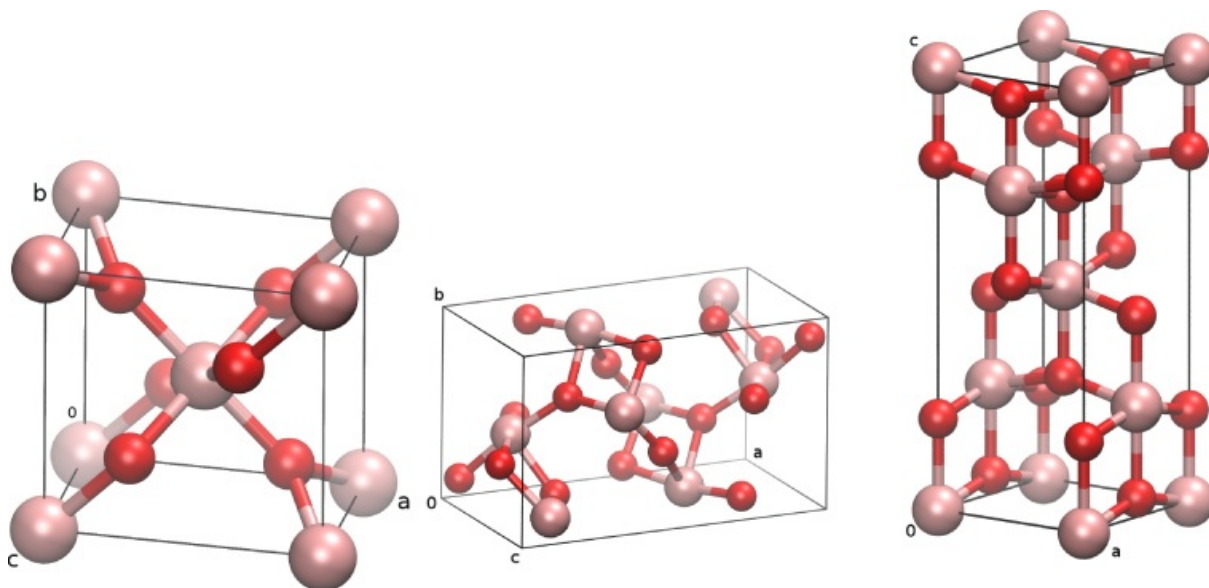
Source: Özgür et al. [128]

2.2.4 Titanium dioxide (TiO_2)

Titanium dioxide (TiO_2), also known as titanium(IV) oxide or titania, is the naturally occurring oxide of titanium. In nature, TiO_2 occurs as the minerals rutile, anatase, and brookite, and TiO_2 is commonly sourced from ilmenite, rutile, and anatase. Titanium dioxide has a wide range of applications from paint to sunscreen to food coloring and solar cells. Figure 2.26 illustrates the unit cells of the three TiO_2 structures. The rutile phase is thermodynamically more stable and is preferred in the dye industry. The metastable anatase phase is the most suitable for solar cell applications due to its bandgap ($E_g = 3.2$ eV), which is higher than that for the rutile phase ($E_g = 3.0$). For most dyes used in DSSCs, the TiO_2 conduction band remains slightly below the excited energy level, which allows efficient electron injection. Moreover, the high refraction index $n = 2.5$ leads to efficient scattering from the incident light on the porous photoanode, resulting in better light absorption.

The advantages of TiO_2 extend to charge transport. In particular, the high dielectric constant ($\epsilon = 80$ for anatase phase) provides good electrostatic protection for the injected electron with respect to oxidized dye, which is adsorbed on the oxide surface. This injected electron is protected from recombination before it is reduced by the mediator

Figure 2.26: Stick-and-ball representation of TiO_2 crystal structures: rutile, brookite, and anatase (left to right).



Source: Moellmann et al. [132]

electrolyte. Thus, the injected electron diffuses quickly through the film. This diffusion is approximately 10^4 times faster than that for a charged ion in solution; however, the diffusion is much smaller than the diffusion in a nanocrystalline semiconductor. This lower mobility can be attributed to the very high internal surface area of the mesoporous structure, which contains a high density of defects capable of trapping electrons [133].

The requirements for electron transport layers (ETL) involve high electron mobility and transparency in the visible region to allow transmission of light into the active layer. These requirements limit the number of materials that have these characteristics, among which is the well-known and widely used titanium oxide [134, 135]. In general, thin TiO_2 films have been introduced as ETL because of their large bandgap (3.7 eV) and well-matched energy levels (valence band of ≈ 8.1 eV and conduction band of ≈ 4.4 eV). Thus, these films facilitate electron injection and transport and simultaneously block the hole collection at the cathode [136].

2.2.5 Vanadium oxide (V_2O_5)

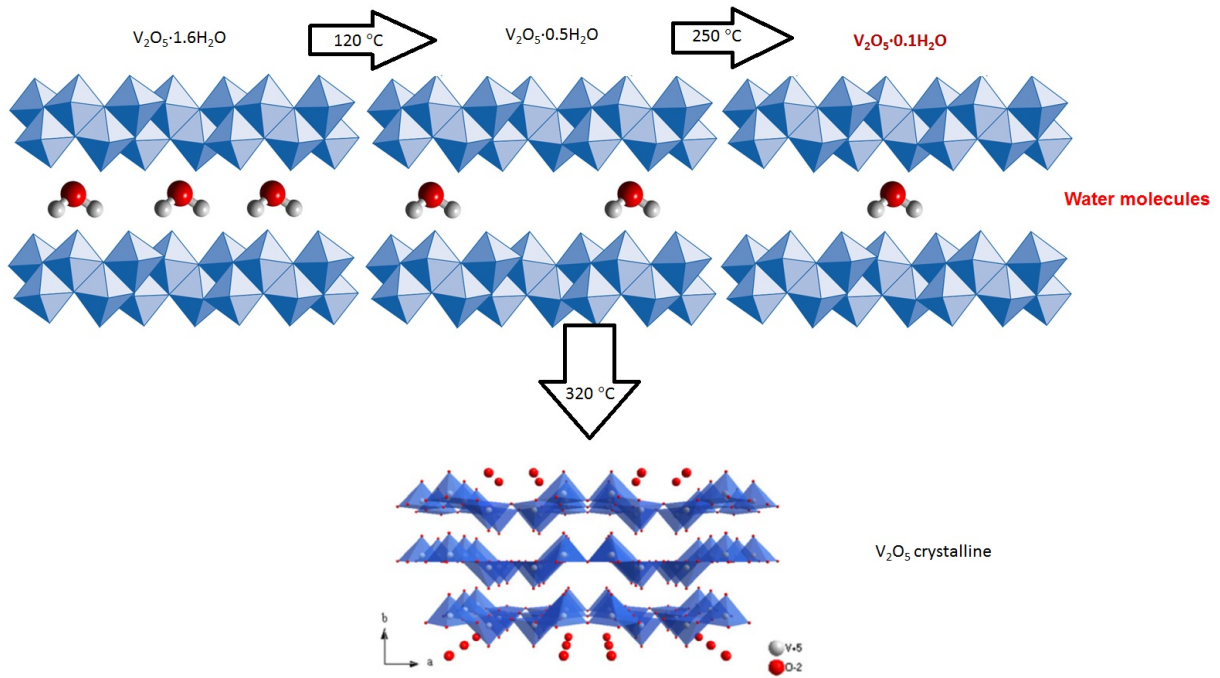
Vanadium oxide (V_2O_5) is an inorganic compound commonly known as vanadium pentoxide. Generally, V_2O_5 is a brown/yellow solid; however, when precipitated from an

aqueous solution, its color is deep orange. Because of its high oxidation state, it serves as both an amphoteric oxide and an oxidizing agent. Industrially, V_2O_5 is the most important compound of vanadium as a principal precursor to vanadium alloys and as a widely used industrial catalyst [137]. The mineral form of this compound, shcherbinaite, is extremely rare and almost always found among fumaroles. The mineral trihydrate, $V_2O_5 \cdot 3H_2O$, is also known by navajoite.

The characteristics of V_2O_5 make it a promising candidate for the hole transport layer (HTL) in organic solar cells. The most widely used synthesis methods employ multistep techniques for preparing this HTL, such as the suspension of V_2O_5 nanoparticulates obtained from the hydrolysis of vanadium (III) acetylacetonate [104] or the fabrication of a bronze V_2O_5 HTL from a suspension of metal oxide (MO) obtained after the reaction between a metal powder and H_2O_2 [138]. One of the most widespread fabrication methods is the application of sol-gels made from vanadium (V) oxitriisopropoxide (ViPr) [105, 139–142], an expensive compound known for its toxicity. A water-based synthesis route has been proposed by Livage [143, 144]. The water-based V_2O_5 was successfully applied in OSCs with improved efficiency and stability [102, 145].

In comparison with V_2O_5 prepared using the oxitriisopropoxide precursor, which leaves an organic residue, water-based V_2O_5 is less expensive, more stable, more environmental friendly, and leaves no residue. Because the water-based V_2O_5 is synthesized in water, the pristine thin films are hydrated with some water molecules between the layered V_2O_5 structure. To prepare a crystalline thin film, the film must be annealed up to 320°C . Figure 2.27 shows how the water molecules are removed with increasing annealing temperatures. At 320°C , no water molecules remain, and the film is completely crystalline. Pristine V_2O_5 thin films synthesized from the Livage [143] recipe are hydrated $V_2O_5 \cdot 1.6H_2O$. Heating the sample at 120°C releases water molecules from the V_2O_5 slabs, resulting in $V_2O_5 \cdot 0.5H_2O$. The second dehydration takes place at 250°C , obtaining 0.1 water molecules per V_2O_5 . The crystalline form of V_2O_5 without water is obtained after heating the sample above 320°C .

Figure 2.27: Process of elimination of water molecules from V_2O_5 hydrated thin film through heating.



Source: Liu et al. [146]

2.2.6 Synthesis of oxide semiconductors

2.2.6.1 Electrodeposition

Electrodeposition is emerging as a method for synthesizing semiconductor thin films and nanostructures, especially chalcogenides and oxides. The electrodeposition of thin film semiconductors became popular in the 1980s, primarily in the development of inexpensive techniques for fabricating solar cells. Therefore, the requirements of a photovoltaics cell for large-scale terrestrial use, namely high efficiency, stability, and low cost, were met using electrodeposited thin-film semiconductor-based solar cells [147, 148].

The electrodeposition of thin film semiconductors has some advantages over physical and chemical deposition techniques. In particular, electrodeposition is an easy and economical synthesis method that has little to no waste of material. Because of the purification that often results from electrodeposition, very pure starting materials are not required, unlike other methods [148]. Thus, the electrodeposition of semiconducting materials represents a new challenge because this method presents interesting characteristics

for large-area, low-cost, and generally low-temperature processing of materials [149]. Zinc oxide is probably the most studied and versatile MO for solar cell applications. Films of ZnO with remarkable structural quality can be prepared by electrodeposition with different morphologies ranging from arrays of single crystalline microcolumns to continuous films, depending on the substrate activation, solution composition, and deposition time [149].

Thermodynamically, electrodeposition is based on the familiar Nernst equation for the potential E_M of a metal electrode in a given solution:

$$E_m = E_m^0 + \frac{RT}{nF} \ln \left(\frac{a_m^{m+}}{a_m} \right), \quad (2.27)$$

where E_m^0 is the standard potential for the reduction to form M , R is the gas constant, T is the absolute temperature, n is the number of electrons required for the reduction, F is the Faraday constant, and a_m^{m+} and a_m are the activities of M^{m+} in the electrolyte and of M in the deposit, respectively. Truly reversible potentials can be established only if the following conditions are fulfilled [147]:

- (a) All of the processes enabling the electrodeposition of M are fast compared to other competing reactions;
- (b) All soluble intermediate species are present in the solution at equilibrium concentrations;
- (c) The element M is a pure and well-defined phase;
- (d) The deposited crystal grains are in their equilibrium form and state;
- (e) The crystals are not too small, i.e., they exceed crystal sizes of approximately 25 nm for potential errors less than 1 mV.

The above conditions are rarely met in practice, and hence, Kröger [150] has introduced the concept of “quasi-rest potentials” to help explain the zero-current conditions that otherwise approximate the true thermodynamic reversibility. The electrodeposition of M

can occur at potentials that are more negative than the equilibrium potential due to the neglect of interactions of the solute ion M^{m+} with the solvent or with complexing ligands as in eq. 2.27. Such potentials are known as overpotentials (or overvoltage). Moreover, there are many kinetic factors that influence the deposition of elemental semiconductors, such as the rate of the electron transfer reaction, dissociation kinetics of solvated or complexed ions and so on.

2.2.6.2 Hydrothermal synthesis

Hydrothermal synthesis is a special case of the *solvo*thermal process, which is generally defined as a crystal growth method, that occurs via chemical reactions and changes in the solubility of materials in an aqueous solution held at a given temperature and pressure, above ambient conditions, in a closed system [151]. According to classical growth theory, the thermodynamic driving force for hydrothermal growth from a solution is the presence of supersaturation, which could initiate spontaneous crystallization and further growth of the nuclei [152].

Indeed, the hydrothermal method exploits the spontaneous crystallization by increasing the temperature T and pressure p , which are fundamental properties of water. Thus, the solvency of water changes important characteristics such as the ionic product, density, thermal conductivity, viscosity, heat capacity, and dielectric constant, which are all highly p and T dependent. Specific solvent properties can be obtained by tuning the synthesis parameters.

In the synthesis of inorganic compounds, the precursor is often an aqueous solution of simple salts, such as metal chlorides, nitrates, or acetates. These aqueous salts can be precipitated to their corresponding metal hydroxides prior to synthesis using a base, which is often NaOH, KOH, or NH_4OH , along with other additives for pH control, reduction, oxidation, or coating, as necessary. On the other hand, these aqueous salts can be added prior to hydrothermal treatment.

2.2.6.3 Sol-gel

The sol-gel method is a wet-chemical synthesis technique for preparing oxide gels, glasses, and ceramics with a high-degree of purity. Sol-gel is an effective synthesis method because it allows control of the stoichiometry, crystal structure, and particle size. The method is based on controlling the hydrolysis and condensation of alkoxide precursors. In general, the sol-gel process involves transition from a liquid “sol” (colloidal solution) into a “gel” phase [153]. Inorganic metal salts or metal organic compounds such as metal alkoxide are commonly used as precursors. The colloidal suspension is formed after a series of hydrolysis and condensation reactions with the precursors. Then, the sol particles condense into a continuous liquid phase (gel). With further drying and heat treatment, the resulting gel is converted into dense ceramic or glass materials. Generally, three reactions are used to describe the sol-gel process: hydrolysis, alcohol condensation, and water condensation. Because water and alkoxides are immiscible, alcohol is commonly used as co-solvent. With an appropriate co-solvent, the sol-gel precursor mixes well with water to facilitate the hydrolysis.

In summary, the sol-gel method consists of the following steps:

- (a) Hydrolysis and condensation: During the hydrolysis reaction, the alkoxide groups (OR) are replaced with hydroxyl groups (OH) through the addition of water. The subsequent condensation reaction produce oxides with by-products of water (water condensation) or alcohol (alcohol condensation).
- (b) Gelation: In the gelation step, the alkoxide gel precursor undergoes a polymerization (condensation) reaction with by-products of water or alcohol.
- (c) Aging: During this process, further cross-links continue, and the gel shrinks as the covalent links replace non-bonded contacts. The pore sizes and pore wall strengths change with the evolution of the gel structure.
- (d) Drying: The gel has a high ratio of water and three-dimensional interconnected pores inside the structure. Before the pore is closed during the densification process, drying is used to remove the liquid trapped in the interconnected pores.

2.3 References

- [1] L. Etgar. Semiconductor nanocrystals as light harvesters in solar cells. *Materials*, 6:445–459, 2013.
- [2] International Energy Agency (IEA). Key world energy statistics. Technical report, International Energy Agency, 2012.
- [3] P. Würfel. *Physics of Solar Cells: From Principles to New Concepts*. Wiley-Vch, 2005.
- [4] T. Soga. *Nanostructured Materials for Solar Energy Conversion*. Elsevier Scientific, 2006.
- [5] I. Olindo. *Light management in thin-film silicon solar cells*. PhD thesis, Delft University of Technology, 2013.
- [6] Exxon Mobil. Corporate citizenship report. Technical report, Exxon Mobil, 2011.
- [7] T. P. Soubbotina. *Beyond Economic Growth an Introduction to Sustainable Development*. The World Bank, 2000.
- [8] Energy Information Administration (EIA). International energy outlook. Technical report, U.S. Energy Information Administration, 2013.
- [9] European Photovoltaic Industry Association (EPIA). Global market outlook for photovoltaics 2013-2017. Technical report, European Photovoltaic Industry Association, 2013.
- [10] I. T. Salamoni and R. Rüther. O potencial brasileiro de geração solar fotovoltaica conectada à rede elétrica: Análise de paridade de rede. In *IX Encontro nacional e V Latino Americano de Conforto no Ambiente Construído.*, 2007.
- [11] F. Kininguer. *Photovoltaics Systems Technology*. Kassel University, 2003.

- [12] F. Zhang, W. Mammo, L. M. Andersson, S. Admassie, M. R. Andersson, and O. Inganäs. Low-bandgap alternating fluorene copolymer/methanofullerene heterojunctions in efficient near-infrared polymer solar cells. *Adv. Mater.*, 18:2169–2173, 2006.
- [13] G. K. Mor, S. Kim, M. Paulose, O. K. Varghese, K. Shankar, J. Basham, and C. A. Grimes. Visible to near-infrared light harvesting in TiO₂ nanotube array-P3HT based heterojunction solar cells. *Nano Lett.*, 9 (12):4250–4257, 2009.
- [14] P. Löper, S. Moon, S. M. de Nicolas, B. Niesen, M. Ledinsky, S. Nicolay, J. Bailat, J. Yum, S. De Wolf, and C. Ballif. Organic-inorganic halide perovskite/crystalline silicon four-terminal tandem solar cells. *Phys.Chem.Chem.Phys.*, 17:1619–1629, 2015.
- [15] W. D. Callister Jr and D. G. Rethwisch. *Materials Science and Engineering an Introduction*. John Wiley & Sons, Inc., 2011.
- [16] R. A. S. Abreu. Caracterização elétrica de células solares de tripla junção - GaInP/GaAs/Ge. Master’s thesis, INPE, 2006.
- [17] U.S. Department of Energy. The solar history. Technical report, U.S. Department of Energy, 2002.
- [18] Albert Einstein. On a heuristic viewpoint concerning the production and transformation of light. *Ann. Phys.*, 322:132–148, 1905.
- [19] Paul Hersch and Kenneth Zweibel. *Basic Photovoltaic Principles and Methods*. United States Government, 1982.
- [20] S. M. Sze and K. N. Kwok. *Physics of Semiconductor Devices*. John Wiley and Sons, 2007.
- [21] S. M. Rezende. *Materiais e Dispositivos Eletrônicos*. Editora Livraria da Física, 2004.
- [22] J. Nelson. *The Physics of Solar Cells*. Imperial College Press, 2003.

- [23] J. L. Gray. *Handbook of Photovoltaic Science and Engineering*, chapter The Physics of the Solar Cell, pages 82–129. John Wiley & Sons, Ltd., 2011.
- [24] S. J. Fonash. *Solar Cell Device Physics*. Academic Press, 2010.
- [25] I. Gonzalez-Valls. *Vertically-aligned ZnO Nanostructures for excitonic Solar Cells*. PhD thesis, Universidad Autonoma de Barcelona, 2013.
- [26] P. L. Burn and P. Meredith. The rise of the perovskites: the future of low cost solar photovoltaics? *NPG Asia Mat.*, 6:e79, 2014.
- [27] C. Zhang, D. Sun, C-X. Sheng, Y. X. Zhai, K. Mielczarek, A. Zakhidov, and Z. V. Vardeny. Magnetic field effects in hybrid perovskite devices. *Nature Physics*, 11, 2015.
- [28] X. Li, M. Tschumi, H. Han, S. S. Babkair, R. A. Alzubaydi, A. A. Ansari, S. S. Habib, M. K. Nazeeruddin, S. M. Zakeeruddin, and M. Grätzel. Outdoor performance and stability under elevated temperatures and long-term light soaking of triple-layer mesoporous perovskite photovoltaics. *Energ. Technol.*, 3:1–5, 2015.
- [29] J. Kim, H. Hiroi, T. K. Todorov, O. Gunawan, M. uwahara, T. Gokmen, D. Nair, M. Hopstaken, B. Shin, Y. S. Lee, W. Wang, H. Sugimoto, and D. B. Mitzi. High efficiency $\text{Cu}_2\text{ZnSn}(\text{S},\text{Se})_4$ solar cells by applying a double $\text{In}_2\text{S}_3/\text{CdS}$ emitter. *Adv. Mater.*, 2014.
- [30] X. Lin, J. Kavalakkatt, M. Ch. Lux-Steiner, and A. Ennaoui. Inkjet-printed $\text{Cu}_2\text{ZnSn}(\text{S}, \text{Se})_4$ solar cells. *Adv. Sci.*, 1500028:1–6, 2015.
- [31] M. Pavan, S. Rühle, A. Ginsburg, D. A. Keller, H. Barad, P. M. Sberna, D. Nunes, R. Martins, A. Y. Anderson, A. Zaban, and E. Fortunato. $\text{TiO}_2/\text{Cu}_2\text{O}$ all-oxide heterojunction solar cells produced by spray pyrolysis. *Sol. Energy Mater. Sol. Cells*, 132:549–556, 2015.
- [32] T. Minami, Y. Nishi, and T. Miyata. High-efficiency Cu_2O -based heterojunction

solar cells fabricated using a Ga_2O_3 thin film as n-type layer. *Appl. Phys. Express*, 6:044101, 2013.

- [33] W. Y. Liang. Exciton. *Phys. Educ.*, 5:226–228, 1970.
- [34] RLE Center for Excitonics/Massachusetts Institute of Technology. Exciton formation. <http://eecs-newsletter.mit.edu/tags/excitons/>, 2015. [Online; accessed 8-May-2015].
- [35] D. Neamen. *Semiconductor Physics and Devices*. Mc Graw Hill, 1997.
- [36] B. A. Gregg. Excitonic solar cells. *J. Phys. Chem. B*, 107:4688–4698, 2003.
- [37] E. Unger. *Excitonic Dye Solar Cells*. PhD thesis, Uppsala University, 2012.
- [38] B. O'Regan and M. Grätzel. A low-cost, high-efficiency solar cell based on dye-sensitized colloidal TiO_2 films. *Nature*, 353:737–740, 1991.
- [39] L. Han, A. Islam, H. Chen, C. Malapak, B. Chiranjeevi, S. Zhang, X. Yang, and M. Yanagida. High-efficiency dye-sensitized solar cell with a novel co-adsorbent. *Energy Environ. Sci.*, 5:6057, 2012.
- [40] A. Sacco, A. Lamberti, R. Gazia, S. Bianco, D. Manfredi and N. Shahzad, F. Cappelluti, S. Ma, and E. Tresso. High efficiency dye-sensitized solar cells exploiting sponge-like ZnO nanostructures. *Phys. Chem. Chem. Phys.*, 14:16203–16208, 2012.
- [41] M. McCune, W. Zhang, and Y. Deng. High efficiency dye-sensitized solar cells based on three-dimensional multicolor ZnO nanowire arrays with “caterpillar-like” structure. *Nano Lett.*, 12:3656–3662, 2012.
- [42] L. Cojocar, C. Olivier, T. Toupance, E. Sellier, and L. Hirsch. Size and shape fine-tuning of SnO_2 nanoparticles for highly efficient and stable dye-sensitized solar cells. *J. Mater. Chem. A*, 1:13789, 2013.
- [43] I. Chung, B. Lee, J. He, R. P. H. Chang, and M. G. Kanatzidis. All-solid-state dye-sensitized solar cells with high efficiency. *Nature*, 485:486–490, 2012.

- [44] M. K. Nazeeruddin, , A. Kay, I. Rodicio, R. Humphry-Baker, E. Muller, P. Liska, N. Vlachopoulos, and M. Grätzel. Conversion of light to electricity by cis-xzbis(2,2'-bipyridyl-4,4'-dicarboxylate) ruthenium(ii) charge-transfer sensitizers ($X = \text{Cl}^-$, Br^- , I^- , CN^- , and SCN^-) on nanocrystalline TiO_2 electrodes. *J. Am. Chem. Soc.*, 115:6382, 1993.
- [45] M. K. Nazeeruddin, S. M. Zakeeruddin, R. Humphry-Baker, M. Jirousek, P. Liska, N. Vlachopoulos, V. Shklover, C. H. Fisher, and M. Grätzel. Acid-base equilibria of (2,2'-bipyridyl-4,4'-dicarboxylic acid) ruthenium(ii) complexes and the effect of protonation on charge-transfer sensitization of nanocrystalline titania. *Inorg. Chem.*, 38:6298, 1999.
- [46] M. K. Nazeeruddin, P. Pechy, T. Renouard, S. M. Zakeeruddin, R. Humphry-Baker, P. Comte, P. Liska, L. Cevey, E. Costa, V. Shklover, L. Spiccia, G. B. Deacon, C. A. Bignozzi, and M. Grätzel. Engineering of efficient panchromatic sensitizers for nanocrystalline TiO_2 . *J. Am. Chem. Soc.*, 123:1613, 2001.
- [47] A. Yella, H.W. Lee, H.N. Tsao, C. Yi, A.K. Chandiran, M.K. Nazeeruddin, E.W. Diau, C.Y. Yeh, S.M. Zakeeruddin, and M. Grätzel. Porphyrin-sensitized solar cells with cobalt (ii/iii) -based redox electrolyte exceed 12 percent efficiency. *Science*, 334:629, 2011.
- [48] J. Cid, J. Yum, S. Jang, M. K. Nazeeruddin, E. Martínez-Ferrero, E. Palomares, J. Ko, M. Grätzel, and T. Torres. Molecular cosensitization for efficient panchromatic dye-sensitized solar cells. *Angew. Chem. Int. Ed.*, 46:8358–8362, 2007.
- [49] K. Hara, K. Sayama, Y. Ohga, A. Shinpo, S. Suga, and H. Arakawa. A coumarinderivative dye sensitized nanocrystalline TiO_2 solar cell having a high solar-energy conversion efficiency up to 5.6%. *Chem. Commun.*, 6:569–570, 2001.
- [50] L. Schmidt-Mende, U. Bach, R. Humphry-Baker, T. Horiuchi, H. Miura, S. Ito, S. Uchida, and M. Grätzel. Organic dye for highly efficient solid-state dye-sensitized solar cells. *Adv. Mater.*, 17:813–815, 2005.

- [51] Y. J. Chang and T. J. Chow. Highly efficient triarylene conjugated dyes for sensitized solar cells. *J. Mater. Chem.*, 21:9523–9531, 2011.
- [52] H. Zhou, L. Wu, Y. Gao, and T. Ma. Dye-sensitized solar cells using 20 natural dyes as sensitizers. *J. Photochem. Photobiol. A*, 219:188–194, 2011.
- [53] M. R. Narayan. Review: Dye sensitized solar cells based on natural photosensitizers. *Renew. Sust. Energ. Rev.*, 16:208–215, 2012.
- [54] A. W. L. Vallejo, A. C. S. Qui nones, and A. J. S. Hernandez. *Solar Cells - Dye-Sensitized Devices*, chapter The Chemistry and Physics of Dye-Sensitized Solar Cells, pages 399–419. InTech, 2011.
- [55] S. Poomana and R. M. Mehra. Effect of electrolytes on the photovoltaic performance of a hybrid dye ZnO solar cell. *Sol. Energy Mater. Sol. Cells*, 91:518–524, 2007.
- [56] A. Hagfeldt, G. Boschloo, L. Sun, L. Kloo, and H. Pettersson. Dye-sensitized solar cells. *Chem. Rev.*, 110:6595–6663, 2010.
- [57] B. G. Kim, C. G. Zhen, E. J. Jeong, J. Kieffer, and J. Kim. Organic dye design tools forefficiente photocurrent generation in dye-sensitized solar cells: Exciton binding energy and electron acceptors. *Adv. Funct. Mater*, 22:1606–1612, 2012.
- [58] S. Mathew, A. Yella, P. Gao, R. Humphry-Baker, B. F.E.Curchod, N. Ashari-Astani, I. Tavernelli, U. Rothlisberger, M. K. Nazeeruddin, and M. Grätzel. Dye-sensitized solar cells with 13% efficiency achieved through the molecular engineering of porphyrin sensitizers. *Nature Chemistry*, 6:242–247, 2014.
- [59] H. Hoppe and N. S. Sariciftci. Organic solar cells: An overview. *J. Mater. Res.*, 19:1924–1945, 2004.
- [60] G. Yu, J. Gao, J. Hummelen, F. Wudl, and A. J. Heeger. Polymer photovoltaic cells: Enhanced efficiencies via a network of internal donor-acceptor heterojunctions. *Science*, 270:1789–1791, 1995.

- [61] J. J. M. Halls, C. A. Walsh, N. C. Greenham, R. H. Friend E. A. Marseglia, S. C. Moratti, and A. B. Holmes. Efficient photodiodes from interpenetrating polymer networks. *Nature*, 376:498–500, 1995.
- [62] M. J. Rice and Y. N. Gartstein. Theory of photoinduced charge transfer in a molecularly doped conjugated polymer. *Phys. Rev. B*, 53:10764, 1996.
- [63] J. J. M. Halls, J. Cornil, D. A. dos Santos, R. Sibley, D. H. Wang, A. B. Holmes, J. L. Bredas, and R. H. Friend. Charge- and energy-transfer processes at polymer/polymer interfaces: A joint experimental and theoretical study. *Phys. Rev. B*, 60:5721, 1999.
- [64] L. Wang, H. Liu, R. M. Konik, J. A. Misewich, and S. S. Wong. Carbon nanotube-based heterostructures for solar energy applications. *Chem. Soc. Rev.*, 42:8134–8156, 2013.
- [65] P. A. van Hal, R. A. J. Janssen, G. Lanzani, G. Cerullo, M. Zavelani-Rossi, and D. Silvestri. Full temporal resolution of the two-step photoinduced energy–electron transfer in a fullerene–oligothiophene–fullerene triad using sub - 10 fs pump–probe spectroscopy. *Chem. Phys. Lett.*, 345:33–38, 2001.
- [66] B. C. Zerza, C. J. Brabec, G. Cerullo, S. D. Silvestri, and N. S. Sariciftci. Ultrafast charge transfer in conjugated polymer-fullerene composites. *Synth. Met.*, 119:637–638, 2001.
- [67] P. Peumans, A. Yakimov, and S. R. Forrest. Small molecular weight organic thin-film photodetectors and solar cells. *J. Appl. Phys.*, 93:3693–3723, 2003.
- [68] C. W. Tang. Two-layer organic photovoltaic cell. *Appl. Phys. Lett.*, 48:183–185, 1986.
- [69] C. Y. Yang and A. J. Heeger. Morphology of composites of semiconducting polymers mixed with C₆₀. *Synth. Met.*, 83:85–88, 1996.

- [70] S. E. Shaheen, C. J. Brabec, and N. S. Sariciftci. 2.5% efficient organic plastic solar cells. *Appl. Phys. Lett.*, 78:841–843, 2001.
- [71] C. Liu, C. Yi, K. Wang, Y. Yang, R. S. Bhatta, M. Tsige, S. Xiao, and X. Gong. Single-junction polymer solar cells with over 10% efficiency by a novel two-dimensional donor-acceptor conjugated copolymer. *ACS Appl. Mater. Interfaces*, 7(8):4928–4935, 2015.
- [72] J. Y. Kim, K. Lee, N. E. Coates, and D. Moses T. Nguyen M. Dante A. J. Heeger. Efficient tandem polymer solar cells fabricated by all-solution processing. *Science*, 317:222–225, 2007.
- [73] J. You, L. Dou, K. Yoshimura, T. Kato, K. Ohya, T. Moriarty, K. Emery, C. Chen, J. Gao, G. Li, and Y. Yang. A polymer tandem solar cell with 10.6% power conversion efficiency. *Nature Communications*, 4 (1446):1–10, 2013.
- [74] Y. Liu, C. Chen, Z. Hong, J. Gao, Y. Yang, H. Zhou, L. Dou, G. Li, and Y. Yang. Solution-processed small-molecule solar cells: breaking the 10% power conversion efficiency. *Scientific Reports*, 3 (3356):1–8, 2013.
- [75] X. Che, X. Xiao, J. D. Zimmerman, D. Fan, and S. R. Forrest. High-efficiency, vacuum-deposited, small-molecule organic tandem and triple-junction photovoltaic cells. *Adv. Energy Mater.*, 4(18):1614, 2014.
- [76] A. R. M. Yusoff, D. Kim, H. P. Kim, Fabio Kurt Shneider, Wilson Jose da Silva, and J. Jang. A high efficiency solution processed polymer inverted triple-junction solar cell exhibiting a power conversion efficiency of 11.83%. *Energy Environ. Sci.*, 8(1):303–316, 2015.
- [77] G. Li, V. Shrotriya, J. Huang, Y. Yao, T. Moriarty, K. Emery, and Y. Yang. High-efficiency solution processable polymer photovoltaic cells by self-organization of polymer blends. *Nature Materials*, 4:864 – 868, 2005.
- [78] F. C. Krebs, S. A. Gevorgyana, and J. Alstrup. A roll-to-roll process to flexible

- polymer solar cells: model studies, manufacture and operational stability studies. *J. Mater. Chem.*, 19:5442–5451, 2009.
- [79] C. J. Brabec. Organic photovoltaics: technology and market. *Sol. Energy Mater. Sol. Cells*, 83:273–292, 2004.
- [80] C. J. Brabec, N. S. Sariciftci, and J. C. Hummelen. Plastic solar cells. *Adv. Funct. Mater.*, 11:15–26, 2001.
- [81] B. C. Thompson and J.-M. J. Fréchet. Polymer-fullerene composite solar cells. *Angew. Chem., Int. Ed.*, 47:58–77, 2008.
- [82] R. Kroon, M. Lenes, J. C. Hummelen, P. W. M. Blom, and B. de Boer. Small bandgap polymers for organic solar cells (polymer material development in the last 5 years). *Polym. Rev.*, 48:531–582., 2008.
- [83] Tim Jones. Organic electronics. Web site, April 2015. URL http://www2.warwick.ac.uk/fac/sci/chemistry/research/jones/jonesgroup/research_old/organicelectronics/.
- [84] T. Ameri, G. Dennler, C. Lungenschmied, and C. J. Brabec. Organic tandem solar cells: A review. *Energy Environ. Sci.*, 2 (4):347–363, 2009.
- [85] T. Ameri, N. Li, and C. J. Brabec. Highly efficient organic tandem solar cells: a follow up review. *Energy Environ. Sci.*, 6:2390–2413, 2013.
- [86] J. You, L. Dou, Z. Hong, G. Li, and Y. Yang. Recent trends in polymer tandem solar cell research. *Prog. Polym. Sci.*, <http://dx.doi.org/10.1016/j.progpolymsci.2013.04.005>, 2013.
- [87] G. Dennler, H.-J. Prall, R. Koeppe, M. Egginger, R. Autengruber, and N. S. Sariciftci. Enhanced spectral coverage in tandem organic solar cells. *Applied Physics Letters*, 89 (7):073502–073505, 2006.
- [88] Thomas Rieks Andersen. *Organic Based Solar Cells with Morphology Control*. PhD thesis, Danish Technical University, 2013.

- [89] L. Etgar, P. Gao, Z. Xue, Q. Peng, A. K. Chandiran, B. Liu, M. K. Nazeeruddin, and M. Gratzel. Mesoscopic $\text{CH}_3\text{NH}_3\text{PbI}_3/\text{TiO}_2$ heterojunction solar cells. *J. Am. Chem. Soc.*, 134:17396–17399, 2012.
- [90] K. Zhu, N. R. Neale, A. Miedaner, and A. J. Frank. Enhanced charge-collection efficiencies and light scattering in dye-sensitized solar cells using oriented TiO_2 nanotubes arrays. *Nano Lett.*, 7 (1):69–74, 2007.
- [91] X. Feng, K. Zhu, A. J. Frank, C. A. Grimes, and T. E. Mallouk. Rapid charge transport in dye-sensitized solar cells made from vertically aligned single-crystal rutile TiO_2 nanowires. *Angew. Chem.*, 124:2781–2784, 2012.
- [92] I. Robel, V. Subramanian, M. Kuno, and P. V. Kamat. Quantum dot solar cells. harvesting light energy with CdSe nanocrystals molecularly linked to mesoscopic TiO_2 films. *J. Am. Chem. Soc.*, 128 (7):2385–2393, 2006.
- [93] H. Jin, S. Choi, R. Velu, S. Kim, and H. J. Lee. Preparation of multilayered cdse quantum dot sensitizers by electrostatic layer-by-layer assembly and a series of post-treatments toward efficient quantum dot-sensitized mesoporous TiO_2 solar cells. *Langmuir*, 28:5417–5426, 2012.
- [94] D. Zhang, W. C. H. Choy, F. Xie, W. E. I. Sha, X. Li, B. Ding, K. Zhang, F. Huang, and Y. Cao. Plasmonic electrically functionalized TiO_2 for high-performance organic solar cells. *Adv. Funct. Mater.*, 23:4255–4261, 2013.
- [95] Z. Lin, C. Jiang, C. Zhu, and J. Zhang. Development of inverted organic solar cells with TiO_2 interface layer by using low-temperature atomic layer deposition. *Appl. Mater. Interfaces*, 5:713–718, 2013.
- [96] Y. Zhao and K. Zhu. Charge transport and recombination in perovskite $(\text{CH}_3\text{NH}_3)\text{PbI}_3$ sensitized TiO_2 solar cells. *J. Phys. Chem. Lett.*, 4:2880–2884, 2013.
- [97] H. Luo, T. Takata, Y. Lee, J. Zhao, K. Domen, and Yushan. Photocatalytic activity enhancing for titanium dioxide by co-doping with bromine and chlorine. *Chem. Mater.*, 16:846–849, 2004.

- [98] S. Chambon, A. Rivaton, J. L. Gardette, and M. Firon. Photo and thermal degradation of MDMO-PPV:PCBM blends. *Sol. Energy Mater. Sol. Cells*, 91:394–398, 2007.
- [99] I. Gonzalez-Valls and M. Lira-Cantu. Vertically-aligned nanostructures of ZnO for excitonic solar cells: a review. *Energy Environ. Sci.*, 2:19–34, 2009.
- [100] M. H. Kumar, N. Yantara, S. Dharani, M. Grätzel, S. Mhaisalkar, P. P. Boix, and N. Mathews. Flexible, low-temperature, solution processed ZnO-based perovskite solid state solar cells. *Chem. Comm.*, 49:11089–11091, 2013.
- [101] B. N. Illy, A. C. Cruickshank, S. Schumann, R. da Campo, T. S. Jones, S. Heutz, M. A. McLachlan, D. W. McComb, D. J. Riley, and M. P. Ryan. Electrodeposition of ZnO layers for photovoltaic applications: controlling film thickness and orientation. *J. Mater. Chem.*, 21:12949–12957, 2011.
- [102] G. Teran-Escobar, J. Pampel, J. M. Caicedo, and M. Lira-Cantu. Low-temperature, solution-processed, layered V_2O_5 hydrate as the hole-transport layer for stable organic solar cells. *Energy Environ. Sci.*, 6:3088–3098, 2013.
- [103] J. Wu, Y. Zhang, P. Xua, W. Guoa, L. Shena, and S. Ruan. Role of solution-processed V_2O_5 in P3HT:PCBM based inverted polymer solar cells. *Synthetic Metals*, 170:7–10, 2013.
- [104] H. Q. Wang, N. Li, N. S. Guldal, and C. J. Brabec. Nanocrystal v_2o_5 thin film as hole-extraction layer in normal architecture organic solar cells. *Org Electron.*, 13(12):3014–3021, 2012.
- [105] T. T. Larsen-Olsen, T. R. Andersen, B. Andreasen, A. P. L. Bottiger, E. Bundgaard, K. Norrman, J. W. Andreasen, M. Jorgensen, and F. C. Krebs. Roll-to-roll processed polymer tandem solar cells partially processed from water. *Sol Energ Mat Sol C.*, 97:43–49, 2012.
- [106] S. Chen, J. R. Manders, S. Tsang, and F. So. Metal oxides for interface engineering in polymer solar cells. *J. Mater. Chem.*, 22:24202–24212, 2012.

- [107] M. T. Greiner, M. G. Helander, W. Tang, Z. Wang, J. Qiu, and Z. Lu. Universal energy-level alignment of molecules on metal oxides. *Nat. Mat.*, 11.(1):76–81, 2012.
- [108] M. T. Greiner, L. Chai, M. G. Helander, W. Tang, and Z. Lu. Transition metal oxide work functions: The influence of cation oxidation state and oxygen vacancies. *Adv. Funct. Mater.*, 22(21):4557–4568, 2012.
- [109] C. Qiu, C. Qiu, Z. Xie, H. Chen, M. Wong, and H. S. Kwok. Comparative study of metal or oxide capped indium-tin oxide anodes for organic light-emitting diodes. *J. Appl. Phys.*, 93(6):3253–3258, 2003.
- [110] H. M. Zhang and W.C.H. Choy. Highly efficient organic light-emitting devices with surfacemodified metal anode by vanadium pentoxide. *J. Phys. D: Appl. Phys.*, 41: 062003, 2008.
- [111] J. Meyer, K. Zilberberg, T. Riedl, and A. Kahn. Electronic structure of vanadium pentoxide: An efficient hole injector for organic electronic materials. *Journal of Applied Physics*, 110(3):033710, 2011.
- [112] H. J. Bolink, E. Coronado, D. Repetto, M. Sessolo, E. M. Barea, J. Bisquert, G. Garcia-Belmonte, J. Prochazka, and L. Kavan. Inverted solution processable oleds using a metal oxide as an electron injection contact. *Adv. Funct. Mater.*, 18: 145–150., 2008.
- [113] H. J. Bolink, E. Coronado, D. Repetto, and M. Sessolo. Air stable hybrid organic-inorganic light emitting diodes using ZnO as the cathode. *Appl. Phys. Lett.*, 91: 223501, 2007.
- [114] H. Lee, I. Park, J. Kwak, D. Y. Yoon, and C. Lee. Improvement of electron injection in inverted bottom-emission blue phosphorescent organic light emitting diodes using zinc oxide nanoparticles. *Appl. Phys. Lett.*, 96:153306, 2010.
- [115] E. Voroshazi, B. Verreet, A. Buri, R. Müller, D. Nuzzo, and P. Heremans. Influence of cathode oxidation via the hole extraction layer in polymer:fullerene solar cells. *Organic Electronics*, pages 736–744, 2011.

- [116] J. Meyer, S. Hamwi, M. Kröger, W. Kowalsky, T. Riedl, and A. Kahn. Transition metal oxides for organicelectronics: Energetics, device physics and applications. *Adv. Mater. (Weinheim, Ger.)*, 24:5408–5427, 2012.
- [117] M. T. Greiner and Z. Lu. Thin-film metal oxides in organic semiconductor devices: their electronic structures, work functions and interfaces. *NPG Asia Mater.*, 5(55): 1–15, 2013.
- [118] N. A. Ramos-Delgado, L. Hinojosa-Reyes, I. L. Guzman-Mar, M. A. Gracia-Pinilla, and A. Hernández-Ramírez. Synthesis by sol-gel of WO_3/TiO_2 for solar photocatalytic degradation of malathion pesticide. *Catal. Today*, 209:35–40, 2013.
- [119] H. M. Pathan, W. Y. Kim, K. Jung, and O. Joo. A chemical route to room-temperature synthesis of nanocrystalline TiO_2 thin films. *Appl. Surf. Sci.*, 246:72–76, 2005.
- [120] Y. Masuda, T. Ohji, and K. Kato. Room-temperature synthesis of tin oxide nanoelectrodes in aqueous solutions. *Thin Solid Films*, 518(2):850–852, 2009.
- [121] P. B. Ahirrao, B. R. Sankapal, and R. S. Patil. Nanocrystalline p-type-cuprous oxide thin films by room temperature chemical bath deposition method. *J. Alloys Compd.*, 509(18):5551–5554, 2011.
- [122] C. Hsiao, A. Hsiao, and S. Chen. Design of hole blocking layer with electron transport channels for highperformance polymer light-emitting diodes. *Adv. Mater. (Weinheim, Ger.)*, 20(10):1982–1988, 2008.
- [123] L. C. Palilis, M. Vasilopoulou, A. M. Douvas, D. G. Georgiadou, S. Kennouc, N. A. Stathopoulou, V. Constantoudis, and P. Argitis. Solution processable tungsten polyoxometalate as highly effective cathode interlayer for improved efficiency and stability polymer solar cells. *Sol. Energy Mater. Sol. Cells*, 114:205–213, 2013.
- [124] N.L. Tarwal, A.V. Rajgure, A.I. Inamdar, R.S. Devane, I.Y. Kim, S.S. Suryavanshi, Y.R. Ma, J.H. Kim, and P.S. Patil. Growth of multifunctional ZnO thin films by spray pyrolysis technique. *Sensors and Actuators A: Physical*, 199:67–73, 2013.

- [125] M. Kim, J. W. Hennek, H. S. Kim, M. G. Kanatzidis, A. Facchetti, and T. J. Marks. Delayed ignition of autocatalytic combustion precursors: Low-temperature nanomaterial binder approach to electronically functional oxide films. *J. Am. Chem. Soc.*, 134(28):11583–11593, 2012.
- [126] L. Wu, Y. Yu, X. Han, Y. Zhang, Y. Zhang, Y. Lia, and J. Zhi. An electroless-plating-like solution deposition approach for large-area flexible thin films of transition metal oxide nanocrystals. *J. Mater. Chem. C*, 2:2266–2271, 2014.
- [127] Y. Park, S. Noh, D. Lee, J. Kim, and C. Lee. Study of the cesium carbonate (Cs_2CO_3) inter layer fabricated by solution process on p3ht:pcbm solar cells. *Mol Cryst Liq Cryst.*, 9:20–27, 2011.
- [128] Ü. Özgür, Y. I. Alinov, C. Liu, A. Teke, M. A. Reshchikoc, S. Dogan, V. Avrutin, S. J. Cho, and H. Morkoç. A comprehensive review of ZnO materials and devices. *J. Appl. Phys.*, 98:041301, 2005.
- [129] S. J. Pearton, D. P. Norton, K. Ip, Y. W. Heo, and T. Steiner. Recent progress in processing and properties of ZnO. *Prog. Mater. Sci.*, 50:293–340, 2005.
- [130] M. Quintana, T. Edvinsson, A. Hagfeld, and G. Boschloo. Comparison of dye-sensitized ZnO and TiO_2 solar cells: studies of charge transport and carrier lifetime. *J. Phys. Chem. C*, 111:1035, 2007.
- [131] K. Keis, C. Bauer, G. G. Boschloo, A. Hagfeld, K. Westermark, H. Rensmo, and H. Siegbahn. Nanostructured ZnO electrodes for dye-sensitized solar cell applications. *J. Photochem. Photobiol. A*, 148:57–64, 2002.
- [132] J. Moellmann, S. Ehrlich, R. Tonner, and S. Grimme. A dft-d study of structural and energetic properties of TiO_2 modifications. *J. Phys.: Condens. Matter*, 24(424206):1–8, 2012.
- [133] A. F. Nogueira. *Células Solares de “Grätzel” com Eletrólito Polimérico*. PhD thesis, Instituto de Química (Unicamp), 2001.

- [134] K. S. Yeo, S. Nakaob, Y. Hirosea, T. Hasegawaa, and Y. Matsuo. Application of sputter-deposited amorphous and anatase TiO_2 as electroncollecting layers in inverted organic photovoltaics. *Org. Electron.*, 14(7):1715–1719, 2013.
- [135] I. Sasajima, S. Uesaka, T. Kuwabara, T. Yamaguchi, and K. Takahashi. Flexible inverted polymer solar cells containing an amorphous titanium oxide electron collection electrode. *Org. Electron.*, 12(1):113–118, 2011.
- [136] H. Y. Sun, J. Weickert, H. C. Hesse, and L. Schmidt-Mende. Uv light protection through TiO_2 blocking layers for inverted organic solar cells. *Sol. Energy Mater. Sol. Cells*, 95(12):3450–3454, 2011.
- [137] G. Bauer, V. Güther, H. Hess, A. Otto, O. Roidl, H. Roller, and S. Sattelberger. Vanadium and vanadium compounds. *Ullmann's Encyclopedia of Industrial Chemistry*, 2000.
- [138] F. Xie, W.C.H. Choy, C. Wang, X. Li, S. Zhang, and J. Hou. Low temperature solution precessed hydrogen molybdenum and vanadium bronzes for an efficient hole transport layer in organic electronics. *Advanced Materials*, 25(14):2051–2055, 2013.
- [139] K. Zilberberg, S. Trost, J. Meyer, A. Kahn, A. Behrendt, D. Lützenkirchen-Hecht, R. Frahm, and T. Riedl. Inverted organic solar cells with sol-gel processed high work-function vanadium oxide hole-extraction layers. *Adv. Funct. Mater.*, 21(24):4776–4783, 2011.
- [140] C. P. Chen, Y.D. Che, and S.C. Chuang. High-performance and highly durable inverted organic photovoltaics embedding solution-processable vanadium oxides as an interfacial hole-transporting layer. *Advanced Materials*, 23(33):3859–3863, 2011.
- [141] I. Hancox, L. A. Rochford, D. Clare, M. Walker, J. J. Mudd, P. Sullivan, S. Schumann, C. F. McConville, and T. S. Jones. Optimization of a high work function solution processed vanadium oxide hole-extracting layer for small molecule and polymer organic photovoltaic cells. *J.Phys.Chem.C*, 117:49–57, 2013.

- [142] K. Zilberberg, S. Trost, H. Schmidt, and T. Riedl. Solution processed vanadium pentoxide as charge extraction layer for organic solar cells. *Adv. Energy Mater.*, 1(3):377–381, 2011.
- [143] J. Livage. Vanadium pentoxide gels. *Chem. Mater.*, 3(4):578–593, 1991.
- [144] J. Livage. Hydrothermal synthesis of nanostructured vanadium oxides. *Materials*, 3:4175–4195, 2010.
- [145] A. Morais, J. P. C. Alves, F. A. S. Lima, M. Lira-Cantu, and A. F. Nogueira. Enhanced photovoltaic performance of inverted hybrid bulkheterojunction solar cells using TiO_2 / reduced graphene oxide films as electron transport layers. *J. Photon. for Energy*, 5(1):057408, 2015.
- [146] F. Liu, S. Song, D. Xue, and H. Zhang. Selective crystallization with preferred lithium-ion storage capability of inorganic materials. *Nanoscale Res. Lett.*, 7(149):1–17, 2012.
- [147] G. F. Fulop and R. M. Taylor. Electrodeposition of semiconductors. *Annu. Rev. Mater. Res.*, 15:197–210, 1985.
- [148] C. D. Lokhande and S. H. Pawar. Electrodeposition of thin film semiconductors. *Physica Status Solid (a)*, 111:17–39, 1989.
- [149] D. Lincot. Electrodeposition of semiconductors. *Thin Solid Films*, 487:40–48, 2005.
- [150] F. A. Kröger. Cathodic deposition and characterization of metallic or semiconducting binary alloys or compounds. *J. Electrochem. Soc.*, 125:2028–2034, 1978.
- [151] W. Shi, S. Song, and H. Zhang. Hydrothermal synthetic strategies of inorganic semiconducting nanostructures. *Chem. Soc. Rev.*, 42(13):5714–5743, 2013.
- [152] J. J. Richardson and F. F. Lange. Controlling low temperature aqueous synthesis of ZnO. 1. thermodynamic analysis. *Cryst. Growth Des.*, 9(6):2570–2575, 2009.
- [153] J. D. Wright and N. A. J. M. Sommerdijk. *Sol-gel Materials: Chemistry and applications. Advanced Chemistry Texts*. Gordon and Breach Science Publishers, 2001.

3. CHARACTERIZATION TECHNIQUES

A number of techniques were used to characterize the materials synthesized for this thesis. In this chapter, these techniques are briefly presented to support the discussion of results.

3.1 X-ray diffraction

One primary technique for gaining knowledge about the crystalline structure of materials is X-ray diffraction (XRD). When this technique is applied to thin films, even more information can be acquired, such as the preferential orientation of growth.

The diffraction pattern of a polycrystalline material could be considered to be a collection of reflections, which are each described by a peak height, position, width, and area. The integrated area is proportional to the Bragg intensity I_k , where K corresponds to a reflection's Miller indexes set (hkl) . Moreover, I_k is proportional to the square of the absolute value of the structure factor, $|F_k|^2$.

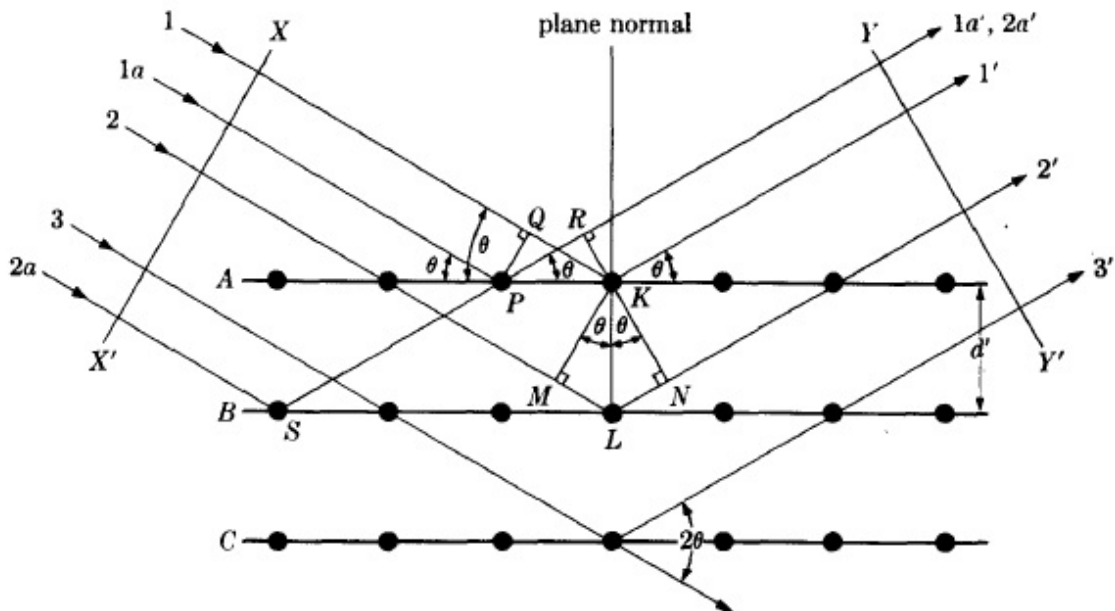
The diffraction of X-rays by a crystalline material can be described considering a monochromatic beam with a specific wavelength (λ) focused on a crystal, which is composed of parallel atomic planes (hkl) arranged periodically in space. The beam is focused on the crystal at angle θ , which is referred to as the Bragg angle. The electrons from the atoms composing the crystal are excited and vibrate at the same frequency as that of the incident X-ray. The diffracted beam will also form an angle θ with the crystal planes, and consequently, the diffracted beams will be parallel, as shown in Fig. 3.1. The constructive interference of diffracted waves occurs when the paths taken by the X-ray beam reflected by two or more planes hkl is different by an integer multiple of the wavelength. This

relation is known as Bragg's law, which can be written as:

$$n\lambda = 2d_{hkl} \sin \theta, \quad (3.1)$$

where d_{hkl} is the interplanar distance, θ is the diffraction angle, λ is the wavelength of the incident X-ray radiation, and n is an integer.

Figure 3.1: The X-ray diffraction of crystallographic planes.



Source: Cullity [1]

3.2 Electron microscopy

Electronic microscopy techniques offer a significant advantage in terms of the maximum resolution when compared with optical microscopy. While the maximum resolution for the best optical microscopes is ~ 300 nm, modern transmission electron microscopes (TEMs) can reach sub-Angstrom resolution. Optical microscopes are primarily limited by the wavelength of visible light, while electronic microscopes are limited by the wavelength

of a high-energy electron beam, which is much smaller than that of visible light [2].

According to de Broglie's equation, the wavelength of any particle can be expressed by

$$\lambda = \frac{h}{mv}, \quad (3.2)$$

where m is the particle mass, v is its velocity, and h is Plank's constant. Assuming that the acceleration voltage in an electron gun is V , then the electron energy is

$$eV = \frac{mv^2}{2}. \quad (3.3)$$

From eq. 3.3, it follows that

$$mv^2 = 2eV. \quad (3.4)$$

Multiplying both sides of eq. 3.4 by m , it follows that

$$m^2v^2 = 2meV. \quad (3.5)$$

Substituting eq. 3.2 in eq. 3.5, the following equation can be obtained for the incident wavelength:

$$\lambda = \frac{h}{(2meV)^{1/2}}. \quad (3.6)$$

Typical operating voltages in TEM are of the order of 100 kV which yields an electron wavelength of 0.00370 nm. For these energies, the relativistic mass of the electron must be considered. Performing the same calculations for a scanning electron microscope (SEM), where typical voltages are of the order of 10 kV, electron wavelengths of about 0.01 nm are obtained. In both cases, the obtained wavelength is less than the interatomic distance in solids.

In addition to a magnification that is almost one million times higher than that for an optical microscope, an electron microscope offer additional advantages. For example, the TEM can simultaneously provide information about the real and reciprocal space because the electron diffraction patterns can be recorded. Moreover, the TEM has two essential operation modes: diffraction mode and image mode. The information obtained

in diffraction mode is derived mainly from the elastic scattering of the incident beam by the specimen [3]. If the scattering centers in the specimen are arrayed in an orderly, regular manner (as in a crystal), the scattering is coherent and results in spot patterns. On the other hand, if the specimen is poly-crystalline, ring patterns are expected. The diffraction pattern in TEM is usually obtained from a specific area of the specimen obtained by inserting a selecting aperture. In this case, the operation is called selected-area electron diffraction (SAED). In the image mode there are basically two kind of mechanisms for the image formation. Diffraction contrast imaging and phase contrast imaging. In the diffraction contrast imaging mode, both non-diffracted or diffracted beam are used to form the image, while all other beams are removed from the image by using of an objective aperture. The images can be acquired in bright field (BF) or dark field (DF). In BF imaging, only the transmitted beam is allowed to pass the objective aperture to form images, with mass-thickness contrast. In DF imaging, only diffracted beams are allowed to pass the aperture to form images. Phase contrast or high resolution imaging HREM use all of the diffracted and non diffracted beams and add them back together, to form a phase contrast image. In order to obtain a HREM image, a large objective aperture is used. Phases and intensities of diffracted and transmitted beams are combined to form a phase contrast image.

In SEM a number of signals can be analyzed using various electron beam interactions with the sample, such as backscattered electrons, secondary electrons, characteristic X-rays, continuum X-rays, fluorescent X-rays, cathode luminescence, and current in the sample, among others.

3.3 Energy dispersive X-ray spectroscopy

Energy dispersive X-ray spectroscopy is an analytical technique used for performing elemental analysis of a sample, which is based on the interaction of X-ray excitations within a sample. The EDX characterization capabilities are largely due to the fundamental principle that each element has a unique atomic structure, allowing also only one set of peaks in the X-ray emission spectrum. Most EDX spectrometers are coupled to an

electronic microscope and use the high energy electron beam as the X-ray excitation. In this way, EDX can be used to evaluate the chemical composition of the region of focus in the microscope.

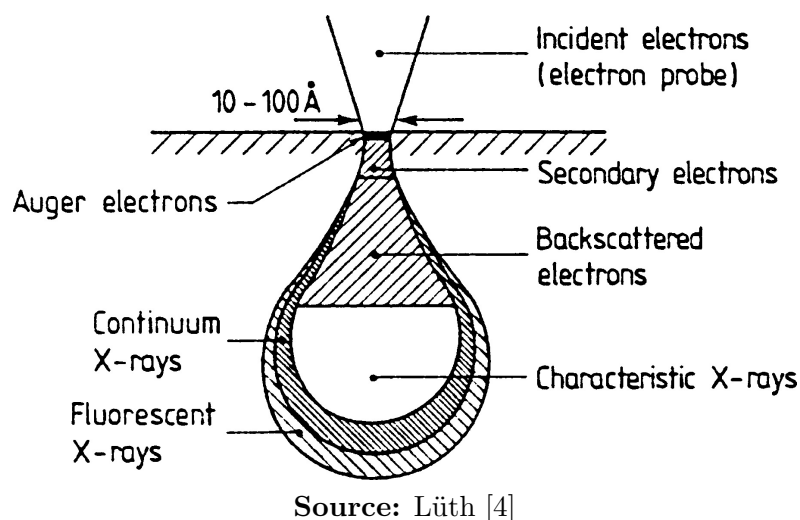
The X-rays emitted by a sample under electronic excitation as well as the corresponding energy loss by the primary electron beam are characteristics of the chemical constituents of the sample. The characteristic X-ray spectrum can provide both qualitative and quantitative information about the sample, thus enabling a correlation between the microstructure and the chemical composition of the sample.

The absorption of X-ray photons by matter is weak, and thus, the emitted photons originate from a depth range that is essentially determined by the penetration depth of the high-energy primary electrons. Depending on the material and the primary energy, the information depth ranges from 0.1–10 μm . The characteristic difference between the information depth and the volume probed by the different techniques is shown schematically in Fig. 3.2. Backscattered electrons and X-ray photons originate typically from a pear-shaped zone below the surface, while the low-energy secondary electrons and Auger electrons carry information from the small, narrow neck of the “pear.” The shape of the probed region arises from the elastic and inelastic scattering of high-energy primary electrons. Moreover, the X-ray probe offers better depth analysis for the investigation of layered structures.

3.4 Photoelectron spectroscopy

Photoelectron spectroscopy techniques are based on electron emission from the sample when the sample is stimulated by external radiation. Photoelectron spectroscopy offer some of the most versatile techniques for characterizing a surface. In this work, both X-ray photoelectron spectroscopy (XPS) and ultraviolet (UV) photoelectron spectroscopy (UPS) are considered.

Figure 3.2: Schematic overview of the pear-shaped volume probed by different microprobe signals (electron and X-ray emission) when a primary electron beam is incident on the solid surface. The Auger electrons originate from a depth of 5–20 Å, whereas the X-ray information depth is 0.1–10 μm with much less spatial resolution.



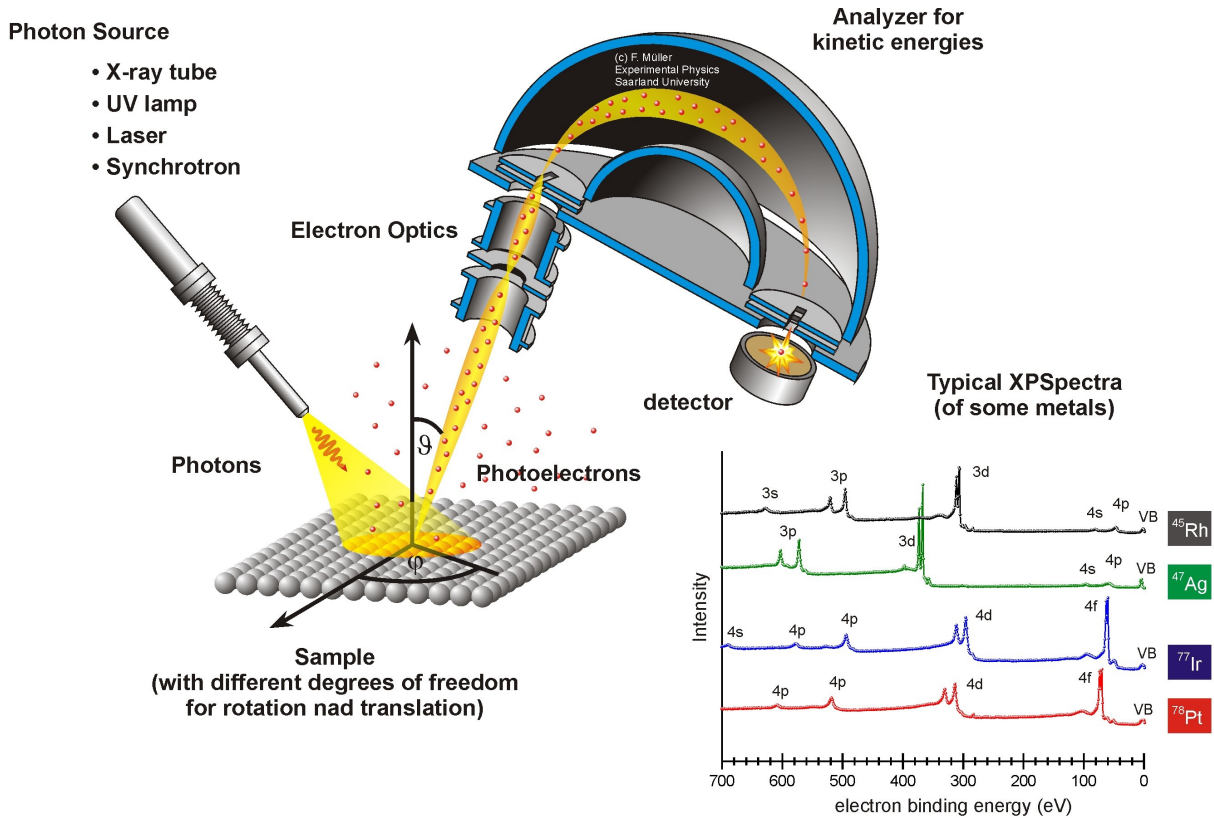
3.4.1 X-ray photoelectron spectroscopy

In X-ray photoelectron spectroscopy, X-ray radiation causes the electron ejection within a sample. Thus, X-rays are used to excite a sample, and electrons are emitted as a response. The emitted electrons are then collected and recorded with respect to their kinetic energy, giving rise to a spectrum that reveals important information about the sample.

The electron emission is due to the photoelectric effect, and an ultra-high vacuum (10^{-9} torr) system is required for detecting such electrons. When the experiment is performed, the incident X-ray beam has a diameter ranging from ~ 1 –10 mm and a penetration depth of approximately 1 μm. The electrons can be excited in any part of this volume; however, only electrons from a small volume, which has a diameter ranging from 0.01–1 mm and a depth of only 10 nm, have sufficient energy to be ejected from the sample and contribute to the XPS signal. Because all the information is obtained from a maximum depth of ~ 10 nm, XPS provides information only from the surface of the samples. The typical setup for XPS measurements is illustrated in Fig. 3.3.

When a X-ray photon strikes a sample, all of its energy can be absorbed by a single electron, which leads to its ejection from the sample with a certain kinetic energy. This

Figure 3.3: Schematic drawing of a typical XPS setup with a photon source (X-rays, UV light, laser, or synchrotron radiation), a sample, which can be manipulated with different linear and rotational degrees of freedom, electron optics, an energy dispersive analyzer, and a detector. The XP spectra (intensity vs. binding energy) are shown for four different metals with the element specific distribution of their core-level photoemission.



Source: Jacobs [5]

process is known as the photoelectron effect. The kinetic energy for an ejected electron can be expressed by

$$KE = h\nu - BE - \phi, \quad (3.7)$$

where KE is the measured kinetic energy, $h\nu$ is the incident X-ray photon energy, and BE is the binding energy, which had to be overcome before the electron could be ejected. Moreover, ϕ is the work function of the sample, which can easily be calibrated.

The electron binding energy can be calculated from the kinetic energy. The binding energy is correlated with the atomic number Z of the material comprising the sample. Thus, a characteristic value for each material can be obtained. The XPS spectrum is taken with respect to the binding energy and is not related to the kinetic energy [6].

Equation 3.7 can be rewritten as follows:

$$BE = hv - KE - \phi. \quad (3.8)$$

After the electron is ejected, a hole appears in its place, and an electron from an outer layer can fill the hole. The excess energy, which is due to the difference in energy levels between the outer electron and the hole, could be released in the form of X-rays in a phenomena known as X-ray fluorescence. On the other hand, the excess energy could be transferred to a neighboring electron, which could also be ejected from the sample. If the neighboring electron is also ejected, this electron is referred to as an Auger electron.

To interpret the results from the XPS spectrum, an energy scale must be defined, and the energy on this scale is typically measured with respect to the Fermi level. In this way, the binding energy, which is the energy of interest in an XPS experiment, could be defined as the difference between the energy at the core level and the Fermi level. Moreover, the energy for Auger electrons will be related to the difference in energy between electron energy levels.

The XPS technique is very sensitive to the surface, precisely because the electrons in this energy range cannot travel long distances in a solid before they are scattered and lose their characteristic energy. Assuming that the attenuation of electron energy is due primarily to inelastic scattering and considering the following Beer-Lambert Law:

$$I = I_0 \exp\left(-\frac{d}{\lambda \cos \theta}\right), \quad (3.9)$$

approximately 95% of the signal is obtained from the first 5 nm of the sample surface.

3.4.2 Ultraviolet photoelectron spectroscopy

If the area of interest is restricted only to the electrons in the valence shell, photons with less energy could be used to analyze the material, such as photons in the ultraviolet range rather than X-rays. This technique is referred to as photoelectron spectroscopy by ultraviolet radiation, which is commonly known as UPS. The energy of photons in UPS

is on the order of 20–40 eV, which is considerably less than that of XPS.

One major feature of UPS allows the determination of the work function and valence band maximum (VBM) for semiconductors. In general, the UPS spectra consists of two principal components: (1) primary electrons that did not suffer inelastic collisions, and (2) secondary electrons, which are primary electrons that have lost varying amounts of energy. The primary electrons result in distinct spectral features (peaks) that mirror the density of states (DOS) of the sample (to a first-order approximation), while the secondary electrons have a roughly continuous energy spectrum down to zero kinetic energy, which is superimposed with the primary electron spectrum.

From the initial spectrum, the highest kinetic energy can be determined, which corresponds to VBM for an unknown binding energy. The lowest kinetic energy is zero. With these two values, the ionization energy E_{ion} can be calculated as follows:

$$EK = h\nu - E_{ion}. \quad (3.10)$$

To determine the work function of the semiconductor, the analyzer must be calibrated. This calibration essentially provides a reference in which the Fermi edge of the analyzer is on the energy scale. Then, the semiconductor sample can be connected to the analyzer by mounting it on the sample plate. This immediately equilibrates the semiconductor Fermi level with that of the analyzer, i.e., the “internal” kinetic energy spectrum of the semiconductor becomes calibrated. Then, the absolute values for the work function and the VBM binding energy can be extracted.

3.5 Ultraviolet-visible absorption spectroscopy

The ultraviolet-visible (UV-Vis) spectra can be used to calculate the electronic band gap of semiconductor thin films. Semiconductor materials exhibit high absorption for photons with energies greater than the band gap energy, which results in a sharp increase in absorption at energies close to the band gap.

The band gap energy of semiconductors can be measured using Tauc's plot of E with respect to $\alpha^2 E^2$ [7, 8], where E the energy in electron-volts and α is the absorption coefficient. The absorption coefficient can be calculated from the Beer-Lambert Law:

$$I = I_0 e^{-\alpha t}, \quad (3.11)$$

where I_0 is the intensity of incident light, α is the absorption coefficient, and t is the film thickness. Then, considering

$$I/I_0 = T, \quad (3.12)$$

where T is the transmittance, it follows from eq. 3.11 that

$$\alpha = \frac{1}{t} \ln \left(\frac{1}{T} \right). \quad (3.13)$$

From E and α , the Tauc plot can be obtained. Using the positions where the curve crosses the x-axis, the direct band gap can be estimated.

3.6 Raman spectroscopy

Raman spectroscopy provides information about molecular vibrations that can be used for sample identification and quantification. In this technique, a monochromatic light source (i.e., laser) is applied to a sample, and the scattered light is detected. The majority of the scattered light has the same frequency as the excitation source; this is known as Rayleigh or elastic scattering. A very small amount of the scattered light (5–10% of the incident light intensity) is shifted due to interactions between the incident electromagnetic waves and the vibrational energy levels of the molecules in the sample. The Raman spectrum for a sample is obtained by plotting the intensity of this “shifted” light with respect to the frequency. The frequency shift between the emitted photon and the excited photon indicates the characteristic vibrational modes in the material. There are two types of Raman shift. If the incident photons transfer energy to the lattice in the form of phonons, which means that the final vibrational state is more energetic than the

initial state, the emitted photon possesses a lower energy (frequency) to conserve the total energy of the system. This process is designated as a Stokes shift. On the other hand, if the final vibrational state is less energetic than the initial state, the emitted photon possesses a higher frequency; this process is considered an anti-Stokes shift [9]. Generally, the Raman spectra are plotted with respect to the laser frequency such that the Rayleigh band lies at 0 cm^{-1} . On this scale, the band positions will lie at frequencies corresponding to the energy levels of different functional group vibrations.

3.7 References

- [1] B. D. Cullity. *Elements of X-Ray diffraction*. Addison-Wesley Publishing Company INC., 1978.
- [2] D. Brandon and W. D. Kaplan. *Microstructural Characterization of Materials*. John Wiley & Sons, Ltd, 2008.
- [3] D. B. Williams and C. B. Carter. *Transmission Electron Microscopy*. Plenum Press, 1996.
- [4] H. Lüth. *Solid Surfaces, Interfaces and Thin Films*. Springer-Verlag, 2010.
- [5] K. Jacobs. <http://jacobs.physik.uni-saarland.de/english/instrumentation/uhvl.htm>. website, April 2015.
- [6] F. Jonh, F. W. Sticle, E. P. Sobol, and P. Kenneth. *Handbook of X-ray Photoelectron Spectroscopy*. Physical Electronisc, New York, 1989.
- [7] J. Tauc, R. Grigorovici, and A. Vancu. Optical properties and electronic structure of amorphous germanium. *phys. stat. sol*, 15:627–637, 1966.
- [8] J. Tauc. Optical properties and electronic structure of amorphous ge and si. *Mat. Res. Bull.*, Vol. 3:37–46, 1968.
- [9] D. K. Schroder. *Semiconductor material and device characterization*. Wiley-Interscience, 2006.

4. ELECTRODEPOSITED ZINC OXIDE THIN FILMS FOR DYE SENSITIZED SOLAR CELLS

In this chapter, nanostructured ZnO thin films were electrochemically grown on fluorine-doped tin oxide (FTO) substrates. The morphology was tuned by modifying the synthesis parameters. The synthesis was performed by applying $\text{Zn}(\text{NO}_3)_2 \cdot 6\text{H}_2\text{O}$ as the sole component of the aqueous electrolyte without capping agents. The ZnO thin films were characterized by X-ray diffraction (XRD), Raman spectroscopy, energy-dispersive X-ray spectroscopy (EDX), X-ray photoelectron spectroscopy (XPS), ultraviolet photoelectron spectroscopy (UPS), ultraviolet-visible (UV-Vis) spectroscopy, scanning electron microscopy (SEM), and transmission electron microscopy (TEM). The as-deposited films were applied as electrodes in dye sensitized solar cells (DSSCs). The performance of the cells was investigated using current density vs. voltage $J - V$ curves and incident photon-to-charge-carrier efficiency (IPCE) measurements. SEM analysis demonstrated a direct relation between the ZnO morphology and Zn precursor concentration. Moreover, lower concentrations resulted in a more porous morphology. Increasing the amount of dye adsorbed on ZnO decreased the power conversion efficiency (PCE) of the final DSSCs. The best cell presented the following parameters: open circuit voltage $V_{oc} = 0.59$ V, short circuit current $J_{sc} = 7.64$ mA/cm², fill factor $FF = 50.41\%$, and power conversion efficiency $PCE = 2.27\%$.

4.1 Introduction

Recently, ZnO has emerged as promising candidate for applications in excitonic solar cells (XSCs). Different ZnO nanostructures, such as nanowires, nanotubes, nanobelts, nanotetrapods, and mesoporous thin films, have been successfully obtained using low-

cost techniques such as hydrothermal and electrochemical synthesis [1–6]. Though TiO_2 is the most commonly used semiconductor oxide for XSC applications, interest in ZnO XSCs has increased because ZnO has been investigated and successfully applied in this technology [7–9]. Moreover, ZnO presents unique properties that are very similar to those of TiO_2 . In fact, ZnO presents some advantages over TiO_2 such as faster charge transport due to electron mobility and higher conductivity, which is several orders of magnitude higher than that observed for TiO_2 [10, 11].

Among the various synthesis methods developed for producing ZnO nanostructured thin films, electrodeposition is a very attractive technique due to its low cost, scalability, and low temperature processing requirements. Direct control of the film morphology is possible by manipulating the electrodeposition parameters such as the applied current, applied potential, electrolyte concentration, temperature, and pH [12–15]. Moreover, electrochemical deposition of ZnO permits the fabrication of novel nanostructured thin films with superior advantages such as a larger surface area, improved electron mobility, and more efficient charge transport [16–20]. Zhu et al. [21] have shown that a nanorod/nanoparticle composite architecture could improve the performance of TiO_2 DSSCs. Furthermore, different ZnO nanostructures have been successfully applied in DSSCs [22–25].

In this work, ZnO thin films were obtained by electrodeposition under different synthesis parameters. These films were morphologically, compositionally, and structurally characterized. Photoanodes developed with these films were applied in DSSCs.

4.2 Water-based fabrication of ZnO

The commercialization and maturity of excitonic solar cell technology (organic, hybrid, and dye-sensitized solar cells) can only be accomplished by maximizing the device efficiency and lifetime while minimizing fabrication costs. High-quality ZnO thin films can be synthesized using water-based fabrication techniques, minimizing cost while retaining good device quality. The primary water-based technique utilized in this work is electrodeposition. Hydrothermal synthesis is also utilized, as discussed in the following chapter.

4.2.1 *Electrodeposition of ZnO*

The approach used for electrodepositing chalcogenides [26, 27] has been extended to many metallic oxides. In metallic oxide electrodeposition, the simplest deposition reaction is based on the reduction of an oxygen precursor in presence of dissolved metallic ions [16]. The electrodeposition of ZnO may be accomplished using nitrates or oxygen [12, 28].

The electrodeposition of ZnO nanostructures is generally based on the generation of OH^- ions at the surface of a working electrode by the electrochemical reduction of a precursor in a Zn^{2+} solution. To date, three precursors have been used for the hydroxide formation: O_2 , H_2O_2 , and NO_3^- [9, 23].

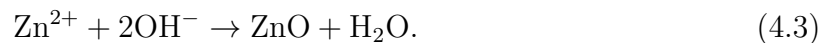
The electrochemical reduction of O_2 occurs either by a two-electron process or a four-electron process. As a function of the electrolyte and cathode properties [29], the two-electron process is described by



while the four-electron process is described by



The generation of hydroxide ions induces an increase of the local pH close to the cathode. Moreover, Zn^{2+} and OH^- ions react. This reaction leads to the precipitation of ZnO and to ZnO deposition on the surface of the cathode described by [29]



For the H_2O_2 and NO_3^- ions, the electroreduction is governed by one of the following processes [23]:





In these reactions, ZnO crystallizes in the Wurtzite structure, and the stacking sequences of Zn^{2+} and O^{2-} along the major c -axis creates a polar crystal. The surfaces perpendicular to the major axis (the $[0002]$ directions) are composed uniquely of either Zn^{2+} or O^{2-} ions and are, therefore, polar. Hence, the electrostatic force will attract negative ions from the solution onto the positive polar face, which allows anisotropic growth of the crystal along the c -axis [9, 30].

4.2.2 *Practical matters*

Electrodeposition is performed in two ways, namely the potentiostatic and galvanostatic methods. In the galvanostatic mode, the deposition is carried out by passing a constant current between two electrodes immersed in an electrolyte. In this kind of deposition, the potential of the electrodes is not given much importance and deposition is standardized at optimum current. In the potentiostatic mode the deposition is carried out in an electrolytic cell containing an extra reference electrode [31] in addition to the regular working electrode (cathode) and counter or auxiliary electrode. The deposition is carried out at a constant potential of the working electrode with respect to the reference electrode [31]. The potentiostatic method is more precise due to the application of the exact reduction potential at the working electrode, resulting in high-quality films [32].

4.3 Experimental procedure

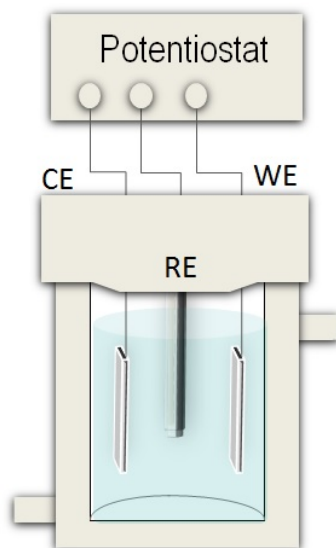
4.3.1 *Synthesis of nanostructured ZnO thin films*

Nanostructured ZnO thin films were fabricated by an electrochemical deposition process. The film deposition was performed by applying $\text{Zn}(\text{NO}_3)_2 \cdot 6\text{H}_2\text{O}$ as the sole component of the aqueous electrolyte and by avoiding the use of a capping agent. A Pt foil

and FTO-coated glass (SOLEMS[®]) with a sheet resistance of 50–70 Ω/\square were used as the counter electrode and working electrode, respectively. The potential was applied with respect to a Ag(s)/AgCl(s)/Cl_(aq)⁻ (Saturated KCl) reference electrode. The potential was applied by a VersaSTAT 3[®] potentiostat (Princeton Applied Research) that was also used to record the data.

The experimental set up used for the electrodeposition of ZnO thin films is shown in Fig. 4.1. Three different concentrations of zinc nitrate were used for the aqueous solution: 12.5 mM, 25 mM, and 50 mM. For all procedures, the temperature was held at 80°C through the use of a hot plate, and the applied potential was -1.0 V. The reaction time ranged from 0.5 h to 2 h. The crystal structure, morphology, and composition of the as-deposited ZnO nanostructured thin films were characterized by XRD, SEM, and EDX, respectively.

Figure 4.1: The experimental set up used in this work for the electrodeposition of ZnO electrodes. The working electrode (WE), counter electrode (CE), and reference electrode (RE) were all connected to the potentiostat.



Source: Own author

4.3.2 *Structural, morphological and electrical characterization of the films*

The zinc oxide thin films were structurally characterized by X-ray diffraction and Raman spectroscopy. X-ray diffraction analyses between 20 and 80° were performed with a Rigaku Rotaflex RU200 B instrument using $\text{CuK}\alpha_1$ radiation. Raman measurements were performed with a Jobin Yvon T64000 micro-Raman Triple Spectrometer using an excitation wavelength of 532 nm. The chemical composition of the films was evaluated by energy dispersive X-ray spectroscopy and X-ray photoelectron spectroscopy. EDX analysis were performed using the electron beam from the SEM as the X-ray excitation source with an acceleration voltage of 20 KV. The X-rays were analyzed with an Inca 250 SSD XMax20 detector, which is Peltier cooled with 20 mm² active area and 129 eV resolution. The XPS measurements were performed using equipment from SPECS[®] with an energy analyzer (PHOIBOS[®] 150) using Al K α (1486.6 eV) radiation as the X-ray source. All spectra were adjusted according to the value of the C 1s peak at (284.8 ± 0.1 eV). The fitting was performed using the CASA XPS application software. Morphological characterization was carried out by means of scanning and transmission electron microscopy. The electronic microscopy images for this work were obtained using the following equipment. Scanning electron microscopy (SEM, FEI Quanta 650FEG ESEM) equipped with an energy dispersive X-ray spectroscopy (EDX) analyzer (Inca 250 SSD XMax20 detector). Transmission electron microscopy (TEM, 200 kV JEM 2011) equipped with an EDS detector (Oxford Linca). The band diagrams for the studied thin films were determined with the help of UV-Vis spectroscopy and ultraviolet photoelectron spectroscopy measurements. UV-Vis analysis of solutions and thin films was performed with a Shimadzu 1800 spectrophotometer. UPS analyses were obtained using equipment from SPECS with a PHOIBOS 150 energy analyzer. The UV radiation source was a He lamp (He 1 21.2 eV) with an experimental resolution of 0.15 eV. The samples were forward biased at 5 V and 10 V to provide sufficient energy for detecting the secondary cut-off electrons.

4.3.3 Solar cell fabrication and characterization

The as-deposited ZnO thin films were immersed in a 0.5 mM/L ethanolic solution of N719 dye for 1 h to provide dye loading for ZnO. After dye loading, the working electrodes were used to assemble DSSCs. The platinized FTO counter electrode was prepared by electron beam physical vapor deposition (EBPVD) with a Pt layer thickness of 50 nm. The working and counter electrodes were bonded together with hot-melt sealing foil. A commercially available liquid iodide-iodine electrolyte, from Solaronix[®], was introduced through a small hole on the Pt counter electrode through capillary forces by applying vacuum. Finally, the DSSCs were hermetically sealed with a small piece of glass, which closed the filling hole. Photoelectrochemical tests were performed by measuring the $J - V$ characteristic curves under simulated AM 1.5 solar illumination at 100 mW/cm^{-2} using the Steuernagel Solarkonstant[®] KHS1200 sun simulator. $J - V$ curves were measured using a Keithley[®] 2601 multimeter. IPCE measurements were performed with a quantum efficiency (QE)/IPCE measurement system from Oriel[®] at 10 nm intervals between 300 and 700 nm. The results were not corrected for intensity losses due to light absorption or due to reflection by the glass support.

4.4 Structural, morphological, compositional, and electrical analysis

In this work, the optimization of the reaction time and the concentration of zinc nitrate in the aqueous electrolyte received particular attention. Samples 1, 2, and 3 were deposited from a 50-mM zinc nitrate electrolyte for 0.5 h (sample 1) and 2 h in four steps of 0.5 h each (samples 2 and 3). Sample 2 was cleaned with deionized water and dried with nitrogen between two consecutive 0.5 h steps and was left in air between cycles. Sample 3 was maintained in the electrolyte solution between cycles. For samples 4 and 5, the total reaction time was 2 h, performed in one single step, with 25-mM and 12.5-mM zinc nitrate concentration, respectively. Table 4.1 summarizes the deposition conditions for the preparation of each electrode.

Table 4.1: Samples and deposition conditions for the electrodeposited ZnO thin films.

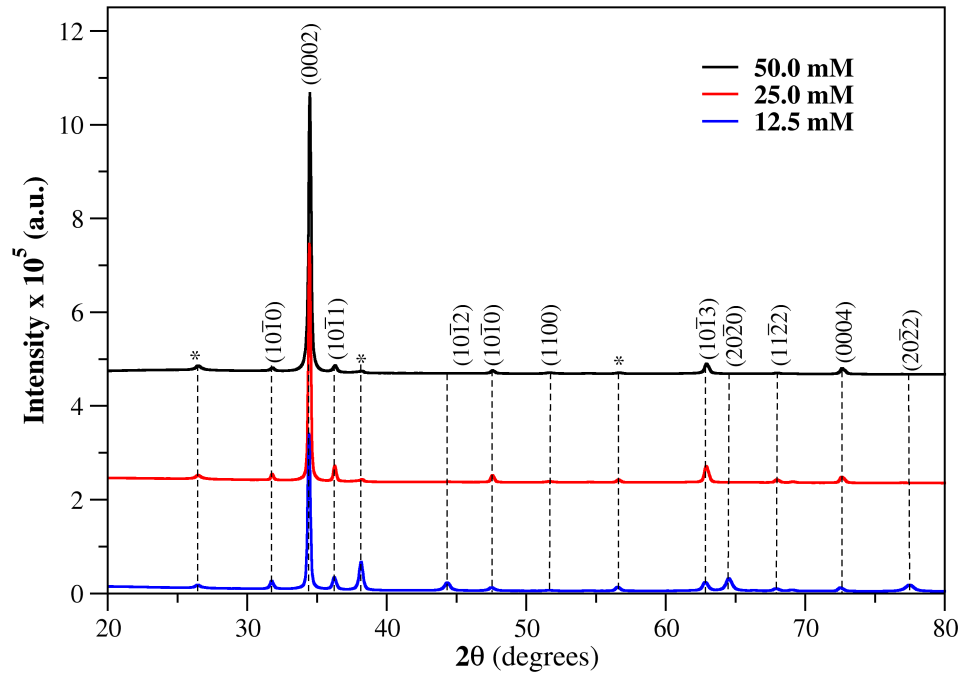
Sample	Electrolyte concentration (mM)	Reaction time (h)	Number of steps	Contact with air
1	50	0.5	1	No
2	50	2	4	Yes
3	50	2	4	No
4	25	2	1	No
5	12.5	2	1	No

Source: Own author

4.4.1 X-ray diffraction

Figure 4.2 shows XRD diffractograms for samples 3, 4 and 5. For now on the results will be mainly focused on the samples 3, 4 and 5 since they were synthesized in electrolytes with different zinc nitrate concentrations, during the same time, 2h, and without air contact. The sample 3 electrode (electrolyte concentration of 50 mM) diffractogram reveals the existence of a single crystalline phase with hexagonal wurtzite structure (CPDS card file number 36-1451, zincite phase). The maximum intensity for typical ZnO corresponds to the (1011) diffraction peak. Therefore, the observation of a strong and narrow (0002) peak suggests that the nanostructure is highly oriented with the *c*-axis perpendicular to the plane of the substrate ([0001] direction). The diffractograms of samples 4 and 5 (electrolyte concentrations of 25 mM and 12.5 mM, respectively) also show a preferential orientation along the (0002) plane but with increasingly lower relative intensity of the (0002) peak. Moreover, the diffractograms of samples 4 and 5 agree with the presence of ZnO as described before. Extra peaks at 2θ equal to 26.5° , 36.3° and 56.6° correspond to the FTO substrate.

Figure 4.2: The XRD diffractograms for the electrodes from samples 3, 4, and 5.



Source: Own author

4.4.2 Raman spectroscopy

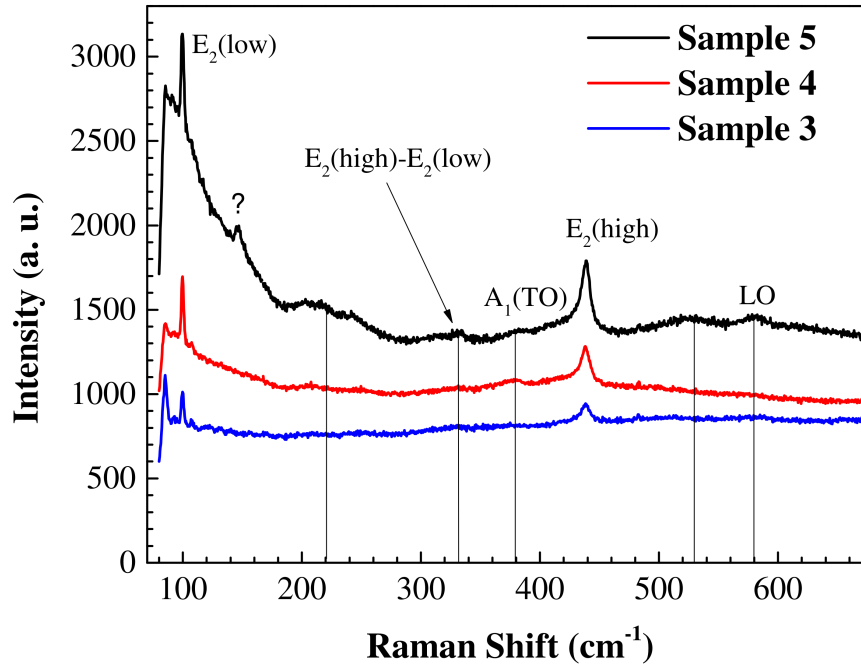
The XRD results for samples 3, 4, and 5 suggest the formation of a wurtzite structure with preferential growth along the c -axis. In Raman spectroscopy, ZnO with a wurtzite structure is shown by four Raman active modes: $A_1 + E_1 + 2E_2$ [33]. The characteristic Raman features for this symmetry are the E_2 (low) and E_2 (high) phonon modes at about 99 cm^{-1} and 437 cm^{-1} , respectively. The low-wavenumber E_2 mode predominantly involves the vibration of the heavy Zn sublattice, while the high-wavenumber E_2 mode is primarily associated with the vibration of the lighter O sublattice. Because of the strong occurrence of E_2 modes in standard backscattering experiments, these modes can be considered to be a Raman fingerprint for ZnO [34, 35]. On the other hand, both A_1 and E_1 modes are infrared active and polar. Thus, these modes are divided into longitudinal-optical (LO) and transversal-optical (TO) components [36]. The $A_1(\text{LO})$ phonon mode at about 577 cm^{-1} is allowed in this symmetry, but it occurs with very weak intensity

in this well-ordered ZnO. The $E_1(\text{LO})$ mode, when observed in this configuration, can be attributed to interband Fröhlich interaction in nonideal ZnO. Finally, an additional feature occurs at about 332 cm^{-1} , which could be attributed to the E_2 (high)– E_2 (low) difference mode based on its behavior and frequency position.

Figure 4.3 shows the Raman spectra for samples 3, 4, and 5, using a green (532 nm) exciting source. In all samples, the presence of clear peaks at 99 cm^{-1} and 437 cm^{-1} , which are ascribed as E_2 (low) and E_2 (high) vibrational modes, respectively, confirms the formation of wurtzite-structured ZnO along the c -axis. Sample 3 presents only these fingerprint peaks for wurtzite ZnO; the $A_1(\text{LO})$ phonon mode at about 577 cm^{-1} , which is correlated to V_O and/or Zn_i defects [37], is not observed, indicating good crystalline quality. In addition to the E_2 peaks in sample 4, a very weak peak at 380 cm^{-1} is observed, which is due to the $A_1(\text{TO})$ vibrational mode. In addition to the E_2 peaks, sample 5 presents both LO and TO components for the A_1 vibrational mode. The occurrence of the $A_1(\text{TO})$ mode at about 378 cm^{-1} and the rather strong $A_1(\text{LO})$ mode at about 577 cm^{-1} indicate reduced structural quality in these regions. Moreover, the spectrum from sample 5 also presents broad peaks centered around 220 cm^{-1} and 530 cm^{-1} , which can be related to structural defects, along with a visible peak at 332 cm^{-1} , which is ascribed to E_2 (high) – E_2 (low).

The Raman spectroscopy results are in good agreement with the XRD results. Sample 3 possesses a stronger c -orientation, while samples 4 and 5 present additional features in addition to the strong c -orientation. The Raman spectra suggest that the sample 5 thin film contains more defects, while the XRD results suggest that sample 5 was grown in a more dispersed way than samples 3 and 4.

Figure 4.3: Raman spectra for as-prepared ZnO thin films in samples 3, 4, and 5.

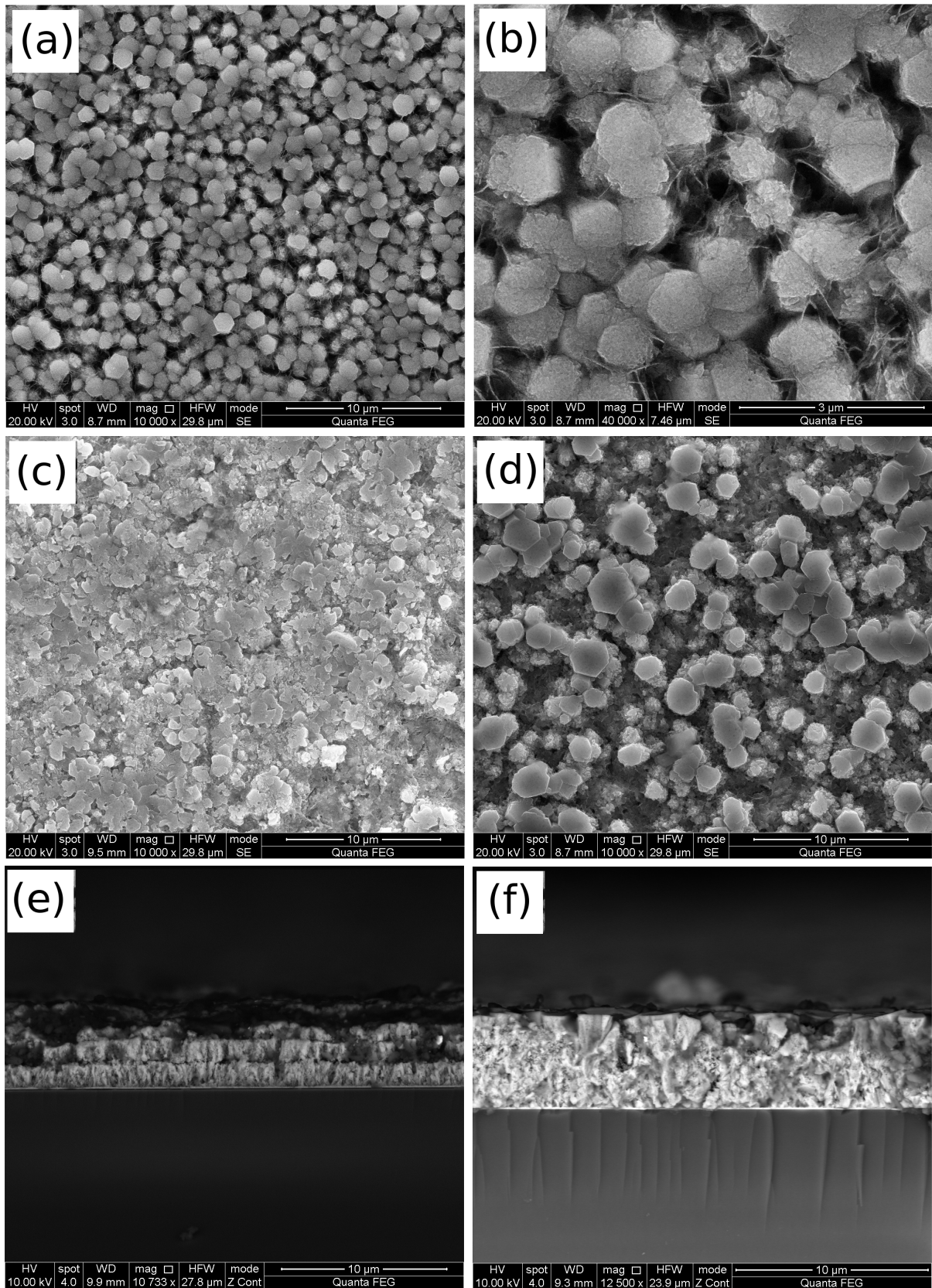


Source: Own author

4.4.3 Electron microscopy

The influence of the deposition reaction time and contact with air on film morphology was studied. Films grown from 50-mM zinc nitrate electrolyte (samples 1, 2, and 3) were used in this study. Figure 4.4(a) shows the SEM micrograph (top view) of sample 1, which presents a very dense array of vertically aligned nanorods. In the higher magnification view shown in Fig. 4.4(b), a different microstructure was formed in the region between the nanorods. The deposition of vertically aligned nanorods confirms the XRD results because the ZnO was crystallized in the wurtzite crystal structure, which presents with hexagonal symmetry and consists of tetrahedrally coordinated Zn and O atoms in alternating layers along the c -axis. These layers are uniquely composed of either Zn^{2+} or O^{2-} ions and are, therefore, polar [9]. The polar (0001) plane has a higher surface energy and leads to fast crystal growth along the [0001] direction, resulting in the formation of one-dimensional ZnO nanostructures [30].

Figure 4.4: The SEM micrographs of electrodes from (a) sample 1 (top view), (b) sample 1 (top view) with a higher magnification, (c) sample 2 (top view), (d) sample 3 (top view), (e) sample 2 (cross-sectional view), and (f) sample 3 (cross-sectional view).



Source: Own author

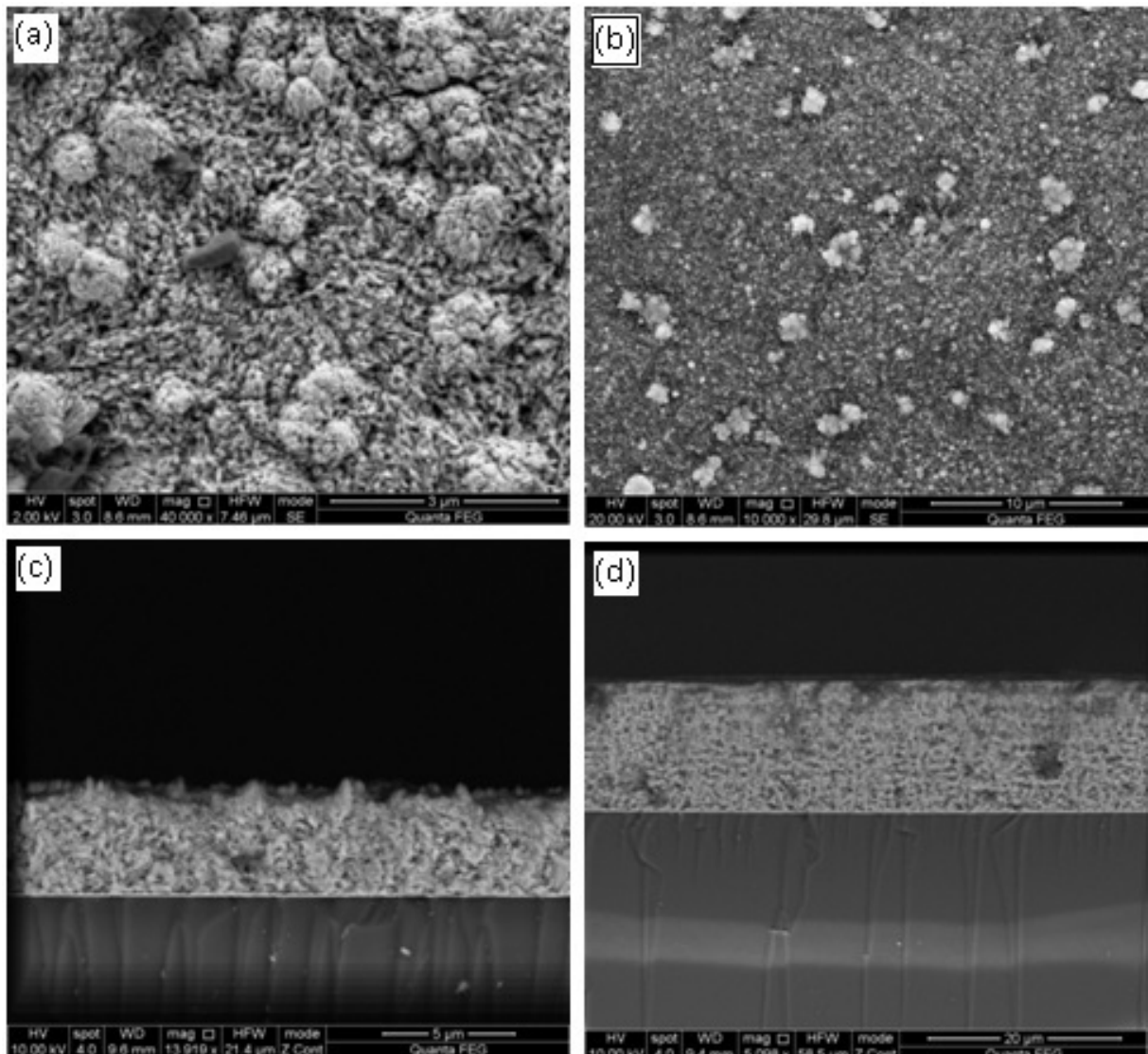
Although the internal structure of ZnO favors anisotropic growth along the [0001] direction, the surrounding conditions during the electrodeposition process may affect the ZnO growth [38], which could explain the different morphology observed between the nanorods. Moreover, this growth mechanism could also be responsible for the coalescence between adjacent nanorods observed in the microstructure of sample 2, as shown in Fig. 4.4(c). Moreover, the growth of a porous nanostructure is observed between the nanorods of sample 3 (Fig. 4.4(d)). According to Ludwig et al. [39], there is a strong correlation between the amount of electrochemically deposited ZnO and the morphology of the thin film. The total amount of electrochemically deposited ZnO can be estimated from the total charge deposited per area (integrated from the monitored current density with respect to time). In this study, the average current density for all deposited films was 1.3 mA/cm². This high current density probably led to the fast growth rate of the ZnO nuclei as well as the growth of ZnO along the other directions. As a result, different nanostructures were formed and coalesced between the nanorods.

Figure 4.4(e) shows the cross-sectional micrograph for sample 2. The effect of air contact between consecutive deposition steps is observed by discontinued layers that correspond to each of the four 0.5-h steps. Sample 3 was also grown in four deposition cycles, but the sample remained inside the electrolyte (no air contact) between consecutive steps. Thus, the sample does not contain discontinued layers, as shown in Fig. 4.4(f).

The influence of the zinc precursor concentration on the morphology of the films was also investigated. In this study, samples 4 and 5 were grown from 25 mM and 12.5 mM electrolyte solutions, respectively, in a single step of 2 h without changing any other parameters. The high-density current during the electrochemical reaction together with low concentrations of the zinc precursor in the aqueous electrolyte led to the novel nanostructures shown in Fig. 4.5. Figures 4.5(a) and 4.5(b) show top view images of the electrodes grown from 25 mM and 12.5 mM electrolyte solutions, respectively. In these images, porous films are observed rather than the vertically aligned nanorods found in samples grown from 50 mM electrolytes. The cross-sectional views of these same films, shown in Figs. 4.5(c) and 4.5(d), do not show vertically aligned structures, suggesting that

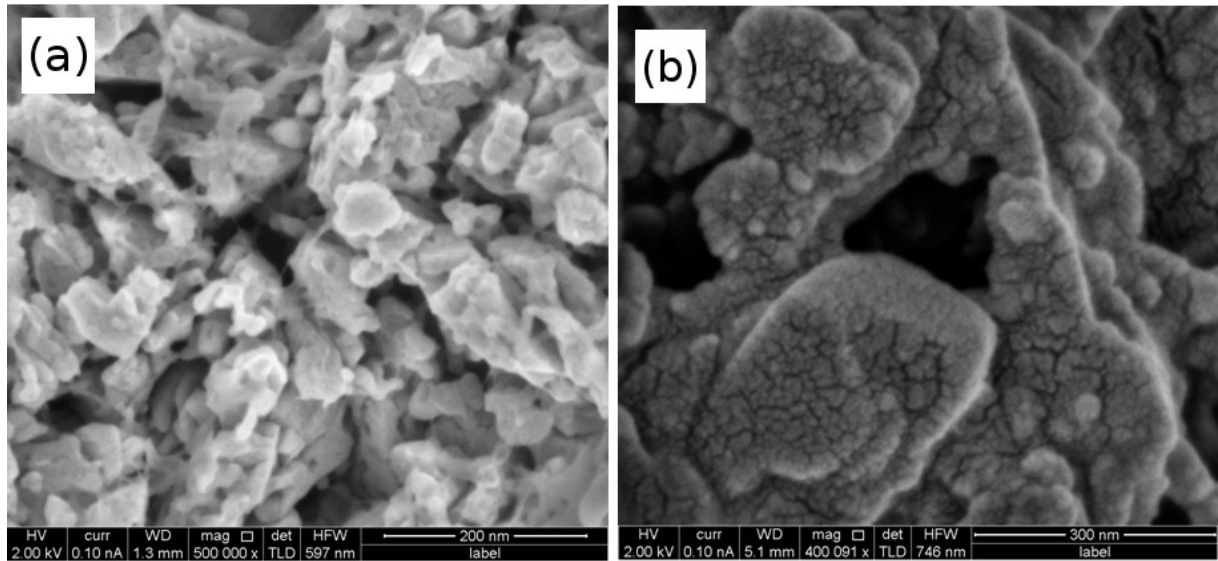
the films were not grown along the c -axis. This result agrees with the XRD results, which showed a lower relative intensity of the (0002) peaks for these samples, as well as with the Raman spectroscopy results, which showed a more complex structure for sample 5. In fact, the high-resolution SEM images of sample 5 (12.5 mM) show the formation of a mesoporous nanostructure (see Fig. 4.6).

Figure 4.5: The SEM micrographs of electrodes from (a) sample 4 (top view), (b) sample 5 (top view), (c) sample 4 (cross-sectional view), and (d) sample 5 (cross-sectional view).



Source: Own author

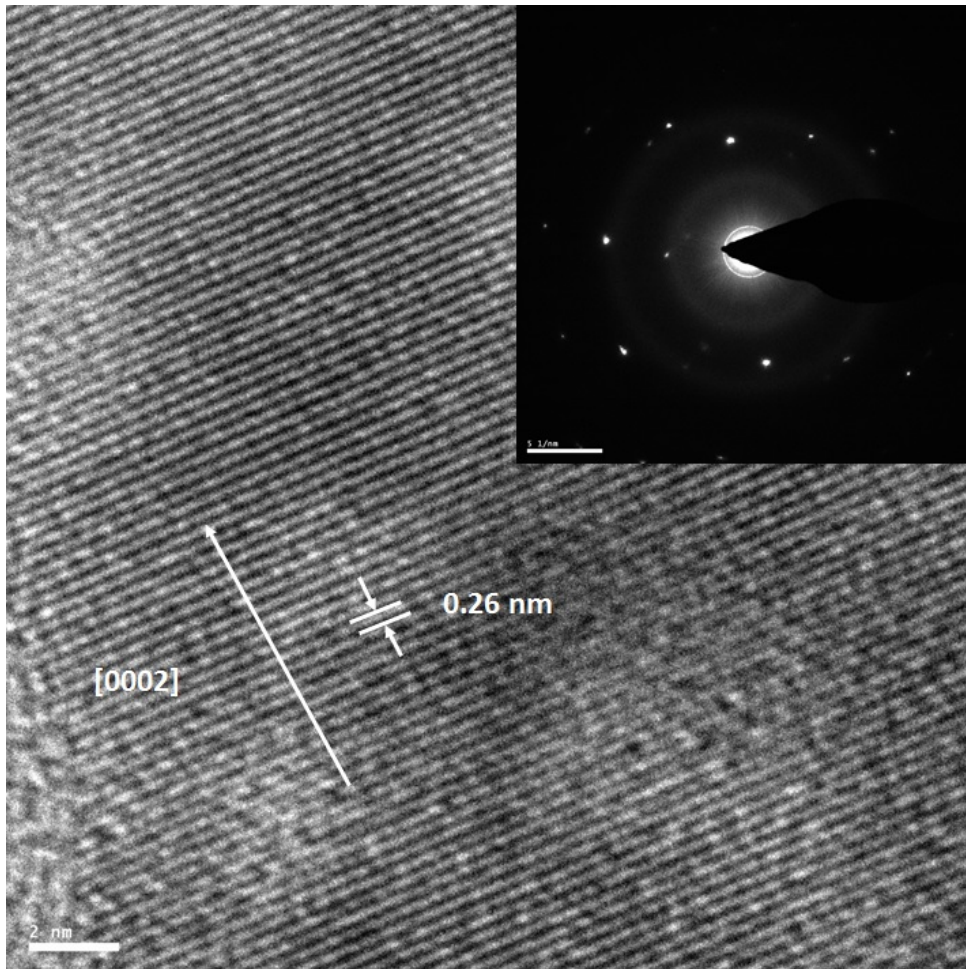
Figure 4.6: High-resolution SEM micrographs of the sample 5 electrode: (a) top view, and (b) cross-sectional view.



Source: Own author

The TEM images together with the selected-area electron diffraction (SAED) pattern confirm the crystallinity of the samples. Figure 4.7 shows a high-resolution TEM image for sample 5, where the crystallographic planes are clearly observed. The presence of the planes confirms the crystallinity of the sample, and the measured distance of 0.26 nm corresponds to the (0002) direction. The inset shows a representative SAED pattern for this sample. According to this pattern, additional planes contribute to the electron diffraction, such as $(20\bar{2}0)$, (0004) , and $(20\bar{2}2)$.

Figure 4.7: The high-resolution TEM image for sample 5. The inset shows the SAED pattern for an specific area of the sample.



Source: Own author

4.4.4 Energy dispersive X-ray spectroscopy

According to Table 4.2, which shows the EDX results of films deposited with and without air contact (samples 2 and 3, respectively), air contact evidently influences the film composition as well as the microstructure. Films grown with air contact between deposition steps show an excess of oxygen content with respect to zinc, while films grown without air contact show stoichiometric ZnO composition. The excess oxygen can be explained by the reaction of the ZnO surface with oxygen from the air, forming an insulating layer of zinc hydroxide (ZnOH). The X-rays forming the EDX spectrum comes from the bulk of the films. As shown in sample 3, only the surface of the film was in contact with

air, and the EDX spectra does not show excess oxygen. Sample 2 was in contact with air three times before the film deposition was complete, and the EDX data for this sample shows an excess of oxygen, which suggests the formation of ZnOH thin layer.

Table 4.2: EDX results for the composition of ZnO electrodes formed from samples 2 and 3.

Sample	O %at.	Zn %at.	Ratio O:Zn
with air contact	56.07	43.93	1.28
without air contact	50.37	49.63	1.01

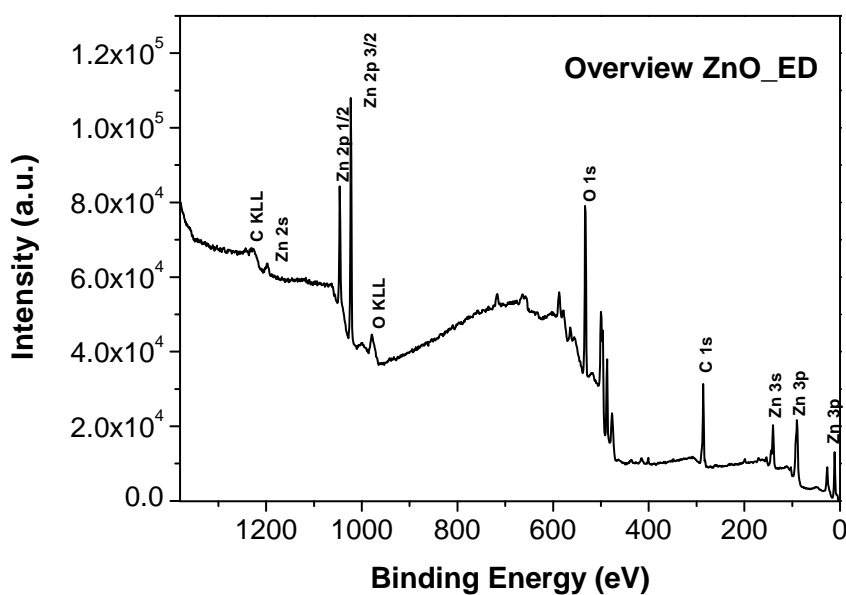
Source: Own author

4.4.5 X-ray photoelectron spectroscopy

The XPS technique also allows the quantification of elements in a material. In contrast with the bulk sensitivity of EDX, this technique is surface sensitive. The XPS spectrum for sample 5, which was electrodeposited for 2 h without air contact, is shown in Fig. 4.8, and C, Zn, and O were observed on the surface of the thin film. The quantification analyses for the surface reveal an excess of oxygen at the surface and are summarized in Table 4.3. The ratio of O:Zn at the surface of the film is approximately 3:1, which is far from that expected by the stoichiometry.

The XPS is a very powerful technique that can provide information about the chemical states of the compositional elements. The Zn $2p$ core-level XPS spectrum for ZnO (Fig. 4.9(a)) shows doublet spectral lines at the binding energies around 1022 eV (Zn $2p$ $3/2$) and around 1045 eV (Zn $2p$ $1/2$) with a spin-orbit splitting of 23 eV, which coincides with the results for Zn^{2+} in ZnO. The O $1s$ core-level XPS spectrum for the thin film is shown in Fig. 4.9(b). The O $1s$ core-level analysis may also provide information about the existence of H, because H in ZnO tends to strongly bond with oxygen atoms [40]. To calibrate the photo-electron binding energy, the C $1s$ peak for C–C bonds was assigned to 284.8 eV. The O $1s$ spectra can be de-convoluted into three different peaks [41–44]:

Figure 4.8: An overview of the XPS results for electrodeposited ZnO thin films.



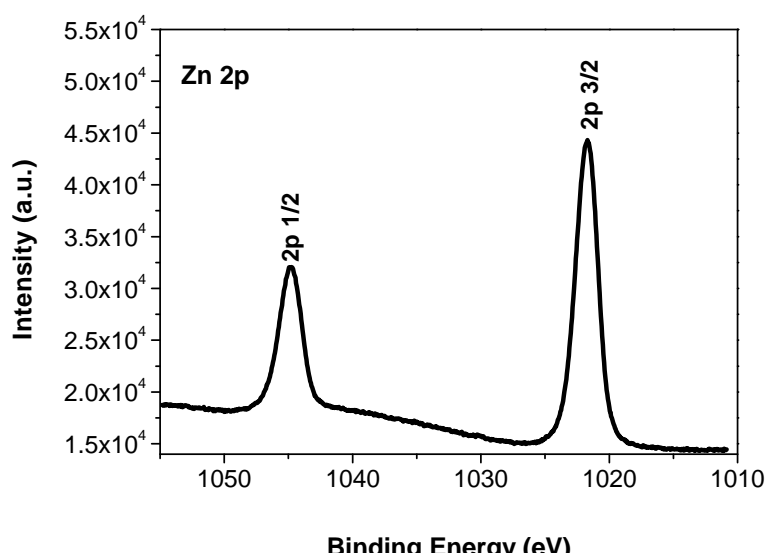
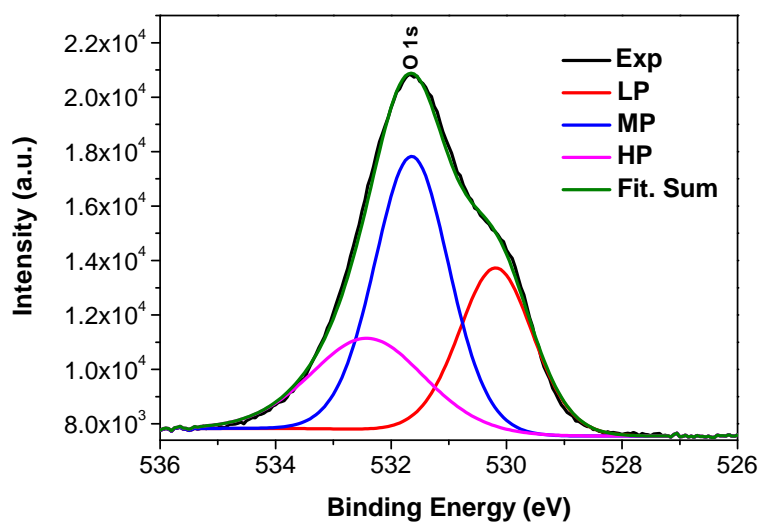
Source: Own author

(i) a peak at a lower binding energy (LP), centered at 530.2 eV, was assigned to the O $1s$ core level (O^{2-}) in the ZnO wurtzite structure surrounded by Zn atoms with their full complement of nearest neighbour oxygen ions [45], (ii) a middle binding energy peak (MP) around 531.7 eV is associated with hydroxidic oxygen [46], and (iii) high binding energy peak (HP), centered at 532.4 eV, corresponds to weakly adsorbed surface species, which are usually ascribed to nonstoichiometric near-surface oxygen, oxygen atoms in carbonate ions on the surface of ZnO, surface hydroxylation, adsorbed H_2O , or adsorbed O_2 . Considering only the oxygen bonded to Zn in wurtzite structure ZnO, the quantification becomes closer to the stoichiometry, but an oxygen deficiency can be observed (Table 4.3). This oxygen deficiency suggests the presence of oxygen vacancies, which can cause changes in the ZnO energy levels.

Table 4.3: XPS results for the composition of the sample 5 ZnO electrodes.

Analysis	O %at.	Zn %at.	ratio O:Zn
Regions	74.30	25.70	2.89
Components	45.63	54.37	0.84

Source: Own author

Figure 4.9: high-resolution XPS spectra for (a) Zn 2*p* and (b) O 1*s*.a) Zn 2*p*b) O 1*s*

Source: Own author

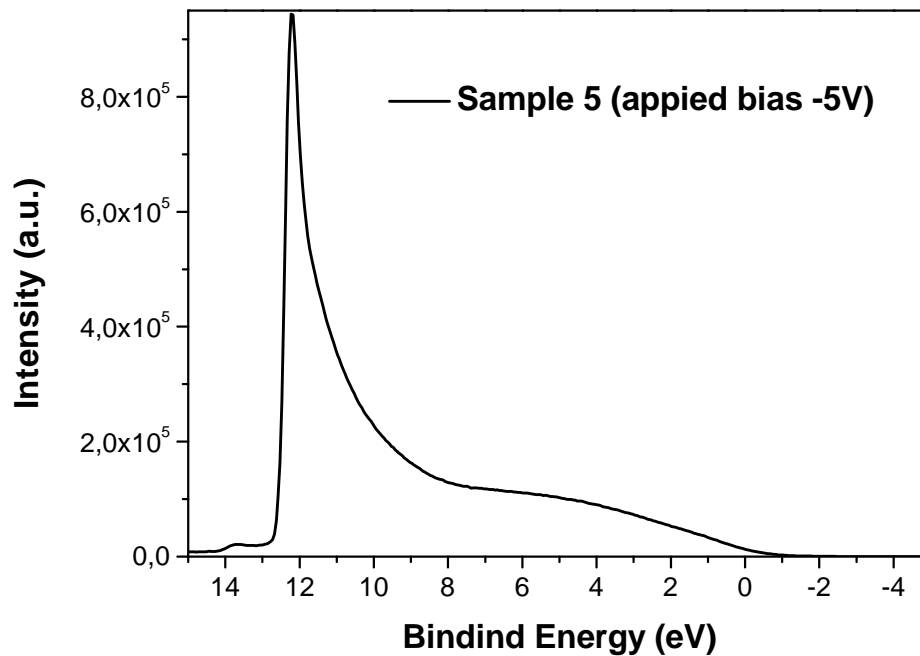
4.4.6 Band diagram

The band alignment of ZnO with the dye, electrolyte, and FTO has a crucial importance for the functionality of ZnO-based DSSCs. From the UPS spectrum, the ionization energy can be calculated by [47]:

$$IP = h\nu - E_{SEC} + E_{VBE} \quad (4.8)$$

where IP is the ionization energy, which is defined as the distance from the valence band maximum (VBM) and the vacuum level, E_{SEC} is the secondary electron cutoff energy, and E_{VBE} is the valence band edge energy. Figure 4.10 shows the valence band UPS spectrum for sample 5.

Figure 4.10: Valence band UPS spectrum for sample 5.

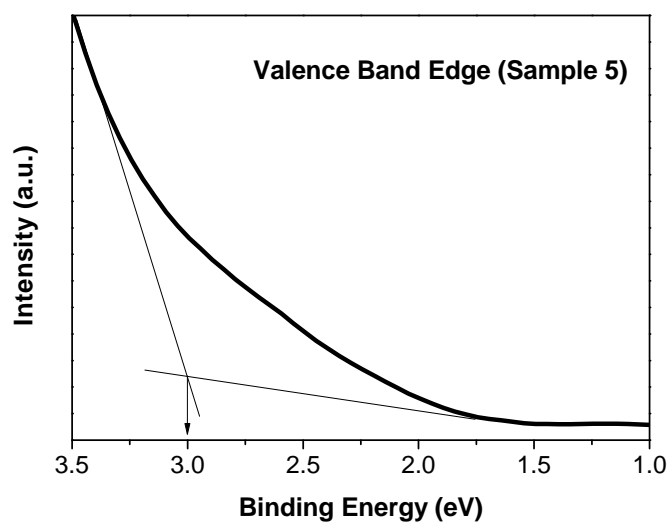


Source: Own author

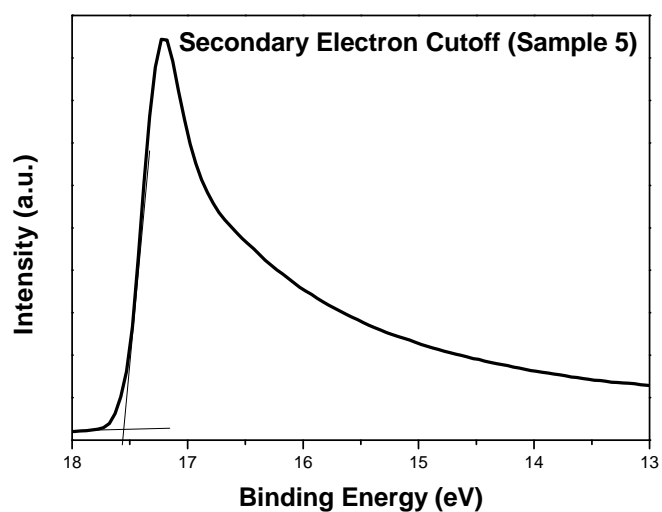
The values of E_{SEC} and E_{VBE} can be directly obtained from the valence band UPS spectrum as illustrated in Fig. 4.11. With these values and eq. 4.8, IP can be determined. For this sample, the value of E_{SEC} is 17.5 eV, and the value of the E_{VBE} is 3.0 eV. Hence, the calculated value of IP is 6.7 eV.

Figure 4.11: Details of valence band edge and secondary electron cutoff obtained for an electrodeposited ZnO thin film, sample 5.

a) Valence Band Edge



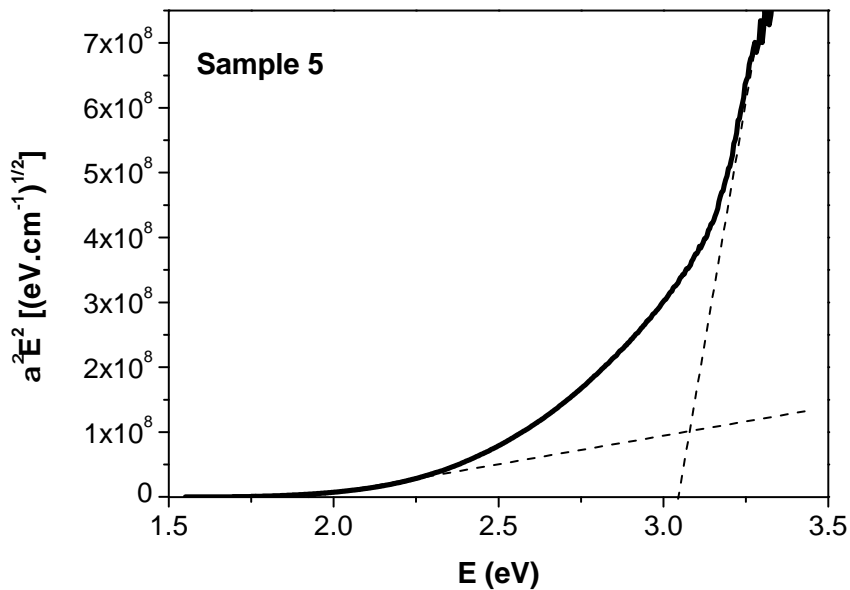
b) Secondary Electron Cutoff



Source: Own author

Another important feature for the construction of the band alignment diagram is the optical bandgap, which can be estimated using Tauc's plot. Figure 4.12 shows Tauc's plot for sample 5. According to Fig. 4.12, the optical bandgap (E_g) for sample 5 is 3.1 eV. The difference between the nominal bandgap $E_g = 3.37$ eV at 300 K for ZnO [48–50] and the E_g^{opt} value given by Fig. 4.12 indicates the presence of optically active defects in this sample. This means that the corresponding defects are characterized within the bandgap by this energetic amount from either the valence or conduction band. The true nature of these defects still needs to be determined, but these defects may depend on the method of crystal growth. For sample 5, the difference $E_g - E_g^{opt}$ is around 0.27 eV, which agrees with the expected value for defective ZnO. A larger $E_g - E_g^{opt}$ difference of 0.85 eV has already been reported [51, 52]. The difference observed in sample 5 could be attributed to oxygen vacancies, which create an energy level within the bandgap close to the conduction band minimum, narrowing the bandgap [53–55].

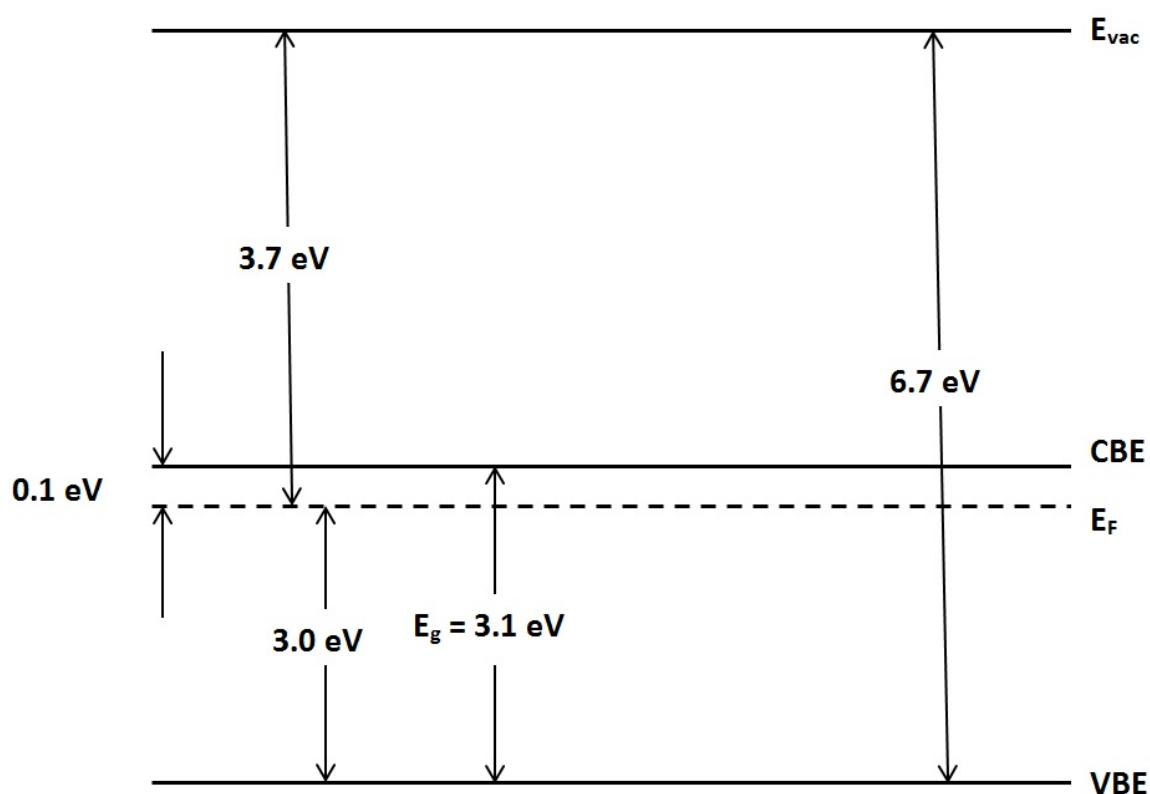
Figure 4.12: Tauc's plot: calculation of bandgap of electrodeposited ZnO thin films, sample 5.



Source: Own author

Once IP , VBE , and E_g have been determined, the value for the work function arises naturally as $\Phi = 3.7$. This value for the work function agrees with the value previously reported from Schlesinger et al. [56]. With this data, the energy band diagram for sample 5 can be obtained, as shown in Fig. 4.13. In summary, the valence band edge is shifted by 3.0 eV with respect to the Fermi level. The optical band gap was determined to be 3.1 eV, and consequently, the conduction band edge is shifted by 0.1 eV with respect to the Fermi level. The work function Φ for this thin film is 3.7 eV, and the ionization energy is 6.7 eV.

Figure 4.13: Band diagram for sample 5.

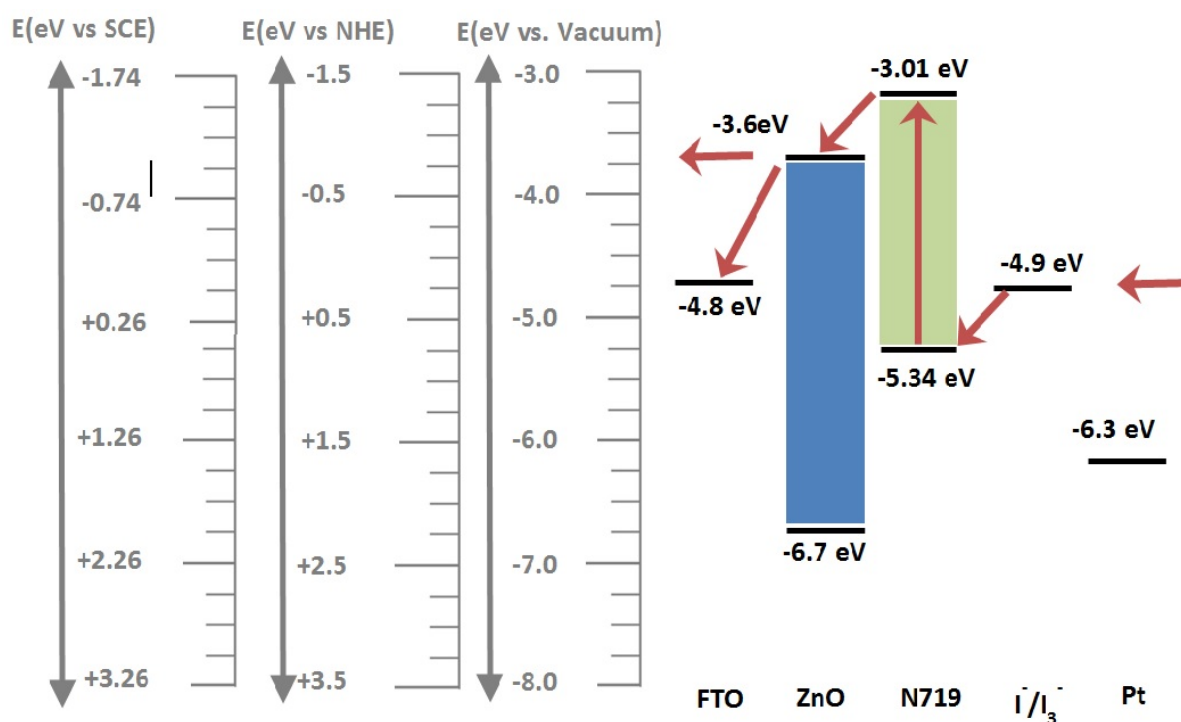


Source: Own author

Finally, in Fig. 4.14, the band diagram alignment of the electrochemically deposited ZnO working electrode (sample 5) is shown with other DSSC constituents, including the

Ru-based, N719 dye, the regenerate electrolyte I^-/I_3^- , the FTO substrate, and the counter electrode, which is composed by a conductive glass activated with a platinum catalyst.

Figure 4.14: Band alignment for a DSSC using sample 5 as the working electrode.

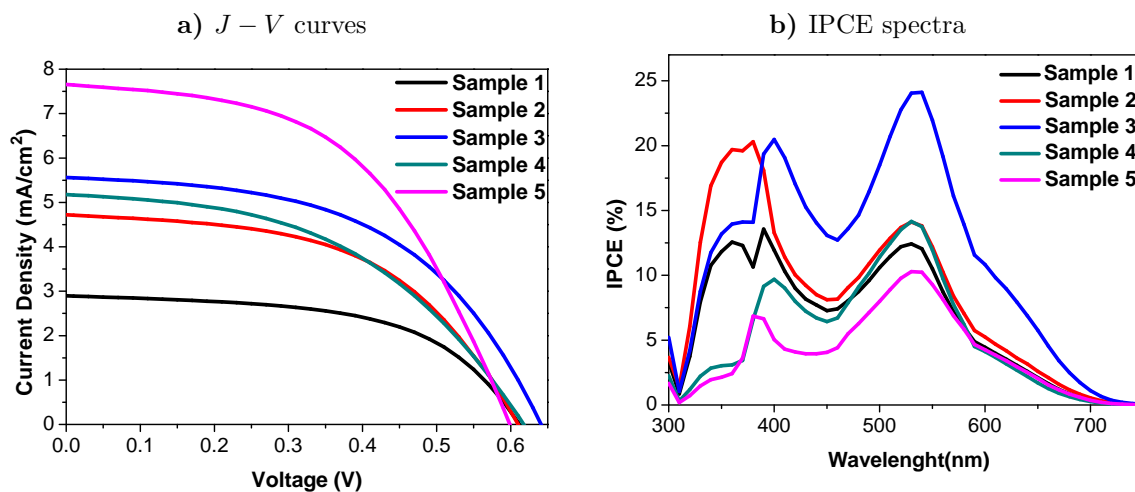


Source: Own author

4.5 Photovoltaic performance

The electrodes described above were used without any further treatment as photoanodes in DSSCs. The solar cells were tested under simulated AM 1.5 solar illumination at 100 mW/cm^2 . Figure 4.15 shows the $J - V$ curves and IPCE spectra for the best cell of each set, while Table 4.4 shows the photovoltaic parameters for those cells. All DSSCs presented J_{sc} greater than 2.89 mA/cm^2 , V_{oc} greater than 0.59 V , fill factor FF greater than 46.58% , and power conversion efficiency PCE greater than 0.97% . These values are in good agreement with those recently reported for ZnO thin films deposited in similar way without any post-deposition treatment [57, 58].

Figure 4.15: $J - V$ curves and IPCE spectra for DSSCs assembled with five samples of electrodeposited ZnO thin films.



Source: Own author

The V_{oc} values are approximately the same for all cells. Because V_{oc} for DSSCs is defined as the difference between the redox potential of the mediator and the Fermi level of the nanocrystalline film [59], the Fermi level energies of all thin films are approximately the same. The J_{sc} values tend to increase with decreasing electrolyte concentration. According to the SEM and XRD results, the decrease in the electrolyte concentration leads to more porous films, which is desirable for the best photovoltaic performance. In fact, the solar cell constructed from sample 5 (12.5 mM), which presented a mesoporous nanostructure, showed the maximum J_{sc} value. Moreover, considering the absence of post-deposition treatments, a remarkably high PCE value of 2.27% was obtained for this cell. The improved J_{sc} value can be attributed to the mesoporous structure of the thin film, which allows the absorption of larger amount of dye in monolayers on the ZnO nanostructure. This dye absorption allows for a higher generation of photoelectrons and consequently higher J_{sc} . The series and shunt resistance were determined from the slopes of the $J - V$ curves.

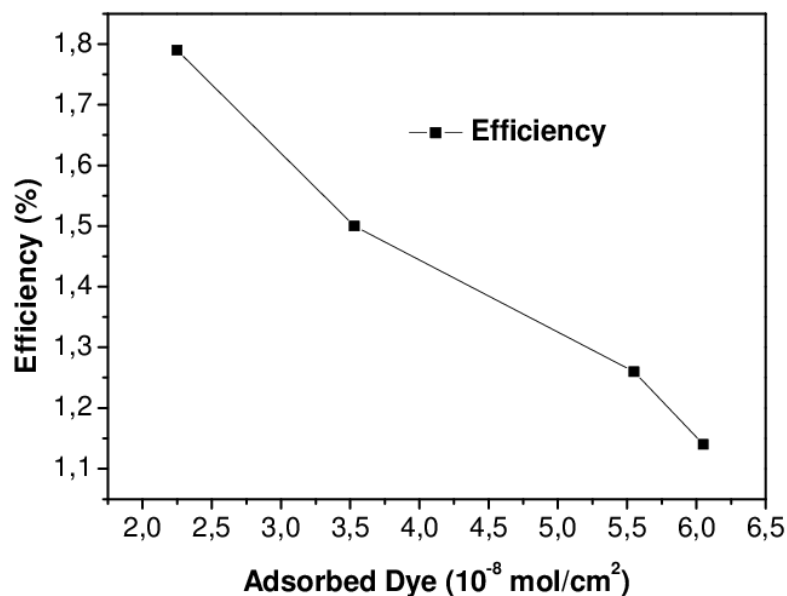
Table 4.4: Photovoltaic parameters for DSSCs assembled with the five ZnO samples.

Sample	J_{sc} (mA/cm ²)	V_{oc} (V)	FF (%)	PCE (%)	R_S (k Ω · cm ²)	R_{Sh} (k Ω · cm ²)
1	2.89	0.60	55.60	0.97	2.25	1.80
2	4.72	0.61	51.95	1.50	0.83	1.06
3	5.55	0.63	50.99	1.79	1.92	1.37
4	5.17	0.61	46.58	1.46	20.00	1.02
5	7.64	0.59	50.41	2.27	0.69	0.84

Source: Own author

The amount of dye adsorbed on the oxide was measured by the dye desorption method, which consists of the separation of the two electrodes, followed by the immersion of the ZnO-dye electrode in an aqueous basic solution of 0.1-mM KOH. The dye desorption occurred in 1 h, with the solution turning pink due to the presence of the N719 dye. At the same time, the ZnO electrode became colorless in a similar process to that observed by Neale et al. [60]. The quantity of dye adsorbed on the ZnO electrode was determined by UV-Vis analysis of the desorbed dye solution using the Lambert-Beer law. The results were corrected by the active area of the DSSCs. The relation between the amount of adsorbed dye and the efficiency for the electrodes grown using the 50-mM zinc nitrate solution is shown in Fig. 4.16. A higher power conversion efficiency was observed for the samples that adsorbed the lowest amount of dye. This result can be explained by dye precipitation on the ZnO nanostructure. According to Keis et al. [61], dye precipitation can occur in the ZnO nanostructure and, as in this case, some dissolution of ZnO could occur due to the acidic carboxylic groups. The resulting Zn²⁺ ions form insoluble complexes with the N719 dye, causing precipitation of these complexes in the pores of the film, which gives rise to a filter effect (inactive dye molecules) [62].

Figure 4.16: Dye desorption study for DSSCs assembled with electrochemically deposited ZnO.

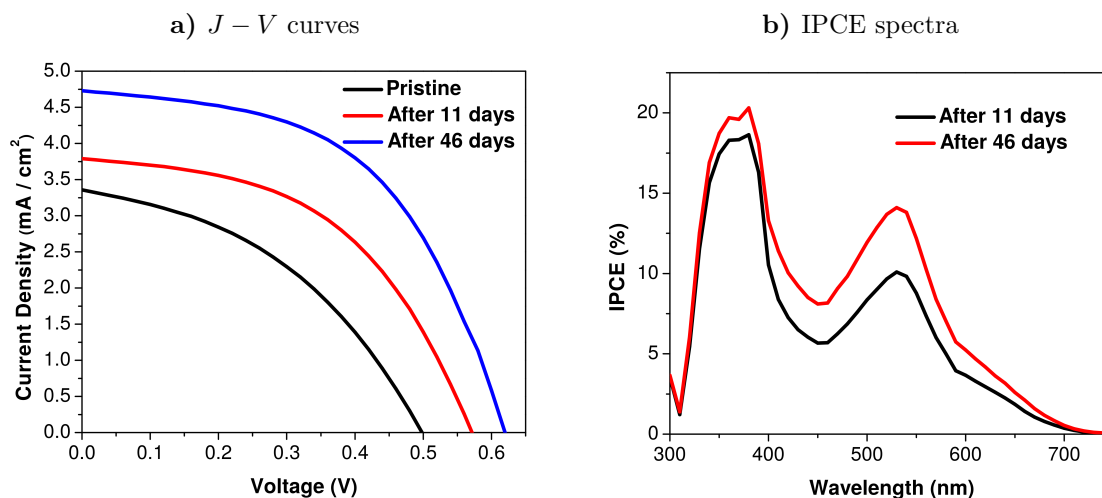


Source: Own author

All of the cells assembled with the electrodeposited ZnO working electrodes present a striking feature: the photovoltaic parameters improve with aging under ambient conditions. Figure 4.17 shows this improvement from changes in the $J - V$ curves and IPCE spectra for sample 2, where this effect was more pronounced. From the $J - V$ curves in Fig. 4.17(a), J_{sc} increases by almost 45%, while V_{oc} increases by about 24%. The increase in J_{sc} agrees with the increase of the peak in the IPCE spectrum in the region where the dye is adsorbed, as shown in Fig. 4.17(b). The PCE improvement for this sample was greater than 200%.

The SEM images for sample 2 show that this sample is very compact, making the electrolyte diffusion inside its structure more difficult. The amount of dye adsorbed for the working electrode in this device was higher than that of other devices, which enabled its improved photovoltaic performance. Thus, the dye probably precipitates at the ZnO surface, which is not desired, and thus does not form a monolayer at the ZnO electrode surface. The massive improvement in the performance of the cell could be attributed to the diffusion of the regenerating electrolyte into the ZnO structure.

Figure 4.17: $J-V$ curves and IPCE spectra for the cell that presents a significant improvement in performance after aging under ambient conditions.

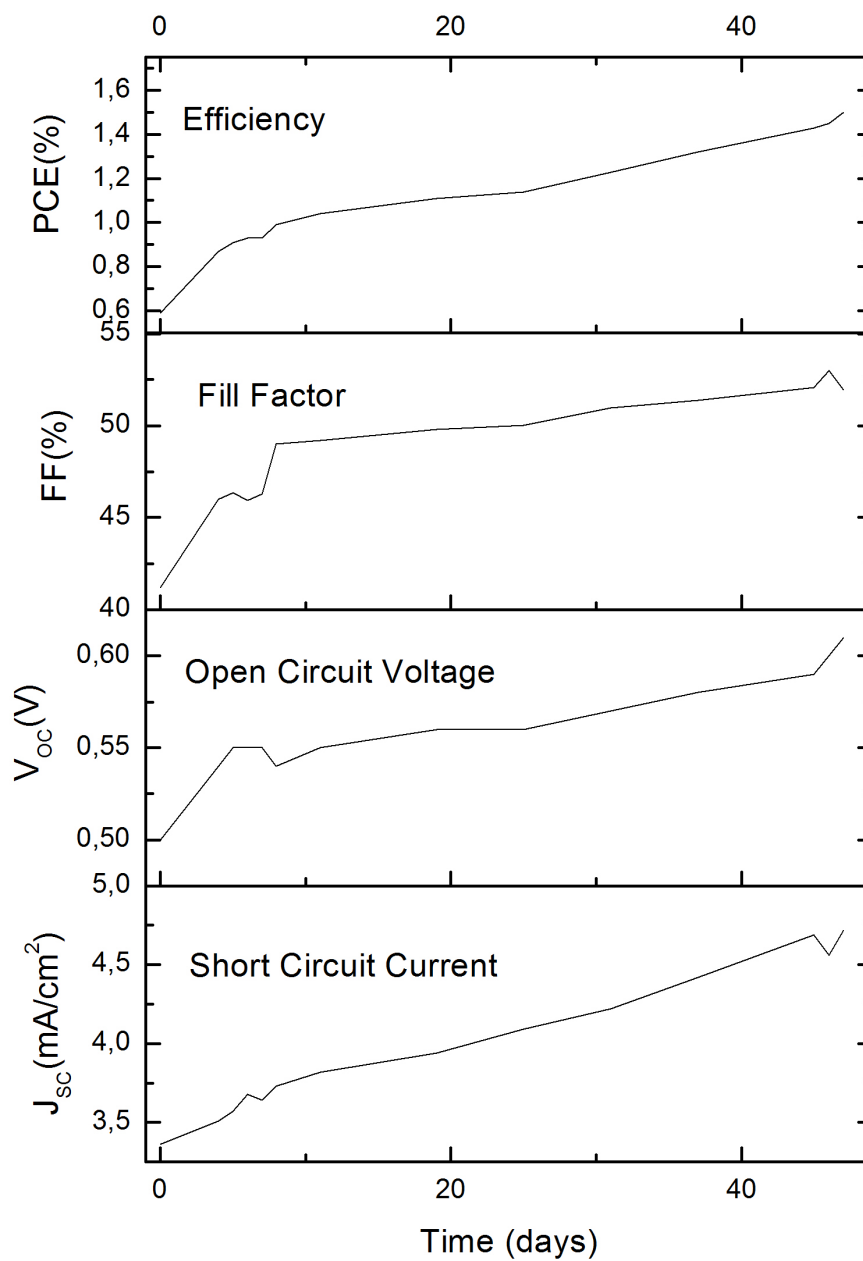


Source: Own author

The redox couple is a key component of DSSCs that can affect the performance of solar cells in many ways. The reduced part of the couple regenerates the photon-oxidized dye. The previously oxidized species diffuses to the counter electrode, where it is reduced. The photovoltage of the device depends on the redox couple because it determines the electrochemical potential at the counter electrode. The redox couple also affects the electrochemical potential of the ZnO electrode through the recombination kinetics between the electrons in ZnO and the oxidized redox species [63]. The slow diffusion of the electrolyte into the ZnO structure can gradually improve the photovoltaics parameters by enabling the more effective regeneration of the dye. This process could tune the energy levels for better alignment and may dissolve some of the precipitated dye from the ZnO surface.

Figure 4.18 shows the evolution of the photovoltaic parameters over time for sample 2. In fact, all parameters increase with time, but it is clear that the primary factor leading to the improved PCE is the increase in the short circuit current. As discussed above, the reason for this improvement is likely the slow diffusion of the redox mediator into the ZnO working electrode.

Figure 4.18: Time evolution of the photovoltaic parameters under ambient conditions for a DSSC assembled with sample 2 electrodes.



Source: Own author

4.6 Conclusions

In this work, ZnO thin films were synthesized using a low cost, electrodeposition technique. The resulting films were used without any post-deposition treatment to assemble DSSCs. All of the assembled photoelectrodes were successfully used in DSSCs. The morphological, structural, and electrical characterization of the samples revealed that the best performance could be obtained with more porous electrodes. Moreover, the amount of adsorbed dye revealed that a large amount of adsorbed dye decreased the PCE, which was probably due to the precipitation of the dye on the porous thin film. After aging under ambient conditions, the PCE of the devices could be improved. A remarkably high PCE of 2.27% was obtained using the cell with a mesoporous nanostructure. For this device, the photovoltaic parameters were $V_{oc} = 0.59$ V, $J_{sc} = 7.64$ mA/cm², $FF = 50.41\%$, and $PCE = 2.27\%$.

4.7 References

- [1] B. Cao, W. Cai, H. Zeng, and G. Duan. Morphology evolution and photoluminescence properties of ZnO films electrochemically deposited on conductive glass substrates. *J. Appl. Phys.*, 99:073516, 2006.
- [2] M. Zi, M. Zhu, L. Chen, H. Wei, X. Yang, and B. Cao. ZnO photoanodes with different morphologies grown by electrochemical deposition and their dye-sensitized solar cell properties. *Ceram. Int.*, 40:7965–7970, 2014.
- [3] C. Kung, H. Chen, C. Lin, Y. Lai, R. Vittal, and K. Ho. Electrochemical synthesis of a double-layer film of ZnO nanosheets/nanoparticles and its application for dye-sensitized solar cells. *Prog. Photovolt: Res. Appl.*, 22:440–451, 2014.
- [4] X. Zou, Y. Liu, C. Wei, Z. Huang, and X. Meng. Electrodeposition combination with hydrothermal preparation of ZnO films and their application in dye-sensitized solar cell. *Journal of Chemistry*, 820708, 2014.

- [5] T. Yoshida and H. Minoura. Electrochemical self-assembly of dye-modified zinc oxide thin films. *Adv. Mater.*, 12:1219–1222, 2000.
- [6] M. S. Akhtar, M. A. Khan, M. S. Jeon, and O. Yang. Controlled synthesis of various ZnO nanostructured materials by capping agents-assisted hydrothermal method for dye-sensitized solar cells. *Electrochim. Acta*, 53:7869–7874, 2008.
- [7] I. Gonzalez-Valls and M. Lira-Cantu. Vertically-aligned nanostructures of ZnO for excitonic solar cells: a review. *Energy Environ. Sci.*, 2:19–34, 2009.
- [8] M. H. Kumar, N. Yantara, S. Dharani, M. Grätzel, S. Mhaisalkar, P. P. Boix, and N. Mathews. Flexible, low-temperature, solution processed ZnO-based perovskite solid state solar cells. *Chem. Comm.*, 49:11089–11091, 2013.
- [9] B. N. Illy, A. C. Cruickshank, S. Schumann, R. da Campo, T. S. Jones, S. Heutz, M. A. McLachlan, D. W. McComb, D. J. Riley, and M. P. Ryan. Electrodeposition of ZnO layers for photovoltaic applications: controlling film thickness and orientation. *J. Mater. Chem.*, 21:12949–12957, 2011.
- [10] T. Pauporté and C. Magne. Impedance spectroscopy study of N719-sensitized ZnO-based solar cells. *Thin Solid Films*, 560:20–26, 2014.
- [11] I. Gonzalez-Valls, Y. Yu, B. Ballesteros, J. Oro, and M. Lira-Cantu. Synthesis conditions, light intensity and temperature effect on the performance of ZnO nanorods-based dye sensitized solar cells. *J. Power Sources*, 196:6609–6621, 2011.
- [12] S. Peulon and D. Lincot. Cathodic electrodeposition from aqueous solution of dense or open-structured zinc oxide films. *Adv. Mater. (Weinheim, Ger.)*, 8:166, 1996.
- [13] S. Peulon and D. Lincot. Mechanistic study of cathodic electrodeposition of zinc oxide and zinc hydroxychloride films from oxygenated aqueous zinc chloride solutions. *J. Electrochem. Soc.*, 145:864–874, 1998.

- [14] M. J. Zheng, L. D. Zhang, G. H. Li, and W. Z. Shen. Fabrication and optical properties of large-scale uniform zinc oxide nanowire arrays by one-step electrochemical deposition technique. *Chem. Phys. Lett.*, 363:123–128, 2002.
- [15] X. Qiu, L. Chen, H. Gong, M. Zhu, J. Han, M. Zi, X. Yang, C. Ji, and B. Cao. The influence of annealing temperature on the interface and photovoltaic properties of cds/cdse quantum dot sensitized ZnO nanorods solar cells. *J. Colloid Interface Sci.*, 430:200–206, 2014.
- [16] T. Pauporté and D. Lincot. Electrodeposition of semiconductor for optoelectronic devices: results on zinc oxide. *Electrochim. Acta*, 45:3345–3353, 2000.
- [17] D. Lincot. Electrodeposition of semiconductors. *Thin Solid Films*, 487:40–48, 2005.
- [18] J. Elias, R. Tena-Zaera, and C. Lévy-Clément. Electrochemical deposition of ZnO nanowire arrays with tailored dimensions. *J. Electroanal. Chem.*, 621:171–177, 2008.
- [19] H. Wei, H. Gong, Y. Wang, X. Hu, L. Chen, H. Xu, P. Liu, and B. Cao. Three kinds of Cu₂/ZnO heterostructures solar cells fabricated with electrochemical deposition and their structure-related photovoltaic properties. *CrysEngComm*, 13:6065–6070, 2011.
- [20] J. Elias, J. Michler, L. Philippe, M. Lin, C. Couteau, G. Lerondel, and C. Lévy-Clément. ZnO nanowires, nanotubes, and complex hierarchical structures obtained by electrochemical deposition. *J. Electron. Mater.*, 40:728–732, 2011.
- [21] M. Zhu, L. Chen, H. Gong, M. Zi, and B. Cao. A novel TiO₂ nanorod/nanoparticle composite architecture to improve the performance of dye-sensitized solar cells. *Ceram. Int.*, 40:2337–2342, 2014.
- [22] O. Lupan, V. M. Guérin, I. M. Tiginyanu, V. V. Ursaki, L. Chow, H. Heinrich, and T. Pauporté. Well-aligned arrays of vertically oriented ZnO nanowires electrodeposited on ito-coated glass and their integration in dye sensitized solar cells. *J. Photochem. Photobiol. A*, 211:65–73, 2010.

- [23] J. Qiu, M. Guo, and X. Wang. Electrodeposition of hierarchical ZnO nanorods-nanosheets structure and their applications in dye-sensitized solar cells. *ACS Appl. Mater. Inter.*, 3:2358–2367, 2011.
- [24] V. M. Guérin, J. Rathousky, and T. Pauporté. Electrochemical desing of ZnO hierarchical structures for dye-sensitized solar cells. *Sol. Energy Mater. Sol. Cells*, 102:8–14, 2012.
- [25] J. Xu, K. Fan, W. Shi, K. Li, and T. Peng. Application of ZnO micro-flowers as scattering layer for ZnO-based dye-sensitized solar cells with enhanced conversion efficiency. *Solar Energy*, 101:150–159, 2014.
- [26] A. Saraby-Reintjes, L. M. Peter, M. E. Özsan, S. Dennison, and S. Webster. On the mechanism of the cathodic electrodeposition of Cadmium Telluride. *J. Electrochem. Soc.*, 140(10):2880–2888, 1993.
- [27] D. Lincot, M. Furlong, M. Froment, M.C. Bernard, R. Cortes, A.N. Tiwari, M. Krejci, and H. Zogg. Heteroepitaxy of chemical bath deposited CdS on single crystal CuInSe₂/Si substrates. In *Technical Digest International PVSEC-9*, 1996.
- [28] M. Izaki and T. Omi. Transparent zinc oxide films prepared by electrochemical reaction. *Appl. Phys. Lett.*, 68:2439, 1996.
- [29] J. Elias, R. Tena-Zera, and C. Lévy-Clément. Electrochemical deposition of ZnO nanowires arrays with tailored dimensions. *J. Electroanal. Chem.*, 621:171–177, 2008.
- [30] B. Xue, Y. Liang, L. Donglai, N. Eryong, S. Congli, F. Huanhuan, X. Jingjing, J. Yong, J. Zhifeng, and S. Xiaosong. Electrodeposition from ZnO nano-rods to nano-sheets with only zin nitrate electrolyte and its photluminescence. *Appl. Surf. Sci.*, 257:10317–10321, 2011.
- [31] R. K. Pandey, S. N. Sahu, and S. Chandra. *Handbook of Semiconductor Electrodeposition*. CRC Press, 1996.

- [32] S. A. Gamboa, P. J. Sebastian, and M. A. Rivera. Characterization of p-CdTe obtained by CVTG tellurization of electrodeposited CdTe. *Sol. Energy Mater. Sol. Cells*, 52:293–299, 1998.
- [33] C. A. Arguello, D. L. Rousseau, and S. P. S. Porto. First-order raman effect in wurtzite-type crystals. *Phys. Rev.*, 181:1351–1363, 1969.
- [34] R. Cuscó, E. Alarcón-Lladó, J. Ibañez, L. Artús, J. Jiménez, B. Wang, and M. J. Callahan. Temperature dependence of raman scattering in ZnO. *Phys. Rev. B*, 75(165202), 2007.
- [35] T. L. Phan. Optical properties of ZnO nanoparticles prepared by mechanical ball milling. *New Phys.: Sae Mulli*, 62:483–487, 2012.
- [36] I. G. Morozov, O. V. Belousova, D. Ortega, M. K. Mafina, and M. V. Kuznetsov. Structural, optical, XPS and magnetic properties of Zn particles capped by ZnO nanoparticles. *J. Alloys Compd.*, 633:237–245, 2015.
- [37] S. J. Chen, Y. C. Liu, Y. M. Lu, J. Y. Zhang, D. Z. Shen, and X. W. Fan. Photoluminescence and raman behaviors of ZnO nanostructures with different morphologies. *J. Cryst. Growth*, 289:55–58, 2006.
- [38] Y. Lin, J. Yang, and X. Zhou. Controlled synthesis of oriented ZnO nanorod arrays by seed-layer-free electrochemical deposition. *Appl. Surf. Sci.*, 258:1491–1494, 2011.
- [39] W. Ludwig, W. Ohm, J. Correa-Hoyos, Y. Zhao, M. Lux-Steiner, and S. Gledhill. Electrodeposition parameters for ZnO nanorods arrays for photovoltaic applications. *Phys. Status Solid A*, 210:1557–1563, 2013.
- [40] G. K.L. Goha, F. F. Lange, S. M. Haile, and C. G. Levi. Hydrothermal synthesis of KNbO₃ and NaNbO₃ powders. *J. Mater. Res.*, 18(2):338–345, 2003.
- [41] M. Sathiya, G. Rouse, K. Ramesha, C. P. Laisa, H. Vezin, M. T. Sougrati, M-L. Doublet, D. Foix, D. Gonbeau, W. Walker, A. S. Prakash, M. B. Hassine, L. Dupont,

- and J-M. Tarascon. Reversible anionic redox chemistry in high-capacity layered-oxide electrodes. *Nat. Mater.*, 12:827–835, 2013.
- [42] B. S. Yang, S. Park, S. Oh, Y. J. Kim, J. K. Jeong, C. S. Hwanga, and H. J. Kim. Improvement of the photo-bias stability of the Zn-Sn-O field effect transistors by an ozone treatment. *J. Mater. Chem.*, 22:10994–10998, 2012.
- [43] J. Zhang, D. Gao, G. Yang, J. Zhang, Z. Shi, Z. Zhang, Z. Zhu, and D. Xue. Synthesis and magnetic properties of Zr doped ZnO nanoparticles. *Nanoscale Res. Lett.*, 6(587): 1–7, 2011.
- [44] S. Bang, S. Lee, Y. Ko, J. Park, S. Shin, H. Seo, and H. Jeon. Photocurrent detection of chemically tuned hierarchical ZnO nanostructures grown on seed layers formed by atomic layer deposition. *Nanoscale Res. Lett.*, 7(290):1–11, 2012.
- [45] N. S. Ramgir, I. S. Mulla, and V. K. Pillai. Micropencils and microhexagonal cones of ZnO. *J. Phys. Chem. B*, 110:3995–4001, 2006.
- [46] C. D Wagner, D. E Passoja, H. F Hillery, T. G. Kinisky, H. A. Six, W. T. Jansen, and J. A. Taylor. Auger and photoelectron line energy relationships in aluminum-oxygen and silicon-oxygen compounds. *J. Vac. Sci. Technol.*, 21(4):933–944, 1982.
- [47] W. Feng, S. Rangan, Y. Cai, E. Galoppini, R. A. Bartynski, and E. Garfunkel. Energy level alignment of polythiophene/ZnO hybrid solar cells. *J. Mater. Chem.*, 2:7034–7044, 2014.
- [48] D. C. Look. Recent advances in ZnO materials and devices. *Mat. Sci. Eng. B*, 80: 383–387, 2001.
- [49] Ü. Özgür, Y. I. Alinov, C. Liu, A. Teke, M. A. Reshchikoc, S. Dogan, V. Avrutin, S. J. Cho, and H. Morkoç. A comprehensive review of ZnO materials and devices. *J. Appl. Phys.*, 98:041301, 2005.
- [50] S. J. Pearton, D. P. Norton, K. Ip, Y. W. Heo, and T. Steiner. Recent progress in processing and properties of ZnO. *Prog. Mater. Sci.*, 50:293–340, 2005.

- [51] F. A. Selim, M. H. Weber, D. Solodovnikov, and K. G. Lynn. Nature of native defects in ZnO. *Phys. Rev. Lett.*, 99(085502):1–4, 2007.
- [52] W. Anwand, G. Brauer, R. I. Grynszpan, T. E. Cowan, D. Schulz, D. Klimm, J. Iek, J. Kuriplach, I. Prochzka, C. C. Ling, A. B. Djurii, V Klemm, G. Schreiber, and D. Rafaja. Characterization of microstructural defects in melt grown ZnO single crystals. *J. Appl. Phys.*, 109(6), 2011.
- [53] J. Wang, Z. Wang, B. Huang, Y. Ma, Y. Liu, X. Qin, X. Zhang, and Y. Dai. Oxygen vacancy induced band-gap narrowing and enhanced visible light photocatalytic activity of ZnO. *Appl. Mater. Interfaces*, 4:4024–4030, 2012.
- [54] S. A. Ansari, M. M. Khan, S. Kalathil, A. Nisar, J. Lee, and M. H. Cho. Oxygen vacancy induced band gap narrowing of ZnO nanostructures by an electrochemically active biofilm. *Nanoscale*, 5:9238–9246, 2013.
- [55] H. Liu, F. Zeng, Y. Lin, G. Wang, and F. Pan. Correlation of oxygen vacancy variations to band gap changes in epitaxial ZnO thin films. *Appl. Phys. Lett.*, 102:181908, 2013.
- [56] R. Schlesinger, Y. Xu, O. T. Hofmann, S. Winkler J. Frisch, J. Niederhausen, A. Vollmer, S. Blumstengel, F. Henneberger, P. Rinke, M. Scheffler, and N. Koch. Controlling the work function of ZnO and the energy-level alignment at the interface to organic semiconductors with a molecular electron acceptor. *Phys. Rev. B*, 87(155311):1–5, 2013.
- [57] Y. Lin, J. Yang, and Y. Meng. Nanostructured ZnO thin films by SDS-assisted electrodeposition for dye-sensitized solar cell applications. *Ceram. Int.*, 39:5049–5052, 2013.
- [58] Y. Meng, Y. Lin, and Y. Lin. Electrodeposition for the synthesis of ZnO nanorods modified by surface attachment with ZnO nanoparticles and their dye-sensitized solar cell applications. *Ceram. Int.*, 40:1693–1698, 2014.

- [59] M. Grätzel. Dye sensitized solar cells. *J. Photochem. Photobiol. A*, 4:145–153, 2003.
- [60] N. R. Neale, N. Kopidakis, J. Lagemaat, M. Grätzel, and A. J. Frank. Effect of a coadsorbent of the performance of dye-sensitized TiO₂ solar cells: Shielding versus band-edge movement. *J. Phys. Chem. B*, 109:23183–23189, 2005.
- [61] K. Keis, J. Lindgren, E. S. Lindquist, and A. Hagfeldt. Studies of the adsorption process of Ru complexes in nanoporous ZnO electrodes. *Langmuir*, 16:4688–4694, 2000.
- [62] A. Hagfeldt, G. Boschloo, L. Sun, L. Kloo, and H. Pettersson. Dye-sensitized solar cells. *Chem. Rev.*, 110:6595–6663, 2010.
- [63] G. Boschloo and A. Hagfeldt. Characteristics of the iodide/triiodide redox mediator in dye-sensitized solar cells. *Acc. Chem. Res.*, 42(11):1819–1826, 2009.

5. HYDROTHERMALLY SYNTHESIZED ZINC OXIDE THIN FILMS FOR DYE SENSITIZED SOLAR CELLS

In this chapter, ZnO nanorods (NRs) were hydrothermally synthesized and investigated for use in dye-sensitized solar cells (DSSCs). The results obtained with these nanorods were compared with the results obtained with the electrodeposited mesoporous ZnO thin films presented in the previous chapter. The NRs were grown on two different fluorine-doped tin oxide (FTO) substrates with different sheet resistances. The influence of the amount of dye adsorbed by ZnO on the solar cell performance was also evaluated. The results reveal that the DSSCs fabricated with more conductive FTO present higher power conversion efficiency (PCE), mainly due to the higher short-circuit current J_{sc} , which can be attributed to the lower series resistance as a consequence of the lower sheet resistance. Moreover, the PCE efficiency is inversely proportional to the dye loading time. The best solar cell assembled with an electrodeposited ZnO working electrode is 9% more efficient than the best device assembled with hydrothermally synthesized ZnO working electrodes. This difference in performance is primarily due to the difference in J_{sc} , which can be attributed to the lower dye precipitation on the solar cell assembled with the electrodeposited ZnO working electrode.

5.1 Introduction

Different ZnO nanostructures can be prepared, such as simple nanoparticles, nanorods, nanobelts, branched nanorods, nanowires, ultra-narrow nanobelts, hierarchical nanostructures, nanocombs, nanosprings, nanospirals, seamless nanorings, core-shell nanostructures, nanocages, and nanoflowers, among many others [1–4]. These nanostructures have been widely used in excitonic solar cells (XSCs), including dye-sensitized solar cells

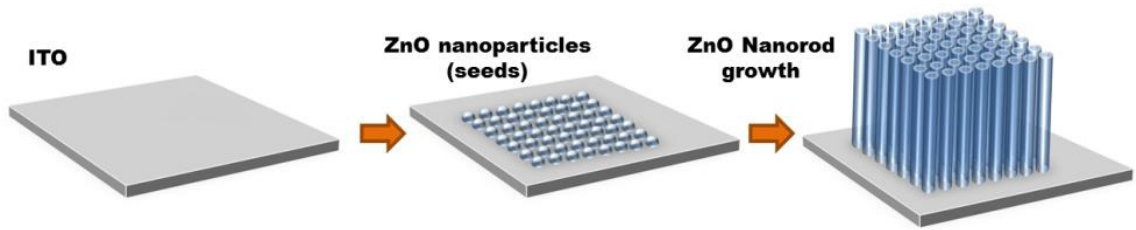
(DSSCs) [5, 6], quantum dot solar cells [7], organic solar cells (OSCs) [8–10], and Perovskite solar cells [11, 12]. In DSSCs, one possible way to obtain faster electron transport replaces the nanoparticle electrode with vertically-aligned nanostructures, which, in turn, improves solar cell efficiency. Moreover, solid hole conductors with slower kinetics require the application of faster electron transport materials such as vertically-aligned nanostructures. The use of vertically aligned ZnO NRs in DSSCs has some drawbacks. The main problem in the use of NRs is their low surface area; an electrode formed with nanorods between 20 and 25 μm has only one-fifth of the surface area of a similar electrode made of nanoparticles. Moreover, the low surface area seems to explain why the reported power conversion efficiencies for bare, vertically aligned ZnO nanorods have not been higher than 2.5%, even when NRs with lengths up to 40 μm are considered [13]. In this work, thin films composed with ZnO nanorods were applied as working electrodes in DSSCs, and the results from ZnO thin films obtained by hydrothermal synthesis and electrochemical deposition are compared.

5.2 Hydrothermal synthesis of ZnO

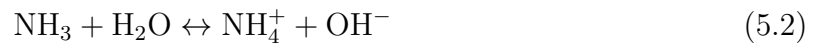
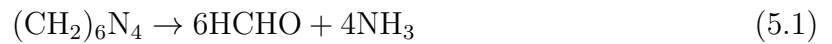
Hydrothermal synthesis, which is also known as chemical bath deposition (CBD), is a low-cost aqueous technique. Though hydrothermal synthesis can be performed at temperatures between 100–1000°C and under pressures between 1 MPa–1000 MPa in a sealed autoclave reactor [14, 15], there are advantages to performing ZnO synthesis at low temperatures ($< 100^\circ\text{C}$) in an aqueous solution under atmospheric pressure, as shown by the large number of studies using such low-cost conditions [13, 16–19]. Figure 5.1 shows the formation of ZnO nanorods on indium-tin-oxide (ITO) substrates from an initial layer of ZnO nanoparticles (NPs).

The hydrothermal technique consists of ZnO formation from the hydrolysis of Zn^{2+} salts in a basic aqueous solution. The basic media is essential for forming ZnO nanostructures, and either strong or weak alkalis can be used. The most commonly used base is hexamethylenetetramine (HMT, $\text{C}_6\text{H}_{12}\text{N}_4$), which acts as pH buffer, controlling the pH value at 6–7 for slowly supplying OH^- anions to the synthesis, according to [16, 17, 21–23]:

Figure 5.1: Schematic representation of the growth of ZnO nanorods on ITO substrates using hydrothermal synthesis from an initial layer of ZnO nanoparticles.



Source: Gonzalez-Valls [20].



Other bases applied in hydrothermal synthesis include NaOH, KOH, and NH_4^+ . When the concentration of Zn^{2+} and OH^- exceeds a critical value, the precipitation of ZnO starts when the solution is heated:



Then, the obtained ZnO in the solution begins nucleation on the substrate surface, which is positioned upside down in the solution, with ZnO NPs. The ZnO NPs act as seeds for the nucleation of ZnO NRs.

The dimensions and quality of the final ZnO NRs depend on the hydrothermal synthesis conditions, such as the zinc concentration in solution, growth time, and growth temperature. Furthermore, the reaction solution should be changed after certain time to renew the precursor materials.

5.3 Experimental procedure

5.3.1 *Synthesis of ZnO nanorod thin films*

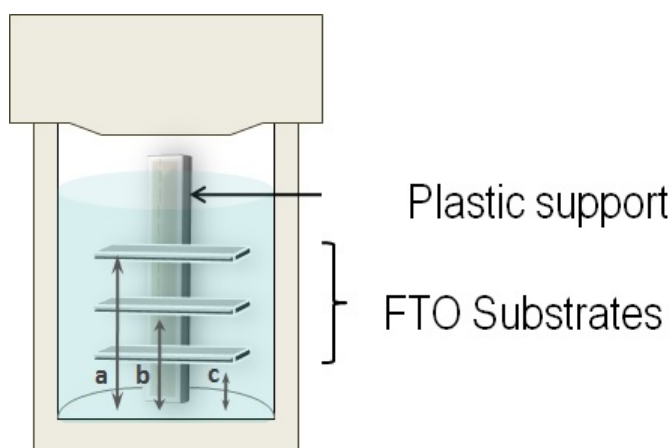
The vertically aligned ZnO NRs were deposited on FTO substrates. For the nanorod synthesis, the transparent conductive oxide (TCO) substrates were first washed with deionized water and soap, rinsed with deionized water (two times) and ethanol, dried under N₂ flux, and cleaned for 20 min in an ultraviolet-surface decontamination system (Novascan[®], PSDUV) connected to an O₂ gas source before use. A ZnO buffer layer of about 80–100 nm was prepared by spin coating a sol-gel layer of ZnO on top of the TCO substrate. The ZnO sol-gel was prepared using the method reported by Lira-Cantu and Krebs [24], Aslan et al. [25]. Briefly, 2.0 g of zinc acetate and 1.07 g of diethanol amine (DEA) were dissolved in 10 mL of isopropanol and heated at 60°C for about 10 min until total dissolution. Then, the solution was diluted with ethanol (1:1) and filtered through a filter with 0.45- μ m pores (Albet[®]). Once the ZnO sol-gel was applied by spin coating, the substrates were annealed at 450°C for 2 h (heating rate of 3°C·min⁻¹). Annealing allows for the formation of a dense ZnO thin film, which can be used as buffer layer to enable better contact between the TCO and ZnO NRs.

A layer of ZnO NPs, which were used as seeds for the growth of ZnO NRs, was spin-coated on top of the ZnO buffer layer. The ZnO nanoparticles were prepared following the method described by Pacholski et al. [26]. Specifically, a solution of 0.03-M KOH in methanol was added dropwise in a refluxing mixture of 0.01-M zinc acetate dehydrate in methanol at 65°C. After 2 h of reflux, the solution was allowed to cool down. Because the suspension of ZnO nanoparticles is known to degrade (agglomerate) with time [27], a freshly prepared suspension was always used. The NP suspension was spin coated on the FTO/ZnO dense layer three times at a speed of 1000 rpm [28]. The substrates were thermally treated at 150°C for 10 min between each deposition.

To grow the ZnO NRs, the substrates were placed face-down in an equimolar aqueous solution of 25-mM zinc nitrate hexahydrate and HMT [16, 17, 29] at 96°C for 12 h, changing the solution after 6 h. Because thermal treatment of the as-synthesized electrodes is known to improve the power conversion efficiency, the samples were dried in

air and sintered at 450°C for 30 min in air before DSSC fabrication. In this work, two FTO substrates, which had differing sheet resistances, were used for the ZnO working electrodes. For the first set of solar cells, the FTO substrate had a sheet resistance in the range of 50–70 Ω/\square . For the second set of solar cells, the sheet resistance was between 10–15 Ω/\square . The experimental set up used for growing the ZnO NR thin films is depicted in Fig. 5.2

Figure 5.2: Experimental set up used for the hydrothermal synthesis of ZnO nanorod thin films on FTO substrates.



Source: Own author.

5.3.2 Structural, morphological and electrical characterization of the films

The zinc oxide thin films were structurally characterized by X-ray diffraction and Raman spectroscopy. X-ray diffraction analyses between 20 and 80° were performed with a Rigaku Rotaflex RU200 B instrument using $\text{CuK}\alpha_1$ radiation. Raman measurements were performed with a Jobin Yvon T64000 micro-Raman Triple Spectrometer using an excitation wavelength of 532 nm. The chemical composition of the films was evaluated by energy dispersive X-ray spectroscopy and X-ray photoelectron spectroscopy. EDX analysis were performed using the electron beam from the SEM as the X-ray excitation source with an acceleration voltage of 20 KV. The X-rays were analyzed with an Inca 250 SSD

XMax20 detector, which is Peltier cooled with 20 mm² active area and 129 eV resolution. The XPS measurements were performed using equipment from SPECS[®] with an energy analyzer (PHOIBOS[®] 150) using Al K α (1486.6 eV) radiation as the X-ray source. All spectra were adjusted according to the value of the C 1s peak at (284.8 \pm 0.1 eV). The fitting was performed using the CASA XPS application software. Morphological characterization was carried out by means of scanning and transmission electron microscopy. The electronic microscopy images for this work were obtained using the following equipment. Scanning electron microscopy (SEM, FEI Quanta 650FEG ESEM) equipped with an energy dispersive X-ray spectroscopy (EDX) analyzer (Inca 250 SSD XMax20 detector). Transmission electron microscopy (TEM, 200 kV JEM 2011) equipped with an EDS detector (Oxford Linca). The band diagrams for the studied thin films were determined with the help of Uv-Vis spectroscopy and ultraviolet photoelectron spectroscopy measurements. UV-Vis analysis of solutions and thin films was performed with a Shimadzu 1800 spectrophotometer. UPS analyses were obtained using equipment from SPECS with a PHOIBOS 150 energy analyzer. The UV radiation source was a He lamp (He 1 21.2 eV) with an experimental resolution of 0.15 eV. The samples were forward biased at 5 V and 10 V to provide sufficient energy for detecting the secondary cut-off electrons.

5.3.3 Solar cell fabrication and characterization

The ZnO thin films were immersed in a 0.5-mM/L ethanolic solution of N719 dye for different times to provide dye loading of the ZnO. After dye loading, the working electrodes were used to assemble DSSCs. The platinized FTO counter electrode was prepared by electron beam physical vapor deposition (EBPVD) with a Pt layer thickness of 50 nm. The working and counter electrodes were bonded together with hot-melt sealing foil. A commercially available liquid iodide-iodine electrolyte was introduced through a small hole on the Pt counter-electrode through capillary forces by applying vacuum. Finally, the DSSCs were hermetically sealed with a small piece of glass, which closed the filling hole. Photoelectrochemical tests were performed by measuring the $J - V$ characteristic curves under simulated AM 1.5 solar illumination at 100 mW/cm⁻² from a Steuer-

nagel Solarkonstant[®] KHS1200 sun simulator. The $J - V$ curves were measured using a Keithley[®] 2601 multimeter. The incident photon-to-charge-carrier efficiency (IPCE) measurements were performed with a quantum efficiency (QE)/IPCE measurement system (Oriental[®]) at 10 nm intervals between 300 and 700 nm. The results were not corrected for intensity losses due to light absorption or due to reflection by the glass support.

5.4 Structural, morphological, compositional, and electrical analysis

The ZnO nanorods were characterized by X-ray diffraction (XRD), Raman spectroscopy, transmission electron microscopy (TEM), scanning electron microscopy (SEM), X-Ray photoelectron spectroscopy (XPS), ultraviolet (UV) photoelectron spectroscopy (UPS), and UV-Vis spectroscopy. The obtained results were compared with the results obtained for electrochemically deposited mesoporous ZnO thin films.

5.4.1 X-ray diffraction

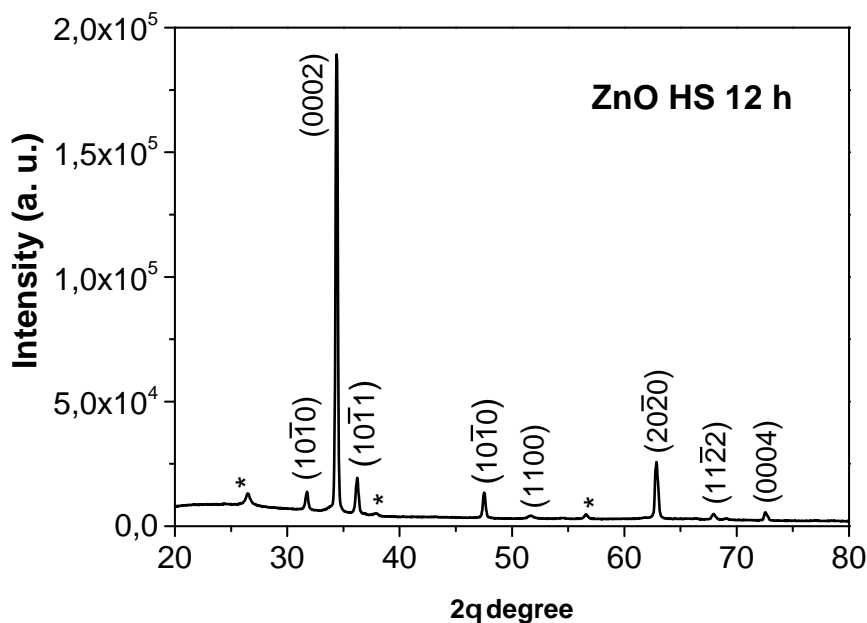
Figure 5.3 shows XRD diffractograms for a typical sample, which reveals the existence of a single crystalline phase with a hexagonal wurtzite structure (CPDS card file number 36-1451, zincite phase). The maximum intensity for typical ZnO corresponds to the (1011) diffraction peak. Therefore, the observed strong and narrow (0002) peak suggests vertically aligned nanorods that are highly oriented along the c -axis, which is perpendicular to the plane of the substrate ([0001] direction). Extra peaks at 2θ equal to 26.5° , 36.3° , and 56.6° correspond to the FTO substrate.

Figure 5.4 shows a comparison between ZnO electrodes obtained by hydrothermal synthesis and electrochemical deposition. Although both films present a preferential growth direction along the c -axis, the film growth by electrodeposition presents intense peaks along the c -axis as well as peaks in directions that are not present in the hydrothermally synthesized ZnO thin film. In fact, the electrodeposited thin film presents a mesoporous structure growing along several directions.

Additionally, the intensity of the peaks for electrochemically deposited thin films are generally high, suggesting that there is more material contributing to the diffraction of

X-rays, which roughly indicates a larger potential surface area for the electrodeposited ZnO thin film.

Figure 5.3: XRD diffractograms for hydrothermally synthesized ZnO thin films.

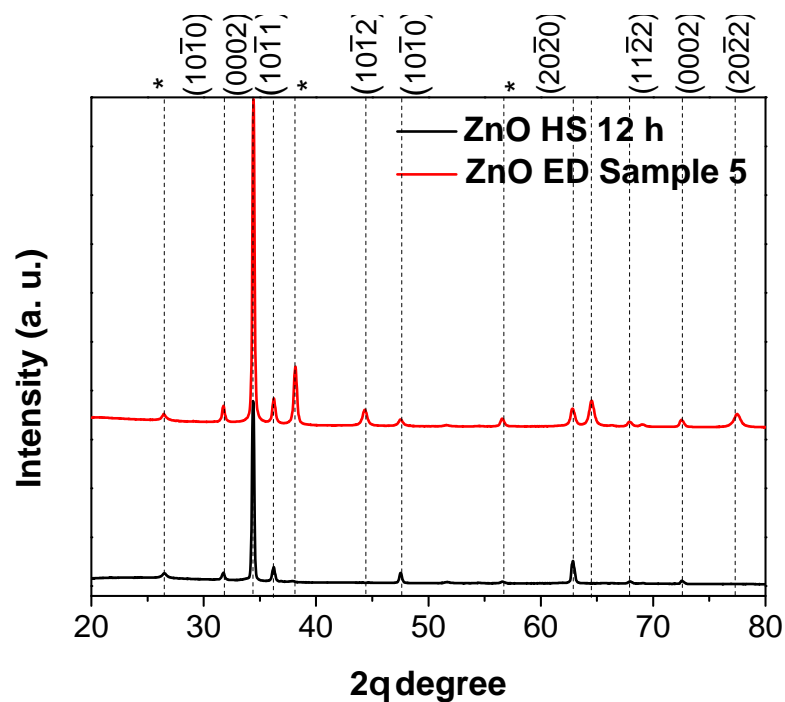


Source: Own author.

5.4.2 Raman spectroscopy

According to Fig. 5.5, the Raman spectrum for a sample of the hydrothermally synthesized ZnO presents characteristic features for wurtzite-structured ZnO, such as E_2 (low) and E_2 (high) phonon modes at about 99 cm^{-1} and 437 cm^{-1} , respectively. As previously mentioned, the low-wavenumber E_2 mode predominantly involves the vibration of the heavy Zn sublattice, while the high-wavenumber E_2 mode is primarily associated with the vibration of the lighter O sublattice. The absence of both A_1 transversal-optical (TO) and A_1 longitudinal-optical (LO) modes could be an indication of the good crystalline quality of the film.

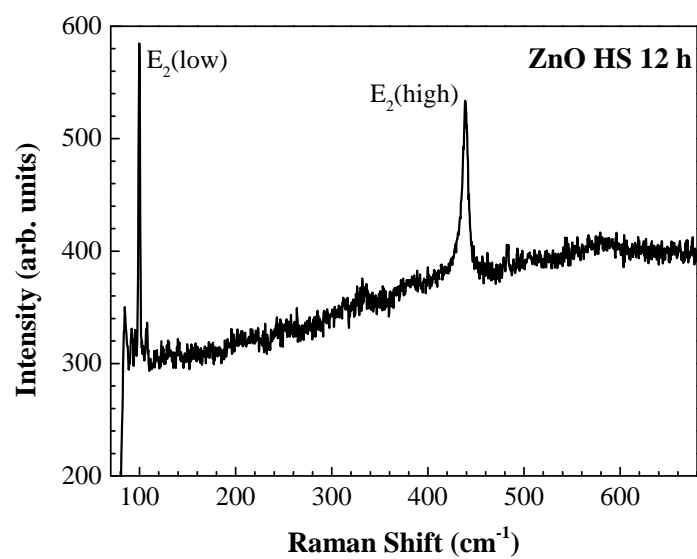
Figure 5.4: Comparison of XRD results for hydrothermally synthesized and electrochemically deposited ZnO thin films.



Source: Own author.

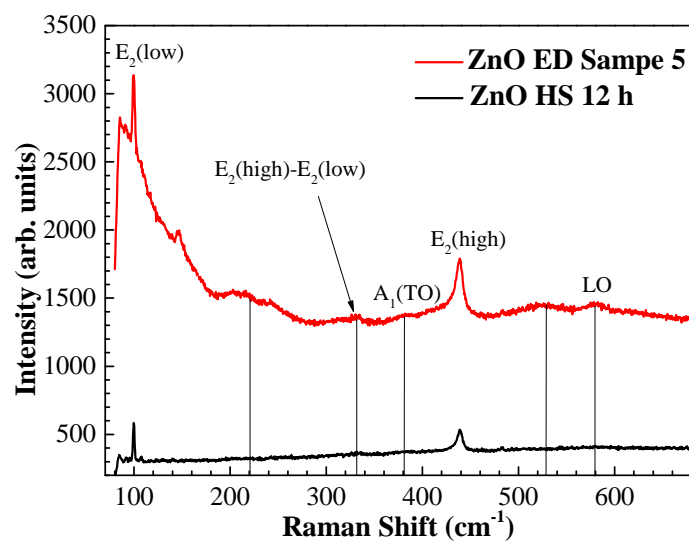
Figure 5.6 shows a comparison of the Raman spectra for a hydrothermally synthesized ZnO thin film and an electrochemically deposited thin film. Both spectra show the fingerprint for wurtzite-structure ZnO aligned with the c -axis [30, 31]. The electrodeposited sample spectrum shows a collection of different peaks assigned to the wurtzite structure as well as peaks indicating the presence of defects. Specifically, both LO and TO components for the A_1 vibrational mode were observed around 220 cm^{-1} and 530 cm^{-1} , respectively, which could be related to structural defects. In addition, a visible peak was observed at 332 cm^{-1} , which is ascribed to $E_2(\text{high}) - E_2(\text{low})$. On the other hand, in the hydrothermally synthesized ZnO spectrum, only peaks due to the wurtzite structure were observed.

Figure 5.5: Raman spectrum for hydrothermally synthesized ZnO thin films.



Source: Own author.

Figure 5.6: Raman spectra comparisons for hydrothermally synthesized and electrochemically deposited ZnO thin films.

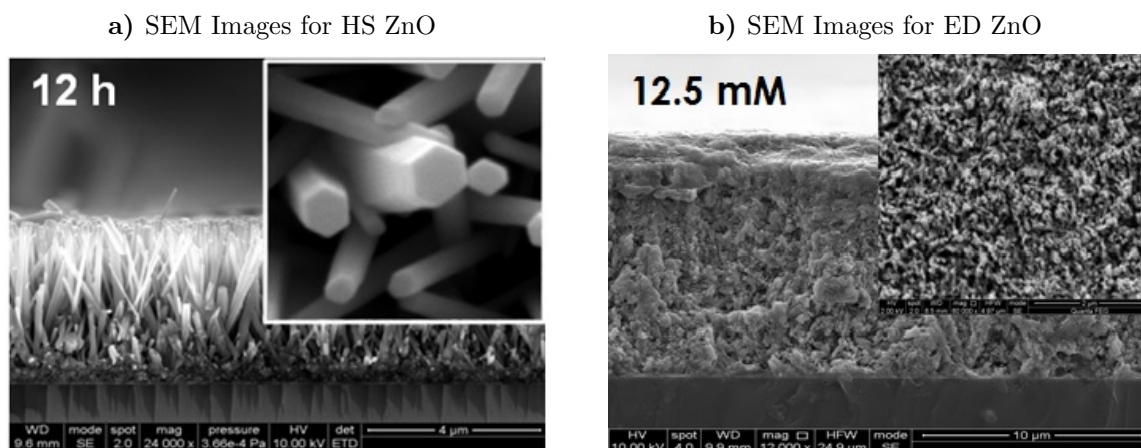


Source: Own author.

5.4.3 Electron microscopy

Figure 5.7(a) shows a cross-sectional SEM image for ZnO NRs grown in 12 h, while the inset shows a top view for the same electrode. From these images, the average NR length is around $3.2\ \mu\text{m}$, while the NR diameters were found to be around $40\ \text{nm}$, even though some NRs presented larger diameters. The larger diameter NRs can be attributed to the coalescence between two or more NRs over time. Figure 5.7(b) shows the electrodeposited ZnO thin film, which has a film thickness of around $12\ \mu\text{m}$. The inset shows the top view of the same electrode, where it is possible to observe the mesoporous nature of the electrodeposited thin film.

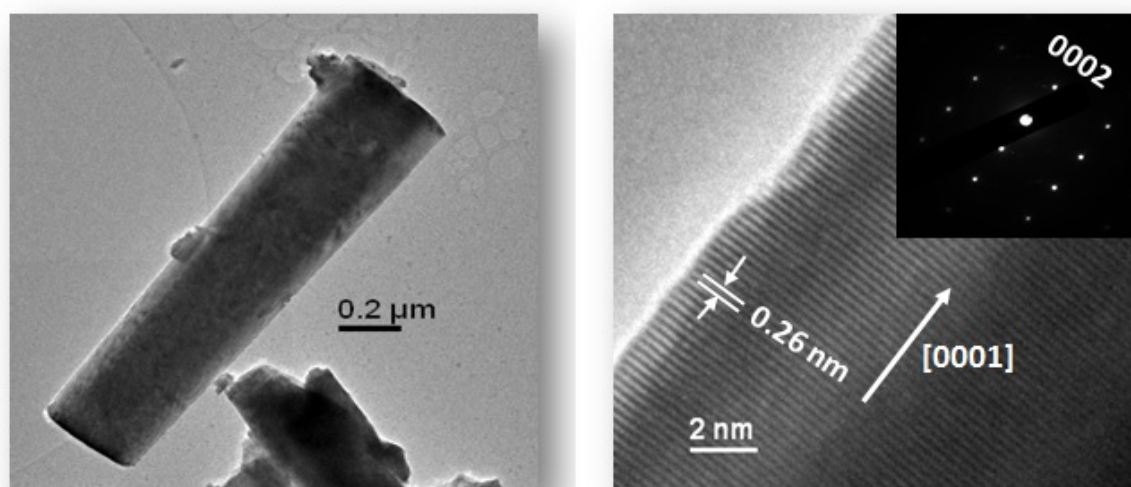
Figure 5.7: SEM images for the ZnO thin films: (a) hydrothermally synthesized ZnO NRs and (b) electrodeposited ZnO mesoporous thin film.



Source: Own author

TEM images for the ZnO NRs are shown in Fig. 5.8. As discussed previously, TEM can simultaneously provide information about the real space (very high resolution images) and reciprocal space because the electron diffraction pattern can be recorded. The images shown in Fig. 5.8 confirm the good crystallinity of the ZnO NRs. The selected-area electron diffraction (SAED) pattern of the NR represents the (0002) and (10 $\bar{1}$ 0) directions from the wurtzite structure, where the NR growth is along the (0002) direction.

Figure 5.8: TEM images for a ZnO NR obtained by hydrothermal synthesis, detail for a single NR and high resolution TEM image with a SAED pattern as inset.

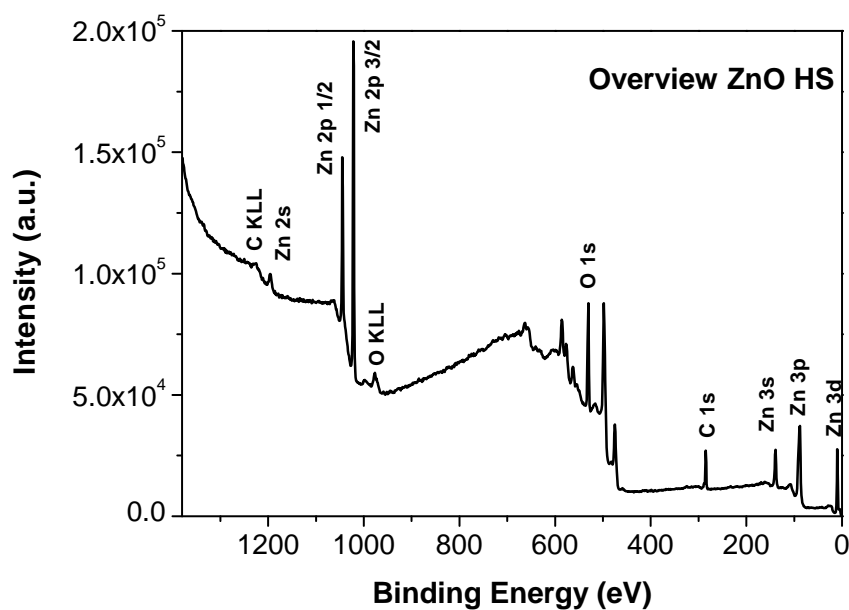


Source: Own author

5.4.4 X-ray photoelectron spectroscopy

The XPS survey for the hydrothermally synthesized ZnO thin film is shown in Fig. 5.9. The XPS spectra reveals the presence of C, Zn, and O at the surface of the thin film. The quantification analyses reveals an excess of oxygen. Nevertheless, when only the oxygen bonded with zinc is considered, the quantification analysis at the surface of the thin film reveals an oxygen deficiency. These data are summarized in Table 5.1.

Figure 5.9: An overview of the XPS results for hydrothermally synthesized ZnO thin films.



Source: Own author

Table 5.1: XPS results for the composition of hydrothermally synthesized ZnO electrodes.

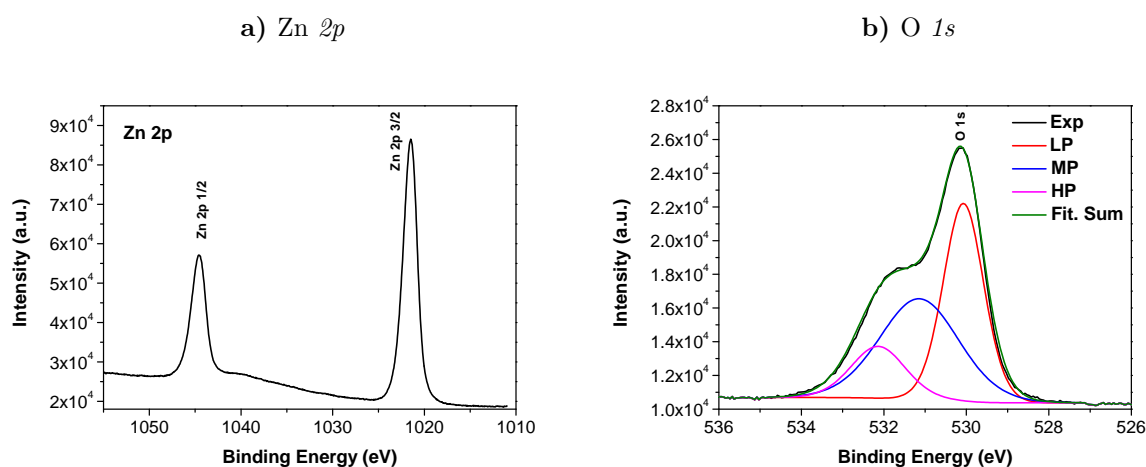
Analysis	O %at.	Zn %at.	ratio O:Zn
Regions	57.32	42.68	1.34
Components	43.31	56.69	0.76

Source: Own author

The Zn $2p$ core-level XPS spectrum for ZnO (Fig. 5.10(a)) shows doublet spectral lines at the binding energies around 1045 eV (Zn $2p$ 1/2) with spin-orbit splitting of 23 eV, which coincides with the results for Zn^{2+} in ZnO. The results of the O $1s$ core-level XPS spectra are shown in Fig. 5.10(b). To calibrate the photo-electron binding energy, the C $1s$ peak for C–C bonds was assigned to 284.8 eV. The O $1s$ spectra can be de-

convoluted into three different peaks [32–35]: (i) a peak at a lower binding energy (LP), centered at 530.1 eV, was assigned to the O $1s$ core level (O^{2-}) in the ZnO wurtzite structure surrounded by the Zn atoms with their full complement of nearest neighbor oxygen ions [36], (ii) a middle binding energy peak (MP) around 531.4 eV is associated with hydroxidic oxygen [37], and (iii) a high binding energy peak (HP), centered at 532.2 eV, corresponds to weakly adsorbed surface species, which are usually ascribed to nonstoichiometric near-surface oxygen, oxygen atoms in carbonate ions on the surface of ZnO, surface hydroxylation, adsorbed H_2O , or adsorbed O_2 . Considering only the oxygen bonded to Zn in wurtzite-structure ZnO, an oxygen deficiency appears, as shown in Table 5.1. This oxygen deficiency suggests the presence of oxygen vacancies, which can cause changes in the ZnO energy levels.

Figure 5.10: High-resolution XPS spectra for (a) Zn $2p$ and (b) O $1s$.



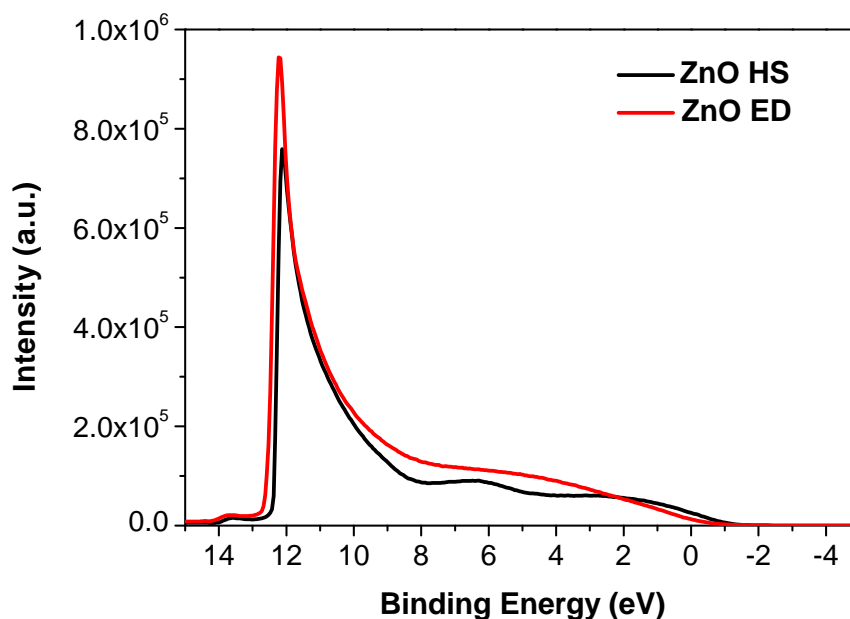
Source: Own author

5.4.5 Band diagram

Understanding the energy band diagram of the working electrode used in DSSCs is fundamentally important. The energy levels can be determined using UPS spectroscopy and UV-Vis spectroscopy. Figure 5.11 shows the valence band UPS spectrum for the hy-

drothermally synthesized ZnO electrode. The spectrum for the electrodeposited electrode (sample 5) is also shown for comparison.

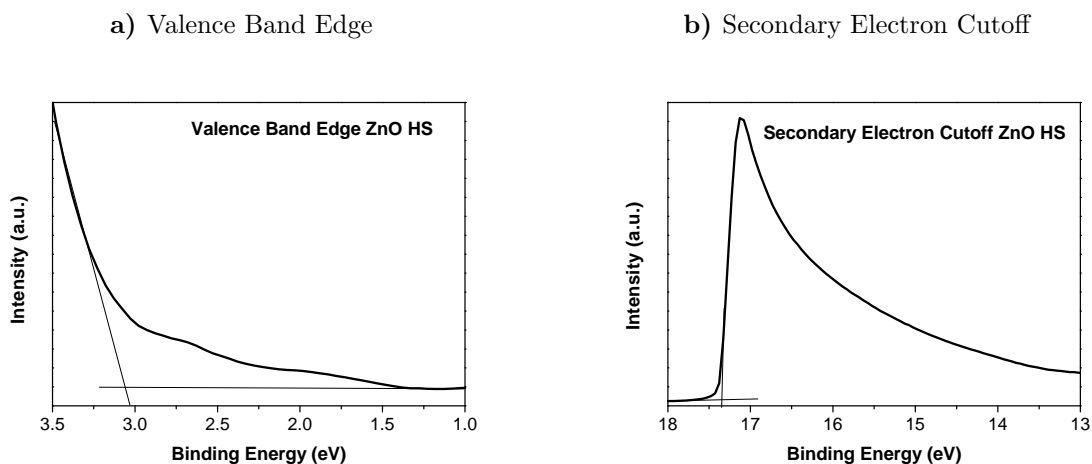
Figure 5.11: Comparison between the valence band UPS spectra for ZnO thin films deposited by hydrothermal synthesis and electrochemical deposition (sample 5). Applied bias of 5 eV



Source: Own author.

The values of the secondary electron cutoff energy (E_{SEC}) and valence band edge energy (E_{VBE}) can be directly acquired from the valence band UPS spectra illustrated in Fig. 5.12. With these values and eq. 4.8, the ionization energy (IP) can be determined. For this sample, the value of E_{SEC} is 17.3 eV, and the value of E_{VBE} is 3.05 eV. Hence, the calculated value of IP is 6.9 eV.

Figure 5.12: Details of the secondary electron cutoff and valence band edge obtained for hydrothermally synthesized ZnO thin films.

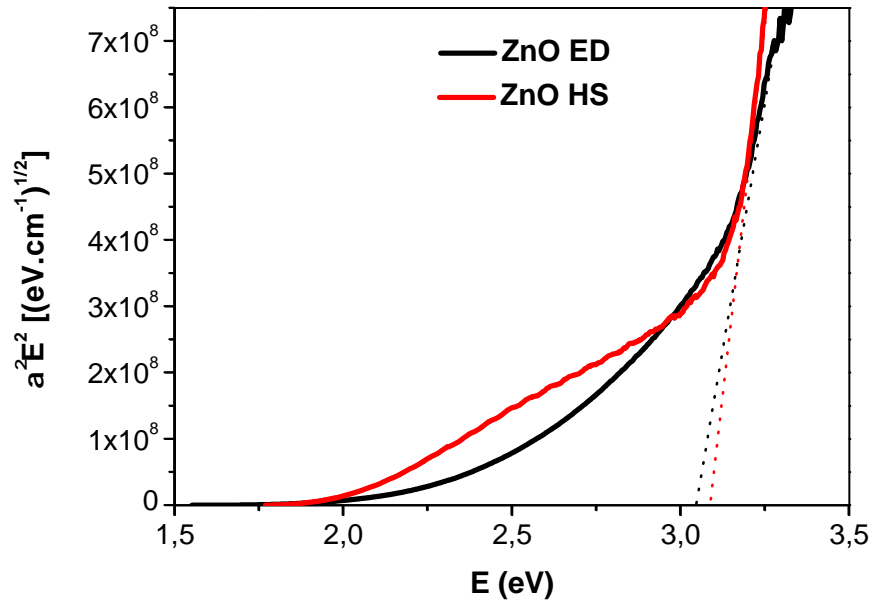


Source: Own author

To complete the band alignment diagram, the optical bandgap is required, which can be estimated using Tauc's plot. Figure 5.13 shows Tauc's plot for the hydrothermally synthesized ZnO as well as the electrodeposited ZnO (sample 5) thin films. According to Fig. 5.13, the optical bandgap (E_g) for the hydrothermally synthesized ZnO electrode is 3.15 eV while that for the electrodeposited ZnO electrode (sample 5) is 3.10 eV. As mentioned previously, the difference between the nominal bandgap $E_g = 3.37$ eV at 300 K for ZnO [38–40] and the E_g^{opt} value given by Fig. 5.13 indicates the presence of optically active defects in this sample. The corresponding defects could be characterized by the difference in energy from either the valence or conduction band.

With IP , VBE , and E_g , the value of the work function can easily be determined as $\Phi = 3.9$ eV. With this data, the energy band diagram can be drawn for the ZnO thin films. The band diagram for the hydrothermally synthesized ZnO is depicted in Fig. 5.14 along with the band diagram for electrodeposited ZnO, for comparison. For the hydrothermally synthesized ZnO thin film, the valence band edge is shifted by 3.05 eV with respect to the Fermi level. The optical band gap was determined to be 3.15 eV, and consequently, the conduction band edge is shifted by 0.1 eV with respect to the Fermi level. The work

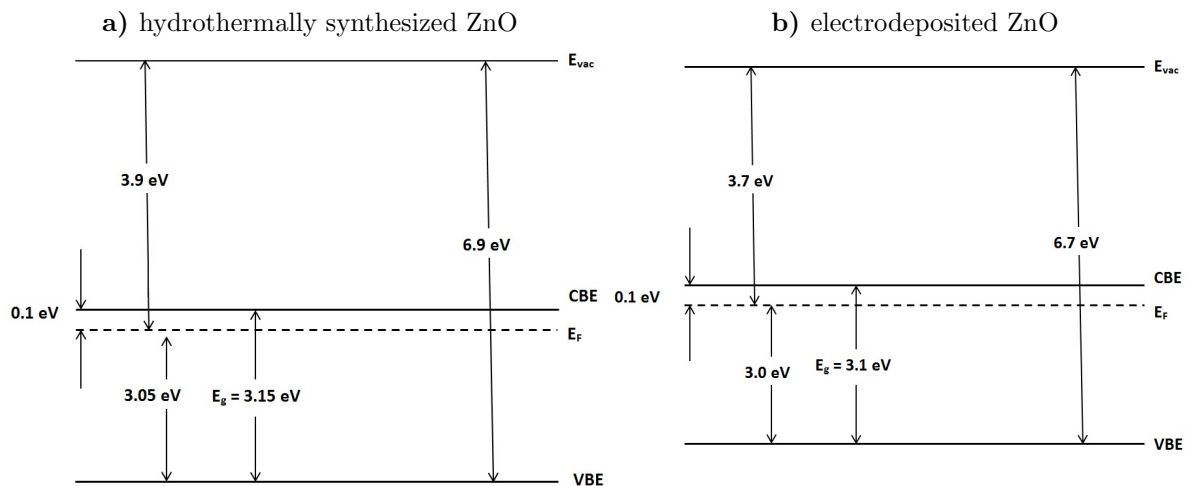
Figure 5.13: Comparison between the optical bandgaps for sample ZnO thin films deposited by hydrothermal synthesis and electrochemical deposition (sample 5).



Source: Own author.

function Φ for this thin film is 3.9 eV, and the ionization energy is 6.9 eV. There is no significant difference between the band diagrams for the hydrothermally synthesized and electrodeposited ZnO electrodes.

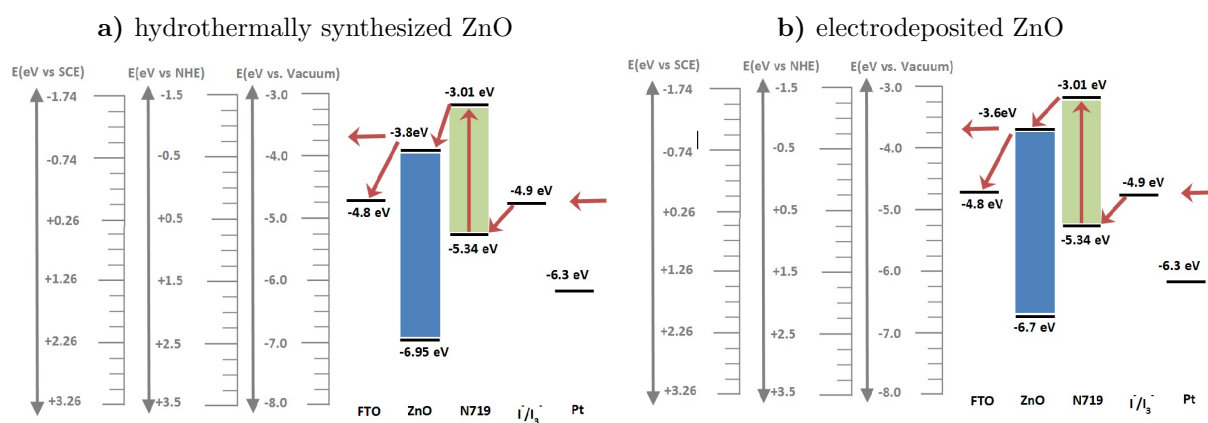
Figure 5.14: Band diagram for hydrothermally synthesized and electrodeposited ZnO thin films.



Source: Own author

Finally, in Fig. 5.15, the band diagram alignment of the hydrothermally synthesized ZnO working electrode is shown with other DSSC constituents, including the Ru-based N719 dye, the regenerate electrolyte I^-/I_3^- , the FTO substrate, and the counter electrode, which is composed of a conductive glass activated with a platinum catalyst. The same band diagram is shown for the electrochemically deposited electrode. In terms of the energy levels, there is no appreciable difference between the two electrodes, and it is not possible to attribute differences in performance to the band alignment between the ZnO electrodes and the other DSSC elements.

Figure 5.15: Band alignment for DSSCs using hydrothermally synthesized and electrochemically deposited ZnO as working electrodes.



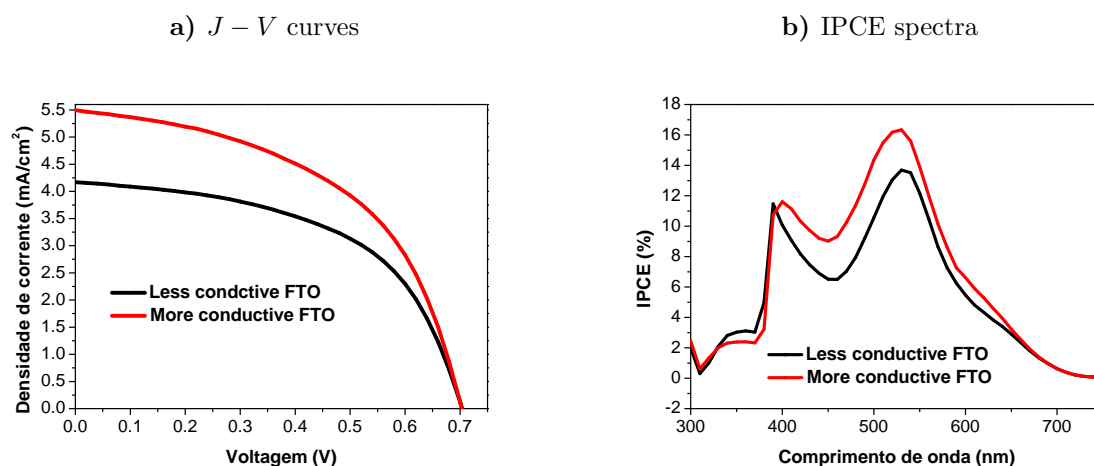
Source: Own author

5.5 Photovoltaic performance

The $J - V$ curves are depicted in Fig. 5.16 for the best DSSC assembled with the less conductive FTO (LC FTO) as well as that assembled with the more conductive FTO (MC FTO). Based on these curves and the data shown in Table 5.2, there are no appreciable differences in V_{oc} or FF when the cells are assembled with LC FTO or with MC FTO. On the other hand, the conductivity of FTO seems to affect the short-circuit current. In fact, J_{sc} is significantly higher for MC FTO devices. The values for the series and

shunt resistance reveal that MC FTO leads to a lower series resistance, which is logical because of the lower resistance of FTO. On the other hand, LC FTO results in high shunt resistance, which is beneficial for the solar cell performance. Figure 5.16 also shows the IPCE spectra for the best cell in each set. The IPCE spectra indicate that the cell assembled with more conductive FTO has high external quantum efficiency, which is in good agreement with the $J - V$ curves. Thus, the higher efficiency for cells assembled with MC FTO is due to a more intense short-circuit current.

Figure 5.16: $J - V$ curve and IPCE spectra for the best devices using ZnO synthesized by hydrothermal synthesis assembled with different FTO substrates.



Source: Own author

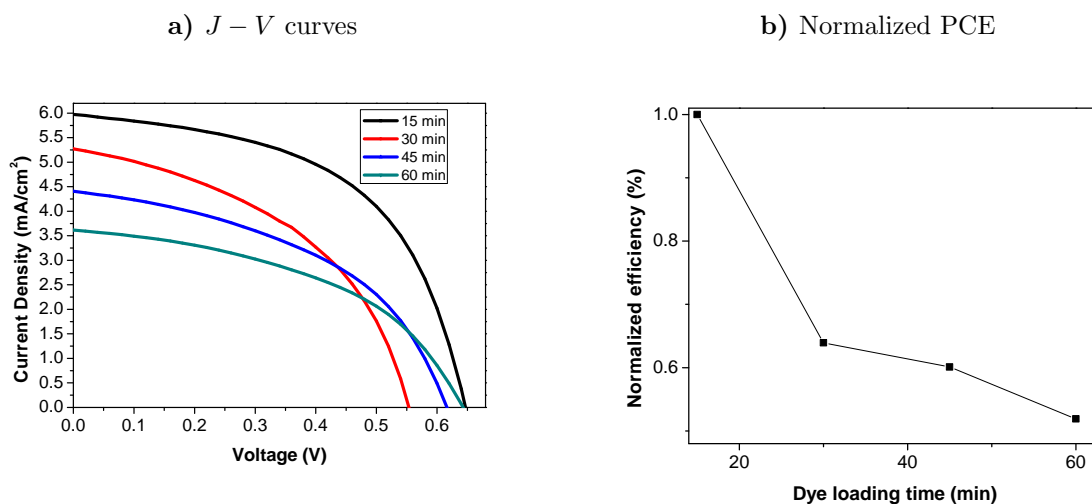
Table 5.2: Photovoltaic parameters for DSSCs assembled with hydrothermally synthesized ZnO on different FTO substrates.

Sample	J_{sc} (mA/cm ²)	V_{oc} (V)	FF (%)	PCE (%)	R_s (k $\Omega \cdot$ cm ²)	R_{sh} (k $\Omega \cdot$ cm ²)
LC FTO	3.78 \pm 0.67	0.67 \pm 0.04	52.57 \pm 2.58	1.34 \pm 0.27	2.25 \pm 0.12	1.21 \pm 0.15
MC FTO	5.29 \pm 0.93	0.69 \pm 0.04	50.84 \pm 0.58	1.83 \pm 0.28	0.95 \pm 0.13	0.65 \pm 0.15

Source: Own author

The dye loading was evaluated by varying the dye loading time from 15 min to 1 h. The $J - V$ curves for different dye loading times is shown in Fig. 5.17(a), and the variation of PCE with respect to the dye loading time is depicted in Fig. 5.17(b). The PCE increases with decreasing dye loading time, which can be explained by the formation of active monolayers of the dye attached to ZnO nanorods. At the same time, the poor performance for longer dye loading times can be explained by the dye precipitation on ZnO [41].

Figure 5.17: $J - V$ curves and normalized PCE for the dye loading time study.



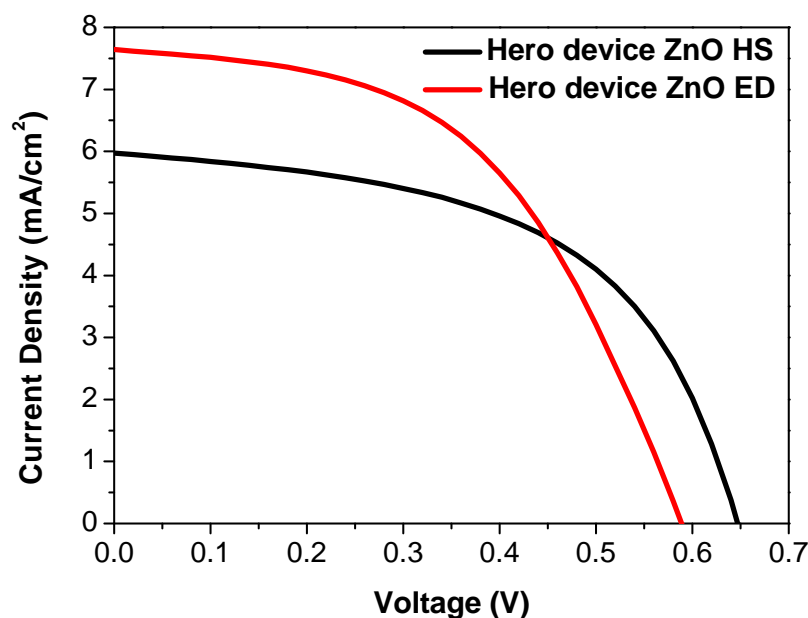
Source: Own author

5.5.1 Comparison between hydrothermally synthesized and electrodeposited ZnO thin films as working electrodes in DSSCs

Figure 5.18 shows the $J - V$ curves for devices assembled with hydrothermally synthesized and electrodeposited ZnO thin films. The best solar cell from the set of hydrothermally synthesized ZnO films had a dye loading time of 15 min, and the best solar cell from the set of electrodeposited ZnO films is sample 5. In general, the solar cells assembled with electrodeposited ZnO present higher J_{sc} values, while the cells assembled

with nanorods present higher V_{oc} values. For the devices shown in Fig. 5.18, J_{sc} is 7.64 mA/cm² for the electrodeposited device and 5.97 mA/cm² for the hydrothermally synthesized device. Moreover, V_{oc} for the hydrothermally synthesized device is 0.64 V while that for the electrodeposited device is 0.59 V. The fill factor FF for the hydrothermally synthesized device is 54.42% while that for the electrodeposited device is 50.41%. The higher FF value for the hydrothermally synthesized device can be attributed to the lower value for the series resistance R_s because R_s primarily affects the FF . Moreover, the hydrothermally synthesized device also has a lower shunt resistance R_{sh} in comparison with the electrodeposited device, which should contribute to the decrease in FF . Both resistances affect FF , but the effect of the series resistance is dominant at this order of magnitude, which explains why FF is higher for the hydrothermally synthesized device than that of the electrodeposited device.

Figure 5.18: Comparison between $J - V$ curves for devices assembled with ZnO working electrodes prepared by hydrothermal synthesis and electrochemical deposition.



Source: Own author.

Table 5.3 shows the photovoltaic parameters for the two prepared devices. The DSSC assembled with the electrodeposited ZnO presented an efficiency, about 9% higher. According to Table 5.3, the main factor leading to this higher efficiency is the higher J_{sc} value, which is 28% higher in the electrodeposited sample than the hydrothermally synthesized sample. Moreover, the high current density could be attributed to the higher dye adsorption of the electrodeposited ZnO. Nevertheless, as discussed previously (Fig. 5.17), the N719 dye tends to precipitate at the surface of the ZnO, giving rise to a filter effect (inactive dye molecules) [42]. In this work, it was demonstrated that a higher amount of adsorbed dye does not lead to higher J_{sc} or better photovoltaic performance; in fact, the results in this work have shown the opposite effect, which can be primarily attributed to the inactive dye molecules. For completeness, the amount of adsorbed dye was determined for these two devices. The amount of dye adsorbed by the electrodeposited ZnO was $4.54 \cdot 10^{-8}$ mol/cm², while that adsorbed by hydrothermally synthesized ZnO was $4.32 \cdot 10^{-8}$ mol/cm². Because the amount of dye adsorbed by both samples is almost the same, the difference in J_{sc} can be attributed to the better adsorption of the dye on the electrodeposited ZnO, which formed monolayers and precipitated less than that in hydrothermally synthesized ZnO.

Table 5.3: Photovoltaic parameters for DSSCs assembled with hydrothermally synthesized and electrochemically deposited ZnO.

ZnO film	J_{sc} (mA/cm ²)	V_{oc} (V)	FF (%)	PCE (%)	R_s k Ω · cm ²	R_{sh} k Ω · cm ²
hydrothermal synthesis	5.97	0.64	54.42	2.08	0.49	0.70
electrodeposition	7.64	0.59	50.41	2.27	0.69	0.84

Source: Own author

5.6 Conclusions

Zinc Oxide NRs prepared by hydrothermal synthesis were successfully applied in DSSCs. SEM images confirm the deposition of vertically aligned nanorods. X-ray diffraction pattern, electron diffraction pattern, and Raman spectroscopy agree that the deposited ZnO is wurtzite structured with preferential growth along the [0002] direction. TEM images confirm the good crystalline quality of the NRs. XPS survey of the thin film surface confirms the presence of Zn, O, and C. High-resolution spectra for O $1s$ and Zn $2p$ also confirm the formation of wurtzite-structured ZnO; these high-resolution spectra further reveals the presence of oxygen vacancies. Tauc's plot, shows a value of 3.15 eV for the optical bandgap, which provides further evidence for the presence of oxygen vacancies. The UPS spectrum was used to determine the ionization energy and valence band maximum. These data were used to draw the band diagram for ZnO as well as the band diagram alignment with the other DSSCs components. The DSSCs performance were characterized using $J - V$ curves and IPCE spectra. The results revealed better photovoltaic performance for the DSSCs assembled with the ZnO working electrode grown on more conductive FTO. The better performance could be ascribed to the higher J_{sc} value as a consequence of the lower series resistance. The dye loading time study reveals that the PCE efficiency increases with decreasing dye loading times. Comparing the best DSSC fabricated with the ZnO NRs and with that fabricated with the mesoporous thin film, it is possible to conclude that the DSSC assembled with the mesoporous thin film has better performance, primarily as a result of the higher J_{sc} value due to the lower dye precipitation on the ZnO surface.

5.7 References

- [1] I. Gonzalez-Valls and M. Lira-Cantu. Vertically-aligned nanostructures of ZnO for excitonic solar cells: a review. *Energy Environ. Sci.*, 2:19–34, 2009.
- [2] Q. Zhang, C. S. Dandeneau, X. Zhou, and G. Cao. ZnO nanostructures for dye-sensitized solar cells. *Adv. Mater.*, 21:4087–4108, 2009.

- [3] F. Zhao, J. Zheng, X. Yang, X. Li, J. Wang, F. Zhao, K. S. Wong, C. Lianga, and M. Wu. Complex ZnO nanotree arrays with tunable top, stem and branch structures. *Nanoscale*, 2:1674–1683, 2010.
- [4] I. Gonzalez-Valls, Y. Yu, B. Ballesteros, J. Oro, and M. Lira-Cantu. Synthesis conditions, light intensity and temperature effect on the performance of ZnO nanorods-based dye sensitized solar cells. *J. Power Sources*, 196:6609–6621, 2011.
- [5] Y. F. Hsu, Y. Y. Xi, A. B. Djurisić, and W. K. Chan. ZnO nanorods for solar cells: Hydrothermal growth versus vapor deposition. *Appl. Phys. Lett.*, 92:133507, 2008.
- [6] A. Al-Hajrya, A. Umar, Y.B. Hahnc, and D.H. Kim. Growth, properties and dye-sensitized solar cells-applications of ZnO nanorods grown by low-temperature solution process. *Superlattices and Microstructures*, 45:529–534, 2009.
- [7] W. Lee, S. K. Min, V. Dhas, S. B. Ogale, and S. Han. Chemical bath deposition of CdS quantum dots on vertically aligned ZnO nanorods for quantum dots-sensitized solar cells. *Electrochem. Commun.*, 11:103–106, 2009.
- [8] K. Yang, C. Xu, L. Huang, L. Zou, and H. Wang. Hybrid nanostructure heterojunction solar cells fabricated using vertically aligned ZnO nanotubes grown on reduced graphene oxide. *Nanotechnology*, 22(40):405401, 2011.
- [9] I. Gonzalez-Valls, D. Angmo, S. A. Gevorgyan, J. S. Reparaz, F. C. Krebs, and M. Lira-Cantu. Comparison of two types of vertically aligned ZnO NRs for highly efficient polymer solar cells. *J. Polym. Sci., Part B: Polym. Phys.*, 51:272–280, 2013.
- [10] Z. Liang, R. Gao, J. Lan, O. Wiranwetchayan, Q. Zhang, C. Li, and G. Cao. Growth of vertically aligned ZnO nanowalls for inverted polymer solar cells. *Sol. Energy Mater. Sol. Cells*, 117:34–40, 2013.
- [11] M. H. Kumar, N. Yantara, S. Dharani, M. Grätzel, S. Mhaisalkar, P. P. Boix, and N. Mathews. Flexible, low-temperature, solution processed ZnO-based perovskite solid state solar cells. *Chem. Comm.*, 49:11089–11091, 2013.

- [12] D. Son, J. Im, H. Kim, and N. Park. 11% efficient perovskite solar cell based on ZnO nanorods: An effective charge collection system. *J. Phys. Chem. C*, 118:16567–16573, 2014.
- [13] Y. C. Qiu, W. Chen, and S. H. Yang. Facile hydrothermal preparation of hierarchically assembled, porous single-crystalline ZnO nanoplates and their application in dye-sensitized solar cells. *J. Mater. Chem.*, 20:1001–1006, 2010.
- [14] A. E. Suliman, Y. Tang, and L. Xu. Preparation of ZnO nanoparticles and nanosheets and their application to dye-sensitized solar cells. *Sol. Energy Mater. Sol. Cells*, 91:1658–1662, 2007.
- [15] F. Xu and L. T. Sun. Solution-derived ZnO nanostructures for photoanodes of dye-sensitized solar cells. *Energy Environ. Sci.*, 4:818–841, 2011.
- [16] L. E. Greene, M. Law, J. Goldberger, F. Kim, J. C. Johnson, Y. Zhang, R. J. Saykally, and P. Yang. Low-temperature wafer-scale production of ZnO nanowire arrays. *Angew. Chem. Int. Ed.*, 42:3031–3034, 2003.
- [17] L. Vayssieres. Growth of arrayed nanorods and nanowires of ZnO from aqueous solutions. *Adv. Mater. (Weinheim, Ger.)*, 15:464–466, 2003.
- [18] Y. Wang and M. Li. Hydrothermal synthesis of single-crystalline hexagonal prism ZnO nanorods. *Mater. Lett.*, 60:266–269, 2006.
- [19] W. X. Zhang and K. Yanagisawa. Hydrothermal synthesis of zinc hydroxide chloride sheets and their conversion to ZnO. *Chemistry of Materials*, 19:2329–2334, 2007.
- [20] I. Gonzalez-Valls. *Vertically-aligned ZnO Nanostructures for excitonic Solar Cells*. PhD thesis, Universidad Autonoma de Barcelona, 2013.
- [21] M. Guo, P. Diao, and S. M. Cai. Hydrothermal growth of well-aligned ZnO nanorod arrays: dependence of morphology and alignment ordering upon preparing conditions. *J. Solid State Chem.*, 178:1864–1873, 2005.

- [22] Q. Ahsanulhaq, A. Umar, and Y. B. Hahn. Growth of aligned ZnO nanorods and nanopencils on ZnO/Si in aqueous solution: growth mechanism and structural and optical properties. *Nanotechnology*, 18:115603–115607, 2007.
- [23] Q. C. Li, V. Kumar, Y. Li, H. T. Zhang, T. J. Marks, and R. P. H. Chang. Fabrication of ZnO nanorods and nanotubes in aqueous solutions. *Chemistry of Materials*, 17:1001–1006, 2005.
- [24] M. Lira-Cantu and F. C. Krebs. Hybrid solar cells based on meh-ppv and thin film semiconductor oxides (TiO_2 , Nb_2O_5 , ZnO, CeO_2 and $\text{CeO}_2\text{-TiO}_2$): Performance improvement during long-time irradiation. *Sol. Energy Mater. Sol. Cells*, 90(14):2076–2086, 2006.
- [25] M. H. Aslan, Y. Oral, E. Mensur, A. Gül, and E. Basaran. Preparation of *c*-axis-oriented zinc-oxide thin films and the study of their microstructure and optical properties. *Sol. Energy Mater. Sol. Cells*, 2:543–552, 2004.
- [26] C. Pacholski, A. Kornowski, and H. Weller. Self-assembly of ZnO: From nanodots to nanorods. *Angew. Chem. Int. Ed.*, 41:1188–1191, 2002.
- [27] M. Ali and M. Winterer. ZnO nanocrystals: Surprisingly ‘alive’. *Chem. Mater.*, 22:85–91, 2010.
- [28] T. Ma, M. Guo, M. Zhang, Y. Zhang, and X. Wang. Density-controlled hydrothermal growth of well-aligned ZnO nanorod arrays. *Nanotechnology*, 18(3):035605, 2007.
- [29] M. Guo, P. Diao, X. Wang, and S. Cai. The effect of hydrothermal growth temperature on preparation and photoelectrochemical performance of ZnO nanorod array films. *J. Solid State Chem.*, 178:3210–3215, 2005.
- [30] R. Cuscó, E. Alarcón-Lladó, J. Ibañez, L. Artús, J. Jiménez, B. Wang, and M. J. Callahan. Temperature dependence of raman scattering in ZnO. *Phys. Rev. B*, 75(165202), 2007.

- [31] T. L. Phan. Optical properties of ZnO nanoparticles prepared by mechanical ball milling. *New Phys.: Sae Mulli*, 62:483–487, 2012.
- [32] M. Sathiya, G. Rousse, K. Ramesha, C. P. Laisa, H. Vezin, M. T. Sougrati, M-L. Doublet, D. Foix, D. Gonbeau, W. Walker, A. S. Prakash, M. B. Hassine, L. Dupont, and J-M. Tarascon. Reversible anionic redox chemistry in high-capacity layered-oxide electrodes. *Nat. Mater.*, 12:827–835, 2013.
- [33] B. S. Yang, S. Park, S. Oh, Y. J. Kim, J. K. Jeong, C. S. Hwanga, and H. J. Kim. Improvement of the photo-bias stability of the Zn-Sn-O field effect transistors by an ozone treatment. *J. Mater. Chem.*, 22:10994–10998, 2012.
- [34] J. Zhang, D. Gao, G. Yang, J. Zhang, Z. Shi, Z. Zhang, Z. Zhu, and D. Xue. Synthesis and magnetic properties of Zr doped ZnO nanoparticles. *Nanoscale Res. Lett.*, 6(587):1–7, 2011.
- [35] S. Bang, S. Lee, Y. Ko, J. Park, S. Shin, H. Seo, and H. Jeon. Photocurrent detection of chemically tuned hierarchical ZnO nanostructures grown on seed layers formed by atomic layer deposition. *Nanoscale Res. Lett.*, 7(290):1–11, 2012.
- [36] N. S. Ramgir, I. S. Mulla, and V. K. Pillai. Micropencils and microhexagonal cones of ZnO. *J. Phys. Chem. B*, 110:3995–4001, 2006.
- [37] C. D Wagner, D. E Passoja, H. F Hillery, T. G. Kinisky, H. A. Six, W. T. Jansen, and J. A. Taylor. Auger and photoelectron line energy relationships in aluminum-oxygen and silicon-oxygen compounds. *J. Vac. Sci. Technol.*, 21(4):933–944, 1982.
- [38] D. C. Look. Recent advances in ZnO materials and devices. *Mat. Sci. Eng. B*, 80:383–387, 2001.
- [39] Ü. Özgür, Y. I. Alinov, C. Liu, A. Teke, M. A. Reshchikoc, S. Dogan, V. Avrutin, S. J. Cho, and H. Morkoç. A comprehensive review of ZnO materials and devices. *J. Appl. Phys.*, 98:041301, 2005.

- [40] S. J. Pearton, D. P. Norton, K. Ip, Y. W. Heo, and T. Steiner. Recent progress in processing and properties of ZnO. *Prog. Mater. Sci.*, 50:293–340, 2005.
- [41] F. A. S. Lima, I. F. Vasconcelos, and M. Lira-Cantu. Electrochemically synthesized mesoporous thin films of ZnO for highly efficient dye sensitized solar cells. *Ceram. Int.*, 2015. <http://dx.doi.org/10.1016/j.ceramint.2015.03.271>.
- [42] A. Hagfeldt, G. Boschloo, L. Sun, L. Kloo, and H. Pettersson. Dye-sensitized solar cells. *Chem. Rev.*, 110:6595–6663, 2010.

6. NATURAL DYES FOR DYE SENSITIZED SOLAR CELLS

In this work, natural dyes extracted from three plants found in northeastern Brazil, *Nerium oleander*, *Duranta repens*, and *Solanum melongena* (eggplant peel), were used as sensitizers for fabricating dye-sensitized solar cells (DSSCs). Different characterization methods were employed to analyze the adsorption of the dyes on titanium oxide (TiO_2) electrodes. The X-ray photoelectron spectroscopy (XPS) and ultraviolet (UV) photoelectron spectroscopy (UPS) analyses together with the optical properties of the films were the most useful analysis techniques. The photoelectrochemical performance of these dyes on DSSCs showed open circuit voltages (V_{oc}) between 0.50 V and 0.55 V, short-circuit photocurrent densities (J_{sc}) from 0.55 mA/cm^2 to 3.74 mA/cm^2 , and fill factors (FF) between 64.66% and 72.56%. The power conversion efficiency (PCE) of the DSSCs sensitized with *Nerium oleander* reached 1.33%. This work is the first study that evaluated the natural dye *Duranta repens* in DSSC, which showed a PCE of 0.74%. The cells prepared with *Solanum melongena* (eggplant peel) presented an efficiency of 0.20% with an average fill factor 71.88%.

6.1 Introduction

Since DSSCs were first reported [1], they have attracted significant attention as emerging photovoltaic technologies. The goal of DSSCs is to mimic photosynthesis by converting light energy into electricity. These cells are composed of a photosensitizer, a transparent conductive oxide (TCO) glass, a semiconductor oxide thin film, and a regenerating electrolyte [2]. Compared to conventional silicon-based solar cells, DSSCs have many advantages such as low-cost production, high power conversion, good efficiency under cloudy and artificial light conditions, semi-transparency, and multi-color range possibilities [3]. In recent years, the power conversion efficiency has been increased to more than 13% [4].

At present, ruthenium polypyridyl complexes (e.g., N719) are the most commonly used sensitizers despite the high cost production, scarcity of ruthenium, and rather meticulous synthesis process. On the other hand, the long-term application of a number of synthetic dyes has detrimental effects on the environment and are associated with allergic, toxic, carcinogenic, and otherwise harmful responses [5]. Thus, the development of new photosensitizers is essential for improved DSSCs.

Natural dyes are interesting light harvesters for DSSCs because they are abundant, biodegradable, and environmentally friendly. Natural photosensitizers in DSSCs have the potential to reach similar performances and stability as those obtained for dyes based on metal complexes. Moreover, natural photosensitizers do not need to rely on noble metal utilization and thus, have lower cost [6–9]. Over the last two decades, various dyes have been considered as suitable sensitizers, such as anthocyanin, flavanoids, carotenoids, and chlorophyll, among others [10–14]. Despite the advantages of natural dyes, the efficiency reached for DSSCs assembled with these dyes is still very low when compared with Ru-based dyes. Devices fabricated with red turnip dye are among the most efficient natural dye-based devices, showing efficiencies around 1.70% [15]. Ito et al. [16] reported that a conversion efficiency of 2.3% was obtained using *Monascus* yellow dye as a sensitizer. Moreover, chlorophyll has been employed as a sensitizer for DSSCs with an efficiency of 4.6% [17].

In this work, natural dyes were extracted from three plants found in Northeastern Brazil: *Nerium oleander*, *Duranta repens*, and *Solanum melongena* (eggplant peel). These dyes were used as sensitizers for fabricating DSSCs. The photoaction in these dyes is due to the presence of anthocyanin. The anthocyanins in *N. oleander* and *S. melongena* have been identified as Myricetin [18] and Nasunin [19], respectively. Moreover, *D. repens* has never been used in DSSCs, and scientific studies on this plant are still emerging. Nevertheless, Iqbal et al. [20] and Veitch and Grayer. [21] have been able to identify the presence of anthocyanins in *D. repens*.

In the sensitization of a wide bandgap semiconductor like TiO_2 , the anthocyanine molecule bonds with the oxide through the carbonyl and hydroxyl groups, improving elec-

tron transfer. While *N. oleander* and *S. melongena* were previously tested in DSSCs [19, 22], this is the first study evaluating the performance of *D. repens* in DSSCs.

6.2 Experimental procedure

6.2.1 Preparation of dye sensitizer solutions

Dyes were obtained from the petals of fresh *N. oleander* and *D. repens* flowers harvested in the Brazilian state of Ceará and from fresh eggplant peel (*S. melongena*) purchased at a local market. Prior to use, the eggplant peel was washed with distilled water and crushed. The flower petals and the crushed eggplant peel were weighed and macerated in solvent using a 1:4 (weight:volume) proportion. The solvent used was ethanol acidified with hydrochloric acid (pH = 2). The macerated materials were kept in the solvent for 24 h, protected from light and under refrigeration (5°C). After 24 h, the resulting dyes were filtered to remove solid fragments and stabilized. The dyes were used without any further purification.

6.2.2 Preparation of electrodes

The working electrodes were prepared on fluorine-doped SnO₂ (FTO) glasses with sheet resistance of 15 Ω/□. Prior to use, the FTO glass was cleaned in a five step process. Step 1 consisted of washing the glasses in a detergent solution under ultrasonic agitation for 10 min. Steps 2 and 3 consisted of twice washing the glasses in deionized water for 10 min under sonication. In step 4, the glasses were washed with ethanol in an ultrasonic bath for 10 min. Finally, in step 5, the electrodes were cleaned for 20 min in UV-surface decontamination system (Novascan, PSD-UV).

The cleaned FTO glasses were treated in a 40-mM TiCl₄ solution for 30 min at 70°C. Four layers of commercially available nanosized TiO₂ paste from Solaronix[®] were applied on top of the treated electrodes using a doctor's blade; each layer was 20 nm thick. A fifth layer of TiO₂ paste was applied with a thickness of 200 nm. Each layer was dried at 125°C for 6 min after deposition. The nanosized TiO₂ working electrodes were sintered under four different conditions: 5 min at 275°C; 5 min at 375°C; 15 min at 450°C; and 15 min

at 500°C. Platinized FTO counter electrodes were prepared by electron beam physical vapor deposition (EBPVD) with a Pt layer thickness of 50 nm.

6.2.3 DSSC assembly

The solar cells were assembled according to the following procedure. The photoanodes were immersed into the natural dye solutions at room temperature for 2 h in the *N. oleander* and *S. melongena* solutions, and for 8 h in the *D. repens* solution. The working and counter electrodes were held together with hot-melt sealing foil. The commercially available liquid iodide-triiodine electrolyte was introduced through a small hole on the Pt counter electrode by capillary forces under applied vacuum. Finally, the DSSCs were hermetically sealed with a small piece of glass, which closed the filling hole.

6.2.4 Characterization

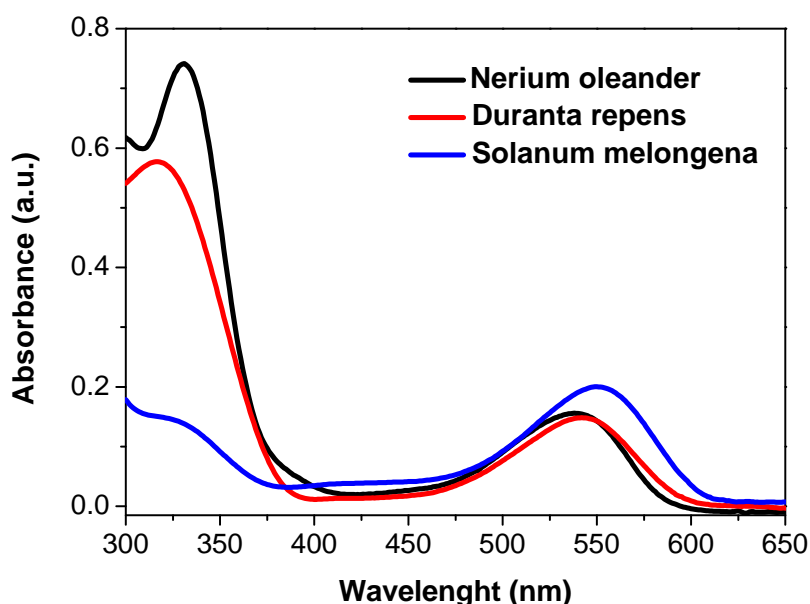
The natural dyes were characterized by means of UV-Vis, XPS, and UPS spectroscopy. The DSSCs were characterized using $J - V$ curves and incident photon-to-charge-carrier efficiency (IPCE) spectra. The absorption spectra of dye solutions were recorded using a UV-vis spectrophotometer (UV-Vis Hewlett-Packard® 8453 Diode-Array) in the 300–650 nm range. The XPS and UPS spectra were recorded using equipment from SPECS® with an energy analyzer (PHOIBOS® 150) using Al K α (1486.6 eV) as the X-ray source. All of the spectra were adjusted according to the value of the C 1s peak at (284.8 \pm 0.1 eV). The fitting was done using the CASA XPS application software. Photoelectrochemical tests were performed by measuring the $J - V$ characteristic curves under simulated AM 1.5 solar illumination at 100 mW/cm⁻² from a Steuernagel Solarkonstant KHS1200® sun simulator. The $J - V$ curves were measured using a Keithley® 2601 multimeter. The IPCE measurements were performed with a quantum efficiency measurement system from Oriel® at 10 nm intervals between 300 and 700 nm. The results were not corrected for intensity losses due to light absorption or due to reflection by the glass support. The cells were also characterized by impedance spectroscopy.

6.3 Results and discussion

6.3.1 Light absorption by natural dyes

The UV-Vis absorption spectra for the three natural dyes are shown in Fig. 6.1. The dyes extracted from *N. oleander*, *D. repens* and *S. melongena* in ethanol and HCl (pH = 2) displayed intense absorption in the 450–600 nm region with peaks at 537 nm, 535 nm, and 549 nm, respectively. These peaks are characteristic of anthocyanins. Anthocyanins generally have a maximum absorption in the visible range at 465–550 nm due to π - π^* charge transfer transitions from the highest occupied molecular orbital (HOMO) to the lowest unoccupied molecular orbital (LUMO). which results in a shift of the electronic charge density from the chromenium portion to the catechol end of the anthocyanin molecule [23–25].

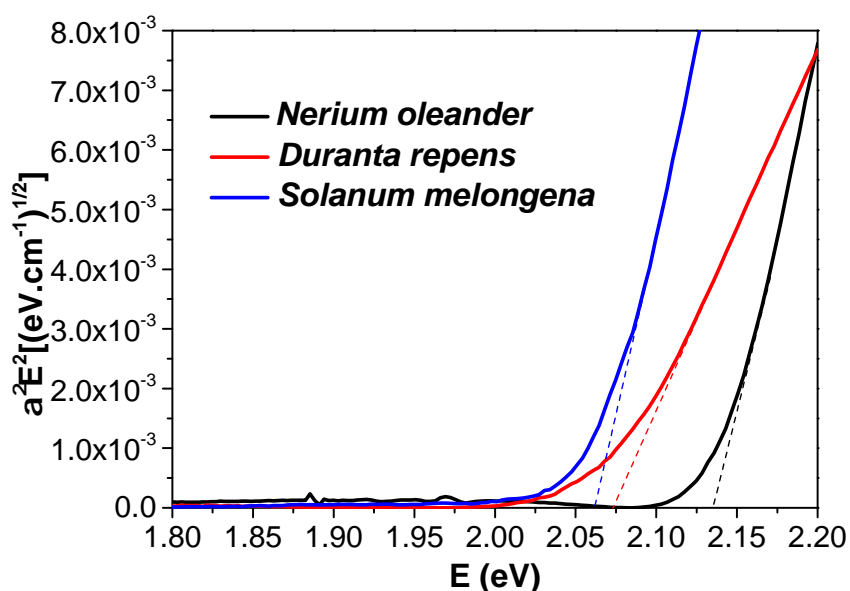
Figure 6.1: UV-Vis absorption spectra of the extracts from the three natural dyes used as sensitizers in DSSCs.



Source: Own author

Using Tauc's plot with the UV-Vis spectra, the optical bandgap can be determined for these natural dyes as shown in Fig. 6.2. According to this graph, the optical bandgaps for these natural dyes are very similar. The determined values are 2.12, 2.07, and 2.06 eV for *N. oleander*, *D. repens*, and *S. melongena*, respectively. The value of the optical bandgap is crucial for determining the band alignment between the natural dyes and the other components of the solar cell, such as the semiconductor working electrode and the regenerating electrolyte. Additional important features for the determination of the band alignment diagram can be obtained from the UPS spectrum.

Figure 6.2: Tauc's plot for the natural dyes used as sensitizers in DSSCs.



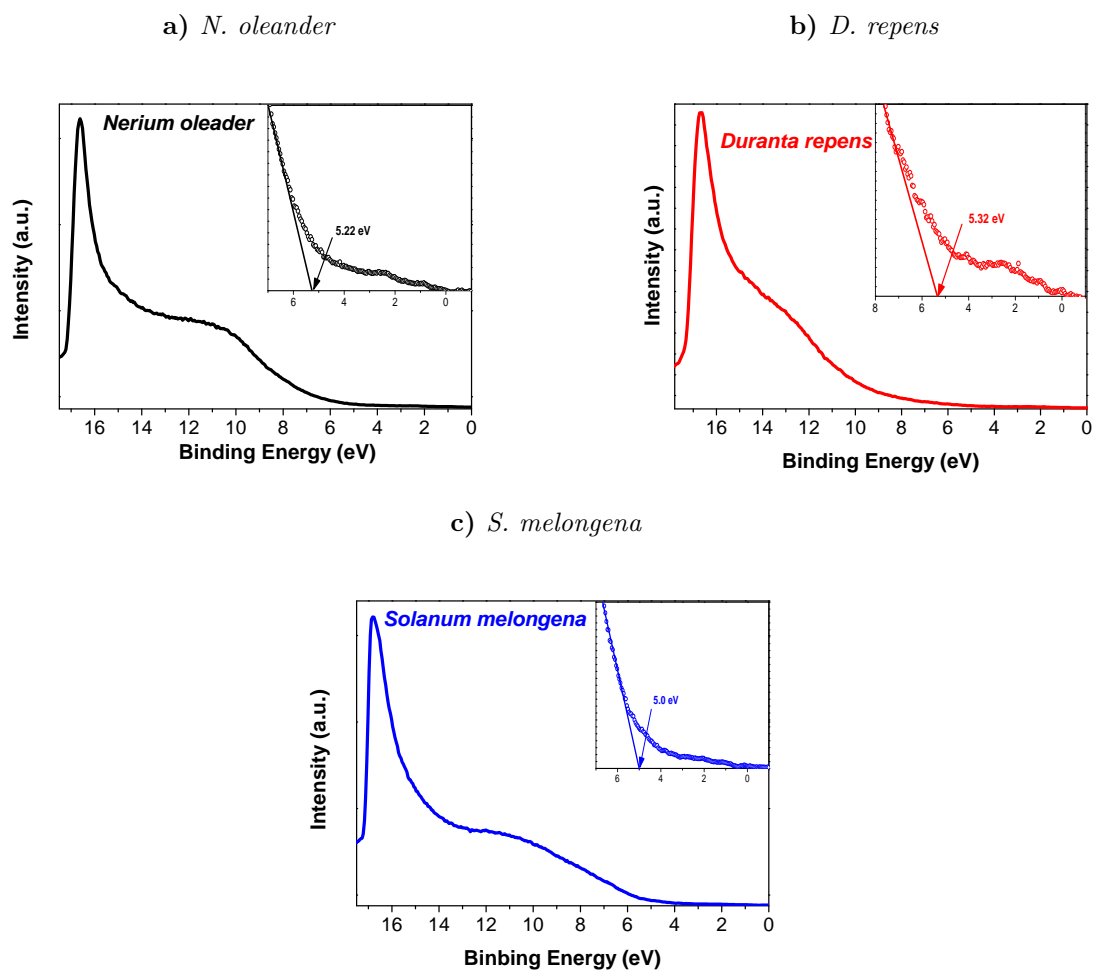
Source: Own author

6.3.2 Determination of the HOMO and LUMO levels of the natural dyes

Figure 6.3(a) shows the measured UPS spectrum of *N. oleander*. The HOMO energy level (vs. vacuum) of *N. oleander* is -5.22 eV, and the band gap is 2.12 eV, as estimated from the UV-Vis absorption spectrum shown in Fig. 6.2. From Fig. 6.3(b), the values of the HOMO level and band gap of *D. repens* are determined to be -4.32 eV and 2.07 eV,

respectively. In Fig. 6.3(c), the same procedure for *S. melongena* leads to values of -5.00 eV and 2.06 eV for the HOMO level and optical bandgap, respectively. According to the HOMO level and band gap values, the LUMO energy level (vs. vacuum) of *N. oleander*, *D. repens*, and *S. melongena* is -3.10 eV, -2.25 eV, and -2.94 eV, respectively.

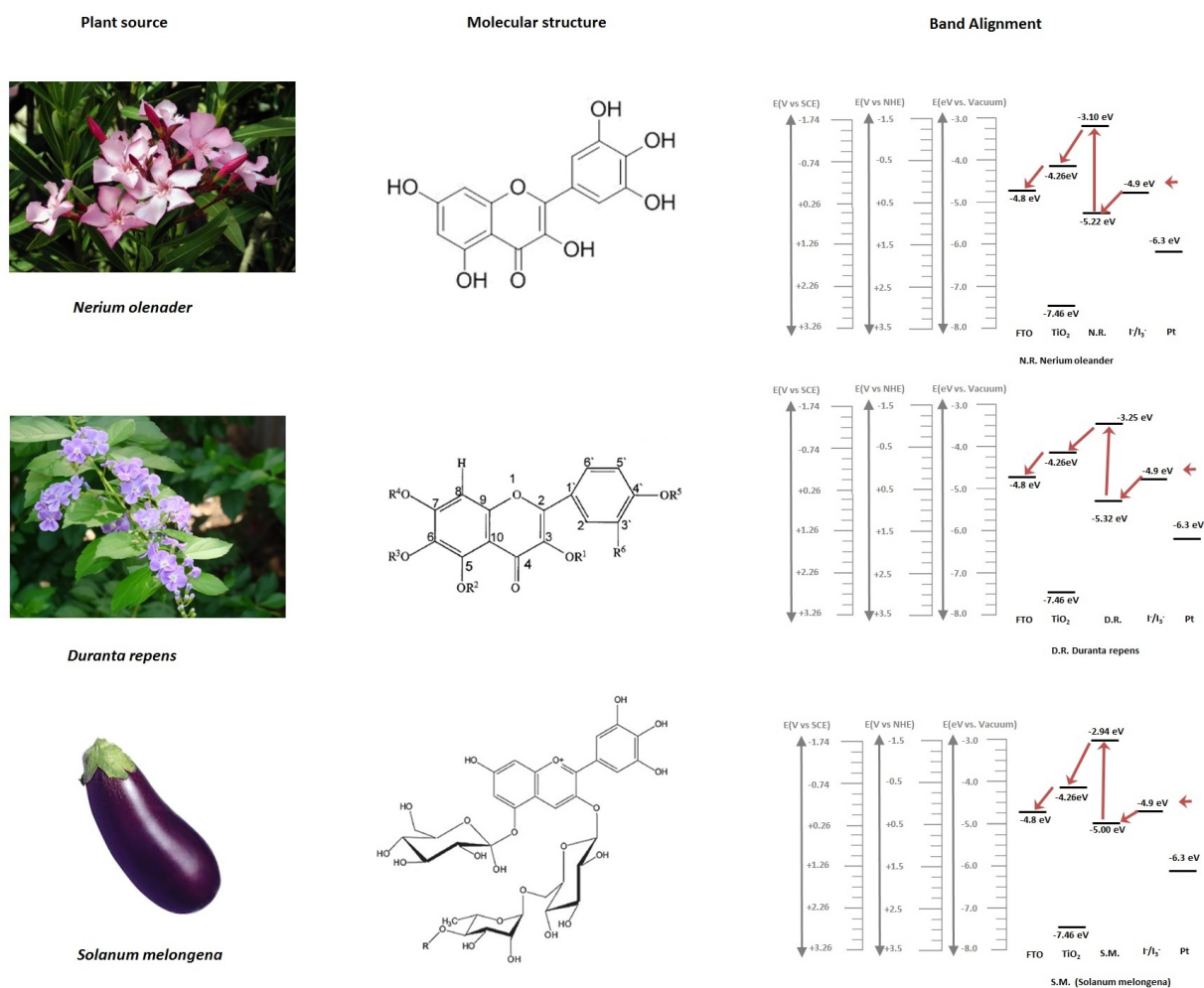
Figure 6.3: Valence band UPS spectra for the natural dyes used as sensitizers in DSSCs. The inset in each graph presents a detailed view of the HOMO level value.



6.3.3 Band diagram

Once the HOMO and LUMO values for each natural dye have been determined, the band alignment diagrams can be constructed. Figure 6.4 shows the band alignment diagrams for the three natural dyes. The three dyes meet the requirements necessary for use as sensitizers in DSSC. In fact, there are no significant differences between the three dyes with regard to the HOMO-LUMO levels and optical bandgap.

Figure 6.4: Band alignment diagrams for the natural dyes with those for other DSSC components.



Source: Rajendran [18], Calogero and Di Marco [19], Anis et al. [26].

6.3.4 Photovoltaic performance

The performance of natural dyes as sensitizers in DSSC was evaluated by open circuit voltage (V_{oc}), short-circuit current (J_{sc}), fill factor (FF), and PCE measurements. The photovoltaic parameters of the DSSCs sensitized with these natural dyes are listed in Table 6.1. The $J - V$ curves for the best performing DSSCs are depicted in Fig. 6.5.

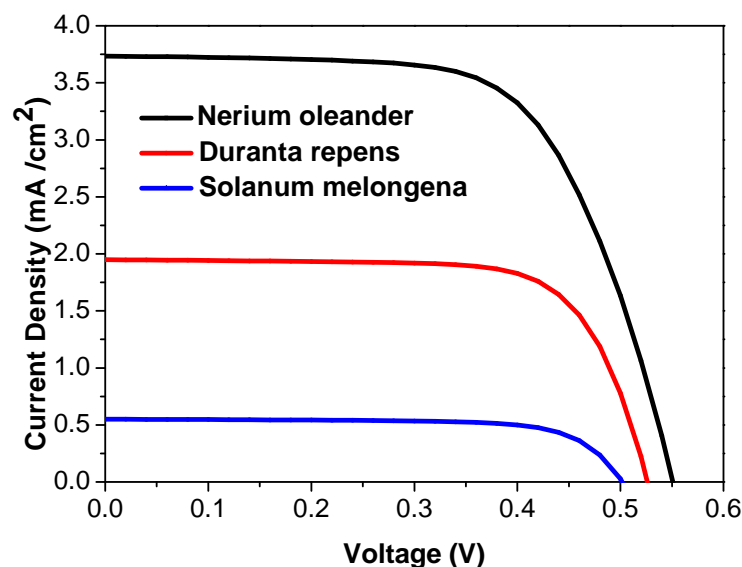
As shown in Table 6.1, the fill factors of these DSSCs are always higher than 64%. The open circuit voltages (V_{oc}) vary from 0.50 V to 0.55 V, short-circuit photocurrent densities (J_{sc}) vary from 0.55 mA/cm⁻² to 3.74 mA/cm⁻², and fill factors (FF) vary between 64.66% and 72.56%. The PCE of the DSSCs sensitized with *N. oleander* reached 1.33%, which is more than two times higher than that for a previously reported device [22, 27, 28]. This study is the first to evaluate the natural dye *D. repens* as a sensitizer, and the PCE value of 0.74% makes it a promising natural sensitizer [27, 28]. The cells prepared with *S. melongena* (eggplant peel) present an efficiency of 0.20% with an average fill factor 71.88%. The efficiency obtained for *S. melongena* is lower than that reported previously [19]. The higher efficiency of *N. oleander* is due to the improved interaction between the dye and the TiO₂ surface, which could facilitate better electron injection for producing a large current density, as shown in Fig. 6.5 and Table 6.1. However, a large injection recombination rate results in a larger dark current, which can reduce the fill factor. This process can be clearly observed in Table 6.1, where the fill factor for *N. oleander* is 64.66% while that for the other natural dyes is higher at 72%.

Table 6.1: Photovoltaic parameters.

Dye	DLT (h)	J_{sc} (mA/cm ²)	V_{oc} (V)	FF (%)	PCE (%)
<i>N. oleander</i>	2	3.74	0.55	64.66	1.33
<i>D. repens</i>	8	1.95	0.53	72.07	0.74
<i>S. melongena</i>	2	0.55	0.50	72.56	0.20

Source: Own author.

Figure 6.5: $J - V$ curves for the DSSCs sensitized with the three natural dyes.



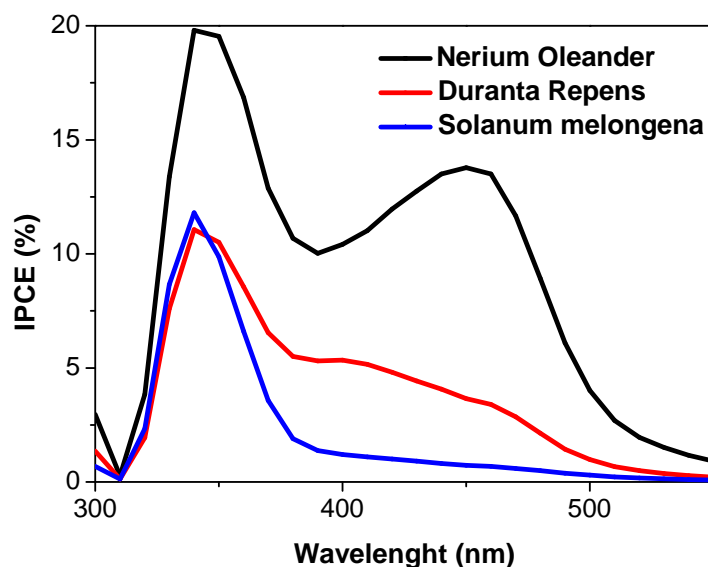
Source: Own author.

Figure 6.6 shows the IPCE curves obtained for the DSSCs using natural dyes as sensitizers. These results are in good agreement with the results presented by Fig. 6.5 and Table 6.1. *N. oleander*, which presents the largest J_{sc} value, also presents the higher IPCE value. The spectrum for this dye shows well-defined peaks around 340 nm and 460 nm. The peak at 340 nm is more intense than the corresponding peak for the other dyes used in this study. The IPCE spectrum for *D. repens* presents only one peak around 340 nm, which has a wide shoulder from 380 to 480 nm. Finally, the IPCE spectrum for *S. melongena* contains only the peak at 340 nm, which has an intensity similar to that for *D. repens*. The absence of the peak at 460 nm for *D. repens* and *S. melongena* is evidence of poor dye adhesion to TiO_2 . Moreover, because *S. melongena* does not have a wide shoulder on the 340 nm peak, its interaction with TiO_2 is poorer than that of *D. repens*.

6.4 Conclusions

In summary, natural dyes from northeast Brazil were extracted using a simple and inexpensive method and were successfully applied as sensitizers for DSSCs. The characterization of these dyes revealed that the absorption is compatible with the optical

Figure 6.6: IPCE spectra for the DSSCs sensitized with the three natural dyes.



Source: Own author.

bandgap and HOMO-LUMO levels of anthocyanins. Moreover, these dyes are suitable for use with the TiO_2 working electrode and I^-/I_3^- redox mediator electrolyte. The dye *N. oleander* presents better performance than the other considered dyes, possibly due to its better interaction with the TiO_2 working electrode.

6.5 References

- [1] B. O'Regan and M. Grätzel. A low-cost, high-efficiency solar cell based on dye-sensitized colloidal TiO_2 films. *Nature*, 353:737–740, 1991.
- [2] A. Hagfeldt, G. Boschloo, L. Sun, L. Kloo, and H. Pettersson. Dye-sensitized solar cells. *Chem. Rev.*, 110:6595–6663, 2010.
- [3] L. M. Gonçalves, V. de Zea Bermudez, H. A. Ribeiro, and A. M. Mendes. Dye-sensitized solar cells: A safe bet for the future. *Energ. Environ. Sci.*, 1:655–667, 2008.
- [4] S. Mathew, A. Yella, P. Gao, R. Humphry-Baker, B. F.E.Curchod, N. Ashari-Astani, I. Tavernelli, U. Rothlisberger, M. K. Nazeeruddin, and M. Grätzel. Dye-sensitized

- solar cells with 13% efficiency achieved through the molecular engineering of porphyrin sensitizers. *Nature Chemistry*, 6:242–247, 2014.
- [5] S. Mohammad, Shahid ul Islam, and F. Mohammad. Recent advancements in natural dye applications: a review. *J. Clean. Prod.*, 53:310–331, 2013.
- [6] M. M. Noora, M. H. Buraidah, M. A. Careem, S. R. Majid, and A. K. Arof. An optimized poly(vinylidene fluoride-hexafluoropropylene)-nai gel polymer electrolyte and its application in natural dye sensitized solar cells. *Electrochimica Acta*, 121:159–167, 2014.
- [7] A. Lim, N. HajiManaf, K. Tennakoon, R. L. N. Chandrakanthi, L. B. L. Lim, J. M. R. S. Bandara, and P. Ekanayake. Higher performance of dssc with dyes from *cladophora* sp. as mixed cosensitizer through synergistic effect. *J. Biophys*, 2015:510467, 2015.
- [8] K. Park, T. Kim, S. Han, H. Ko, S. Lee, Y. Song, J. Kim, and J. Lee. Light harvesting over a wide range of wavelength using natural dyes of gardenia and cochineal for dye-sensitized solar cells. *Spectrochimica Acta Part A: Molecular and Biomolecular Spectroscopy*, 128:868–873, 2014.
- [9] A. Lim, N. T. R. N. Kumara, A. L. Tan, A. H. Mirza, R. L. N. Chandrakanthi, M. Petra, L. C. Ming, G. K. R. Senadeera, and P. Ekanayake. Potential natural sensitizers extracted from the skin of *canarium odontophyllum* fruits for dye-sensitized solar cells. *Spectrochim. Acta Mol. Biomol. Spectrosc.*, 138:596–602, 2015.
- [10] C. Sandquist and J. L. McHale. Improved efficiency of betanin-based dye-sensitized solar cells. *J. Photochem. Photobiol. A*, 221:90–97, 2011.
- [11] D. Zhang, N. Yamamoto, T. Yoshida, and H. Minoura. Natural dye sensitized solar cells. *Mater. Res. Soc. Jpn.*, 27:811–814, 2002.
- [12] K. Wongcharee, V. Meeyoo, and S. Chavadej. Dye-sensitized solar cell using natural dyes extracted from rosella and blue pea flowers. *Sol. Energy Mater. Sol. Cells*, 91:566–571, 2007.

- [13] K. Wattananate, C. Thanachayanont, and N. Tonanon. Orac and vis spectroscopy as a guideline for unmodified red-purple natural dyes selection in dye-sensitized solar cells. *Solar Energy*, 107:38–43, 2014.
- [14] D. Sengupta, B. Mondal, and K. Mukherjee. Visible light absorption and photosensitizing properties of spinach leaves and beetroot extracted natural dyes. *Spectrochim. Acta Mol. Biomol. Spectrosc.*, 148:85–92, 2015.
- [15] G. Calogero, G. Di Marco, S. Cazzanti, S. Caramori, R. Argazzi, A. Di Carlo, and C. A. Bignozzi. Efficient dye-sensitized solar cells using red turnip and turnip and purple wild sicilian prickly pear fruits. *Int. J. Mol. Sci.*, 11:254–267, 2010.
- [16] S. Ito, T. Saitou, H. Imahori, H. Ueharad, and N. Hasegawa. Fabrication of dye-sensitized solar cells using natural dye for food pigment: Monascus yellow. *Energy Environ. Sci.*, 3:905–909, 2010.
- [17] X. F. Wang, C. H. Zhan, T. Maoka, Y. Wada, and Y. Koyama. Fabrication of dye-sensitized solar cells using chlorophylls c1 and c2 and their oxidized forms c'_1 source and view the c'_2 source from *undaria pinnatifida* (wakame). *Chem. Phys. Lett.*, 447:79–85, 2007.
- [18] A. Rajendran. Isolation, characterization, pharmacological and corrosion inhibition studies of flavonoids obtained from nerium oleander and tecoma stans. *Int. J. PharmTech. Res.*, 3(2):1005–1013, 2011.
- [19] G. Calogero and G. Di Marco. Red sicilian orange and purple eggplant fruits as natural sensitizers for dye-sensitized solar cells. *Sol. Energ. Mat. Sol. C.*, 101:1341–1346, 2008.
- [20] K. Iqbal, A. Malik, N. Mukhtar, I. Anis, S. N. Khan, and M. I. Choudhary. a-glucosidase inhibitory constituents from *duranta repens*. *Chem. Pharm. Bull.*, 52:785–789, 2004.
- [21] N. C. Veitch and R. J. Grayer. Flavonoids and their glycosides, including anthocyanins. *Nat. Prod. Rep.*, 25:555–611, 2008.

- [22] J. M. R. C. Fernando and G. K. R. Senadeera. Natural anthocyanins photosensitizers for dye-sensitized solar devices. *Curr. Sci.*, 95:663–666, 2008.
- [23] N. J. Cherepy, G. P. Smestad, M. Gratzel, and J. Z. Zhang. Ultrafast electron injection: implications for a photoelectrochemical cell utilizing an anthocyanin dye-sensitized TiO₂ nanocrystalline electrode. *J. Phys. Chem. B*, 101:9342–9351, 1997.
- [24] G. Calogero, G. Di Marco, S. Caramori, S. Cazzanti, R. Argazzi, and C. A. Bignozzi. Natural dye sensitzers for photoelectrochemical cells. *Energy Environ. Sci.*, 2:1162–1172, 2009.
- [25] H. Chang and Y.-J. Lo. Pomegranate leaves and mulberry fruits as natural sensitizers for dye-sensitized solar cells. *Sol. Energy*, 84(10):1833–1837, 2010.
- [26] I. Anis, E. Anis, S. Ahmed, G. Mustafa, A. Malik, Z. Amtul, and A. Rahman. Thrombin inhibitory constituents from *duranta repens*. *Helvetica Chimica Acta*, 84: 649–655, 2001.
- [27] M. R. Narayan. Review: Dye sensitized solar cells based on natural photosensitizers. *Renew. Sust. Energ. Rev.*, 16:208–215, 2012.
- [28] N. A. Ludin, A. M. A. Mahmoud, A. B. Mohamad, A. A. H. Kadhum, K. Sopian, and N. S. A. Karim. Review on the developement of natural dye photosensitizer for dye-sensitized solar cells. *Renew. Sust. Energ. Rev.*, 31:386–396, 2014.

7. VANADIUM PENTOXIDES FOR ITO-FREE PLASTIC ORGANIC SOLAR CELLS

In this chapter, the application of V_2O_5 in organic solar cells is discussed. Here, V_2O_5 was fabricated on a flexible indium tin oxide (ITO)-free substrate and applied in single junction devices with inverted and normal architectures and as part of the recombination layer in polymer tandem solar cells. The results for V_2O_5 were compared with those for poly(3,4-ethylenedioxythiophene):poly(styrenesulfonate) (PEDOT:PSS) in reference devices. Both water-based V_2O_5 and V_2O_5 synthesized from vanadium (V) oxitriisopropoxide (ViPr) were investigated. The best single junction device reached a power conversion efficiency (PCE) of 1.71% and the best tandem device reached a PCE of 1.11%.

7.1 Introduction

In the last decade, organic optoelectronic devices have been attracting growing scientific interest due to their multiple advantages such as high flexibility, easy processing, low fabrication cost, and large area fabrication. These unique advantages make organic optoelectronic devices highly promising candidates for organic solar cells [1–6], organic memory devices [7–9], organic thin-film transistors [10–12], organic light-emitting diodes [13–15], organic photodetectors [16–18], and organic sensors [19, 20], among others. Solution-processed bulk-heterojunction (BHJ) solar cells have also gained serious attention during the last few years as future photovoltaic technologies for low-cost power production. Organic photovoltaics (OPVs) are, potentially low-cost, printable devices that show promise as next-generation renewable energy sources. Nevertheless, OPV commercialization is only feasible through printing technologies such as slot-die coating, gravure coating, knife-over-edge coating, off-set coating, spray coating, inkjet printing, pad printing, and screen

printing [21]. With lower OPV costs, ITO, which is commonly used as a transparent electrode, is one of the primary expenses in current photovoltaic devices [22, 23]. As an alternative to ITO, combinations of highly conductive PEDOT:PSS (HC-P) with metals grids have been extensively investigated [24, 25]. Though PEDOT:PSS is the most common hole transport layer in OPV, a significant disadvantage of PEDOT:PSS is its hygroscopic nature, which has been a stability limiting factor for devices based on PEDOT:PSS [26]. Thus, replacing PEDOT:PSS with a humidity stable alternative could improve the stability of printable OPVs. Among these alternatives, V_2O_5 has been extensively investigated [27, 28]. In this work, water-based V_2O_5 has been used as the hole transport layer in single inverted and normal configuration ITO-free OPVs and as part of the recombination layer of tandem ITO-free OPVs.

7.2 Experimental

Single junction devices: Both inverted and normal architectures were considered. The active, electron transport, and hole transport layers were slot-die coated using a lab-roll coater, and the silver grid on the back electrode was printed through the use of a small flexographic printing roll.

Tandem devices: All layers were compressed between Flextrode[®]. The back electrode was slot-die coated using the same preparation as that used for single junction devices.

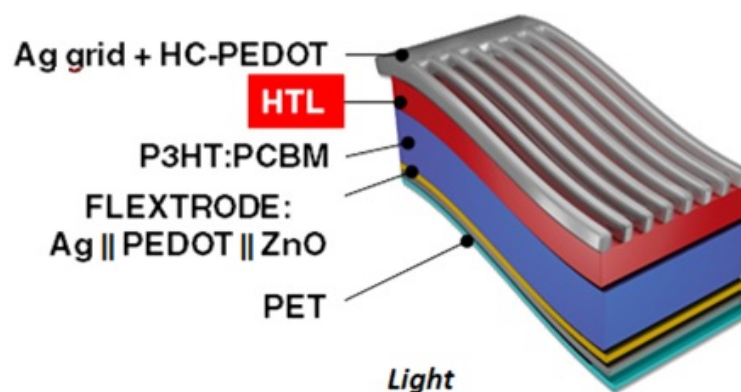
The use of a roll coater enabled control of the coating as well as the temperature, adapting perfectly to the slot-die head and to the flexographic printing roll.

7.2.1 Materials

Single junction devices (inverted architecture): The coating was performed on Flextrode[®]. The coating comprises a highly conductive metal grid, semi-transparent conductor, and hole blocking layer. The active layer for the single junction device was composed of poly(3-hexylthiophene-2,5-diyl) (P3HT; electronic grade from Rieke[®]) and methanofullerene phenyl-C61-butyric acid methyl ester (60PCBM; technical grade from

Solenne BV[®]). Water-based V_2O_5 and PEDOT:PSS (Clevios SV3 from Heraeus[®]) comprised the hole transport layer (HTL). The V_2O_5 was diluted with isopropyl alcohol in the ratio 1:2 (w/w), and the PEDOT:PSS was diluted to a viscosity of 300 mPa s. Furthermore, highly conductive PEDOT:PSS (Clevios PH1000 from Heraeus[®]) was used to improve the contact between the HTL and the back electrode. This HC-P was diluted with isopropyl alcohol in the ratio 10:3 (w/w), its sheet resistivity was $60 \Omega/\square$. The back silver grid was printed using a screen-printing silver paste (PV410 from Dupont[®]). The structure of the ITO-Free flexible OPV is shown in Fig. 7.1, illustrating the stacking of the layers comprising the solar cell. Specifically, the first layer is Flextrode[®], followed by the active layer, HTL, and finally the back electrode. In some cases, the back electrode was composed of highly conductive PEDOT and silver ink; in other cases, only the silver ink was used on top of the HTL.

Figure 7.1: Structure of the ITO-Free flexible OPV.



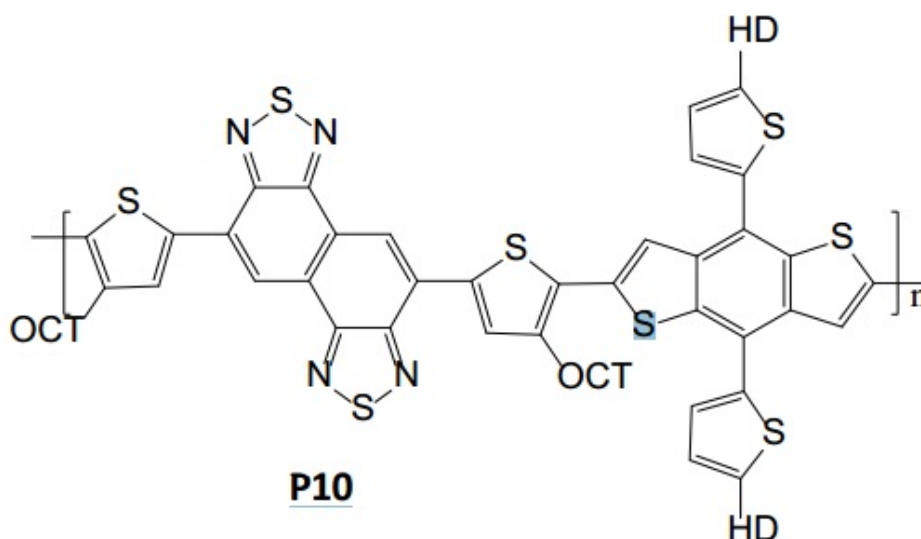
Source: Own author.

Single junction devices (normal architecture): Two different plastic electrodes were considered. The first electrode was a highly conductive metal grid and semi-transparent conductor, which was formed on top of the poly(ethylene terephthalate) (PET) (SN1). The second electrode consisted of PET with a highly conductive silver

nanowire layer (SN2). Both electrodes were provided by Dr. Frederik Krebs of the Department of Energy Conversion and Storage, Technical University of Denmark. For this geometry, the first slot-die-coated layer was HTL, which was composed of V_2O_5 diluted with isopropyl alcohol in the ratio 1:2 (w/w). The active layer was the same as that from the inverted architecture, and the electron transport layer (ETL) was composed of ZnO nanoparticles in acetone with a concentration of 49 mg/ml. The back silver grid was printed using a screen-printing silver paste (PV410 from Dupont[®]).

Tandem devices: For the tandem devices, the first active layer was composed of P3HT:60PCMB using the same synthesis as that for single junction devices. The low bandgap (LBG) poly(2,7-carbazolenevinylene) (P10) polymer shown in Fig. 7.2 was used in the second active layer, which was composed of P10:PCBM. In the interlayer, ZnO nanoparticles in acetone with a concentration of 49 mg/ml were employed. Water-based V_2O_5 and PEDOT:PSS (Clevios SV3 from Heraeus[®]) were used as HTL similarly to that used for the single junction devices.

Figure 7.2: Structure of the LBG polymer P10 which was used as an active material for the second active layer.

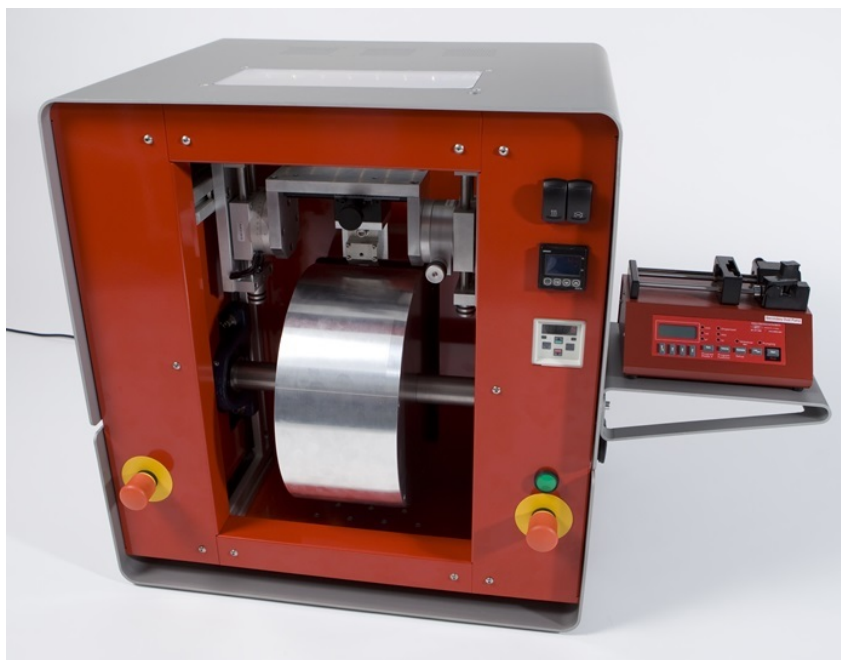


Source: Own author.

7.2.2 Coating procedure

All coatings were performed using a homemade mini-roll coater shown in Fig. 7.3 developed by Dr. Krebs' group.

Figure 7.3: Mini-roll coater used to fabricate ITO-free OSCs and TPSCs.



Source: Department of Energy Conversion and Storage, Technical University of Denmark.

Single junction devices (inverted architecture): Flextrode[®] was mounted on the roller using heat-stable tape (3M). The coating procedure began with slot-die coating of the active layer, which consisted of P3HT:PCBM (1:1 by weight) dissolved in chlorobenzene (40 mg/ml) with an additional 10% chloroform and 3% chloronaphthalene. The solution flow was set to 0.1 ml/min, and the web was set to 1.3 m/min. The temperature was held at 70°C. For the reference device, the back PEDOT:PSS layer was slot-die coated on the active layer. The coating was conducted at 80°C with a web speed of 0.5 m/min. The V₂O₅ layer was slot-die coated on the active layer at 90°C with a web speed of 1.0 m/min. The flow of the solution was varied to give different thicknesses; the

applied flows were 0.20 ml/min, 0.15 ml/min, and 0.10 ml/min, resulting in the theoretical dry thickness of 80, 60, and 40 nm, respectively. The highly conductive PEDOT:PSS was slot-die coated on top of the HTL at 70°C with a web speed of 0.4 m/min. The back silver electrode was applied by flexographic printing of heat-curing silver paste PV410 (Dupont®). The silver paste was added to the flexographic roll and further transferred to the substrate with a web speed of 1.2 m/min and roll temperature of 80°C.

Single junction devices (normal architecture): The electrode (SN1 or SN2) was mounted on the roller using heat-stable tape (3M). The coating procedure began with slot-die coating of the V₂O₅ layer at 90°C with different web speeds and applied flows to optimize the thickness of the layers. The active layer, which was the same as that used for the inverted architecture, was slot-die coated. Then, the ZnO electron transport layer was slot-die coated at a web speed of 0.8 ml/min and dried at a temperature of 70°C. The silver paste was added to the flexographic roll and further transferred to the substrate with a web speed of 1.2 m/min and roll temperature of 80°C.

Tandem devices: The layers were slot-die coated exactly in the same way. The interlayer was composed of V₂O₅ and ZnO. These two layers were slot-die coated as follows. The V₂O₅ layer was slot-die coated on the active layer at 90°C with a web speed of 1.0 m/min with an applied flow of 0.10 ml/min. The ZnO layer was slot-die coated at a web speed of 0.8 ml/min and dried at a temperature of 70°C to ensure an insoluble ZnO film. The second active layer consisting of P10:PCBM (2:3 by weight), dissolved in chlorobenzene with an addition of 2% chloronaphthalene, was slot-die coated following the same parameters for the other active layers. The highly conductive PEDOT:PSS was slot-die coated on top of the HTL at 70°C with a web speed of 0.4 m/min. The back silver electrode was applied by flexographic printing of heat-curing silver paste PV410 (Dupont®). For the reference device, PEDOT:PSS was slot-die coated between the V₂O₅ and ZnO using the same conditions as those for the reference single junction device.

7.3 Application of water-based V_2O_5 in flexible ITO-free OPVs

Water-based V_2O_5 was applied as the HTL in printable, flexible ITO-free OPVs, and it was applied as part of the recombination layer in tandem OPVs. The results obtained with water-based V_2O_5 were compared with reference solar cells assembled with the PEDOT:PSS-based HTL as well as with the ViPr-based V_2O_5 HTL. First, the investigation assessed how the performance of solar cells is affected by the variation in the thickness of the V_2O_5 layer. These tests indicate that the PCE improves when the thickness of the layer decreases, as shown in Fig. 7.4. The theoretical thickness of thin films deposited by the slot-die technique can be calculated as follows:

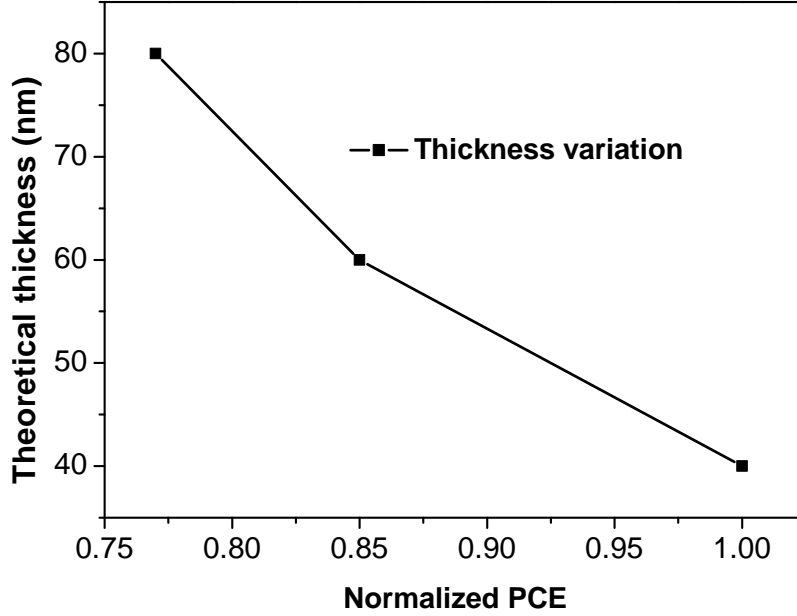
$$d = \frac{d}{v \cdot w} \cdot \frac{c}{\rho}, \quad (7.1)$$

where f is the flow rate [cm^3/min]; v is the coating speed [cm/min]; w is coating width [cm]; c is the concentration of the solids in the ink [g/cm^3], and ρ is the density of material in the final film [g/cm^3]. According to Fig. 7.4, the PCE for organic solar cells tends to increase with decreasing V_2O_5 thickness, and the optimum theoretical thickness was found to be around 40 nm.

7.3.1 Comparison between V_2O_5 and PEDOT:PSS as HTL for ITO-free plastic OPVs

Next, various solar cells were fabricated using V_2O_5 as the HTL. To provide a reference for the performance of V_2O_5 , a number of solar cells were fabricated with PEDOT:PSS as the HTL. The comparison of the photovoltaic parameters for solar cells developed with V_2O_5 or PEDOT:PSS HTLs is shown in Table 7.1. The data reveal that solar cells assembled with V_2O_5 present, on average, better performance than those assembled with PEDOT:PSS. Considering only the best performing samples, the V_2O_5 -based device is more efficient. On average, there is no appreciable difference between the open circuit voltage V_{oc} or fill factor FF . The difference in these parameters is on the order of 3%. On the other hand, the difference in the short circuit current J_{sc} is much more pronounced,

Figure 7.4: Relationship between the theoretical thickness of the V_2O_5 layer and the normalized PCE.



Source: Own author.

being approximately 16% higher for cells with V_2O_5 when compared with the reference (PEDOT:PSS) devices. Consequently, J_{sc} is the primary factor leading to the better performance of the V_2O_5 -based device.

Table 7.1: Photovoltaic parameters for ITO-free OSCs: PEDOT:PSS or V_2O_5 as HTL.

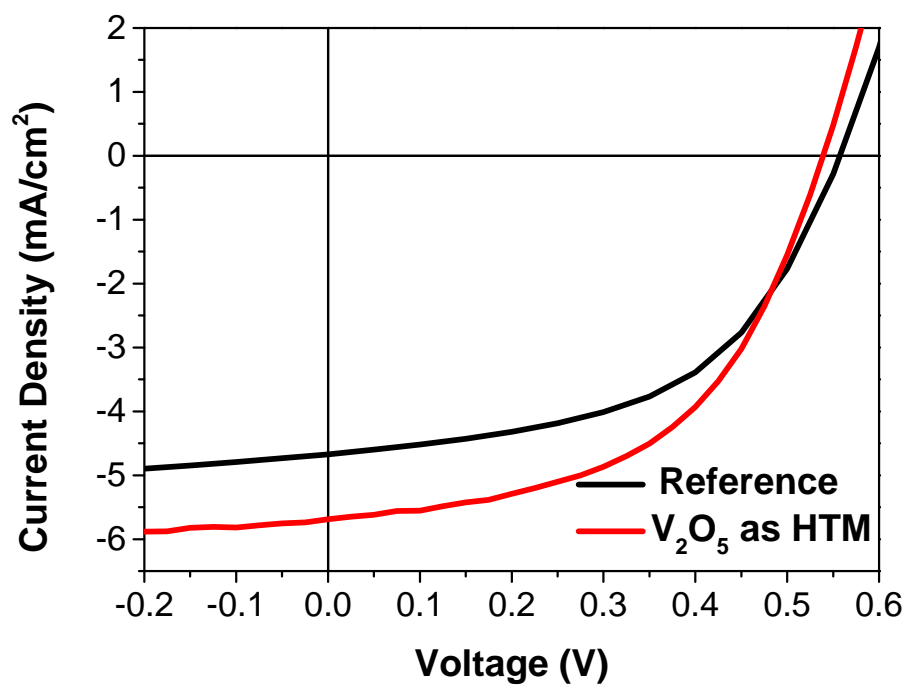
HTL		J_{sc} (mA/cm ²)	V_{oc} (V)	FF (%)	η (%)
PEDOT:PSS	avg	4.48±0.22	0.56±0.01	51.29±0.66	1.27±0.07
	max	4.67	0.56	52.27	1.36
V_2O_5	avg	5.18±0.40	0.54±0.01	53.29±1.61	1.49±0.07
	max	5.69	0.54	51.98	1.59

Source: Own author

The voltage vs. current $J - V$ curves for both devices are shown in Fig. 7.5, where it is possible to graphically compare the two devices. The main factor causing difference

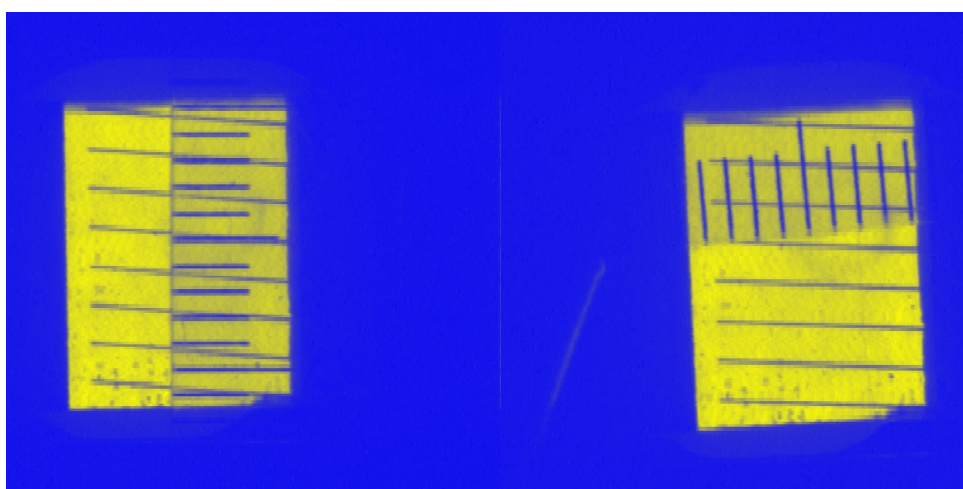
in performance for these solar cells is J_{sc} . The best solar cell based on V_2O_5 was then measured using another solar simulator because such equipment provides a better spectral mismatch factor and allows temperature control, leading to a more accurate measurement. In addition to the use of this more accurate solar simulator, the active area for this solar cell was determined using light-beam induced-current (LBIC) images. In LBIC microscopy [29], a focused beam of light is scanned over the active area of the organic solar cell while simultaneously recording the photoelectric response I_{sc} . The resulting map of the LBIC is a two-dimensional (2D) image showing the relative degree of current within the probed area. The LBIC images used to calculate the active area for this device are shown in Fig. 7.6. Using this more accurate system, characterization of the best solar cell based on V_2O_5 shows an increase of the PCE. The PCE measured in the standard solar simulator was 1.59%, while the measured PCE was 1.71% in the more accurate system. Figure 7.7 shows the $J - V$ curve and the incident photon-to-charge-current efficiency (IPCE) spectrum for the best solar cell based on V_2O_5 , measured with the more accurate system.

Figure 7.5: Comparison between PEDOT:PSS and V_2O_5 as HTL in inverted devices.



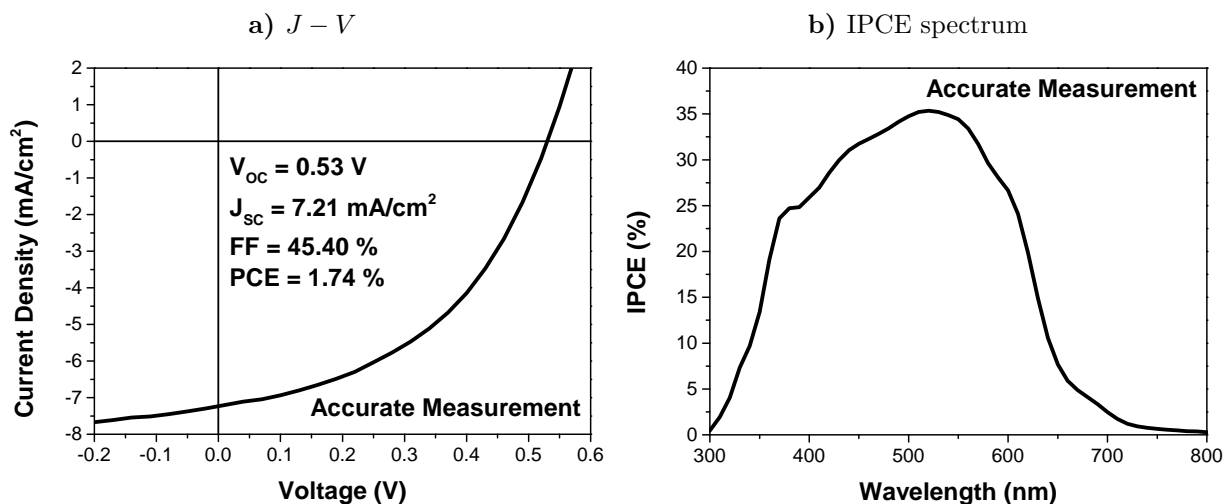
Source: Own author

Figure 7.6: The LBIC images for the best OSCs with V_2O_5 as the HTL in inverted device.



Source: Own author

Figure 7.7: $J - V$ curve measured on the accurate solar simulator, and the IPCE spectrum for the best inverted OSC with V_2O_5 as the HTL.

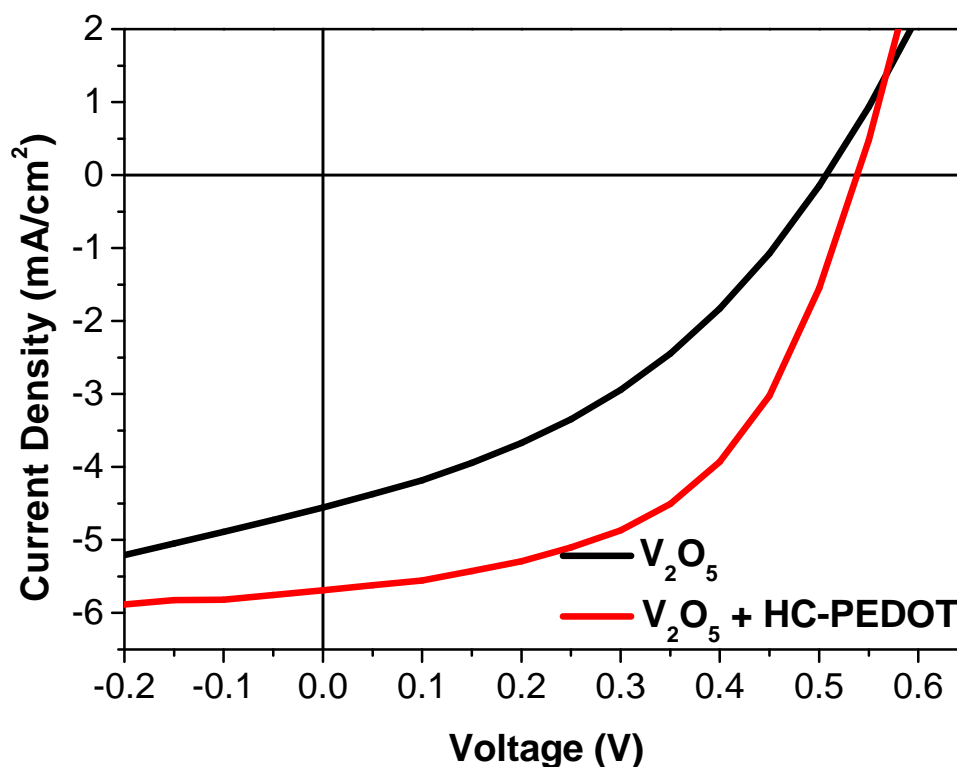


Source: Own author

7.3.2 Comparison between water-based V_2O_5 and $ViPr$ -based V_2O_5 as the HTL for ITO-free plastic OPVs

As mentioned before, two kinds of back electrodes were considered: one composed of a layer of HC-P and silver ink and another composed of only silver ink, which was printed directly on top of the V_2O_5 layer. The presence of HC-P improved the performance of the solar cells by improving all of the photovoltaic parameters, as can be seen in the $J - V$ curves shown in Fig. 7.8. Specifically, HC-P is used to improve the electrical contact between V_2O_5 and the silver ink because the conductivity of V_2O_5 is low in comparison. Nevertheless, solar cells fabricated without HC-P reached 55% of the efficiency of those fabricated with HC-P. Optimizing the conductive properties of the V_2O_5 buffer layer could suppress the use of HC-P at the back electrode. Specifically, eliminating HC-P could contribute to the improved stability of the solar cells because the hygroscopic nature of PEDOT is problematic for the stability of such devices [30–34].

Figure 7.8: Effect of the use of highly conductive PEDOT:PSS as part of the back electrode.



Source: Own author

Table 7.2 summarizes the parameters for OSCs assembled with water-based V_2O_5 , with and without HC-P. The data reveal that no significant voltage drop occurs when HC-P is removed, which indicates that a suitable energy level alignment is preserved. The decrease in J_{sc} and FF is on the order of 20%, which could be caused by the undesirable values of the series resistance R_s and shunt resistance R_{sh} .

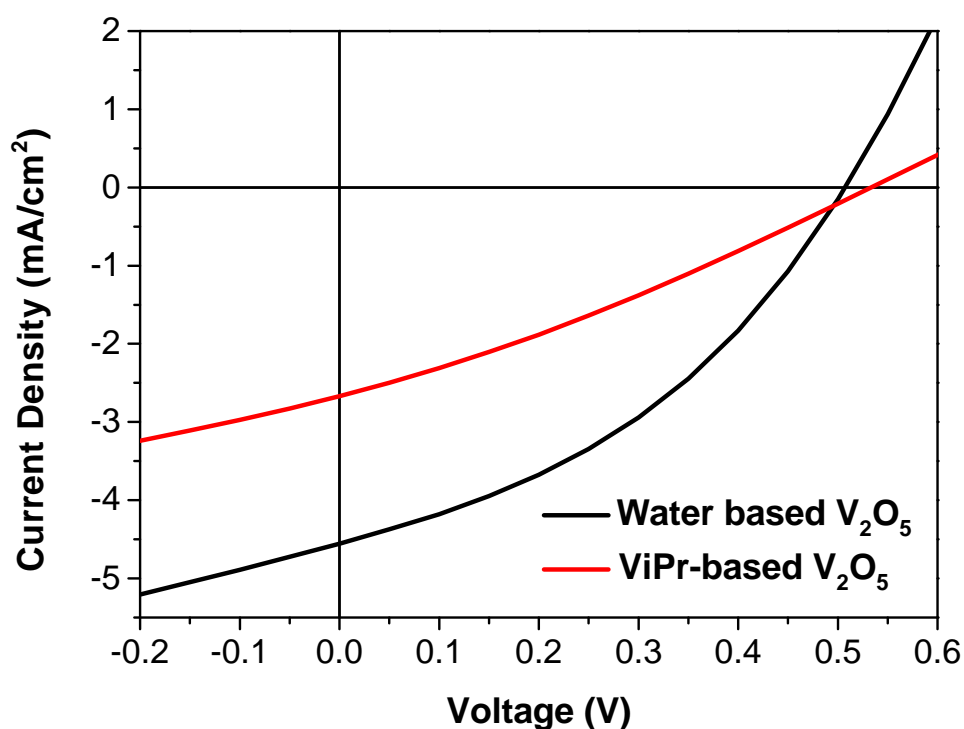
Table 7.2: Comparison of the photovoltaic parameters for OSCs with and without highly conductive PEDOT on the back electrode.

HC-PEDOT	J_{sc} (mA/cm ²)	V_{oc} (V)	FF (%)	PCE (%)
with	5.69	0.54	51.98	1.59
without	4.55	0.51	40.82	0.88

Source: Own author

After identification the effects of removing HC-P from the back electrode, the two different types of V_2O_5 were compared for the HTL. The first sample was synthesized using vanadium(V) oxytriisopropoxide [35–37], which is a compound known for its high toxicity, reactivity, and cost; the other sample was fabricated using water-based V_2O_5 synthesis[27, 38], which is much more environmental friendly, inexpensive, and free from organic residues. In Fig. 7.9, the two V_2O_5 samples used in this study are compared. In addition to the advantages highlighted above, the use of water-based V_2O_5 in this study leads to much better performing solar cells.

Figure 7.9: Comparison between water-based V_2O_5 and ViPr-based V_2O_5 as HTL.

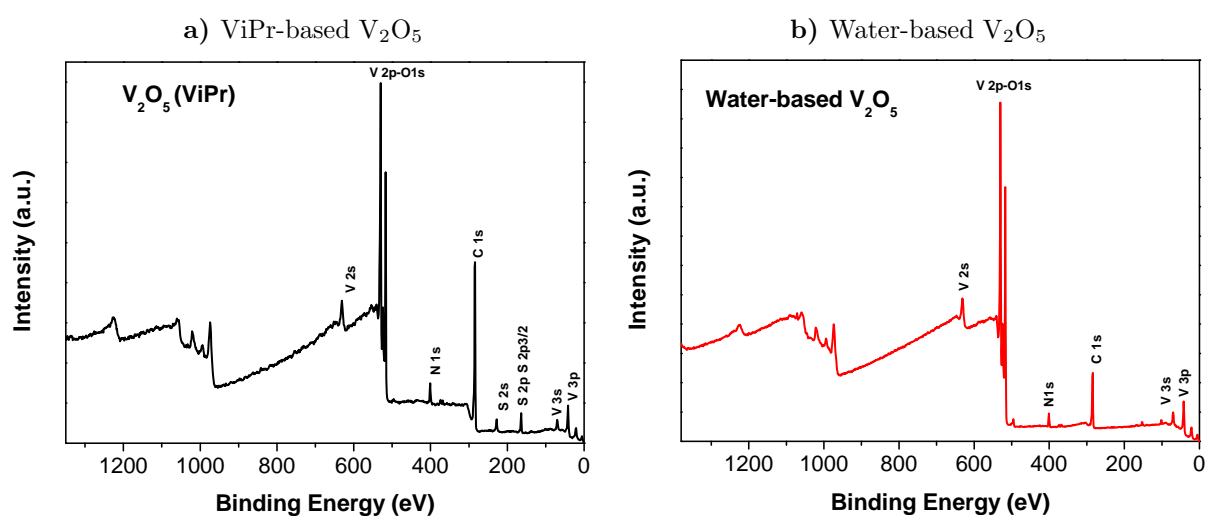


Source: Own author

To understand the differences in performance for the solar cells with two different V_2O_5 samples, the thin films were characterized using X-ray photoelectron spectroscopy (XPS) and ultraviolet (UV) photoelectron spectroscopy (UPS). Figure 7.10 shows the XPS spectra (overview) for the two V_2O_5 samples. Specifically, XPS shows that both

films contain vanadium, oxygen, carbon, and nitrogen, while only the ViPr-based V_2O_5 sample contains sulphur. The XPS spectra were obtained from real solar cells, where the V_2O_5 is deposited on top of the polymers. The presence of sulphur is an indication that the XPS spectra included results from the polymer under V_2O_5 because P3HT contains sulphur. As the theoretical thickness for this thin film ranges from 40 to 120 nm, the X-Ray source does not provide enough energy to eject an electron under the V_2O_5 . If sulphur is observed in the spectrum, the V_2O_5 layer must not cover the entire polymer layer, and the X-Ray beam reaches zones where there is no V_2O_5 on top of the polymer, causing the appearance of the sulphur signal from P3HT. In the spectrum from the water-based V_2O_5 , there is an absence of the S peak, which means that only V_2O_5 is being measured. To be more precise, additional peaks due to carbon and nitrogen could be observed, which could be ascribed to contamination at the surface. Because the XPS technique is very surface sensitive, it is difficult to avoid contamination. The peak ascribed to carbon in the ViPr-based V_2O_5 sample is more intense than the V 2p-O 1s peak from water-based V_2O_5 . This high, relative intensity indicates a higher C content, which could be attributed to organic residue remaining from synthesis of ViPr-based V_2O_5 .

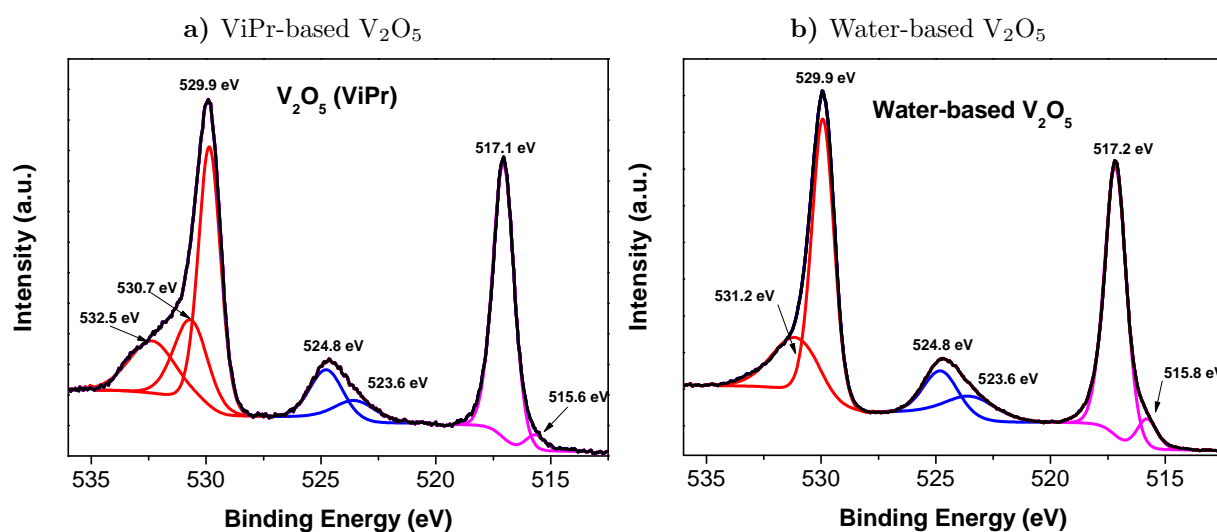
Figure 7.10: XPS survey for V_2O_5 thin films.



Source: Own author

The results of V $2p$ core-level XPS spectrum as well as those for the O $1s$ spectrum are shown in Fig. 7.11. The spectra for the two V_2O_5 samples present only slight differences. Both spectra present the doublet spectral lines of V $2p$, which are observed at the binding energy around 517 eV (V $2p\ 3/2$) and around 524 eV (V $2p\ 1/2$) with a spin-orbit splitting of 5 eV. These results coincide with those for V^{5+} in V_2O_5 [39–41]. The peak at 529.9 eV corresponds to O $1s$ core-level and is due to O^{-2} ions. The V $2p\ 3/2$ peak can be de-convoluted into two different peaks. For both spectra, there is a small shoulder centered around 516 eV. This peak can be attributed to V^{4+} , which is commonly observed in the hydrated form of V_2O_5 [42] as well as in reduced films [43]. The O $1s$ core-level can also be de-convoluted into two peaks for water-based V_2O_5 and three peaks for ViPr-based V_2O_5 .

Figure 7.11: High-resolution XPS spectra of the V $2p$ and O $1s$ core-levels.



Source: Own author

In the case of water-based V_2O_5 , in addition to the characteristic peak due to O^{-2} at 529.9 eV, there is another weak peak centered at 531.2 eV, which is associated with hydroxidic oxygen that was expected for hydrated V_2O_5 . On the other hand, in the ViPr-based V_2O_5 , the peak was de-convoluted into peaks at 529.9 eV (characteristic peak of

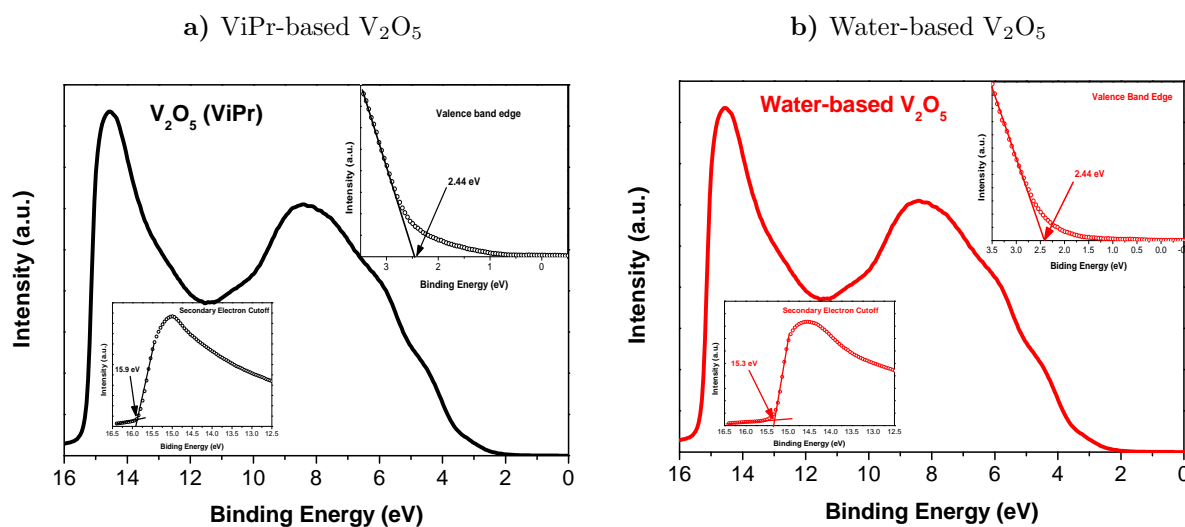
V₂O₅), 530.7 eV, and 532.5 eV, which are usually ascribed to nonstoichiometric near-surface oxygen and oxygen atoms in carbonate ions, respectively. The presence of this peak together with observed residual carbon in the XPS survey indicate the presence of organic residues on the ViPr-based V₂O₅ thin film. Binding energy (BE) values of the main peaks and their assignment are detailed in Table 7.3.

Table 7.3: Binding energy values (in eV) of the main peaks in the XPS spectra of V₂O₅.

Peak	ViPr-based V ₂ O ₅ (mA/cm ²)	water-based V ₂ O ₅	assignment
V 2 <i>p</i> 3/2	515.6	515.8	V ⁴⁺
V 2 <i>p</i> 3/2	517.1	517.2	V ⁵⁺
V 2 <i>p</i> 1/2	524.8	524.8	V ⁵⁺
O 1 <i>s</i>	529.9	529.9	O ²⁻
O 1 <i>s</i>	530.7	531.2	H ₂ O
O 1 <i>s</i>	532.5		Organic C-O

Source: Own author

The full He I (21.22 eV) scan of the UPS analyses is depicted in Fig. 7.12, and the insets show the detail of the valence band edge and the secondary electron cutoff. The work function can be determined by the difference between $h\nu$ and the energy due to the secondary electron cutoff. Thus, the work function for ViPr-based V₂O₅ is determined to be 5.3 eV while that for water-based V₂O₅ is 5.9 eV. The valence band edge with respect to the Fermi level for both types of V₂O₅ is the same at 2.44 eV. The ionization energy is then 7.76 eV for ViPr-based V₂O₅ and 8.3 eV for water-based V₂O₅.

Figure 7.12: Valence band UPS spectra V_2O_5 .

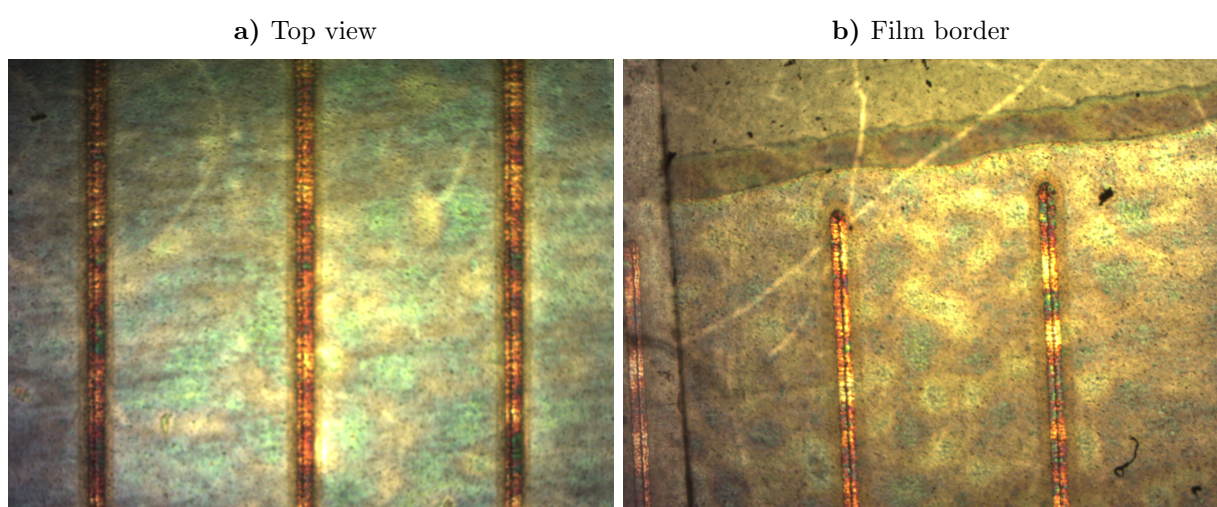
Source: Own author

7.3.3 Application of V_2O_5 as HTL in normal configuration, ITO-free flexible OPVs

Water-based V_2O_5 has also been considered in devices with normal configuration. However, a significant amount of effort is required because all of the technology for Flextrade[®] was developed for the inverted configuration. In this study, the first attempt utilized some of the technology for the inverted configuration devices. The front electrode for the inverted configuration is composed of PET/Ag metal grid/highly conductive PEDOT/ZnO. For the front electrode, the structure was precisely the same for the Flextrade[®], replacing ZnO with V_2O_5 . Water-based V_2O_5 is readily deposited on top of the highly conductive PEDOT, and the films have good quality, as shown in Fig. 7.13. From the top view, the film clearly covers the whole substrate, and there is no discontinuity or aggregation observed in this image. In Fig. 7.13(b), the well-defined border can be observed. Nevertheless, even though the films seem to have good quality, the obtained results show that many things must be tailored in this electrode for it to be suitable for normal configuration OSCs. As before, the results for V_2O_5 are always compared with the results for PEDOT:PSS under the same assembly conditions, as shown in Fig. 7.14.

Table 7.4 summarizes the photovoltaic parameters for the two devices. The OSCs based on V_2O_5 show better performance than those fabricated with PEDOT:PSS, having better J_{sc} , V_{oc} , FF , and PCE. The solar cell with V_2O_5 has PCE of 0.12% while that with PEDOT has PCE of 0.08%. Neither value is close to 1.71%, which is the best result obtained for the inverted configuration with V_2O_5 as the HTL.

Figure 7.13: Optical microscopy images for V_2O_5 applied in the normal OSC configuration.



Source: Own author

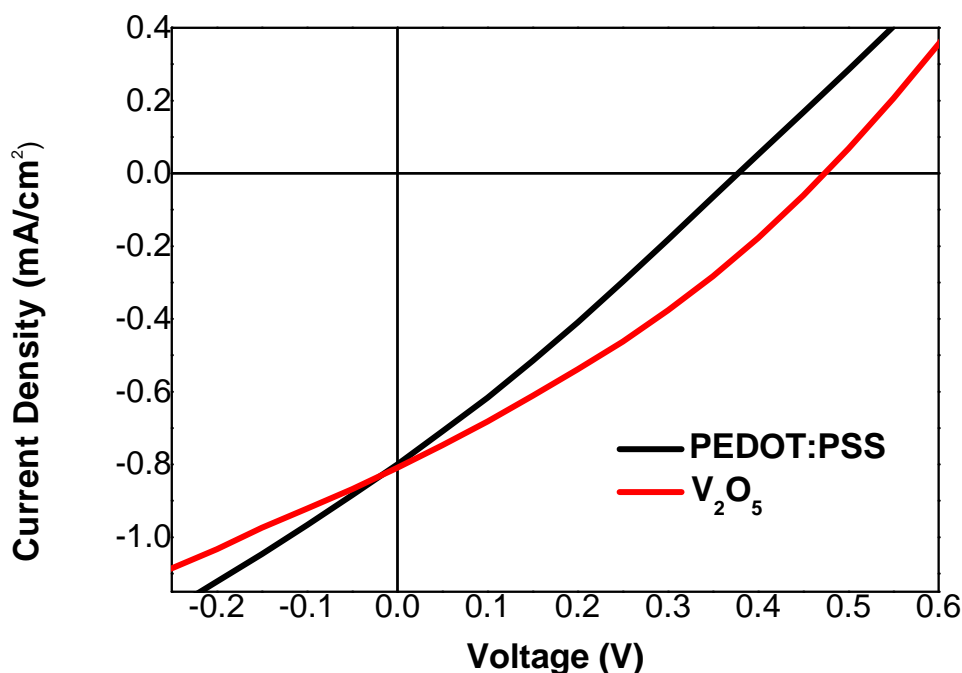
Table 7.4: Comparison of the photovoltaic parameters for normal configuration OSCs with PEDOT:PSS or V_2O_5 as HTL.

HTL	J_{sc} (mA/cm ²)	V_{oc} (V)	FF (%)	PCE (%)
PEDOT:PSS	0.80	0.38	27.18	0.08
V_2O_5	0.81	0.47	30.26	0.12

Source: Own author

To improve the performance of the normal configuration devices, the second approach

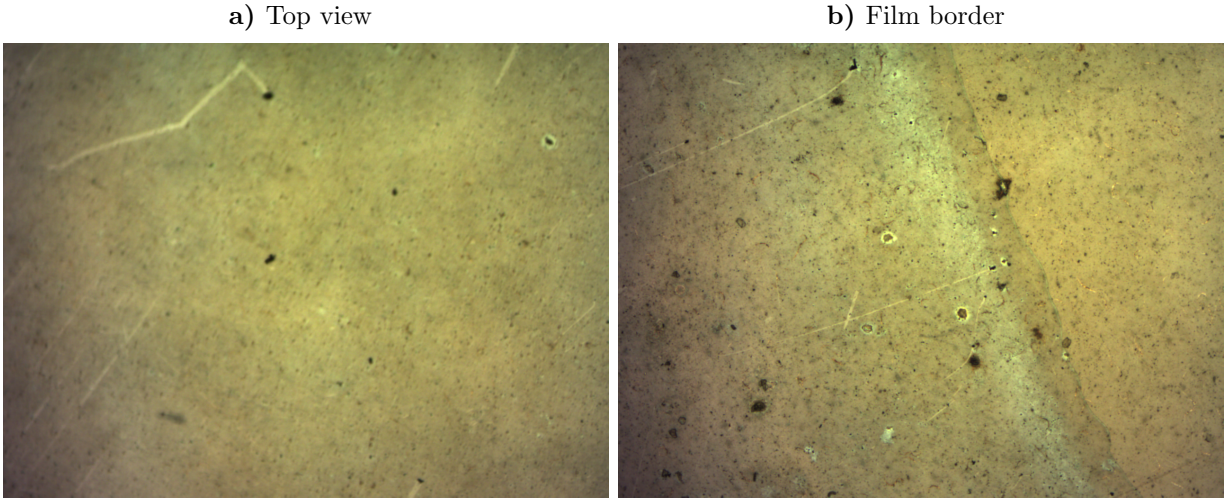
Figure 7.14: Comparison between water-based V_2O_5 and PEDOT:PSS in normal configuration OSCs.



Source: Own author

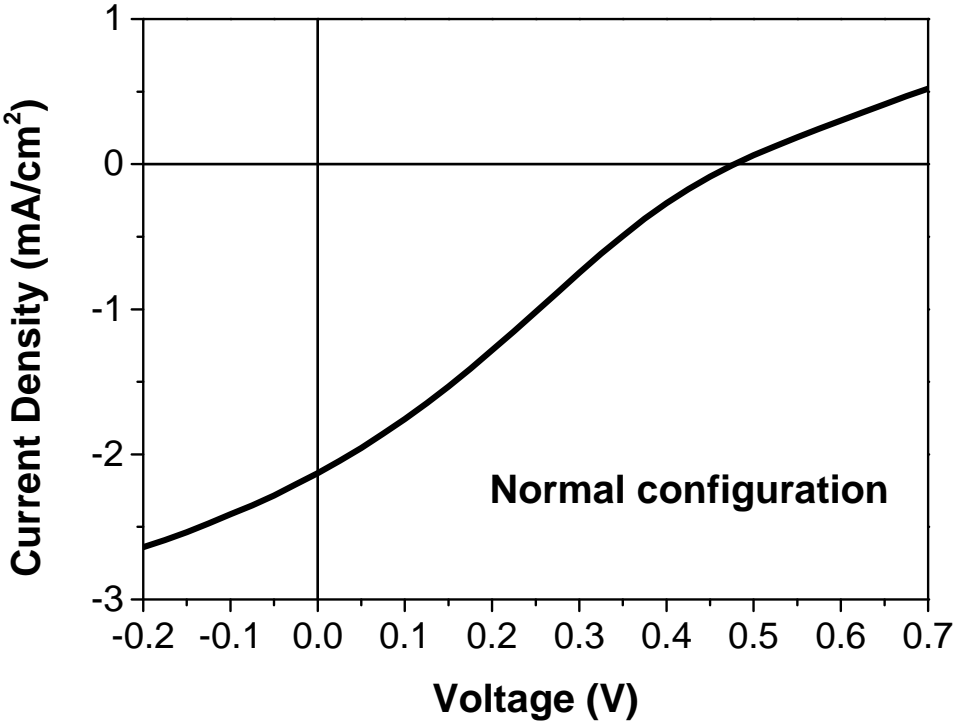
replaced the Flextrode[®] from the inverted configurations device with another structure. In this new structure, a PET substrate covered with silver nanowires was used as front electrode. As before, the V_2O_5 thin films were well coated with the substrate. Figure 7.15 shows the optical microscopy images for V_2O_5 on top of the silver nanowires, showing that V_2O_5 is well deposited on top of the silver nanowires. In this approach, J_{sc} increased considerably, and this increment is the main factor that leads to better performing solar cells. The $J - V$ curve for the best device is shown in Fig. 7.16. For this device, the short circuit current J_{sc} is 2.13 mA/cm^2 , and the open circuit voltage V_{oc} is 0.48 V . A discrete S shape can be observed in the curve close to the V_{oc} value, decreasing the FF , which is very low at 25.52% . Even with this S-shaped curve and very low FF , the PCE for this device based on silver nanowires is remarkably high when compared with others using HC-P and the silver grid. For the device considered in Fig. 7.16, PCE is 0.26% , which is more than twice that for the best OSCs assembled with the adapted Flextrode[®].

Figure 7.15: Optical microscopy images for V_2O_5 applied in normal configuration OSCs on top of silver nanowires.



Source: Own author

Figure 7.16: $J - V$ curve for the best performing normal configuration OSC.



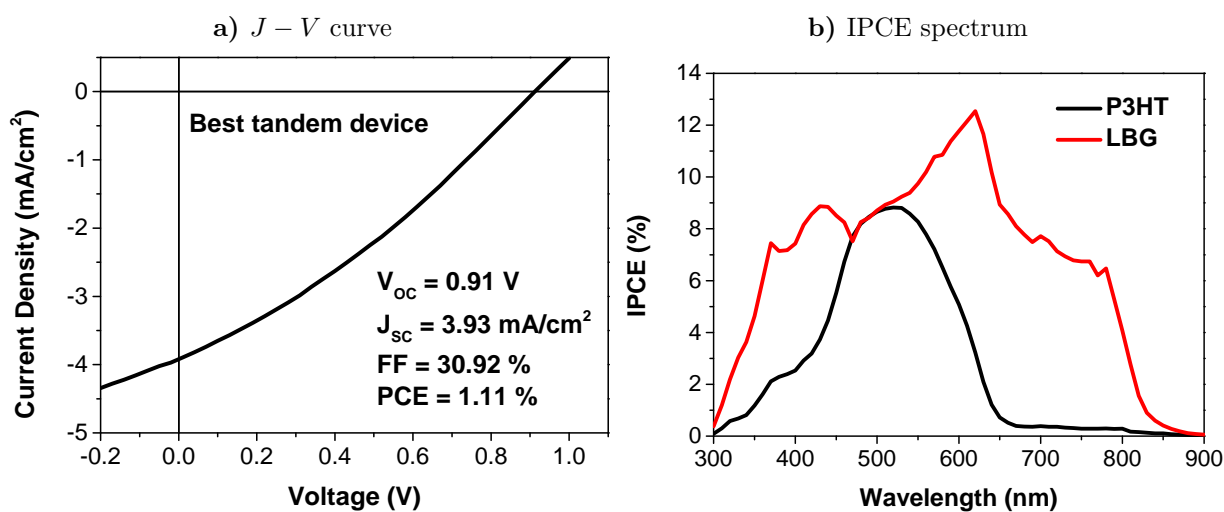
Source: Own author

7.3.4 Application of V_2O_5 as part of the recombination layer in tandem OPVs

In recent years tandem polymer solar cells (TPSCs) have attracted much attention, leading to very impressive efficiency records [44–48]. However, these efficiencies have only been achieved on solar cells with small areas using rigid glass substrates, which require slow and energy-intensive fabrication steps. Few studies have attempted roll-to-roll (R2R) processed TPSCs. Li et al. [49] succeeded in fabricating a TPSCs with 5.56% efficiency on a flexible plastic substrate using R2R compatible coating; however, the device utilized a pre-fabricated transparent ITO front electrode and an evaporated back electrode of MoOx and silver. Larsen-Olsen et al. [35] successfully demonstrated TPSCs fabricated by R2R slot-die coating. However, the efficiencies were limited, and these devices also used pre-fabricated ITO electrodes. The first all-printed and coated TPSCs were reported recently by Andersen et al. [50], presenting a roll-coated TPSC consisting of 12 layers.

The most widely used recombination layer consists of PEDOT:PSS as HTL and ZnO as ETL. Chou et al. [51] demonstrated TPSCs with efficiencies up to 5.1% could be fabricated using metal oxides instead of PEDOT:PSS. In this study, flexible, ITO-free TPSCs have been fabricated using V_2O_5 instead of PEDOT:PSS. All layers were deposited by coating techniques. A transparent V_2O_5 thin film functions as a hole transport and collecting layer for the first cell and acts as a stable foundation, enabling the fabrication of the second cell in the tandem cell architecture. The structure of these devices was composed of two subcells. The first active layer consisted of P3HT:PCBM, and the second active layer consisted of the LBG P10 polymer (see Fig. 7.2). The two subcells were linked by a recombination layer composed of V_2O_5 and ZnO to enable stacking the two inverted configuration OSCs in the TPSC. Figure 7.17 illustrates the $J - V$ curve and IPCE spectrum for the best tandem device. The tandem architecture for these devices, as well as the coating procedures were exactly the same as those used by [50], changing only the HTL to V_2O_5 . The $J - V$ curve and IPCE spectrum demonstrate that was possible to assemble TPSCs with V_2O_5 as part of the recombination layer, reaching PCE up to 1.11%, which is close to the 1.33% for the optimized TPSCs obtained with PEDOT:PSS [50].

Figure 7.17: $J - V$ curve and IPCE spectrum for a TPSC using V_2O_5 as part of the recombination layer.



Source: Own author

7.4 Conclusions

In summary, V_2O_5 was successfully applied in ITO-free OSCs and TPSCs. In single junction devices, the OSCs fabricated with water-based V_2O_5 show better performance than devices fabricated with PEDOT:PSS as HTL. A comparison between the two different preparations of V_2O_5 for HTL reveals that water-based V_2O_5 leads to more efficient devices than ViPr-based V_2O_5 . Water-based V_2O_5 was also considered as the HTL in normal configuration devices, and OSCs based on V_2O_5 outperformed the reference devices with PEDOT:PSS. Water-based V_2O_5 were also used as part of the recombination layer in TPSCs, demonstrating PCE as high as 1.11%. Finally, flexible OSCs have been assembled at ICN2 reaching efficiencies that approach the efficiencies reached by the rigid glass-based, spin coated devices.

7.5 References

- [1] C. W. Tang. Two-layer organic photovoltaic cell. *Appl. Phys. Lett.*, 48:183–185, 1986.
- [2] S. E. Shaheen, C. J. Brabec, and N. S. Sariciftci. 2.5% efficient organic plastic solar cells. *Appl. Phys. Lett.*, 78:841–843, 2001.

- [3] G. Li, V. Shrotriya, J. Huang, Y. Yao, T. Moriarty, K. Emery, and Y. Yang. High-efficiency solution processable polymer photovoltaic cells by self-organization of polymer blends. *Nature Materials*, 4:864 – 868, 2005.
- [4] B. Roth, A. E. Rudenko, and B. C. Thompson F. C. Krebs. Photochemical stability of random poly(3-hexylthiophene-co-3-cyanothiophene) and its use in roll coated ITO-free organic photovoltaics. *J. Photon. Energy*, 5(057205):1–9, 2015.
- [5] S. Holliday, R. S. Ashraf, C. B. Nielsen, M. Kirkus, J. A. Röhr, C. Tan, E. Collado-Fregoso, A. Knall, J. R. Durrant, J. Nelson, and I. McCulloch. A rhodanine flanked nonfullerene acceptor for solution-processed organic photovoltaics. *J. Am. Chem. Soc.*, 137:898–904, 2015.
- [6] Y. Jiang, C. Cabanetos, M. Allain, P. Liua, and J. Roncali. Manipulation of the band gap and efficiency of a minimalist push-pull molecular donor for organic solar cells. *J. Mater. Chem. C*, 3:5145–5151, 2015.
- [7] C. W. Chu, J. Ouyang, J. Tseng, and Y. Yang. Organic donor-acceptor system exhibiting electrical bistability for use in memory devices. *Adv. Mater.*, 17:1440–1443, 2005.
- [8] B. C. Das, B. Szeto, D. D. James, Y. Wu, and R. L. McCreery. Ion transport and switching speed in redox-gated 3-terminal organic memory devices. *J. Electrochem. Soc.*, 161(12):H831–H838, 2014.
- [9] D. Yoo, Y. Song, J. Jang, W. Hwang, S. Jung, S. Hong, J. Lee, and T. Lee. Vertically stacked microscale organic nonvolatile memory devices toward three-dimensional high integration. *Org. Electron.*, 21:198–202, 2015.
- [10] H. Klauk. Organic thin-film transistors. *Chem. Soc. Rev.*, 39:2643–2666, 2010.
- [11] W. Huang, K. Besar, R. LeCover, P. Dullloor, J. Sinha, J. F. Martínez-Hardigree, C. Pick, J. Swavola, A. D. Everett, J. Frechette, M. Bevan, and H. E. Katz. Label-free brain injury biomarker detection based on highly sensitive large area organic thin film transistor with hybrid coupling layer. *Chem. Sci.*, 5:416–426, 2014.

- [12] A. Liess, L. Huang, A. Arjona-Esteban, A. Lv, M. Gsänger, V. Stepanenko, M. Stolte, and F. Würthner. Organic electronics: Organic thin film transistors based on highly dipolar donor-acceptor polymethine dyes. *Adv. Funct. Mater.*, 25(1):167, 2015.
- [13] Q. Zhang, B. Li, S. Huang, H. Nomura, and H. Tanaka and C. Adachi. Efficient blue organic light-emitting diodes employing thermally activated delayed fluorescence. *Nature Photon.*, 8:326–332, 2014.
- [14] D. Xia, B. Wang, B. Chen, S. Wang, B. Zhang, J. Ding, L. Wang, X. Jing, and F. Wang. Self-host blue-emitting iridium dendrimer with carbazole dendrons:nondoped phosphorescent organic light-emitting diodes. *Angew. Chem. Int. Ed.*, 53:1048–1052, 2014.
- [15] H. Nakanotani, T. Higuchi, T. Furukawa, K. Masui, K. Morimoto, M. Numata H. Tanaka Y. Sagara T. Yasuda, and C. Adachi. High-efficiency organic light-emitting diodes with fluorescent emitters. *Nat. Commun.*, 5(4016):1–7, 2014.
- [16] P. Peumans, V. Bulović, and S. R. Forrest. Efficient, high-bandwidth organic multi-layer photodetectors. *Appl. Phys. Lett.*, 76(26):3855–3857, 2000.
- [17] J. Lee, P. Jadhav, and M. A. Baldo. High efficiency organic multilayer photodetectors based on singlet exciton fission. *Appl. Phys. Lett.*, 95:033301, 2009.
- [18] W. Peng, Y. Liu, C. Wang, R. Hu, J. Zhang, D. Xu, and Y. Wang. A highly sensitive near-infrared organic photodetector based on oxotitanium phthalocyanine nanocrystals and light-induced enhancement of electron tunnelling. *J. Mater. Chem. C*, 3:5073–5077, 2015.
- [19] R. Rathore and J. K. Kochi. Cofacial phenylene donors as novel organic sensors for the reversible binding of nitric oxide. *J. Org. Chem.*, 63:8630–8631, 1998.
- [20] C. Zhang, D. Sun, C-X. Sheng, Y. X. Zhai, K. Mielczarek, A. Zakhidov, and Z. V. Vardeny. Magnetic field effects in hybrid perovskite devices. *Nature Physics*, 11, 2015.

- [21] F. C. Krebs. Fabrication and processing of polymer solar cells. a review of printing and coating techniques. *Sol. Energ. Mat. Sol. C.*, 93:394–412, 2009.
- [22] F. C. Krebs. Roll-to-roll fabrication of monolithic large-area polymer solar cells free from indium-tin-oxide. *Sol. Energy Mater. Sol. Cells*, 93:1636–1641, 2009.
- [23] F.C. Krebs, T. Tromholt, and M. Jorgensen. Upscaling of polymer solar cell fabrication using full roll-to-roll processing. *Nanoscale*, 2:873–886, 2010.
- [24] K. Tvingstedt and O. Ingan as. Electrode grids for ito free organic photovoltaic devices. *Adv. Mater.*, 19:2893–2897, 2007.
- [25] J. Zou, H.-L. Yip, S.K. Hau, and A.K.Y. Jen. Metal grid/conducting polymer hybrid transparent electrode for inverted polymer solar cells. *Appl. Phys. Lett.*, 96:203301–203303, 2010.
- [26] N. Espinosa, H. F. Dam, D. M. Tanenbaum, J. W. Andreasen, M. Jorgensen, and F. C. Krebs. Roll-to-roll processing of inverted polymer solar cells using hydrated vanadium(v)oxide as a pedot:pss replacement. *Materials*, 4:169–182, 2011.
- [27] G. Teran-Escobar, J. Pampel, J. M. Caicedo, and M. Lira-Cantu. Low-temperature, solution-processed, layered V_2O_5 hydrate as the hole-transport layer for stable organic solar cells. *Energy Environ. Sci.*, 6:3088–3098, 2013.
- [28] X. Bao, Q. Zhu, T. Wang, J. Guo, C. Yang, D. Yu, N. Wang, W. Chen, and R. Yang. Simple O_2 plasma-processed V_2O_5 as an anode buffer layer for high-performance polymer solar cells. *ACS Appl. Mater. Interfaces*, 7(14):7613–7618, 2015.
- [29] F. C. Krebs, editor. *Stability and Degradation of Organic and Polymer Solar Cells*. John Wiley & Sons, Ltd, 2012.
- [30] K. Kawano, R. Pacios, D. Poplavskyy, J. Nelson, D. D. C. Bradley, and J. R. Durrant. Degradation of organic solar cells due to air exposure. *Sol. Energy Mater. Sol. Cells*, 90:20, 2006.

- [31] F. C. Krebs and K. Norrman. Analysis of the failure mechanism for a stable organic photovoltaic during 10 000 h of testing. *Prog. Photovolt: Res. Appl.*, 15:697–712, 2007.
- [32] F. C. Krebs M. Jorgensen, K. Norrman. Stability/degradation of polymer solar cells. *Sol. Energy Mater. Sol. Cells*, 92:686, 2008.
- [33] E. Voroshazi, B. Verreet, A. Buri, R. Müller, D. Nuzzo, and P. Heremans. Influence of cathode oxidation via the hole extraction layer in polymer:fullerene solar cells. *Organic Electronics*, pages 736–744, 2011.
- [34] Y. Suh, N. Lu, S. H. Lee, W. S. Chung, K. Kim, B. Kim, M. J. Ko, and M. J. Kim. Degradation of a thin ag layer induced by poly(3,4ethylenedioxythiophene):polystyrene sulfonate in a transmission electron microscopy specimen of an inverted polymer solar cell. *Acs Appl. Mater. Interfaces*, 4: 5118–5124, 2012.
- [35] T. T. Larsen-Olsen, T. R. Andersen, B. Andreasen, A. P. L. Bottiger, E. Bundgaard, K. Norrman, J. W. Andreasen, M. Jorgensen, and F. C. Krebs. Roll-to-roll processed polymer tandem solar cells partially processed from water. *Sol Energ Mat Sol C.*, 97:43–49, 2012.
- [36] K. Zilberberg, S. Trost, H. Schmidt, and T. Riedl. Solution processed vanadium pentoxide as charge extraction layer for organic solar cells. *Adv. Energy Mater*, 1(3): 377–381, 2011.
- [37] K. Zilberberg, S. Trost, J. Meyer, A. Kahn, A. Behrendt, D. Lützenkirchen-Hecht, R. Frahm, and T. Riedl. Inverted organic solar cells with sol-gel processed high work-function vanadium oxide hole-extraction layers. *Adv. Funct. Mater.*, 21(24): 4776–4783, 2011.
- [38] A. Morais, J. P. C. Alves, F. A. S. Lima, M. Lira-Cantu, and A. F. Nogueira. Enhanced photovoltaic performance of inverted hybrid bulkheterojunction solar cells

- using TiO_2 / reduced graphene oxide films as electron transport layers. *J. Photon. for Energy*, 5(1):057408, 2015.
- [39] Y-S. Hu, X. Liu, J-O. Müller, R. Schlögl, J. Maier, and D. S. Su. Synthesis and electrode performance of nanostructured V_2O_5 by using a carbon tube-in-tube as a nanoreactor and an efficient mixed-conducting network. *Angew. Chem. Int. Ed.*, 48: 210–214, 2009.
- [40] M. Li, F. Kong, H. Wang, and G. Li. Synthesis of vanadium pentoxide (V_2O_5) ultralong nanobelts via an oriented attachment growth mechanism. *CrystEngComm*, 13:5317–5320, 2011.
- [41] H. Yu, X. Rui, H. Tan, J. Chen, X. Huang, C. Xu, W. Liu, D. Y. W. Yu, H. H. Hng, H. E. Hoster, and Q. Yan. Cu doped V_2O_5 flowers as cathode material for high-performance lithium ion batteries. *Nanoscale*, 5:4937–4943, 2013.
- [42] V. Bondarenka, S. Kaciulis, Z. Martunas, A. Reza, G. J. Babonas, and A. Pasiskevicius. XPS and optical properties of sol-gel processed vanadium pentoxide films. *Lith. J. Phys.*, 48:341–348, 2008.
- [43] J. Światowska-Mrowiecka, F. Martin, V. Maurice, S. Zanna, L. Klein, J. Castle, and P. Marcus. The distribution of lithium intercalated in V_2O_5 thin films studied by XPS and ToF-SIMS. *Electrochim. Acta*, 53:4257–4266, 2008.
- [44] J. Y. Kim, K. Lee, N. E. Coates, and D. Moses T. Nguyen M. Dante A. J. Heeger. Efficient tandem polymer solar cells fabricated by all-solution processing. *Science*, 317:222–225, 2007.
- [45] A. G. F. Janssen, T. Riedl, S. Hamwi, H.-H. Johannes, and W. Kowalsky. Highly efficient organic tandem solar cells using an improved connecting architecture. *Appl. Phys. Lett.*, 91(7), 2007.
- [46] A. Hadipour, B. de Boer, and P. W. M. Blom. Organic tandem and multi-junction solar cells. *Adv. Funct. Mater.*, 18(2):169–181, 2008.

- [47] L. Dou, J. You, J. Yang, C. Chen, Y. He, S. Murase, T. Moriarty, K. Emery, G. Li, and Y. Yang. Tandem polymer solar cells featuring a spectrally matched low-bandgap polymer. *Nature Photon.*, 6:180–185, 2012.
- [48] J. You, L. Dou, K. Yoshimura, T. Kato, K. Ohya, T. Moriarty, K. Emery, C. Chen, J. Gao, G. Li, and Y. Yang. A polymer tandem solar cell with 10.6% power conversion efficiency. *Nature Communications*, 4 (1446):1–10, 2013.
- [49] W. Li, A. Furlan, K. H. Hendriks, M. M. Wienk, and René A. J. Janssen. Efficient tandem and triple-junction polymer solar cells. *J. Am. Chem. Soc.*, 135(15):5529–5532, 2013.
- [50] T. R. Andersen, H. F. Dam, B. Andreasen, M. Hsel, M. V. Madsen, S. A. Gevorgyan, R. R. Sondergaard, M. Jorgensen, and F. C. Krebs. A rational method for developing and testing stable flexible indium- and vacuum-free multilayer tandem polymer solar cells comprising up to twelve roll processed layers. *Sol. Energy Mater. Sol. Cells*, 120:735–743, 2014.
- [51] C. Chou, W. L. Kwan, Z. Hong, L. Chen, and Y. Yang. A metal-oxide interconnection layer for polymer tandem solar cells with an inverted architecture. *Adv. Mater.*, 23, 2011.

8. STABILITY OF ORGANIC SOLAR CELLS

8.1 Introduction

Organic solar cells (OSCs) have been an exciting topic of research for the last few decades as they present several potential advantages compared with conventional inorganic solar cells, including lighter weight, greater flexibility, and inexpensive large area fabrication using printing techniques. In fact, polymer solar cells are more suitable for printable solar cells. Substantial progress in organic solar cell technology has improved the device efficiency, which reaches almost 12% [1]. Compared to the extensive research efforts devoted to improving the power conversion efficiency (PCE), the stability of OSCs has attracted significantly less attention, which could be partially due to the high complexity of the degradation mechanism [2]. This emerging technology is at a pre-commercial stage of development, and there are several challenges that must be addressed before commercialization would be feasible. To be competitive in the renewable energy market, further improvements with respect to the efficiency and lifetime of the OSCs are essential. While the operational lifetime of Si solar cells is in the range of 25 years, the operational organic photovoltaic (OPV) lifetime under full solar illumination ($1 \text{ sun} = 100 \text{ mW/cm}^2$) has only recently reached a few years [3–7].

Degradation mechanisms in OPV are complex and include a variety of processes: photo-bleaching of the conjugated polymers, trap generation in the polymer, fullerene moieties of the photoactive layer [8, 9], degradation of the hole and electron transport layer [10], ion migration from the electrodes [8], morphological changes [11], and so on. These processes are almost inseparable as they can be caused by the same factors, namely exposure of the device to light, heat, oxygen, and/or water [12]. In addition to improving the design and synthesis of active materials, interface engineering has emerged as a key factor in increasing the efficiency and stability [13–20]. For facilitating charge extrac-

tion, the interface between the electrodes and the active organic layers is modified by particular treatments, or dedicated interlayers are chosen to match the electronic levels of the electrodes with the transport levels of the organic materials [21]. In this chapter, interfacial engineering to increase the stability of OSCs is presented. The use of the high work function semiconductor oxide V_2O_5 as the hole transport layer (HTL) as well as the use of reduced graphene oxide as the interlayer in these devices were evaluated.

8.2 Experimental

8.2.1 *Sample preparation*

Two types of devices were evaluated with respect to stability. The first devices were glass-based devices with glass/fluorine-doped tin oxide (FTO)/ZnO/poly(3-hexylthiophene-2,5-diyl) (P3HT):[6,6]-phenyl-C61-butyric acid methyl ester (PCBM)/ V_2O_5 /Ag. The other considered devices were Flextrode[®]-based devices, which had the same structure, but the devices are flexible. For flexible devices, the stability was evaluated using V_2O_5 or poly(3,4-ethylenedioxythiophene):poly(styrenesulfonate) (PEDOT:PSS) as the HTL. The flexible plastic solar cells were assembled as described in the previous chapter.

For glass-based devices, all layers, with the exception of Ag, were deposited layer-by-layer using a spin-coating technique starting from the FTO layer. The silver back electrode, which has a thickness of 100 nm, was evaporated on top of the V_2O_5 in a UNIVEX[®] 350G thermal evaporator from Oerlikon[®], placed inside a glovebox.

The ZnO precursor was prepared as proposed by Krebs et al. [22]. In particular, 5.94 g of $Zn(OAc)_2 \cdot 2H_2O$ was dissolved in 250 ml of MeOH and heated up to 60°C. At this temperature, 3.02 g of KOH was added, and the solution was refluxed for 3 h at °C. The precipitated particles were then allowed to settle for 12 h before the mixture was carefully decanted. The precipitate was dissolved in 100-ml MeOH, and after resuspension, the particles were allowed to settle for another 12 h. Following the previous synthesis method, MeOH was removed, and the particles were dissolved in 40 ml of chlorobenzene or isopropanol. The concentration of ZnO was determined and then diluted in 49 mg/ml of acetone. For stabilization, 2-(2-methoxyethoxy) acetic acid (MEAA) at 2% w/w or

2-[2-(2-Methoxyethoxy)ethoxy]acetic acid MEEAA at 4% w/w was added with respect to the weight of ZnO. The ZnO nanoparticles suspended in acetone were spin coated on the previously cleaned FTO substrate with a speed of 3000 rpm and an acceleration of 3000 rpm/s over 40 s. After deposition, the ZnO thin films were annealed at 140°C for 30 min.

The active layer composed of P3HT:PCBM (30:30 mg) in chlorobenzene was spin coated on top of the ZnO layer with a speed of 1000 rpm and an acceleration of 500 rpm/s over 40 s. The synthesis of the $V_2O_5 \cdot H_2O$ xerogel was performed by the cationic exchange method [23]. Briefly, 4.5 g of sodium metavanadate ($NaVO_3$; Sigma) was dissolved in water at 80°C. Once cold, the solution was passed through a cationic exchanger (DOWEX50 WX2 50-100[®], Sigma[®]). Water-based V_2O_5 cannot be directly deposited on the polymers due to its polarity. To deposit the V_2O_5 thin film on top of the active layer, isopropanol must be added to the as-prepared V_2O_5 xerogel (1:1 ratio), which changes its polarity and enables deposition. The V_2O_5 layer was then spin coated on top of the active layer with a speed of 3000 rpm. The solution was released on the sample for about 10 s, when the final speed was reached. After deposition, the V_2O_5 layer was dried at 120°C for 15 s to remove the isopropanol. After evaporation, the device was annealed at 120°C for 10 min.

8.2.2 Stability tests

The stability tests were performed according to the International Summit on OPV Stability (ISOS) standards [24]. Initially, the samples were analyzed according to the ISOS-D-1 standard, where the samples are kept under atmospheric conditions without any source of light. To understand the protective effect of encapsulation, two sets of devices were tested, with and without encapsulation. Another set of samples were tested according to the ISOS-O-1 standard, where the samples were tested outdoors in real operational conditions. For this test, a sun tracker was used to keep the samples under 1 sun of solar illumination for as long as possible. A third set of samples was tested according to the ISOS-L-1 standard, where the samples are held under artificial illumination (solar simulator) without controlling the temperature or relative humidity. For the ISOS-L-1

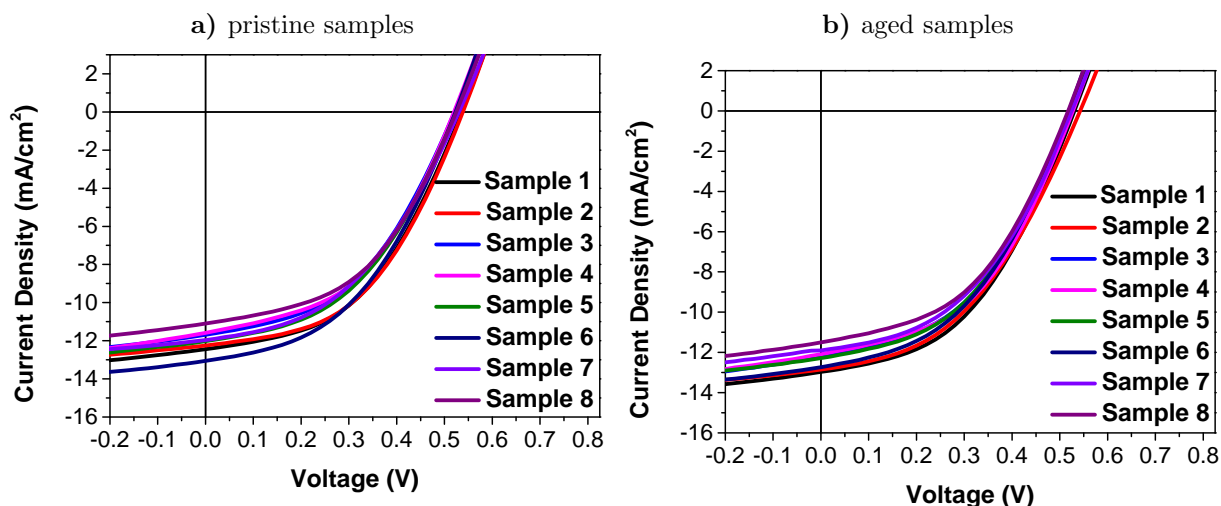
standard, the use of the solar simulator makes the temperature slightly high. During the tests, the temperature was approximately 55°C.

8.3 Results and discussion

8.3.1 Degradation under inert atmosphere in dark

Prior to the application of the ISOS standards to evaluate the stability of the OSCs, the devices were kept under an inert atmosphere, which contained less than 1 ppm of O₂ and H₂O, for approximately 90 days after fabrication. The $J - V$ curve and the incident photon-to-charge-current efficiency (IPCE) spectra for these devices were measured immediately after fabrication and after 90 days in the glove box. These results are shown in Fig. 8.1 while and Table 8.1 summarizes the average photovoltaic parameters under these circumstances. The results reveal that there is no evidence of degradation in OSCs.

Figure 8.1: $J - V$ curves for OSCs before and after an aging time of 90 days inside a glove box.



Source: Own author

Table 8.1: Average photovoltaic parameters of OSCs before and after an aging time of 90 days inside a glove box.

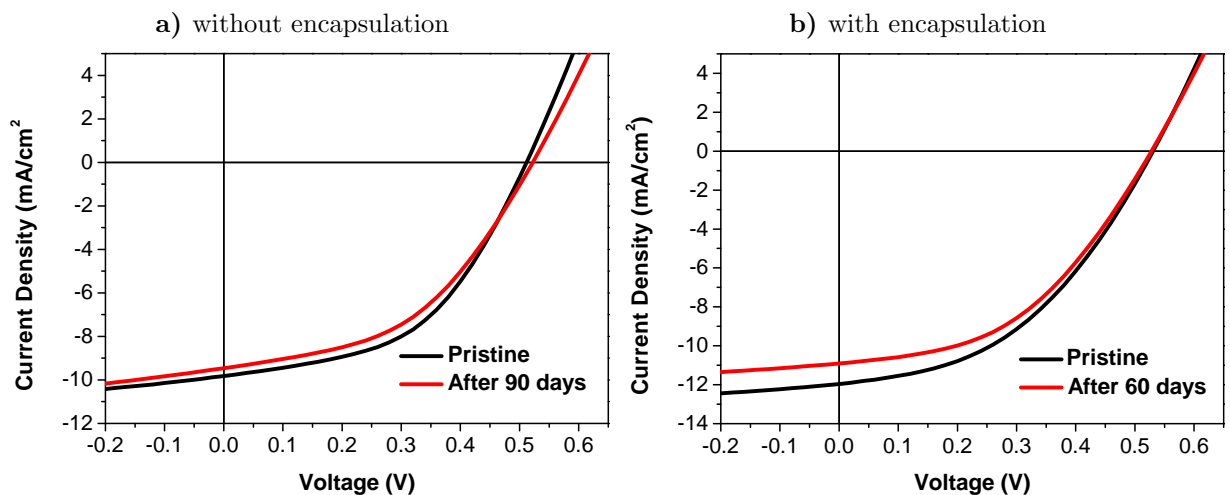
condition	J_{sc} (mA/cm ²)	V_{oc} (V)	FF (%)	PCE (%)
pristine	12.01±0.53	0.53±0.01	45.98±1.32	2.91±0.16
after 90 days	12.32±0.50	0.53±0.00	45.12±0.95	2.92±0.12

Source: Own author

8.3.2 Degradation of OSCs according to the ISOS-D-1 standard

After being removed from the glove box, the stability of the samples was evaluated by following the ISOS-D-1 standard to verify the efficacy of encapsulation on the protection of solar cells. Part of the samples were encapsulated with glass-glass and an UV-curable epoxy, while the remaining samples were evaluated without any encapsulation. Figure 8.2 shows how the $J - V$ curves for the best performing sample evolved over 60 days. In both cases, the primary factor causing stability changes in the OSCs is the decreasing short circuit current J_{sc} . However, based on the $J - V$ curves, only for the best performing devices, encapsulation does not seem to be effective in protecting OSCs.

Figure 8.2: $J - V$ curves, for best performing, OSCs aged in air for 60 days without and with encapsulation, according to the ISOS-D-1 standard.



Source: Own author

Table 8.2 summarizes the photovoltaic parameters for cells with and without encapsulation. On average, the main factor causing degradation is the decreasing value of J_{sc} . For encapsulated devices, the value of the J_{sc} decreases by about 10% in 60 days while that for the non-encapsulated samples decreases by 18%. The values for the open circuit voltage V_{oc} and fill factor FF are nearly constant after 60 days in air. The PCE decreases by approximately 8% for the encapsulated devices and 15% for the non-encapsulated devices. On average, encapsulation can protect the OSCs from losses in J_{sc} , consequently preserving its PCE. Nevertheless, OSCs without encapsulation could be more stable than encapsulated OSCs.

Table 8.2: Average photovoltaic parameters of OSCs aged in air for 60 days without and with encapsulation, according to the ISOS-D-1 standard.

encapsulation	condition	J_{sc} (mA/cm ²)	V_{oc} (V)	FF (%)	PCE (%)
yes	pristine	11.70±0.28	0.52±0.00	45.40±0.98	2.78±0.01
	after 60 days	10.60±0.44	0.53±0.01	46.10±1.27	2.56±0.06
no	pristine	9.71±0.50	0.51±0.01	47.40±1.32	2.32±0.16
	after 60 days	7.99±0.71	0.52±0.01	47.03±1.83	1.97±0.20

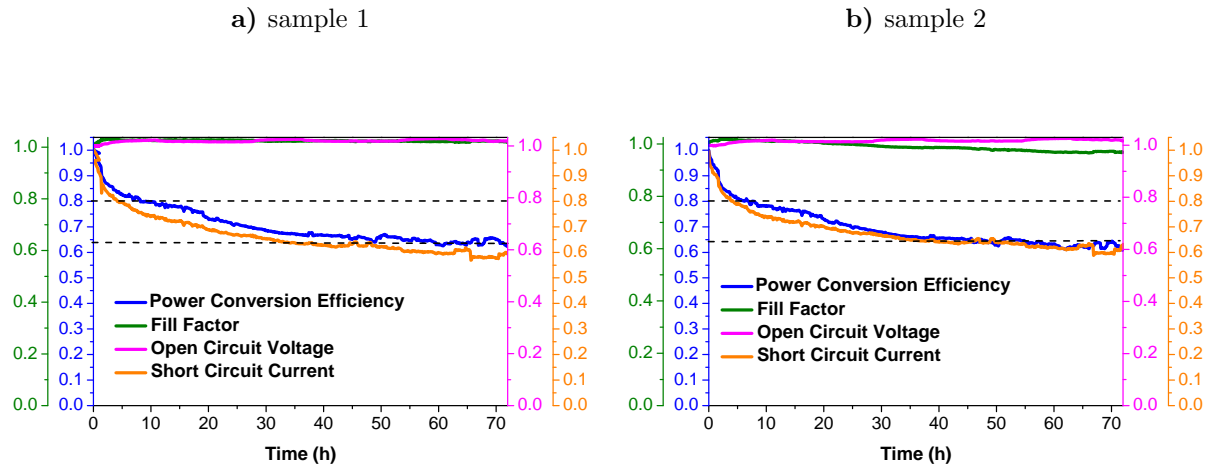
Source: Own author

8.3.3 Degradation of OSCs according to the ISOS-L-1 standard

To quickly determine the stability of these devices, two samples were submitted to an accelerated test, where the samples were kept under 1 sun of constant irradiation using a solar simulator. The samples were studied for 72 h. The working temperature was around 55°C.

Figure 8.3 shows how the photovoltaic parameters evolution for the two considered OSCs. In both samples, the main factor causing degradation of the OSCs is the decreasing value of J_{sc} . Moreover, the variation of PCE with time follows the trend for J_{sc} with time. In the 72-h study period, V_{oc} slightly increases. The FF remains almost constant for sample 1 and decreases slightly for sample 2. The initial efficiency loss for OSCs, called “burn in,” seems to originate from the decrease in J_{sc} caused by the bulk degradation of the active layer induced by solar radiation [25–27].

Figure 8.3: Time evolution of the photovoltaic parameters for two OSCs under accelerated degradation test (solar simulator conditions) for 72 h, according to the ISOS-L-1 standard.



Source: Own author

At this point, the variables important for the degradation analysis of OSCs are defined. The definitions for the most common variables have been provided by the OPV community through consensus protocols [24]:

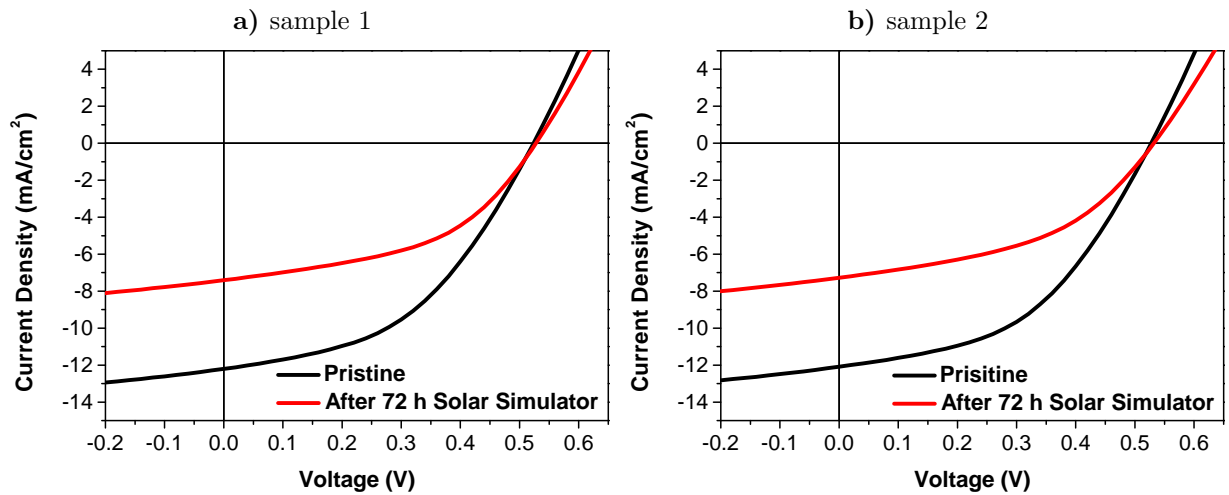
1. (E_0, T_0) , where E_0 is the initial testing measurement of an OPV device immediately after final fabrication of the device at time $T_0 = 0$.
2. (E_S, T_S) , where E_S is a second testing measurement of an OPV device, defined arbitrarily by the user at time T_S after the fabrication of a device.

3. (E_{80}, T_{80}) , where E_{80} is the testing measurement of an OPV device after the device has decayed 20% from the initial testing measurement of E_0 . The time required decay to E_{80} is T_{80} .
4. (E_{S80}, T_{S80}) , where E_{S80} is the testing measurement of an OPV device after the device has decayed 20% from the second testing measurement E_S . Here, T_{S80} is the time required to decay to E_{S80} .

For both samples, there is a clear burn-in time. Assuming the burn-in time is T_{80} , the burn-in time for both devices is about 8 h. The secondary measurement time T_S is set to T_{80} . Then, at the end of the 72-h experiment, both samples have almost reached T_{S80} .

The $J - V$ curves for both samples were measured before and after the accelerated degradation test, as shown in Fig. 8.4. The primary change after the degradation was a decrease in the value of J_{sc} .

Figure 8.4: $J - V$ curves for OSCs degradation tests under solar simulator conditions over 72 h, according to the ISOS-L-1 standard.



Source: Own author

The comparison of the photovoltaic parameters before and after the degradation are shown in Table 8.3. These results confirm that the values from the open circuit voltage

and fill factor remain almost constant before and after the accelerated degradation test. In fact, for sample 1, V_{oc} and FF slightly increased after the degradation. On the other hand, for sample 2, V_{oc} was not changed, and FF slightly decreased. As a result, the performance of sample 1 was better than that of sample 2 for the same conditions.

Table 8.3: Photovoltaic parameters for OSCs degradation tests under solar simulator conditions over 72 h, according to the ISOS-L-1 standard.

sample	condition	J_{sc} (mA/cm ²)	V_{oc} (V)	FF (%)	PCE (%)
1	pristine	12.21	0.52	45.49	2.91
	after 72 h	7.41	0.53	47.43	1.85
2	pristine	12.09	0.53	46.46	2.96
	after 72 h	7.28	0.53	45.16	1.75

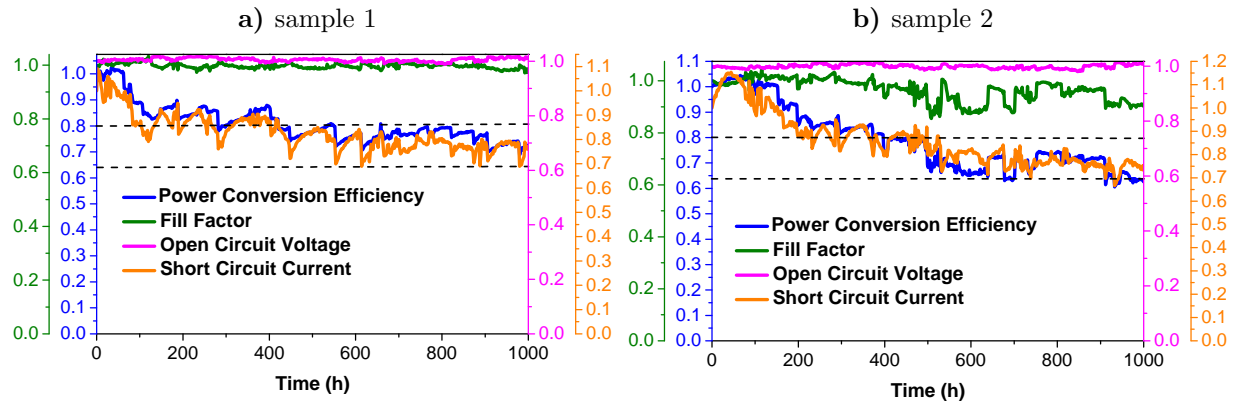
Source: Own author

8.3.4 Degradation of OSCs according to the ISOS-O-1 standard

In this study, four samples were degraded in real outdoor conditions. Two samples based on rigid FTO glass and two samples based on Flextrode[®] were considered. The glass-based OSCs were studied for 1000 h, while the plastic OSCs were studied for 900 h. In both cases, the photovoltaic parameters were recorded every 5 min. Only the data points in which the irradiance is 1 ± 0.1 sun are shown.

The time evolution of the photovoltaic parameters for glass-based solar cells is shown in Fig. 8.5. This case is similar to the ISOS-L-1 case because the losses in PCE follow the decreasing trend of J_{sc} . Both samples show a burn-in process, with T_{80} values of 450 h and 420 h for samples 1 and 2, respectively. Considering $T_S = T_{80}$, T_{S80} is not reached for sample 1 within the 1000 h experimental time. For sample 2, T_{S80} is around 1000 h. For both samples, V_{oc} does not show any appreciable difference during the test. For sample 1, FF remains almost constant while showing some instability and decrease for sample 2 after the first 300 h of experiment.

Figure 8.5: Time evolution of the photovoltaic parameters for two OSCs tested under real outdoor conditions over 1000 h, according to the ISOS-O-1 standard.

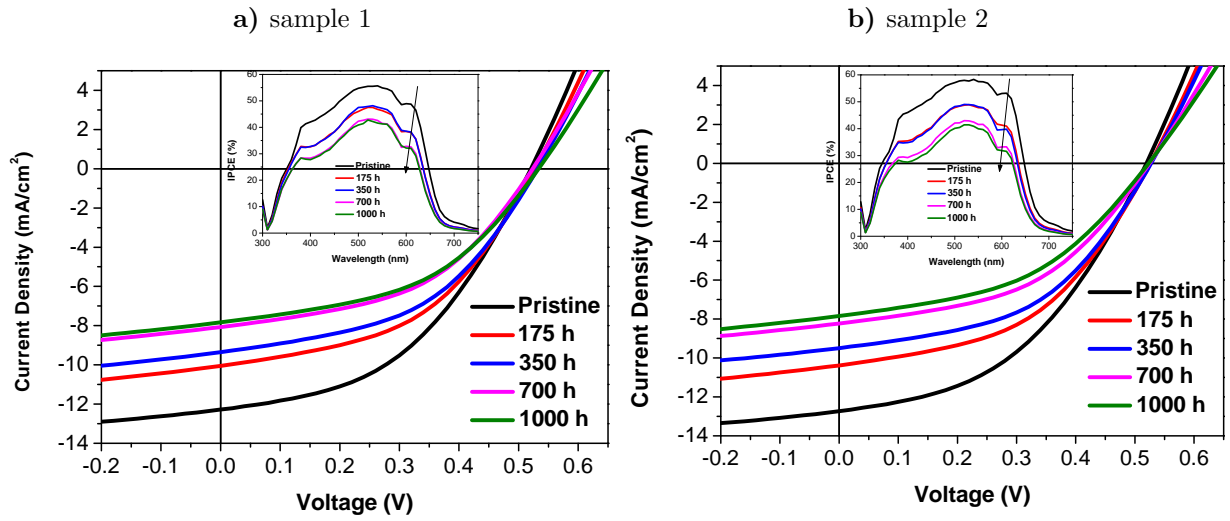


Source: Own author

The photovoltaic parameters were also measured with a solar simulator. The evolution of the $J - V$ curves for both samples is shown in Fig. 8.6. The decrease in J_{sc} as well as the constance of V_{oc} are both observable in this figure. The decrease in J_{sc} is in good agreement with the changes in the IPCE spectra of the samples, showed in the insets. The shape of the spectra are preserved and only change in intensity, which indicates a decrease in the value of J_{sc} .

Table 8.4 shows the photovoltaic parameters associated with the $J - V$ curves shown in Fig. 8.6. The data from Table 8.4 also confirms that the degradation of the solar cells is due to losses on J_{sc} . Moreover, V_{oc} and FF do not present any appreciable change. All of the results from the application of the ISOS-O-1 standard show that the mechanisms of degradation seem to be the same as those responsible for the degradation under accelerated conditions in the ISOS-L-1 standard because the photovoltaic parameters evolve in a very similar way.

Figure 8.6: $J - V$ curves for OSCs degradation tests under real outdoor conditions, according to the ISOS-O-1 standard. Insets show IPCE spectra.



Source: Own author

Table 8.4: Photovoltaic parameters for OSCs degradation tests under real outdoor conditions, according to the ISOS-O-1 standard.

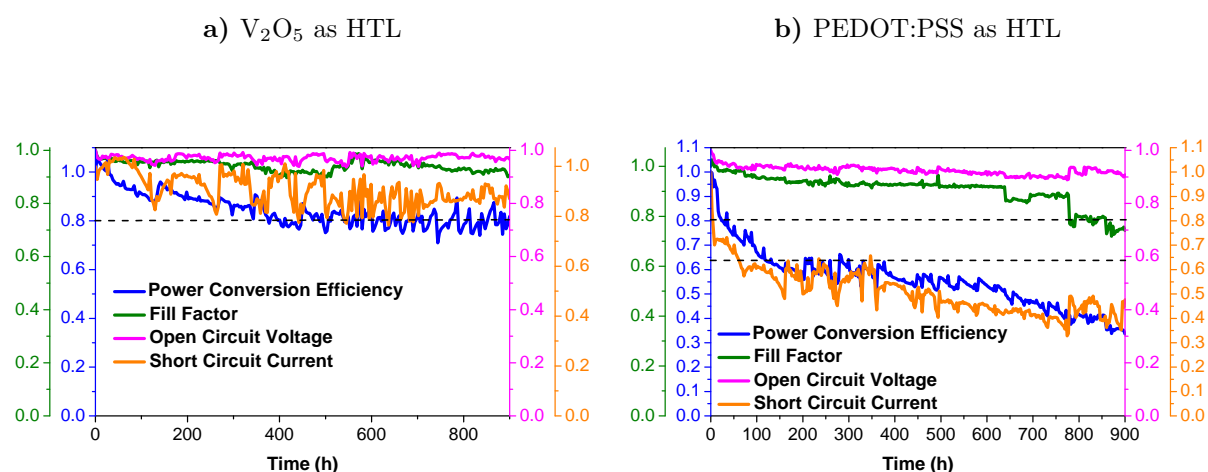
sample	condition	J_{sc} (mA/cm ²)	V_{oc} (V)	FF (%)	PCE (%)
1	pristine	12.28	0.52	45.18	2.89
	after 175 h	10.05	0.53	47.08	2.49
	after 350 h	9.38	0.53	47.12	2.35
	after 700 h	8.10	0.52	46.96	1.99
	after 1000 h	7.83	0.53	46.29	1.93
2	pristine	12.73	0.52	44.36	2.93
	after 175 h	10.38	0.53	44.98	2.57
	after 350 h	9.49	0.52	47.70	2.39
	after 700 h	8.37	0.52	46.45	2.04
	after 1000 h	7.84	0.52	45.08	1.85

Source: Own author

8.3.4.1 V_2O_5 vs. PEDOT:PSS

The V_2O_5 -based and PEDOT:PSS-based HTL for flexible, ITO-free, printable photovoltaic are compared. The stability of two encapsulated OSCs have been tested following the ISOS-O-1 standard. Figure 8.7 shows the time evolution of the photovoltaic parameters for both devices. The results are very similar to the results presented for glass-based devices. The degradation is caused by losses in J_{sc} . The values of V_{oc} and FF are almost constant for the cell using the V_2O_5 -based HTL; however, for the cell using PEDOT:PSS, there is a failure of FF around 650 h. The effect of this failure can be observed in the PCE for this device: PCE reaches a plateau, but decreases after the FF failure.

Figure 8.7: Time evolution of the photovoltaic parameters of plastic OSCs under real outdoor degradation tests using V_2O_5 or PEDOT:PSS as HTL, according to the ISOS-O-1 standard.

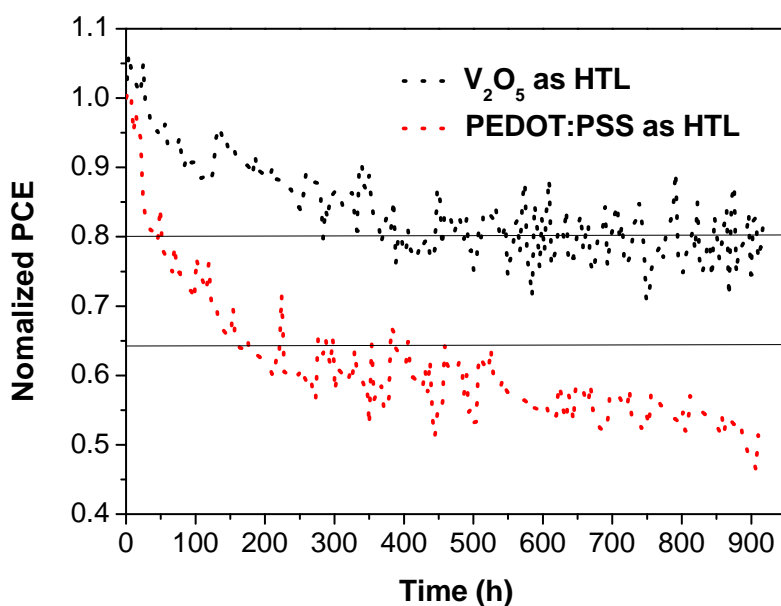


Source: Own author

Figure 8.8 shows the comparison between the two samples, considering only PCE. Both devices present a burn-in process. Nevertheless, T_{80} for both devices is very different. For the best device, which uses V_2O_5 , T_{80} is 400 h while that for the PEDOT:PSS-based device is around 40 h. Considering that $T_S = T_{80}$, T_{S80} is not reached for the V_2O_5 -based OSC because PCE is held around E_{80} for the duration of the experiment. For the PEDOT:PSS-based OSC, T_{S80} is reached at about 150 h, and T_{80} is about 550 h.

The efficiency of these devices seems to stabilize around T_{50} , but failure on FF induces additional losses in PCE.

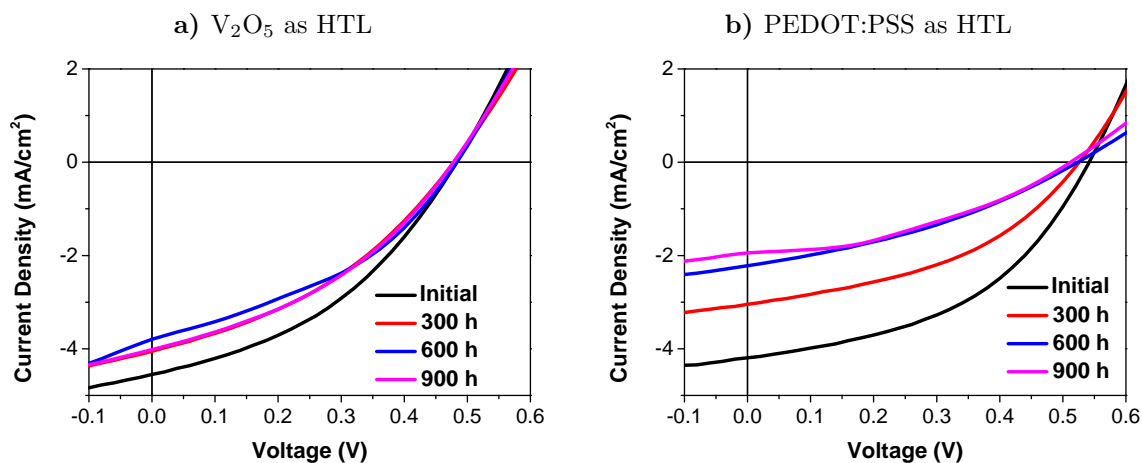
Figure 8.8: Comparison between the PCE evolution for plastic OSCs under real outdoor degradation tests using V_2O_5 (black) or PEDOT:PSS (red) as HTL, according to the ISOS-O-1 standard.



Source: Own author.

The $J - V$ curves for these solar cells, determined at different times during the degradation, are shown in Fig. 8.9. There are remarkable differences between the curves for the two cells. There is no change in V_{oc} and just a slight decrease in J_{sc} for V_2O_5 -based cells. The PEDOT:PSS-based cells, on the other hand, presented a more pronounced decrease in J_{sc} and a reduction in V_{oc} .

Figure 8.9: $J - V$ curves for plastic OSCs under real outdoor degradation tests using V_2O_5 or PEDOT:PSS as HTL, according to the ISOS-O-1 standard.



Source: Own author

8.3.5 Strategies for improving the stability of OSCs

All the results presented so far suggest the solar cells analyzed in this study degrade mainly due to losses in J_{sc} , while FF and V_{oc} values remained almost constant, as it has been reported previously [8]. These losses can be attributed to a number of factors such as poor exciton separation [28], decrease mobility in the active layer [29, 30], increase in charge carrier recombination [31], among others.

Two main degradation pathways of the active layer of OPVs that have been suggested are [8]: (i) morphological degradation of the bulk heterojunction architecture and (ii) chemical degradation of the organic materials. Possible reasons for chemical degradation in poly(3-hexyl-thiophene)(P3HT) are the formation of charge coupled complexes with oxygen [32] and oxidation of the polymer backbone [30].

According to Endale et al. [33], the photodegradation of P3HT results in reduced light absorption, increased series resistance and lower hole mobility. It is well known that more energetic photons like those from UV and blue radiation have the ability to damage the polymers, degrading the active layer of OSCs. In fact, it is generally accepted that UV radiation is able to promote physical or chemical degradation in polymeric materials, as

this energy could be enough to break chemical bonds [34–36]. Hintz et al. [36] reported the photodegradation of P3HT upon illumination with both visible (525 nm) and UV (365 nm) light finding that the degradation products depend strongly on the wavelength of the incident light. For UV irradiation the π -conjugated system and the hexyl side chain are degraded simultaneously, while for visible light only the π -conjugated system is affected. Córcoles et al. [37] suggests that chain break would be the principal degradation mechanism under UV irradiation.

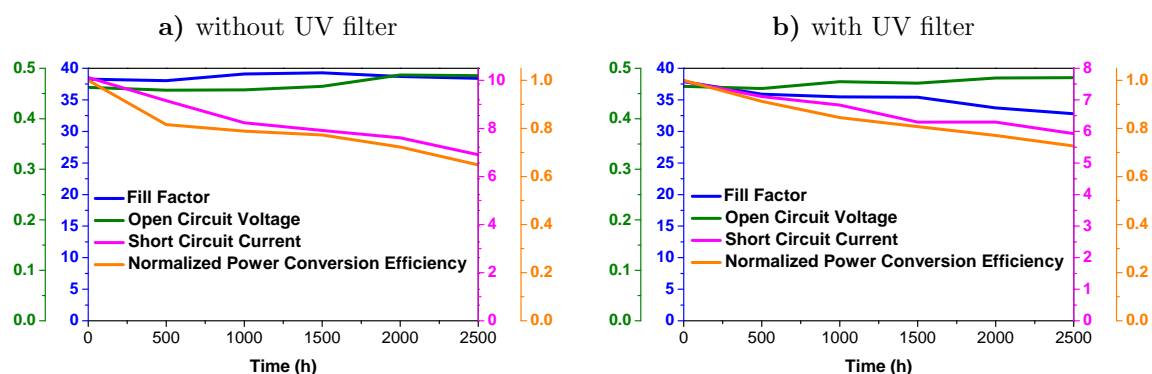
Besides photo induced degradation, another type of chemical degradation is related to oxygen and moisture incorporation as well as with the diffusion of another species into the active layer, the latter being known as interlayer diffusion. In it, the electrode material is slowly dissolved in the other layers, i.e., the electrode material diffuses through the entire device and thus contributing to the overall degradation of the device [30, 31, 38, 39].

In this work, with the aim to avoid the UV component of the solar spectrum, ultraviolet radiation filters have been used in stability tests. Graphene reduced oxide protection layer was tried as protective layer, with the objective to protect the active layer from the oxygen and moisture diffusion as well as from the interlayer diffusion. In the normal configuration devices, there is some evidences that V_2O_5 layer can acts as a UV filter [40], since it absorbs light in the UV region.

8.3.5.1 UV filter

In order to identify the effect of UV-filter protection on the stability of OSCs, identical samples, without and with an UV filter, were tested according to ISOS-O-1 standard during 2500 h. Figure 8.10 shows the evolution of the photovoltaic parameters for these devices during 2500 h stability test. According to Fig. 8.10, the main factor causing degradation in both devices is a decreasing on the value of J_{sc} , which is in good agreement with the results presented in previous sections. During the tests, the other monitored parameters, V_{OC} , and FF changed very little. After 2500 h, the PCE value decreased to 73% and 65% of its initial PCE, for the solar cell with and without UV filter, respectively.

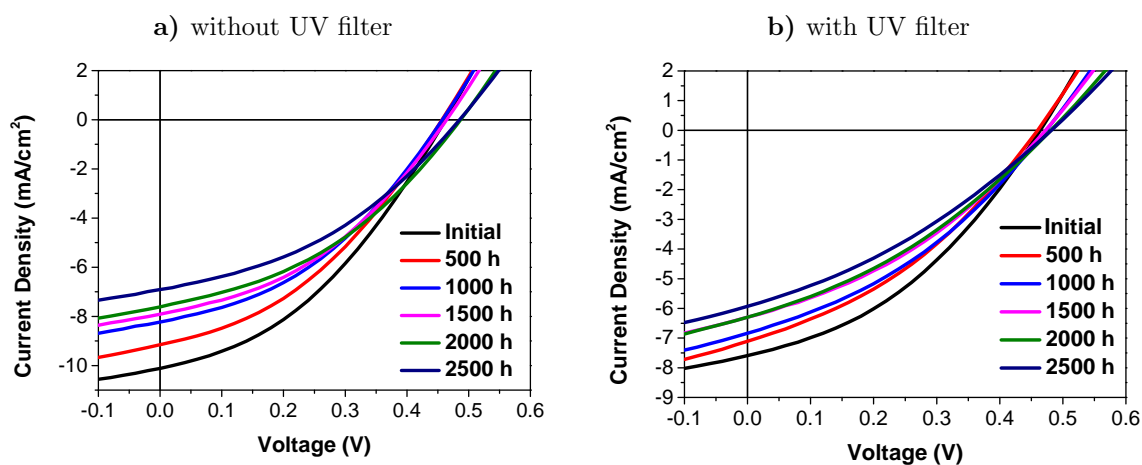
Figure 8.10: Time evolution of the photovoltaic parameters for OSCs without UV filter with UV filter during real outdoor degradation tests according to the ISOS-O-1 standard.



Source: Own author

Figure 8.11 shows $J-V$ curves for cells without and with an UV filter, obtained under real solar illumination. Curves were recorded every 500 h. The overview of these sets of curves provide a better picture for the evolution of the photovoltaic parameters. Absolute values of the photovoltaic parameters are shown in Table 8.5. The analysis of Fig. 8.11 together with the data from Tab. 8.5 makes clear that the values for J_{sc} decreases less for the solar cell with the UV filter. As a consequence of this small decreasing in J_{sc} , the device protected with an UV radiation filter was able to retain more PCE during the stability test.

Figure 8.11: $J - V$ curves for OSCs degradation tests, without and with UV filter, under real outdoor conditions, according to the ISOS-O-1 standard.



Source: Own author

Table 8.5: Photovoltaic parameters for OSCs degradation tests, without and with UV filter, under real outdoor conditions, according to the ISOS-O-1 standard.

UV filter	condition	J_{sc} (mA/cm ²)	V_{oc} (V)	FF (%)	PCE (%)
without	pristine	10.12	0.46	38.88	2.10
	after 500 h	9.15	0.46	38.05	1.71
	after 1000 h	8.23	0.46	39.11	1.65
	after 1500 h	7.91	0.46	39.29	1.62
	after 2000 h	7.61	0.49	38.70	1.51
	after 2500 h	6.90	0.49	38.41	1.36
with	pristine	7.59	0.46	37.88	1.58
	after 500 h	7.11	0.46	35.89	1.44
	after 1000 h	6.84	0.47	35.48	1.34
	after 1500 h	6.29	0.47	35.41	1.28
	after 2000 h	6.29	0.48	33.73	1.22
	after 2500 h	5.93	0.48	32.81	1.15

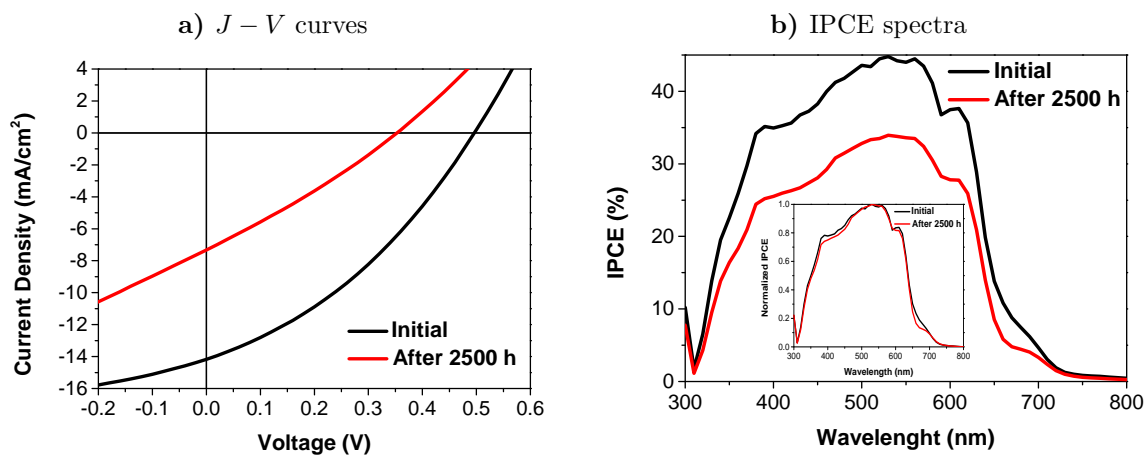
Source: Own author

Figure 8.12 shows $J - V$ curves and IPCE spectra for the cell tested without an UV filter, before and after the ISOS-O-1 stability test. The data were recorded under solar

simulator conditions. Figure 8.13 shows the same data for the device with UV filter. The photovoltaic parameters for these two devices, before and after the stability test are shown in Table 8.6.

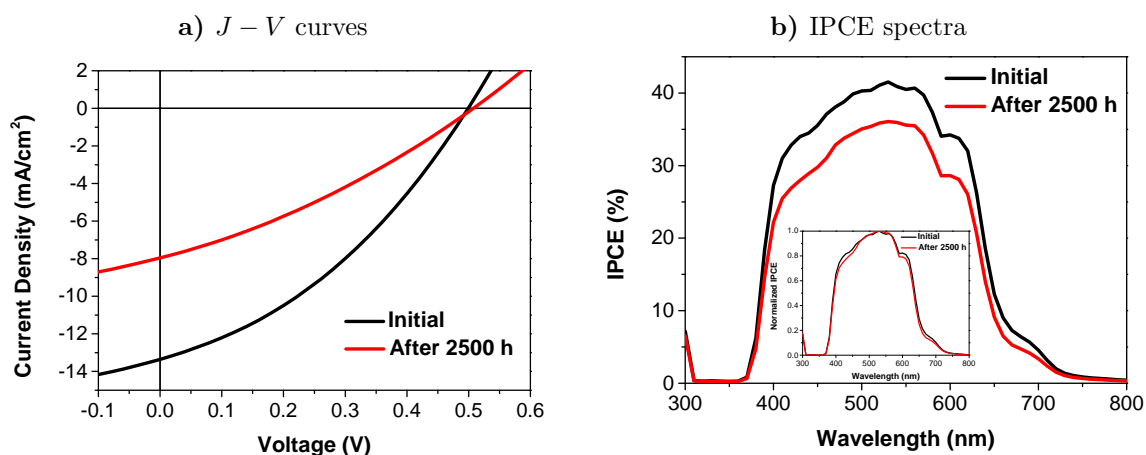
The data show a performance degradation, with decreased photovoltaic parameters, of the cells, both without and with an UV filter, after the 2500-h stability test. The insets of Figs. 8.12(b) and 8.13(b) show the normalized PCE spectra before and after the test. The spectra before and after the test match perfectly in both cases (without and with an UV filter) showing that the IPCE losses are due to decreasing J_{sc} values. The decrease in performance is less accentuated for the device tested with an UV filter which allows the conclusion that the use of the UV filter is beneficial to the long term stability of these OSCs.

Figure 8.12: $J - V$ curves and IPCE spectra for OSCs degradation test, without UV filter, obtained under solar simulator conditions before and after the ISOS-O-1 2500-h stability test. The inset shows normalized IPCE spectra.



Source: Own author

Figure 8.13: $J - V$ curves and IPCE spectra for OSCs degradation tests, with UV filter, obtained under solar simulator conditions before and after the ISOS-O-1 2500-h stability test. The inset shows normalized IPCE spectra.



Source: Own author

Table 8.6: Photovoltaic parameters for OSCs degradation tests, without and with UV filter, obtained under solar simulator conditions, before and after the ISOS-O-1 2500-h stability test.

UV filter	condition	J_{sc} (mA/cm^2)	V_{oc} (V)	FF (%)	PCE (%)
without	pristine	14.17	0.50	35.19	2.47
	after 2500 h	7.32	0.35	28.21	0.73
with	pristine	13.36	0.50	36.01	2.40
	after 2500 h	7.96	0.51	31.35	1.27

Source: Own author

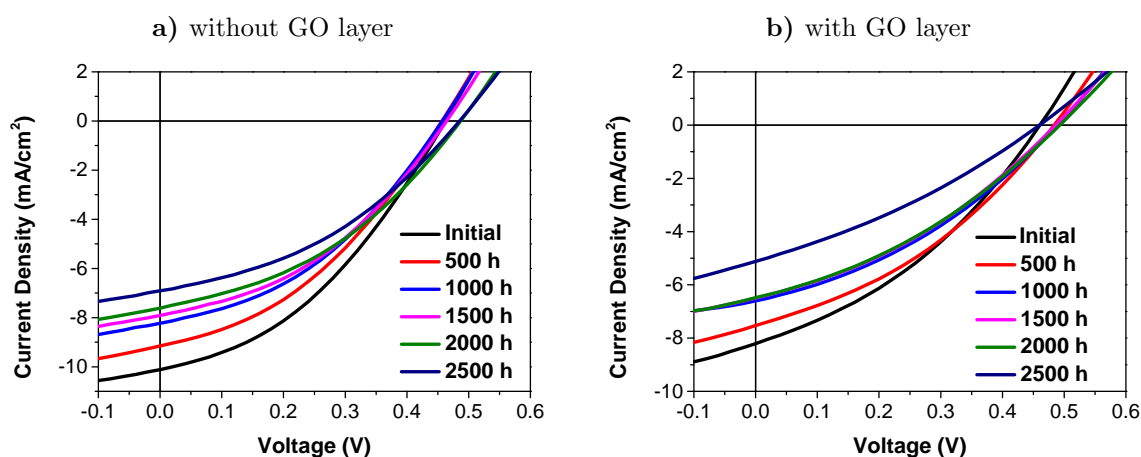
8.3.5.2 Graphene oxide protective layer

Graphene oxide (GO) is a versatility material and has been used for different purposes in OSCs such as hole transport layer [41, 42], electron transport layer [43, 44] or transparent electrode [45, 46]. Graphene is well known as an impermeable material [47, 48]. In the case of graphene oxide, Compton et al. [49] reported that polystyrene-graphene nanocomposites have low O_2 permeability, thus being promising packaging materials.

Chen et al. [50] found that CVD graphene coated on the surface of Cu or Ni protects the metal from oxidation. Therefore, graphene-based materials are excellent environmental barriers [48, 51]. Zhike et al. [52] demonstrated that two or more layers of graphene top electrodes can protect OPVs very well from air contamination because multilayer graphene films are impermeable to air. Due to its properties, graphene oxide is a suitable material to be used as a protective layer on OSCs. It can be used to protect the active layer from oxygen and moisture diffusion as well as from interlayer diffusion.

In this work, graphene oxide was tested as OSCs protective layer, placed in between the active layer and the hole transport layer. A reference device without a GO protective layer and another one with a GO protective layer were tested for 2500 h under real outdoor conditions. Figure 8.14 shows $J - V$ curves recorded every 500 h while Table 8.7 shows the photovoltaic parameters. The data plotted as a function of time is shown in Fig. 8.15.

Figure 8.14: $J - V$ curves for OSCs degradation tests, without and with a GO protective layer, under real outdoor conditions, according to the ISOS-O-1 standard.



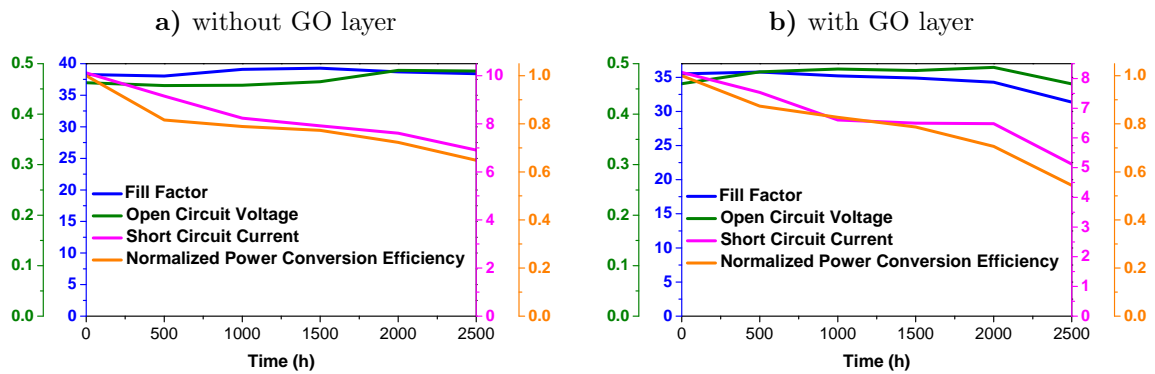
Source: Own author

Table 8.7: Photovoltaic parameters for OSCs degradation tests, without and with a GO protective layer, under real outdoor conditions, according to the ISOS-O-1 standard.

GO layer	condition	J_{sc} (mA/cm ²)	V_{oc} (V)	FF (%)	PCE (%)
no	pristine	10.12	0.46	38.88	2.10
	after 500 h	9.15	0.46	38.05	1.71
	after 1000 h	8.23	0.46	39.11	1.65
	after 1500 h	7.91	0.46	39.29	1.62
	after 2000 h	7.61	0.49	38.70	1.51
	after 2500 h	6.90	0.49	38.41	1.36
yes	pristine	8.21	0.46	35.51	1.63
	after 500 h	7.53	0.48	35.78	1.42
	after 1000 h	6.60	0.49	35.21	1.35
	after 1500 h	6.50	0.49	34.89	1.28
	after 2000 h	6.48	0.49	34.29	1.15
	after 2500 h	5.12	0.46	31.37	0.89

Source: Own author

Figure 8.15: Time evolution of the photovoltaic parameters for OSCs degradation tests, without and with a GO protective layer, under real outdoor conditions, according to the ISOS-O-1 standard.

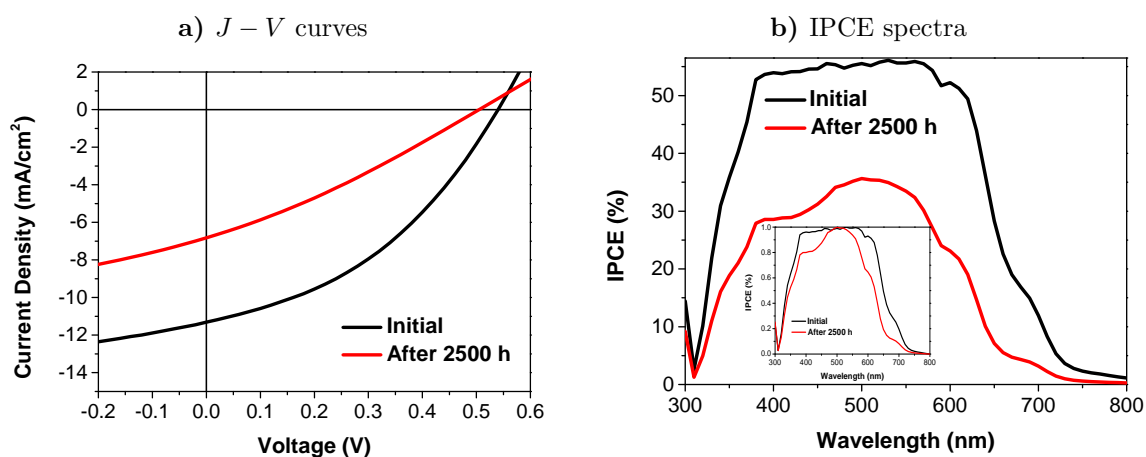


Source: Own author

These devices were also measured under solar simulator conditions and have been characterized regarding the external quantum efficiency, before and after the stability tests. Figure 8.16 shows the $J - V$ curves and IPCE spectra for the solar cell with a

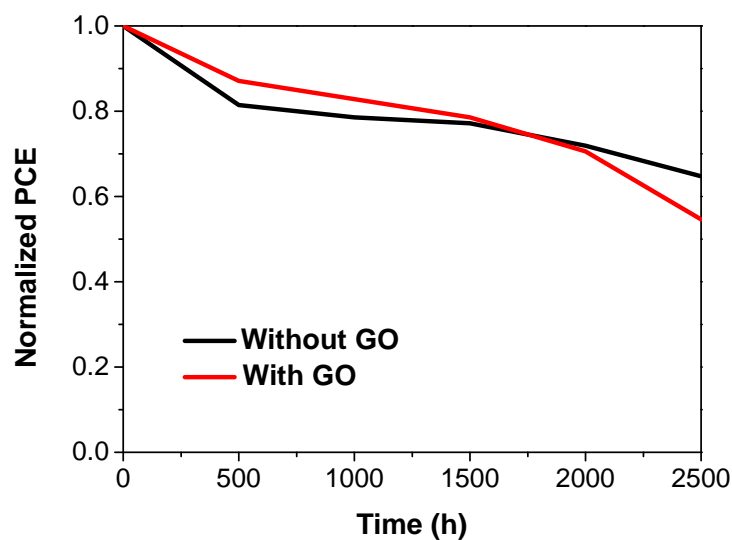
graphene oxide protective layer (see data for the reference device on Fig. 8.12). The inset in Fig. 8.16 shows normalized IPCE spectra. These results indicate that the use of a graphene oxide protective layer seems to be causing a malefic effect on the stability of these organic solar cells. It is important to notice that, while the degradation of the reference devices (without GO) was mainly due to losses in short circuit current, the losses in PCE of samples with a GO layer were due to losses in short circuit current and also fill factor. Looking more closely to the time evolution of PCE for the samples with and without a GO layer, which is depicted in Fig. 8.17, it can be observed that, at least for the first 1500 h, the sample with a GO layer was more stable. It is true that at end of the test the sample with a GO layer is less stable, but it is important to point out that its electrical connectors were more oxidized than those of the sample without the protective layer. This extra oxidation can be the reason for the decrease on fill factor values.

Figure 8.16: $J - V$ curves and IPCE spectra for OSCs degradation tests with a GO protective layer under solar simulator conditions, before and after the ISOS-O-1 2500-h stability test. The inset shows normalized IPCE spectra.



Source: Own author

Figure 8.17: Comparison between the time evolution of PCE for OSC with and without a GO protective layer.

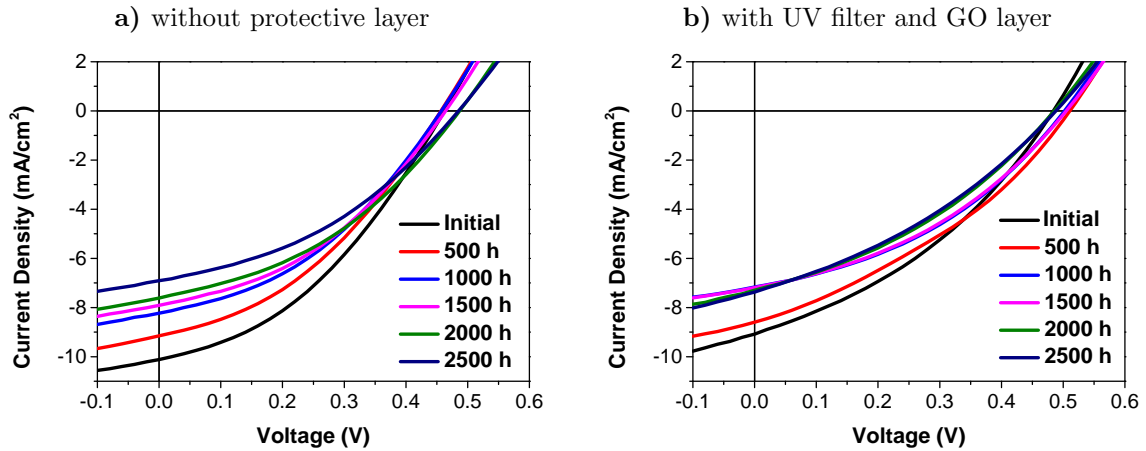


Source: Own author

8.3.5.3 UV filter and graphene oxide protective layer

The effect of a combination of UV filter and graphene oxide protective layer on the stability of OSCs was also evaluated. Figure 8.18 shows $J - V$ curves recorded every 500 h, while Table 8.8 shows the photovoltaic parameters. The data plotted as a function of time is shown in Fig. 8.19.

Figure 8.18: $J - V$ curves for OSCs degradation tests, without and with a combination of UV filter and GO protective layer, under real outdoor conditions, according to the ISOS-O-1 standard.



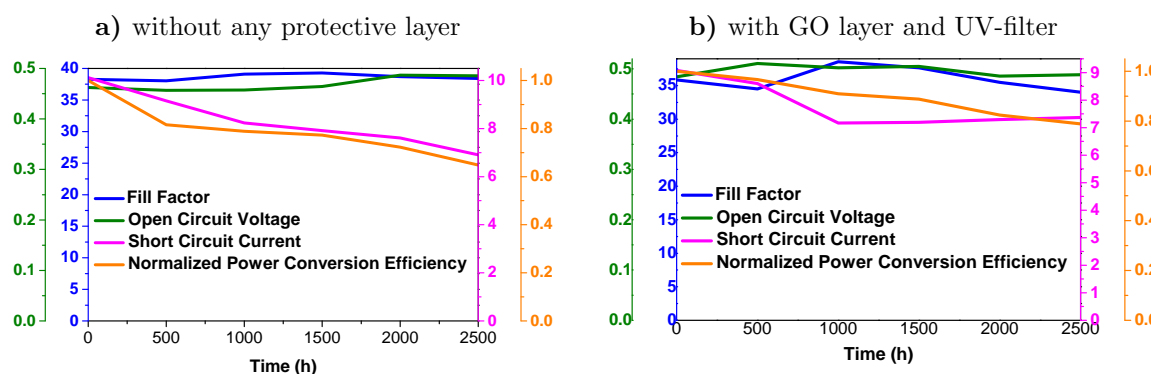
Source: Own author

Table 8.8: Photovoltaic parameters for OSCs degradation tests, without and with a combination of UV filter and GO protective layer, under real outdoor conditions, according to the ISOS-O-1 standard.

UV filter + GO layer	condition	J_{sc} (mA/cm ²)	V_{oc} (V)	FF (%)	PCE (%)
no	pristine	10.12	0.46	38.88	2.10
	after 500 h	9.15	0.46	38.05	1.71
	after 1000 h	8.23	0.46	39.11	1.65
	after 1500 h	7.91	0.46	39.29	1.62
	after 2000 h	7.61	0.49	38.70	1.51
	after 2500 h	6.90	0.49	38.41	1.36
yes	pristine	9.08	0.48	38.62	1.91
	after 500 h	8.60	0.51	34.52	1.84
	after 1000 h	7.17	0.50	38.55	1.73
	after 1500 h	7.19	0.51	37.68	1.69
	after 2000 h	7.30	0.49	35.48	1.57
	after 2500 h	7.37	0.49	34.01	1.50

Source: Own author

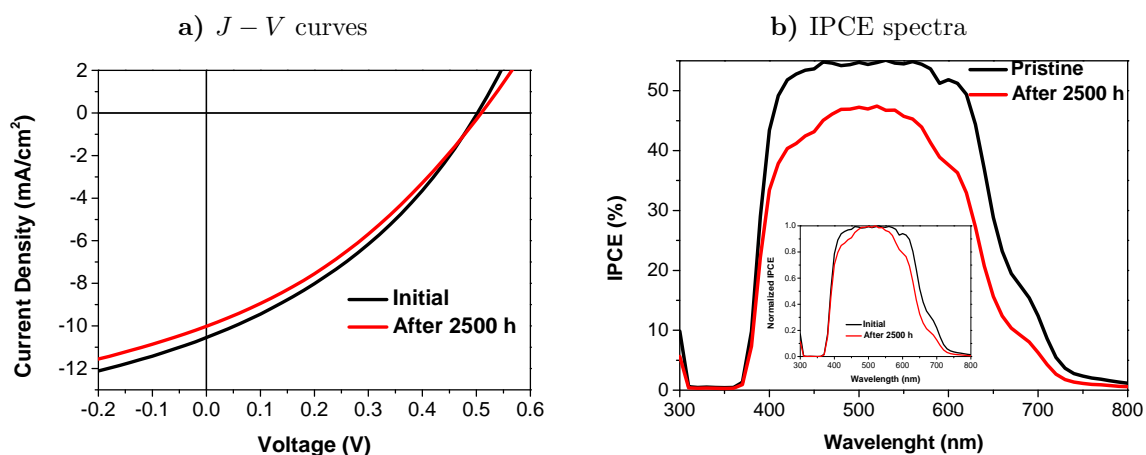
Figure 8.19: Time evolution of the photovoltaic parameters for OSCs degradation tests without and with a combination of UV filter and GO protective layer, under real outdoor conditions, according to the ISOS-O-1 standard.



Source: Own author

Figure 8.20 shows the $J - V$ curves and IPCE spectra for the solar cell protected by a combination of UV filter and graphene oxide protective. This results show that the effect of both protections is much more effective.

Figure 8.20: $J - V$ curves and IPCE spectra for OSCs degradation tests with a combination of UV filter and GO protective layer, before and after the ISOS-O-1 2500-h stability test. The inset shows normalized IPCE spectra.



Source: Own author

8.4 Conclusion

In this chapter the efficiency of OSCs have been tested by means of the application of the ISOS standards; ISOS-D-1, ISOS-L-1 and ISOS-O-1. All the results for the tested have shown that the main factor causing degradation is losses in current density. Two strategies were applied in order to try to improve the stability of these devices. The use of UV-filter and a protective reduced graphene oxide layer. The results have shown that both strategies are effective in improving the stability of OSCs, and the use of both together leads to remarkably efficient device. In one test the long term stability for devices using PEDOT:PSS or V_2O_5 as HTM have been compared and the results showed that V_2O_5 leads to more efficient devices.

8.5 References

- [1] C. Chen, W. Chang, K. Yoshimura, K. Ohya, J. You, J. Gao, Z. Hong, and Y. Yang. An efficient triple-junction polymer solar cell having a power conversion efficiency exceeding 11%. *Adv. Mater.*, 26:5670–5677, 2014.
- [2] Y. Liang and X. Guo. Stability of organic solar cells. In *Organic and Hybrid Solar Cells*. Springer International Publishing, 2014.
- [3] B. Zimmermann, U. Würfel, and M. Niggemann. Longterm stability of efficient inverted p3ht:pcbm solar cells. *Sol. Energ. Mat. Sol. C.*, 93:491–496, 2009.
- [4] J.A. Hauch, P. Schilinsky, S.A. Choulis, R. Childers, M. Biele, and C.J. Brabec. Flexible organic P3HT:PCBM bulk-heterojunction modules with more than 1 year outdoor lifetime. *Sol. Energ. Mat. Sol. C.*, 92:727–731., 2008.
- [5] S.A. Gevorgyan, M.V. Madsen, H.F. Dam, M. Jorgensen, C.J. Fell, K.F. Anderson, B.C. Duck, A. Mescheloff, E.A. Katz, A. Elschner, R. Roesch, H. Hoppe, M. Herme-nau, M. Riede, and F.C. Krebs. Interlaboratory outdoor stability studies of flexible roll-to-roll coated organic photovoltaic modules: stability over 10,000 h. *Sol. Energ. Mat. Sol. C.*, 116:187–196, 2013.

- [6] D. Angmo, P. M. Sommeling, R. Gupta, M. Hösel, S. A. Gevorgyan, J. M. Kroon, G. U. Kulkarni, and F. C. Krebs. Outdoor operational stability of indium-free flexible polymer solar modules over 1 year studied in india, holland, and denmark. *Adv. Eng. Mater.*, 16(8):976–987, 2014.
- [7] R. Roesch, K. R. Eberhardt, S. Engmann, G. Gobsch, and H. Hoppe. Polymer solar cells with enhanced lifetime by improved electrode stability and sealing. *Sol. Energy Mat. Sol. C.*, 117:59–66., 2013.
- [8] F. C. Krebs M. Jorgensen, K. Norrman. Stability/degradation of polymer solar cells. *Sol. Energy Mater. Sol. Cells*, 92:686, 2008.
- [9] M. O. Reese, A. M. Nardes, B. L. Rupert, R. E. Larsen, D. C. Olson, M. T. Lloyd, S. E. Shaheen, D. S. Ginley, G. Rumbles, and N. Kopidakis. Photoinduced degradation of polymer and polymer-fullerene active layers: Experiment and theory. *Adv. Funct. Mater.*, 20:3476–3483, 2010.
- [10] K. Kawano, R. Pacios, D. Poplavskyy, J. Nelson, D. D. C. Bradley, and J. R. Durrant. Degradation of organic solar cells due to air exposure. *Sol. Energy Mater. Sol. Cells*, 90:20, 2006.
- [11] X. Yang, J. K. J. van Duren, R. A. J. Janssen, M. A. J. Michels, and J. Loos. Morphology and thermal stability of the active layer in poly(p-phenylenevinylene)/methanofullerene plastic photovoltaic devices. *Macromolecules*, 37:2151–2158, 2004.
- [12] A. Manor, E. A. Katz, T. Tromholt, and F. C. Krebs. Electrical and photo-induced degradation of ZnO layers in organic photovoltaics. *Adv. Energy Mater.*, 2011(1): 836–843, 2011.
- [13] R. Po, C. Carbonera, A. Bernardi, and N. Camaioni. The role of buffer layers in polymer solar cells. *Energy Environ. Sci.*, 4:285–310, 2011.
- [14] H. Yip and A. K. Y. Jen. Recent advances in solution-processed interfacial materials for efficient and stable polymer solar cells. *Energy Environ. Sci.*, 5:5994–6011, 2012.

- [15] M. T. Greiner, L. Chai, M. G. Helander, W. Tang, and Z. Lu. Transition metal oxide work functions: The influence of cation oxidation state and oxygen vacancies. *Adv. Funct. Mater.*, 22(21):4557–4568, 2012.
- [16] Y. Zhou, C. Fuentes-Hernandez, J. Shim, J. Meyer, A. J. Giordano, H. Li, P. Winget, T. Papadopoulos, H. Cheun, J. Kim, M. Fenoll, A. Dindar, W. Haske, E. Najafabadi, T. M. Khan, H. Sojoudi, S. Barlow, S. Graham, J. Brédas, S. R. Marder, A. Kahn, and B. Kippelen. A universal method to produce low-work function electrodes for organic electronics. *Science*, 336:327–332, 2012.
- [17] Z. He, C. Zhong, S. Su, M. Xu, H. Wu, and Y. Cao. Enhanced power-conversion efficiency in polymer solar cells using an inverted device structure. *Nat Photon*, 6: 591–595, 2012.
- [18] E. L. Ratcliff, B. Zache, and N. R. Armstrong. Selective interlayers and contacts in organic photovoltaic cells. *J. Phys. Chem. Lett.*, 2:1337–1350, 2011.
- [19] S. Chen, J. R. Manders, S. Tsang, and F. So. Metal oxides for interface engineering in polymer solar cells. *J. Mater. Chem.*, 22:24202–24212, 2012.
- [20] R. Steim, F. R. Kogler, and C. J. Brabec. Interface materials for organic solar cells. *J. Mater. Chem.*, 20:2499–2512, 2010.
- [21] S. Trost, T. Becker, K. Zilberberg, A. Behrendt, A. Polywka, R. Heiderhoff, P. Görrn, and T. Riedl. Plasmonically sensitized metal-oxide electron extraction layers for organic solar cells. *Sci. Rep.*, 5(7765):1–9, 2015.
- [22] F. C. Krebs, Y. Thomann, R. Thomann, and J. W. Andreasen. A simple nanostructured polymer/ZnO hybrid solar cell-preparation and operation in air. *Nanotechnology*, 19(42):1–12, 2008.
- [23] I. Boyano, M. Bengoechea, I. de Meaza, O. Miguela, I. Canterob, E. Ochoteco, H. Grandea, M. Lira-Cantú, and P. Gomez-Romero. Influence of acids in the Ppy/V₂O₅ hybrid synthesis and performance as a cathode material. *Journal of Power Sources*, 174(2):1206–1211, 2007.

- [24] M. O. Reese, S. A. Gevorgyan, M. Jorgensen, E. Bundgaard, S. R. Kurtz, D. S. Ginley, D. C. Olson, M. T. Lloyd, P. Morvillo, E. A. Katz, A. Elschner, O. Haillant, T. R. Currier, V. Shrotriya, M. Hermenau, M. Riede, K. R. Kirovi, G. Trimmel, T. Rath, O. Inganäs, F. Zhang, M. Andersson, K. Tvingstedt, M. Lira-Cantu, D. Lairdm, C. McGuinness, S. Gowrisanker, M. Pannone, M. Xiao, J. Hauch, and Roland Stei. Consensus stability testing protocols for organic photovoltaic materials and devices. *Sol. Energy Mater. Sol. Cells*, 95(5):1253–1267, 2011.
- [25] M. Manceau, A. Rivatona, J. Gardette, S. Guillerez, and N. Lemaître. Light-induced degradation of the P3HT-based solar cells active layer. *Sol. Energy Mater. Sol. Cells*, 95(5):1315–1325, 2011.
- [26] T. Tromholt, M. Manceau, M. Helgesen, J. E. Carlé, and F. C. Krebs. Degradation of semiconducting polymers by concentrated sunlight. *Sol. Energy Mater. Sol. Cells*, 95(5):1308–1314, 2011.
- [27] E. Voroshazi, B. Verreet, T. Aernouts, and P. Heremans. Long-term operational lifetime and degradation analysis of P3HT: PCBM photovoltaic cells. *Sol. Energy Mater. Sol. Cells*, 95(5):1303–1307, 2011.
- [28] S. Bertho, G. Janssen, T. J. Cleij, B. Conings, W. Moons, A. Gadisa, J. D’Haen, E. Goovaerts, L. Lutsen, J. Manca, and D. Vanderzande. Effect of temperature on the morphological and photovoltaic stability of bulk heterojunction polymer: fullerene solar cells. *Sol. Energy Mater. Sol. Cells*, 92(7):753–760, 2008.
- [29] M. S. A. Abdou, F. P. Orfino, Z. W. Xie, M. J. Deen, and S. Holdcroft. Reversible charge-transfer complexes between molecular-oxygen and poly(3-alkylthiophene)s. *Advanced Materials*, 6(11):838–841, 1994.
- [30] A. Sperlich, H. Kraus, C. Deibel, H. Blok, J. Schmidt, and V. Dyakonov. Reversible and irreversible interactions of poly(3-hexylthiophene) with oxygen studied by spin-sensitive methods. *J. Phys. Chem. B*, 115(46):13513–13518, 2011.

- [31] J. Schafferhans, A. Baumann, A. Wagenpfahl, C. Deibel, and V. Dyakonov. Oxygen doping of P3HT:PCBM blends: Influence on trap states, charge carrier mobility and solar cell performance. *Org. Electron.*, 11(10):1693–1700, 2010.
- [32] M. D. Pace, T. C. Christidis, J. J. Yin, and J. Milliken. Epr of a free-radical in C-60-effect of O₂. *J. Phys. Chem.*, 96(17):6855–6858, 1992.
- [33] T. Endale, E. Sovernigo, A. Radivo, S. D. Zilio, A. Pozzato, T. Yohannes, L. Vaccari, and M. Tormen. Investigation of photodegradation in polymer solar cells blended with different fullerenes derivatives. *Sol. Energy Mater. Sol. Cells*, 141:423–428, 2015.
- [34] R. D. Deanin, S. A. Orroth, R. W. Eliassen, and T. N. Greer. Mechanism of ultraviolet degradation and stabilization in plastics. *Polym. Eng. Sci.*, 10(4):228–234, 1970.
- [35] X. Crispin, S. Marciniak, W. Osikowicz1, G. Zotti, A. W. Denier van der Gon, F. Louwet, M. Fahlman, L. Groenendaal, F. De Schryver, and W. R. Salaneck. Conductivity, morphology, interfacial chemistry, and stability of poly(3,4-ethylene dioxythiophene)-poly(styrene sulfonate): A photoelectron spectroscopy study. *J. Polym. Sci., Part B: Polym. Phys.*, 41(21):2561–2583, 2003.
- [36] H. Hintz, C. Sessler, H. Peisert, H.-J. Egelhaaf, and T. Chassé. Wavelength-dependent pathways of poly-3-hexylthiophene photo-oxidation. *Chem. Mater*, 24(14):2739–2743, 2012.
- [37] L. Córcoles, J. Abad, J. Padilla, and A. Urbina. Wavelength influence on the photodegradation of P3HT:PCBM organic solar cells. *Sol. Energy Mater. Sol. Cells*, 2015.
- [38] K. Norrman, S. A. Gevorgyan, and F. C. Krebs. Water-induced degradation of polymer solar cells studied by H₂¹⁸O labeling. *ACS Appl. Mater. Interfaces*, 1(1):102–112, 2009.
- [39] A. Seemann, H.-J. Egelhaaf, C. J. Brabec, and J. A. Hauch. Influence of oxygen on semi-transparent organic solar cells with gas permeable electrodes. *Org. Electron.*, 10(8):1424–1428, 2009.

- [40] G. Teran-Escobar, J. Pampel, J. M. Caicedo, and M. Lira-Cantu. Low-temperature, solution-processed, layered V_2O_5 hydrate as the hole-transport layer for stable organic solar cells. *Energy Environ. Sci.*, 6:3088–3098, 2013.
- [41] I. P. Murray, S. J. Lou, L. J. Cote, S. Loser, C. J. Kadleck, T. Xu, J. M. Szarko, B. S. Rolczynski, J. E. Johns, J. Huang, L. Yu, L. X. Chen, T. J. Marks, and M. C. Hersam. Graphene oxide interlayers for robust, high-efficiency organic photovoltaics. *J. Phys. Chem. Lett.*, 2(24):3006–3012, 2011.
- [42] S. S. Li, K. H. Tu, C. C. Lin, C. W. Chen, and M. Chhowalla. Solution-processable graphene oxide as an efficient hole transport layer in polymer solar cells. *Acs Nano*, 4:3169–3174, 2010.
- [43] J. Liu, M. Durstock, and L. Dai. Graphene oxide derivatives as hole- and electron-extraction layers for high-performance polymer solar cells. *Energy Environ. Sci.*, 7:1297–1306, 2014.
- [44] J. Liu, M. Durstock, and L. Dai. Graphene oxide derivatives as hole- and electron-extraction layers for high-performance polymer solar cells. *Energy Environ. Sci.*, 7:1297–1306, 2014.
- [45] G. Eda, G. Fanchini, and M. Chhowalla. Large-area ultrathin films of reduced graphene oxide as a transparent and flexible electronic material. *Nat. Nanotechnol.*, 3:270–274, 2008.
- [46] P. R. Kidambi, C. Weijtens, J. Robertson, S. Hofmann, and J. Meyer. Multifunctional oxides for integrated manufacturing of efficient graphene electrodes for organic electronics. *Appl. Phys. Lett.*, 106:063304, 2015.
- [47] D. A. Dikin, S. Stankovich, E. J. Zimney, R. D. Piner, G. H. Dommett, G. Evmenenko, and R. S. Ruoff. Preparation and characterization of graphene oxide paper. *Nature*, 448(7152):457–460, 2007.
- [48] J. S. Bunch, S. S. Verbridge, J. S. Alden, A. M. van der Zande, J. M. Parpia, H. G.

- Craighead, and P. L. McEuen. Impermeable atomic membranes from graphene sheets. *Nano Lett.*, 8(8):2458–2462, 2008.
- [49] O. C. Compton, S. Kim, C. Pierre, J. M. Torkelson, and S. T. Nguyen. Crumpled graphene nanosheets as highly effective barrier property enhancers. *Adv. Mater.*, 22:4759–4763, 2010.
- [50] S. Chen, L. Brown, M. Levendov, W. Cai, S. Y. Ju, J. Edgeworth, X. Li, C. Magnuson, A. Velamakanni, R. D. Piner, J. Kang, J. Park, and R. S. Ruoff. Oxidation resistance of graphene-coated cu and cu/ni alloy. *ACS Nano*, 5:1321–1327, 2011.
- [51] F. Guo, G. Silverberg, S. Bowers, S. P. Kim, D. Datta, and V. Shenoy. Graphene-based environmental barriers. *Environ. Sci. Technol.*, 46:7717–7724, 2012.
- [52] L. Zhike, J. Li, and F. Yan. Package-free flexible organic solar cells with graphene top electrodes. *Advanced Materials*, 25(31):4296–4301, 2013.

9. CONCLUSIONS AND FUTURE WORK

This work explored solution processed transition metal semiconductor oxides (ZnO, TiO₂ and V₂O₅) with focus on their characterization from the materials science point of view as well as their application in next generation dye-sensitized and organic solar cells.

9.1 Conclusions

Electrodeposition - a simple and environmentally friendly growth method - was demonstrated to be efficient to synthesize high-quality ZnO nanostructures/films with good semiconducting properties. The possibility of tuning the semiconductor properties by changing electrodeposition parameters has also been demonstrated. Furthermore, electrodeposited zinc oxide thin films have been applied as working electrodes in efficient DSSCs. As comparison, ZnO nanorods have also been deposited by hydrothermal synthesis on TCO substrates and applied in efficient DSSCs. The semiconductor properties of these thin films and the performance of the DSSCs for both types of ZnO thin films were found to be similar which leads to a conclusion that these films are promising materials to be applied in DSSCs.

Natural dyes were extracted from three plants, which can be found in northeast Brazil, using simple and inexpensive methods and were successfully applied as sensitizers in DSSCs. Such DSSCs were assembled with commercially available TiO₂ as working electrode. The characterization of these natural dyes revealed that their absorption is compatible with the optical band gap and HOMO-LUMO levels of anthocyanins. Moreover, these dyes are suitable for use with the TiO₂ working electrode and I^-/I_3^- redox mediator electrolyte. The dye *N. oleander* presented better performance than the other considered dyes, possibly due to its better interaction with the TiO₂ working electrode.

Vanadium oxide - V_2O_5 - was successfully applied in ITO-free OSCs and TPSCs. In single junction devices, the OSCs fabricated with water-based V_2O_5 showed better performance than devices fabricated with PEDOT:PSS as HTL. A comparison between the two different preparations of V_2O_5 for HTL revealed that water-based V_2O_5 leads to more efficient devices than ViPr-based V_2O_5 . Water-based V_2O_5 was also considered as the HTL in normal configuration devices, and OSCs based on V_2O_5 outperformed the reference devices with PEDOT:PSS. Water-based V_2O_5 were also used as part of the recombination layer in TPSCs, yielding *PCE* values as high as 1.11%. Finally, flexible OSCs reached efficiencies that approach the efficiencies obtained for rigid glass-based, spin coated devices.

The stability of organic solar cells was evaluated by means of the application of ISOS standards ISOS-D-1, ISOS-L-1, and ISOS-O-1. The results revealed that efficiency drops down mainly due to losses in J_{SC} , which can be attributed mainly to damage of the P3HT polymer due to high energy UV photons and to the migration of deleterious species to the active layer. Two strategies were applied to improve the stability of these device: the use of UV filter to eliminate the effect of the high energy photons and the use of a protective reduced graphene oxide (GO) layer. These strategies were shown to be effective at improving the stability of OSCs. The use of a UV filter extended the T_{80} time in 750 h, while the use of GO extended it about 300 h. The use of the combination of both UV filter and GO layers leads to a large improvement in the long term stability since at the end of the experiment the efficiency for these devices were still around T_{80} . During the application of the ISOS-O-1 standard a fair comparison between devices using PEDOT:PSS and V_2O_5 was also performed and the results have shown a better stability for the OSCs that used V_2O_5 as HTM. The T_{80} time for V_2O_5 was increased by a factor of 10.

9.2 Future work

Future work on electrodeposited ZnO must be focused on the application of thin films with another suitable dyes, as the dye used in this study was developed to be used with

TiO₂. For natural dyes, future studies must be focused on further purification of the extracted dyes. As this work is the first to use water based V₂O₅ as HTM for ITO-free plastic solar cells, there are a large amount of work to be done. Future work can be focused on improving the quality of V₂O₅ films in order to enhance cells performance. Moreover, use of highly conductive PEDOT:PSS on the back electrode should be avoided. In terms of stability tests, other tests exploring other ISOS standards with control of temperature and humidity can be applied to improve the understanding of the degradation of such devices and consequently their stability.